Development and Performance Evaluation of the Steel Moment-resisting Knee-braced Frame System Under Seismic and Wind Loads

by

Mahdi Mokhtari

A thesis submitted in partial fulfillment of the requirements for the degree of

Doctor of Philosophy

in

Structural Engineering

Department of Civil and Environmental Engineering

University of Alberta

Abstract

The primary goal of this Ph.D. project is to develop an innovative steel lateral load-resisting system (LLRS), referred to as the Moment-resisting Knee-braced Frame (MKF), to resist wind and earthquake loads. This system is proposed as an alternative to conventional steel LLRSs for applications in multi-storey buildings. Specifically, this research aims to develop analysis and design procedures for the MKF, using numerical simulations, and provide insight into collapse performance under seismic and wind loads, as well as earthquake-induced economic losses.

In the first phase of the research, a design method following the performance-based plastic design procedure is proposed to analyse MKFs and size the structural members. A prototype frame part of an office building is selected to demonstrate the performance of the proposed system and the design method. The MKF is also designed using the conventional elastic approach in accordance with the National Building Code (NBC) of Canada. The seismic design is performed in the framework of the Canadian steel design standard, CSA S16-19, assuming the formation of plastic hinges at the ends of moment-connected beams and the base of the columns. The seismic and collapse performances of the frames are examined using nonlinear static analysis, nonlinear response history analysis (NLRHA), and incremental dynamic analysis (IDA). Fragility curves are developed and used to study the collapse probability of the system.

The second phase of this study involves the development and verification of the seismic design parameters, including the overstrength-related force modification factor, ductility-related force modification factor, deflection amplification factor, and design period relationship for the MKF system. A set of 14 prototype frames is designed as per the 2015 NBC of Canada. Nonlinear static analyses are then carried out to determine the preliminary seismic design parameters. Six new MKFs (assessment frames) are designed using the proposed seismic design parameters, and their seismic

and collapse performances are examined. The results confirm that the MKF shall be designed as a moderately ductile LLRS using overstrength and ductility factors of 1.60 and 3.0, respectively, with a height limit of 40 meters in high seismic regions of Canada.

In the third phase of this Ph.D. project, the earthquake-induced economic loss performance of multi-storey buildings equipped with the steel MKF system was assessed and quantified using a probabilistic storey-based loss estimation procedure. The expected economic losses and the expected annual loss values are then computed and interrogated for six prototype buildings to further our understanding of the structural performance of the MKF. The results indicate that the MKF buildings offer promising seismic loss metrics and that the economic loss of the MKF buildings is governed by non-structural repair costs under frequently occurring seismic events, while collapse and demolition dominate building losses in the case of larger seismic intensities.

The last phase addresses the performance of the MKF system under wind. A 12-storey prototype building equipped with the steel MKF system located in a low seismic region is designed under lateral wind loads per 2020 NBC of Canada. Wind pressure histories consistent with the building aspect ratios scaled to multiple hazard levels are then used to perform NLRHA and IDA to evaluate the response of the MKF at both system and component levels. The results show that the MKF system can meet the serviceability and strength requirements set by the NBC of Canada and ASCE 2019 Prestandard for Performance-Based Wind Design. Furthermore, the MKF system exhibits an acceptable collapse performance with a significant reserve capacity, which can potentially be leveraged for a more balanced wind design with limited inelastic response.

Preface

This doctoral dissertation represents the original work conducted by Mahdi Mokhtari. This study was undertaken in collaboration with Dr. Ali Imanpour, who served as the research supervisor at the Department of Civil and Environmental Engineering of the University of Alberta. The thesis is divided into 7 chapters, with chapters 1 and 2 serving as the introduction and literature review. The subsequent chapters have either been previously published or are currently in preparation for publication, drawing upon the findings of this thesis:

Chapter 3 is based on the published paper titled **Mokhtari M., Islam A., Imanpour A., "Development, seismic performance and collapse evaluation of steel moment-resisting knee braced frame",** ***Journal of Constructional Steel Research,*** **193, 107262, 2022.**

Chapter 4 is based on the published paper titled **Mokhtari M., Imanpour A., "Proposed seismic design parameters for the moment-resisting knee-braced frame system",** ***Engineering Structures*****, 276, 115318, 2023.**

Chapter 5 will be submitted as **Mokhtari M., Moammer O., Imanpour A., "Earthquake-induced Loss Assessment of Buildings with Steel Moment-resisting Knee-braced Frames under Seismic Hazard of Southwestern Canada",** to a journal with some modifications.

Chapter 6 will be submitted as **Mokhtari M., Imanpour A., "Wind Performance Evaluation of Mid-rise Steel Moment-resisting Knee-braced Frame Structures"** to a journal with some modifications.

Part of this study has been published and presented as follows:

- Mokhtari M., Imanpour A., "Comparison of the seismic performance of steel moment-resisting frames and moment-resisting knee braced frames", *Proceedings of the Canadian Society of Civil Engineering Annual Conference*, 2021.

- Mokhtari M., Imanpour A., "Evaluation of the seismic behaviour of modular steel moment-resisting frame structures with knee braces, *Proceedings of the 10th International Conference on Behaviour of Steel Structures in Seismic Areas (STESSA)*, 2022.

The dissertation is concluded in chapter 7 by presenting a summary of the key findings and limitations of this research project as well as by providing some recommendations for future work.

"The secrets of eternity neither you know nor I,

And this mysterious scroll neither you read nor I;

Behind the veil much I discourse with you,

When the veil is lifted neither you shall remain nor I."

Omar Khayyam

(Translated from Persian by Manavaz Alexanderya)

Acknowledgements

First and foremost, I am deeply indebted to my advisor, Dr. Ali Imanpour, for his continued encouragement and exceptional belief in my abilities, and for allowing me to work under his supervision. His insightful feedback, patience, and commitment to my intellectual growth played an essential role in the completion of this work. In addition to the valuable academic support he extended, his presence in my life was influential as he offered unwavering emotional support during times of unexpected personal challenges and hardships. Dr. Imanpour, as simple as it may sound, “Thank you” for everything.

I would like to extend my sincere appreciation to the members of my supervisory committee, Dr. Robert Driver and Dr. Mohamed Al-Hussein, for sharing their wisdom and providing constructive critiques, which certainly enriched the quality of this work. I would also like to thank Dr. Carlos Cruz Noguez and Dr. Saber Moradi who served as my Ph.D. defense examiners and Dr. Yong Li who served as the chair of the meeting.

Special thanks to Dr. Mojgan Yaghoubshahi, Dr. Abolfazl Ashrafi, and Mr. Omid Moammer for their input on the cost estimation of steel structures, ground motion scaling, and seismic-induced loss assessment of steel-framed buildings, and indeed, for their friendship. Moreover, I am highly thankful to Dr. Gerard J. O’Reilly for his input on incremental dynamic analysis using the Trace-Hunt-Fill algorithm. The productive discussions and enlightening remarks by my friends and colleagues at the Steel Centre research group are also highly appreciated.

I would like to acknowledge the financial support provided by the Natural Sciences and Engineering Research Council of Canada (NSERC), the Canadian Institute of Steel Construction (CISC), WF Steel & Crane, the Canadian Welding Bureau (CWB), Alberta Graduate Excellence Scholarship (AGES), CISC G.L. Kulak Scholarship in Steel Structures Research, CISC Centre for

Steel Education and Research (The Steel Centre), and the Department of Civil and Environmental Engineering at the University of Alberta. Without these resources and opportunities, conducting this research would not have been possible.

I am deeply appreciative of my family, especially my lovely parents, Batoul and Ali, and my dear friends, Mohammad R., Mahdi G.M., Saeid S., Mahdi M., Emad A., and many others for their support and understanding throughout this journey. Your love and encouragement have been my rock, and I am forever grateful.

Finally, I am thankful for the presence of those who are not part of my life anymore but had a significant influence on the progress of this research and contributed to my personal well-being and academic growth. This thesis stands as a testament to the collective efforts of a supportive community. Thank you all for being a part of this incredible journey.

Mahdi Mokhtari
April 2024

Table of Contents

List of Tables

List of Figures

List of Abbreviations

ACMR	Adjusted Collapse Margin Ratio
ASCE	American Society of Civil Engineers
BRKB	Bucking Restrained Knee Brace
BRKBF	Buckling-Restrained Knee-Braced Frame
BRKB-TMF	Buckling-Restrained Knee-Braced Truss Moment Frame
CBF	Concentrically Braced Frame
CJP	Complete Joint Penetration
CMR	Collapse Margin Ratio
CSA	Canadian Standards Association
DDI	Deformation Damage Index
DE	Design Earthquake
DKB	Disposable Knee Bracing
DM	Damage Measure
DYM	Designated Yielding Member
EAL	Expected Annual Loss
EBF	Eccentrically Braced Frame
EDP	Engineering Demand Parameter
ESFP	Equivalent Static Force Procedure
ELF	Equivalent Lateral Force
GM	Ground Motion
HTF	Hunt-Trace-Fill
HSS	Hollow Structural Section

IDA	Incremental Dynamic Analysis
IDWA	Incremental Dynamic Wind Analysis
IM	Intensity Measure
KBF	Knee-Braced Frame
KBMF	Knee-Braced Moment Frame
KBRF	Knee-Braced Moment Resisting Frame
KCF	Knee Connection Frame
kN	Kilonewton
LLRS	Lateral Load-Resisting System
LTB	Lateral-Torsional Buckling
MCE	Maximum Considered Earthquake
MKF	Moment-resisting Knee-braced Frame
MPa	Megapascal
MRF	Moment Resisting Frame
MWFRS	Main Wind Force-Resisting System
NBC	National Building Code
NLRHA	Nonlinear Response History Analysis
OpenSees	Open System for Earthquake Engineering Simulation
PBEE	Performance-Based Earthquake Engineering
PBPD	Performance-Based Plastic Design
PBWD	Performance-Based Wind Design
PEER	Pacific Earthquake Engineering Research Center
PFA	Peak Floor Acceleration

PGA	Peak Ground Acceleration
PJP	Partial-Joint Penetration
PSD	Power Spectral Density
RBS	Reduced Beam Section
RSA	Response Spectrum Analysis
RSDR	Residual Storey Drift Ratio
SCBF	Special Concentrically Braced Frame
SCWB	Strong Column/Weak Beam
SDR	Storey Drift Ratio
SE	Service Earthquake
SLS	Serviceability Limit State
SMRF	Special Moment Resisting Frame
SPSC	Single Plate Shear Connection
SSF	Spectral Shape Factor
STD	Standard Deviation
THF	Trace-Hunt-Fill
TPU	Tokyo Polytechnique University
ULS	Ultimate Limit State
USGS	United States Geological Survey
WF	Wide Flange
WTHA	Wind Time History Analysis

CHAPTER 1

INTRODUCTION

1.1. Background

Steel-framed structures shall be designed to dissipate earthquake-induced energy through material nonlinearities. The structural system should also possess sufficient lateral stiffness and strength to transmit the lateral loads to the foundation without brittle failures or collapse.

Steel concentrically Braced Frames (CBFs) provide excellent lateral stiffness and strength. However, their inelastic energy dissipation capacity can be negatively affected by the post-buckling behaviour of their diagonal braces. The lateral strength and stiffness of CBFs can be considerably reduced upon buckling of the diagonal braces, resulting in an asymmetric cyclic response and low ductility capacity [1]. However, steel Eccentrically Braced Frames (EBFs) often dissipate the input seismic energy by yielding their link beams in shear, thus providing a stable and symmetric hysteretic response. Nonetheless, EBFs typically lead to large deformations in the floor beams, which may impose significant upgrade costs after major seismic events [2]. Architectural obstructions and relatively complicated gusset-plate details required for ductile behaviour should also be considered as some of the most significant drawbacks of the braced frames.

Steel moment-resisting frames (MRFs) have long been considered one of the most ductile LLRSs for constructing multi-storey buildings, particularly in high seismic regions. Steel MRFs offer several advantages over other steel LLRSs, including minimum architectural obstructions, significant ductility capacity, and the ability to accommodate long spans. However, there are several constraints associated with the design and construction of conventional MRFs, which limits their application in construction of building structures in moderate and even high seismic regions of

Canada. Some of these constraints include low lateral stiffness, prohibitively expensive strengthening requirements for connections, and high fabrication and inspection costs related to Complete Joint Penetration (CJP) groove welds.

As the construction industry demands more efficient construction with a reduction in cost and environmental impacts, there is an urge for the development of high-performance and resilient LLRSs, e.g., alternatives that can efficiently overcome the constraints associated with conventional steel LLRSs. The primary goal of this research is to propose an innovative steel structural system as an alternative to MRFs, referred to as the Moment-resisting Knee-braced Frame (MKF), designed to effectively withstand lateral wind and earthquake loads in multi-storey building structures. This endeavour involves the development of analysis and design methodologies, while showing the benefits of using the MKF system, compared to conventional MRFs, by providing insight into its design-level, beyond design-level, and collapse performances under both seismic and wind loads.

Two bays of a six-storey multi-bay MKF are shown in Figure 1-1. The MKF consists of intermediate beam segments and interior/exterior column trees that are prefabricated in the shop and shipped to the site for assembly, as illustrated in Figure 1-2. The beams are made of wide-flange (WF) sections with shop-welded end plates. Each column tree covers three stories, given the typical length of wide-flange profiles (i.e., 12 – 15 m), with bolted splice connections to join the next column tree. Column splices are comprised of shop-welded end plate connections. The knee braces and beam stubs are welded to the WF column segments in the shop. Knee braces are expected to be made of round hollow structural sections (HSS), rectangular HSS, or wide-flange profiles (square HSS option is shown in Fig. 1) and joined to beam stub/column connections using gusset plates to create simple connections or end bolted plates to facilitate the development of a

fixed connection. Shear tab or double-angle simple connections are used to connect the beam stubs to the columns. The intermediate beam segments are connected to the beam stubs using field-bolted moment connections. The proposed system benefits from prefabricated steel segments in which CJP welds can be replaced with Partial Joint Penetration (PJP) groove welds reinforced with fillet welds (Figure 1-2) to facilitate the fabrication and erection processes in multi-storey steel structures. However, this aspect should be investigated in detail in future relevant studies.

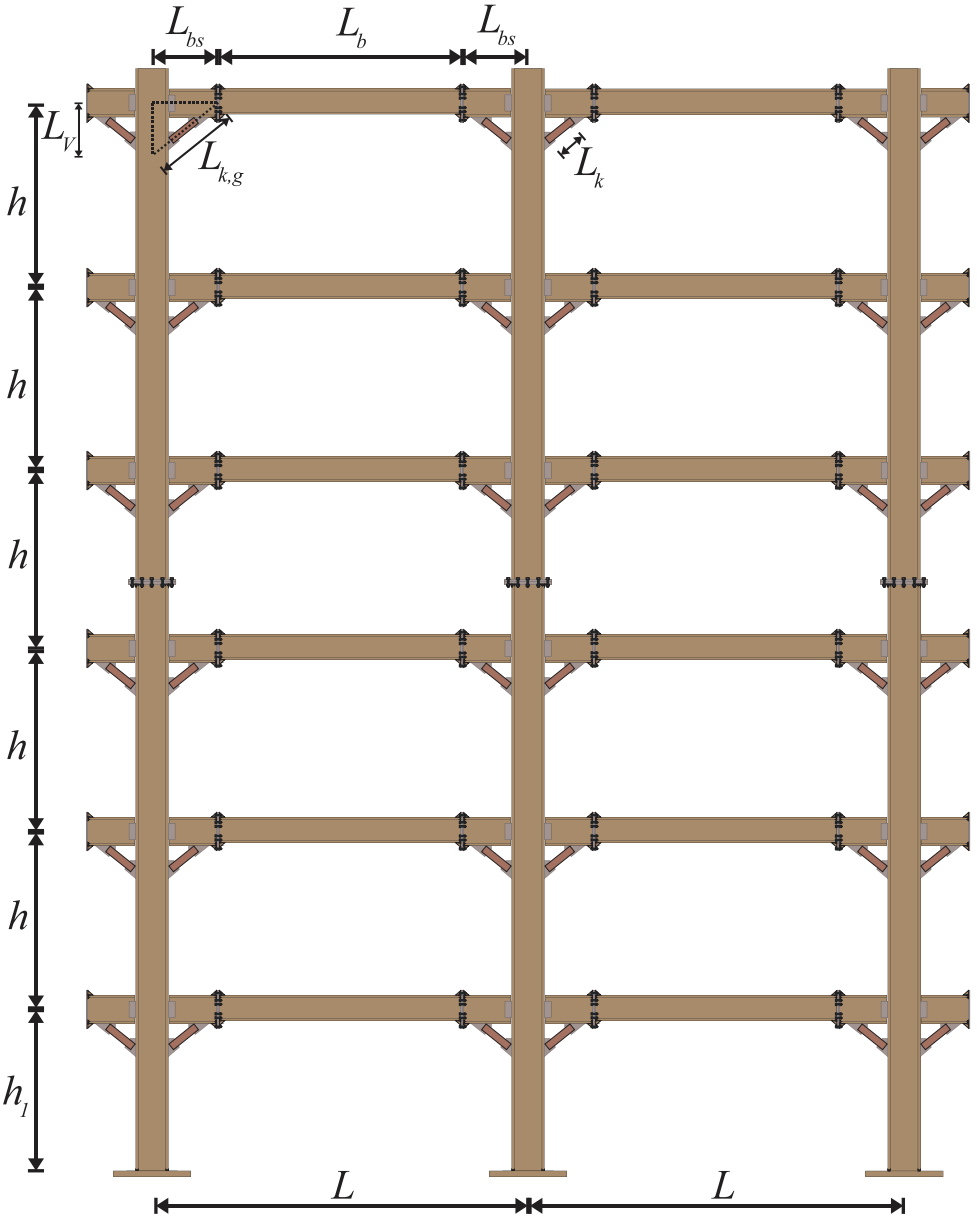

Figure 1-1. Configuration of a six-storey MKF (The height of the first storey is different).

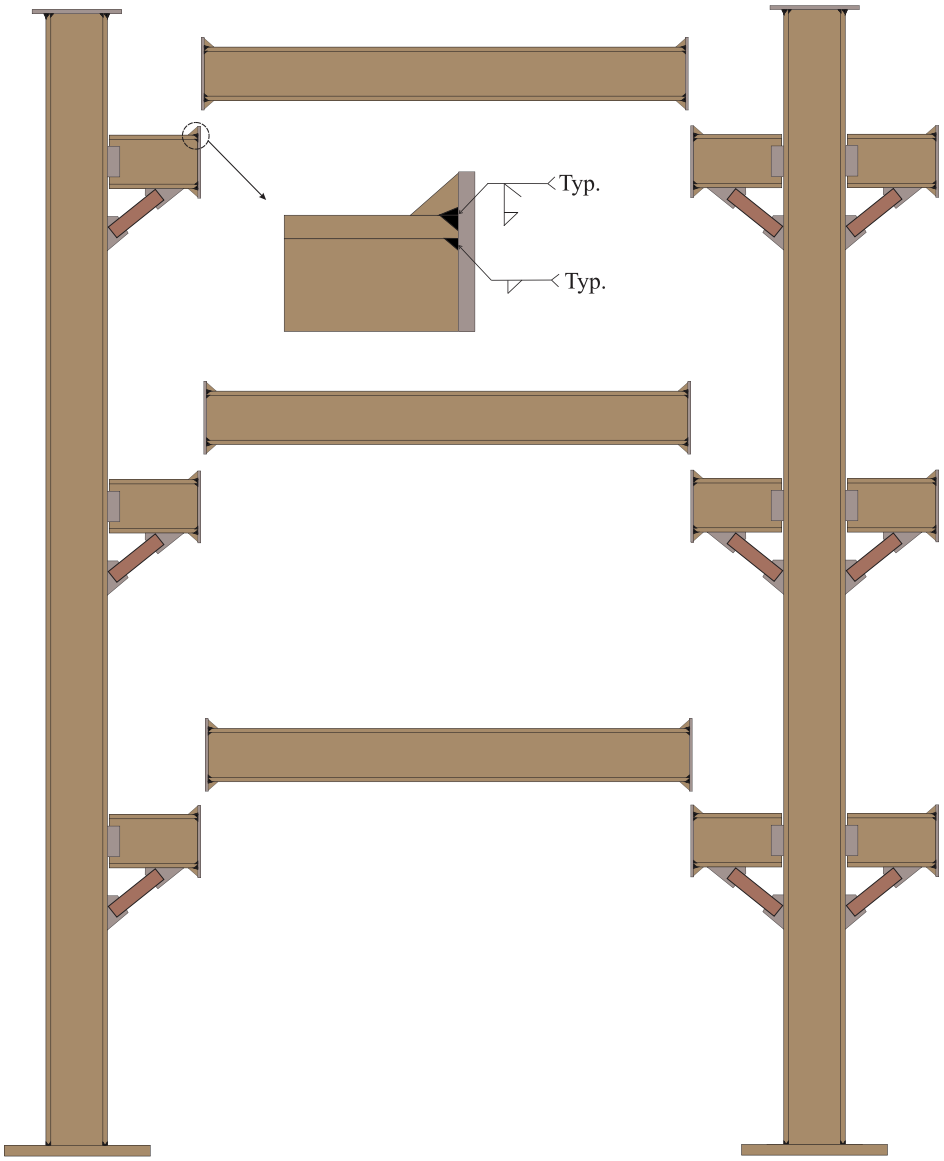

Figure 1-2. Erection sequence and welding details for the proposed MKF system.

The expected plastic mechanism of the proposed system under lateral seismic load is schematically shown in Figure 1-3. This mechanism is assumed as only plausible plastic mechanism throughout this study for developing design guidelines. Further details in this regard will be provided in Chapter 3.

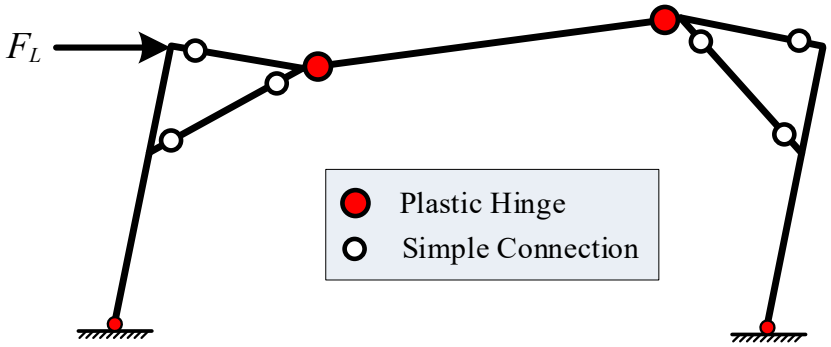

Figure 1-3. MKF desired collapse mechanism (single-storey one-bay frame shown for simplicity).

1.2. Problem Statement

The following research gaps were identified to develop the new MKF system proposed in this Ph.D. research project:

P1) Seismic analysis and design guidelines in the framework of Canadian design practice.

P2) Seismic design parameters, including overstrength- and ductility-related force modification factors according to the requirements of the National Building Code (NBC) of Canada.

P3) Seismic loss performance of the proposed system, considering structural and non-structural damages.

P4) The performance of the system and its reserve capacity under lateral wind loads.

Note that the development of other aspects of the MKF system and experimental validation of the MKF response will be performed in future research projects.

1.2.1. Seismic Design Methodologies and Guidelines

Current seismic provisions prescribed by CSA S16-19 [3] or NBC of Canada [4] do not provide any guidelines on the seismic design of LLRSs equipped with knee braces. Also, it is unclear how geometrical parameters, e.g., braced length ratio and knee brace angle, affect the lateral stiffness, strength, and capacity forces applied to the force-controlled members of the MKF system.

Additionally, design and detailing guidelines should be developed such that the ductility desired in design can be achieved in practice.

Knee brace-to-column connections, as one of the main features of the proposed system, apply concentrated forces to the column trees. Such a large point load can result in significant shear and bending moment demands along the length of columns. This is a unique loading condition for columns as the most critical members of any LLRS since they provide stability to the entire frame. Accordingly, the seismic demands imposed on all steel elements of the MKF system and the load transfer mechanism between Designated Yielding Members (DYMs) and force-controlled elements should be analysed and understood thoroughly. Moreover, all possible limit states that may govern the design should be identified and addressed carefully. Notably, the response of columns must be examined under seismic loading to ensure that the limit states controlled during the design process result in a satisfactory performance and that columns do not experience an undesired failure mechanism.

The seismic demands exerted on DYMs of an MKF can be calculated using either an elastic or plastic analysis method. At the heart of the elastic analysis approach prescribed by the NBC of Canada are the seismic design parameters of a given LLRS, i.e., ductility- and overstrength-related force modification factors. Accordingly, it is crucial to evaluate the seismic design parameters of the MKF system. The conventional elastic analysis method is commonly implemented in seismic design today and requires seismic design parameters along with consistent seismic design guidelines.

As a force-based design approach, the elastic analysis method has several shortcomings that can adversely affect the seismic performance of an LLRS. For instance, the distribution of seismic demands along the height of a steel frame, either obtained through a standard Equivalent Static

Force Procedure (ESFP) [5] or Response Spectrum Analysis (RSA) [5], may not accurately reflect the real inelastic demands expected during an earthquake, thereby leading to inadequate and uneven distribution of plasticity along the frame height. Moreover, LLRSs are designed to possess sufficient strength under seismic demands and enough stiffness to limit lateral deformations in the nonlinear response domain. However, drift limits can dominate the member selection and result in disproportionate member sizes.

A displacement-based plastic analysis method that is independent of seismic design parameters can be developed as a progressive alternative approach to analyse the MKF system under seismic loading. This approach is based on the Performance-Based Plastic Design (PBPD) methodology developed by Leelataviwat and Goel [6]. In the PBPD, the determination of appropriate design lateral load and member-strength hierarchy, selection of a desirable yield mechanism, and structural strength and drift for given hazard levels become part of the design process from the beginning [7]. The methodology is needless of iterations and has been shown to result in more efficient designs and more satisfactory seismic responses compared to the conventional elastic approach for MRFs, EBFs, and CBFs. [7]. However, no PBPD-consistent methodology is available for the proposed MKF system. A PBPD procedure that reflects the behaviour and unique features of the MKF system will provide designers with a robust tool to design MKFs for any given performance objective and hazard level.

1.2.2. Seismic Design Parameters

In the elastic design of an LLRS under seismic loading, the design base shear is computed taking into account the overstrength and ductility capacity in the inelastic range of the material. Similarly, a deflection amplification factor should be applied to the inter-storey drifts obtained from a linear-elastic analysis to determine the expected deformations in the inelastic range under design-level

earthquakes. While the NBC provides seismic design parameters, e.g., overstrength and ductility-related force modification factors, for various conventional LLRSs such as MRFs, CBFs, EBFs, steel plate walls, concrete shear walls etc., no seismic design parameters are available for the MKF system.

1.2.3. Seismic Loss Evaluation

The economic loss due to the damage sustained by structural and non-structural components after a major earthquake event can play a significant role in selecting an LLRS by decision-makers, stakeholders, building owners, and engineers. The seismic loss performance of a new LLRS, such as the MKF system, is considered a vital part of the performance evaluation phase. An LLRS may show satisfactory behaviour under earthquake ground motions in terms of different structural response parameters such as collapse capacity, peak storey drift ratio (SDR), distribution of plasticity throughout designated locations, lateral stiffness, and strength, but fail to provide adequate metrics in terms of earthquake-induced economic loss, e.g., Expected Annual Loss (EAL), which represents the yearly amount that may be spent for earthquake-induced damages. The unique seismic conditions of southwestern Canada, where the complex interaction between tectonic plates in the Pacific Ocean results in three different sources of seismicity, i.e., shallow crustal, subduction intraslab, and subduction interface, further highlight the importance of a seismic loss study since the subduction interface and intraslab earthquakes have the potential to impose large demands on building structures [8, 9]. Moreover, a seismic risk assessment in Vancouver has shown that among different sources of seismicity, subduction interface earthquakes have the highest probability of resulting in losses exceeding $100 billion [10]. Therefore, it is crucial to evaluate the seismic loss performance of the MKF system to ensure that the economic loss and

the key parameters affecting it, such as peak floor acceleration (PFA), residual storey drift ratio (RSDR) and SDR, are limited within reasonable and acceptable ranges.

1.2.4. Performance under Wind Loads

Seismic forces usually govern the design of an LLRS in the high seismic regions of Canada, such as British Colombia. However, most large cities sit on low-to-moderate seismic zones, indicating that the wind load demands likely outweigh the demands imposed by seismic loads and, therefore, govern the structural design of mid- and high-rise buildings. Figure 1-4 shows the storey shear distribution under design -level wind load for a 12-storey MKF located in Toronto, Ontario, on a Class C site. The NBC requires structures to be designed for ultimate limit states under 1.4 times specified wind loads or 1.0 times specified earthquake loads, whichever produces the greatest demands. The design philosophy under wind loads dictates an elastic response, whereas significant material inelasticity is expected under design-level seismic events. Referring to Figure 1-4, it can be observed that the design wind load is larger than the design earthquake load throughout the height of the building and thus governs the design. Accordingly, in contrast to a similar structure located in a high seismic region in which the frame would likely be designed to dissipate energy under seismic loads only, herein, the frame shall be designed and detailed to remain elastic under wind loads.

The inelastic reserve capacity of the MKF system under lateral wind loading is unknown. When the elastic methodology is used under hurricane- or tornado-induced loads, a steel building will need to be several times stronger than a typical building designed for more frequent wind events with lower intensities [11]. Several researchers have investigated the potential for allowing the structures to respond inelastically under extreme wind events. The performance of the MKF system under wind loading should be first evaluated in terms of serviceability requirements and

comfort criteria. Moreover, the behaviour of the system should be studied at both system and component levels for different wind intensities up to collapse.

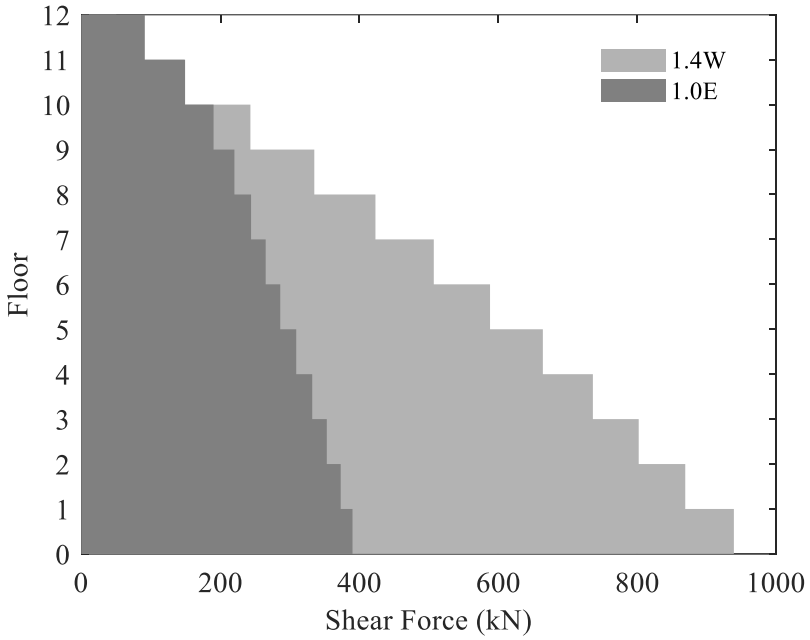

Figure 1-4. Shear force distribution along the height of a 12-storey MKF located in Toronto under design wind and earthquake loads.

1.3. Objectives

The general objective of this Ph.D. research project was to develop and verify a novel steel lateral load-resisting system, MKF. The specific goals of this research project are summarized as follows:

O1) Design Method Development and Seismic Response Evaluation (P1)

O1-1) To propose a plastic analysis procedure under lateral seismic loads.

O1-2) To develop a detailed fibre-based nonlinear numerical model of the system for static and dynamic analyses.

O1-3) To compare the seismic response of the MKF system against conventional steel MRFs.

O1-4) To compare the collapse performance and fragility of the MKF system against conventional steel MRFs.

O2) Development of Seismic Design Parameters (P2)

O2-1) To determine the seismic design parameters, including overstrength and ductility-related force modification factors, in the framework of NBC of Canada.

O2-2) To verify the adequacy of the proposed seismic design parameters.

O3) Seismic Loss Evaluation (P3)

O3-1) To evaluate expected economic losses due to structural and non-structural damages under the seismic hazard of southwestern Canada.

O3-2) To quantify various metrics representing the seismic loss performance of the MKF system such as EAL and loss vulnerability.

O4) Performance Assessment under Wind Loads (P4)

O4-1) To evaluate the performance of structural and non-structural elements of the MKF system under service and design wind loads.

O4-2) To verify the force response of the structural members under design-level wind hazard.

O4-3) To study the collapse behaviour of the MKF system under wind loads beyond the design level hazard.

O4-4) To examine the adequacy of the MKF system in terms of the motion comfort criteria under various levels of wind hazard.

1.4. Methodology

In addition to the literature review, the proposed research included four main phases as follows:

1.4.1. M1) Design Method Development and Seismic Response Evaluation

Seismic design methods were developed for the steel MKF system, and the performance of the system was evaluated using fibre-based numerical simulations. This phase was broken down into four major sub-phases:

1.4.1.1. M1-1) Seismic Analysis and Design Method (O1-1)

A plastic analysis procedure based on the PBPD method was developed to obtain seismic-induced demands. An analysis approach following structural mechanics principles was proposed to account for the axial force demand in intermediate beam segments as well as the P-Δ effects. A design strategy per CSA S16-19 provisions was proposed to determine the size of intermediate beams, knee braces, beam stubs, and columns. The effects of geometrical parameters, including the braced length ratio, the difference between the beam stubs' and intermediate beam segments' depths, the ratio of the beam stubs' cross-sectional area to the intermediate beam segments' cross-sectional area, and brace angle with respect to the horizontal axis was considered in analysis and design.

1.4.1.2. M1-2) Nonlinear Numerical Model Development (O1-2, O1-3, O1-4)

The two-dimensional (2D) nonlinear fibre-based model of the MKF was developed in the *OpenSees* program to study the seismic performance of the system and to verify the proposed analysis and design procedures. Different modelling techniques that include various types of plasticity, e.g., distributed and concentrated, element types, damping coefficients etc., were tested to develop the most reasonable numerical model capable of capturing the key factors that affect the system's response. Further details about the numerical simulation of the MKF system will be presented later.

1.4.1.3. M1-3) Seismic Performance Evaluation (O1-3)

Two prototype MKFs and two prototype MRFs were designed once according to the proposed PBPD method and then based on the ESFP prescribed by the NBC of Canada. The MRF prototypes were intended to provide a baseline for comparing the seismic response of the MKF system. Nonlinear static (pushover) analysis was conducted to evaluate the lateral stiffness, ductility

capacity, and roof yield drift ratio of the MKF. Pushover analysis also helps verify whether the yield mechanism dictated in the design can be achieved.

As recommended by Commentary J of 2015 NBC [12], a suite of 33 ground motion records representing all three sources of seismicity expected in southwestern Canada, including shallow crustal, subduction interface, and subduction intraslab, was selected. The ground motion records were scaled to match, on average, the 2015 NBC design response spectrum at the chosen site. Nonlinear Response History Analysis (NLRHA) was then performed under the ensemble of ground motions to obtain various response parameters, such as the inter-storey drift demands and maximum bending moment in critical points along the columns. The response parameters were used to verify the proposed analysis and design schemes and to verify whether the expected yield mechanism can be achieved when the frame is subjected to seismic loading.

1.4.1.4. M1-4) Collapse Performance Evaluation (O1-4)

Incremental dynamic analyses (IDAs) were performed on the prototype frames designed in Section 1.4.1.3 to study the collapse response of the MKF system and compare it against MRFs. Fragility curves were developed using the lognormal distribution of collapse intensities to compare the probability of collapse of the MKF system and conventional MRFs. In order to increase the efficiency of the method and reduce the computational cost of IDAs, a Trace-Hunt-Fill (THF) algorithm was implemented. Details of this technique will be presented in the following sections. The IDA curve corresponding to each ground motion record was established using 15 individually scaled NLRHAs. For each prototype frame, a total of 495 individual NLRHAs were required to finalize the IDA curves.

1.4.1.5. M2) Seismic Design Parameters

This phase was intended to propose seismic design parameters for the MKF system in the framework of the NBC of Canada. This can aid the implementation of the proposed system in NBC and provide design engineers with appropriate seismic design information. The following sub-phases were considered:

1.4.1.6. M2-1) Determination of Seismic Design Parameters (O2-1)

A total of 14 prototype frames with different span lengths, braced length ratios, knee-brace angles, and number of stories were designed using the seismic design parameters prescribed for Ductile steel MRFs per the 2015 NBC of Canada. Pushover analyses were then carried out on these frames to determine preliminary seismic design parameters, including the overstrength-related (R_o) and the ductility-related (R_d) force modification factors. The results were used to propose a preliminary reduction factor ($R_d R_o$). The overstrength factor was calculated using the FEMA P695 guidelines [13], while the method proposed by Miranda and Bertero [14] was applied to obtain the ductility factor.

1.4.1.7. M2-2) Verification of Proposed Seismic Design Parameters (O2-2)

A total of six index archetype frames called "Assessment Frames" were re-designed using the proposed overstrength and ductility factors. The FEMA P695 methodology adapted for the Canadian design environment was then employed to evaluate and verify the proposed seismic design parameters. In particular, three seismic hazard sources expected in southwestern Canada were considered in the evaluation. A few adjustments needed to be introduced to the original FEMA P695 methodology as it was originally developed for U.S. applications. Among these adjustments were replacing the recommended ensemble of 44 far-field crustal events with the suite of 33 ground motion records selected in this study and re-evaluating the spectral shape effects

using Ground Motion Prediction Equations (GMPEs) developed for different sources of seismicity.

1.4.2. M3) Seismic Loss Evolution

The purpose of this phase was to evaluate the earthquake-induced economic loss due to the damage experienced by structural and non-structural components of steel-framed buildings equipped with the MKF system. Herein, the following sub-phases were considered:

1.4.2.1. M3-1) Refined Numerical Model (O3-1 and O3-2)

The results of past experimental and numerical studies have shown that the partial fixity of shear tab gravity connections typically used in gravity framing can increase the lateral stiffness, strength, and collapse capacity of steel LLRSs, thus reducing the potential for seismic loss to some extent [15-18]. The numerical models developed in Phases I and II were therefore refined and improved to account for the contributions of the gravity load-carrying system. As recommended by Elkady and Lignos [19], Pinching4 material in *OpenSees* was used, and the material parameters were calibrated to capture the overall cyclic behaviour of shear tab gravity connections tested by Liu and Astaneh-Asl [20]. In order to account for the contribution of the gravity framing system to the lateral stiffness and strength, a fictitious 1-bay frame was attached to the main MKF using axially rigid truss links, as discussed in [19].

1.4.2.2. M3-2) Seismic Loss Analysis and Recommendations (O3-2)

The vulnerability of the proposed system to structural and non-structural damages under severe seismic events expected along the Canadian west coast was investigated using the methodology prescribed by Ramirez and Miranda [21]. Six prototype MKFs having 3, 6, and 9 stories were selected and designed once according to the PBPD approach and then in accordance with the NBC elastic RSA method allowing for up to 20% reduction in base shear using the seismic design

parameters proposed in Phase II. IDAs were performed to obtain various Engineering Demand Parameters (EDPs), such as PFA and peak SDR representing the state of damage in the system's key structural and non-structural components, under the ensemble of ground motion records with increasing intensities. In other words, the IDA technique with 15 individual NLRHA per ground motion record was implemented to obtain the EDPs for various hazard levels. The methodology prescribed by FEMA P-58 [22, 23] was then used to analyze repair and replacement costs for the selected site showcasing Canadian applications. Although the FEMA P-58 methodology has been developed mainly for the state of California in the U.S., the "2022 National Construction Estimator" [24] developed for the North American practice shows that the building construction costs in Vancouver and the state of California, on average, can be considered approximately equal, indicating that the FEMA P-58 cost estimations can be applied to evaluate the earthquake-induced loss of buildings in Vancouver. Moreover, site-specific hazard curves obtained from the NBC Seismic Hazard Tool [25] were employed to evaluate the EAL of the prototype MKFs.

The results of repair and replacement cost analyses were used to develop loss vulnerability curves and estimate the expected economic loss associated with different damage states and system components. This information can be finally used by design engineers to help make informed decisions in the design stage by considering anticipated repair and replacement costs for structural and non-structural components under major seismic events.

1.4.3. M4) Performance Evaluation under Wind Loading

This phase was considered to study the behaviour of the steel MKF system, at both system and component levels, when implemented as the LLRS of a wind-sensitive building. This phase consists of the following subphases:

1.4.3.1. M4-1) Evaluation of Structural and Non-Structural Deformations (O4-1)

A prototype building equipped with the steel MKF system in its long direction was designed for wind load demands in a low-seismic region, i.e., Toronto, Ontario, per the recommendations of the 2020 NBC of Canada. A detailed fibre-based numerical model utilizing non-ductile pre-Northridge moment connections at the ends of the intermediate beam segments was developed. Pushover analysis was performed on the prototype MKF to obtain the overstrength factor achieved by wind design. Wind pressure time histories were selected using the records generated from the atmospheric boundary-layer wind tunnel database at Tokyo Polytechnic University [26]. Nonlinear dynamic analyses were then carried out under wind loading time histories scaled to the service- and design-level hazards, and peak SDRs, RSDRs, and cladding deformations were investigated.

1.4.3.2. M4-2) Force Response Evaluation of the Structural Components (O4-2)

The prototype frame was analyzed under design-level wind loading time histories and the force demands developed in all structural components were evaluated. These demands were then compared to the members' capacities to verify whether the structural elements remained elastic as expected in design.

1.4.3.3. M4-3) Collapse Response under Wind Loads (O4-3)

Incremental dynamic wind analyses (IDWAs) were performed on the prototype frame by gradually increasing the intensity of the wind loading time histories until collapse occurred. The mean hourly wind velocity at a standard height of 10 m was selected as the intensity measure and peak SDR was chosen to represent the damage measure. The force–deformation response of selected structural elements was examined under collapse-level wind loads, and the collapse mechanism was investigated.

1.4.3.4. M4-4) Motion Comfort Assessment (O4-4)

Nonlinear dynamic analyses were performed under different levels of wind hazard and maximum PFAs were recorded to study the motion comfort performance of the steel MKF system according to multiple qualitative and quantitative criteria.

1.5. Organization of Thesis

This Ph.D. thesis consists of seven chapters and an appendix:

Chapter 1 presents the introduction and background information.

Chapter 2 provides a review of the past studies on the analysis, design, and evaluation of steel knee-braced systems under static, cyclic, and earthquake loads, seismic collapse evaluation methodologies, economic loss of buildings under seismic loads, and wind performance assessment of steel buildings.

Chapter 3 discusses the plastic design methodology developed for the steel MKF system and compares its seismic performance with conventional steel MRFs. This chapter has been published as a journal paper titled "Development, seismic performance and collapse evaluation of steel moment-resisting knee braced frame" in the *Journal of Constructional Steel Research*. **[M1]**

Chapter 4 elaborates on the evaluation of ductility- and overstrength-related force modification factors for the steel MKF system within the framework of Canadian standards. The collapse and seismic performances of steel MKFs designed per the proposed seismic design parameters are also investigated. This chapter has been published as a journal paper titled "Proposed seismic design parameters for the moment-resisting knee-braced frame system" in the *Engineering Structures* journal. **[M2]**

Chapter 5 presents an investigation of the vulnerability of steel MKFs to economic loss resulting from structural and non-structural damages under earthquake events. The annual probability of

collapse of the MKF system is also estimated and compared against the NBC threshold. Design recommendations are provided to achieve better seismic response, collapse performance, and seismic-induced economic loss metrics. This chapter will be submitted to a journal as a paper titled "Earthquake-induced Loss Assessment of Steel Moment-resisting Knee-braced Frame Buildings under Seismic Hazard of Southwestern Canada". **[M3]**

Chapter 6 provides a discussion on the performance of steel MKFs under wind loading time histories. An investigation of structural and non-structural deformations, force response of structural elements, collapse behaviour, and motion comfort of steel MKFs subjected to wind loads with various intensities is presented. This chapter will be submitted to a journal as a paper titled "Performance Evaluation of Mid-rise Steel Moment-Resisting Knee-Braced Frame Buildings Under Wind Loading". **[M4]**

Chapter 7 summarizes the key findings and limitations of this study, along with the recommendations for future studies.

The Appendix provides the details of ground motion records used in the seismic performance evaluation of the steel MKF system in this research.

CHAPTER 2

LITERATURE REVIEW

2.1. Introduction

This chapter begins with a comprehensive literature survey on the fundamental assumptions and findings of the most relevant experimental and numerical studies on steel LLRSs equipped with knee brace elements. The information provided in these studies is necessary to better understand the response of MKFs under lateral seismic and wind loads, thereby facilitating the formulation of modelling techniques and design criteria. Additionally, as part of the study's broader objectives, a brief review of the past research works on collapse and economic loss evaluation of steel LLRSs is presented in the second and third parts of this chapter. Part four provides an overview of some of the most significant and fundamental studies on mathematical and experimental backgrounds of elements and modelling techniques used in *OpenSees* for the simulation of steel structures. Limited research is available on Performance Based Wind Design (PBWD) and nonlinear response evaluation of steel LLRSs under wind events with varying intensities. This research also addresses the design and nonlinear behaviour of the steel MKF system under experimental wind loading within the framework of Canadian standards. Accordingly, the fifth part of this chapter provides a summary of the related publications to help establish the foundation for evaluating the response of steel MKFs at both system and component levels according to the PBWE assumptions.

2.2. LLRSs With Knee Brace Elements

Various types of LLRSs exist in the literature which resist lateral loads based on knee bracing action. These systems typically are meant to provide a lateral stiffness larger than what is offered by conventional MRFs as well as ductility capacities greater than conventional braced frames.

Knee brace angle, braced length-to-span length ratio, type of connection between the knee elements and the rest of the frame, and cross-sectional properties of the knee brace element are some key factors in the design of knee braced frames. This section is dedicated to presenting a review of the design and response of various steel systems in which knee brace elements are implemented to provide resistance against lateral loads.

2.2.1. Disposable Knee Bracing

Aristizabal-Ochoa introduced the Disposable Knee Bracing (DKB) method in 1986 for single- and multi-storey steel frame construction [27]. As shown in Figure 2-1 [27], the DKB technique is mainly based on implementing two structural elements, i.e., the knee element and the diagonal brace element. The knee member is a fuse-like element intended to dissipate the input seismic energy by forming plastic hinges at its ends and midspan. On the other hand, the diagonal brace is responsible for providing the required lateral stiffness and is designed to behave in the elastic range. The knee element is a disposable beam element that can be replaced upon being damaged after an earthquake. A comparative study between disposable knee bracing and eccentric bracing shear link techniques using simple elastoplastic analyses revealed two significant results. Firstly, disposable knee-braced frames could offer superior seismic performance. Secondly, the degree of fixity at the beam-column joint connections is not as critical in the disposable knee bracing technique as it is in the eccentric bracing shear link approach.

Later, Balendra and his colleagues chose a different name for the system introduced by Aristizabal-Ochoa, calling it the Knee-Braced Frame (KBF), and carried out significant numerical and experimental studies to examine this new LLRS in more detail. In 1989, they proposed two knee brace-to-diagonal connections, as shown in Figure 2-2 [28], and tested Connection I under cyclic loading.

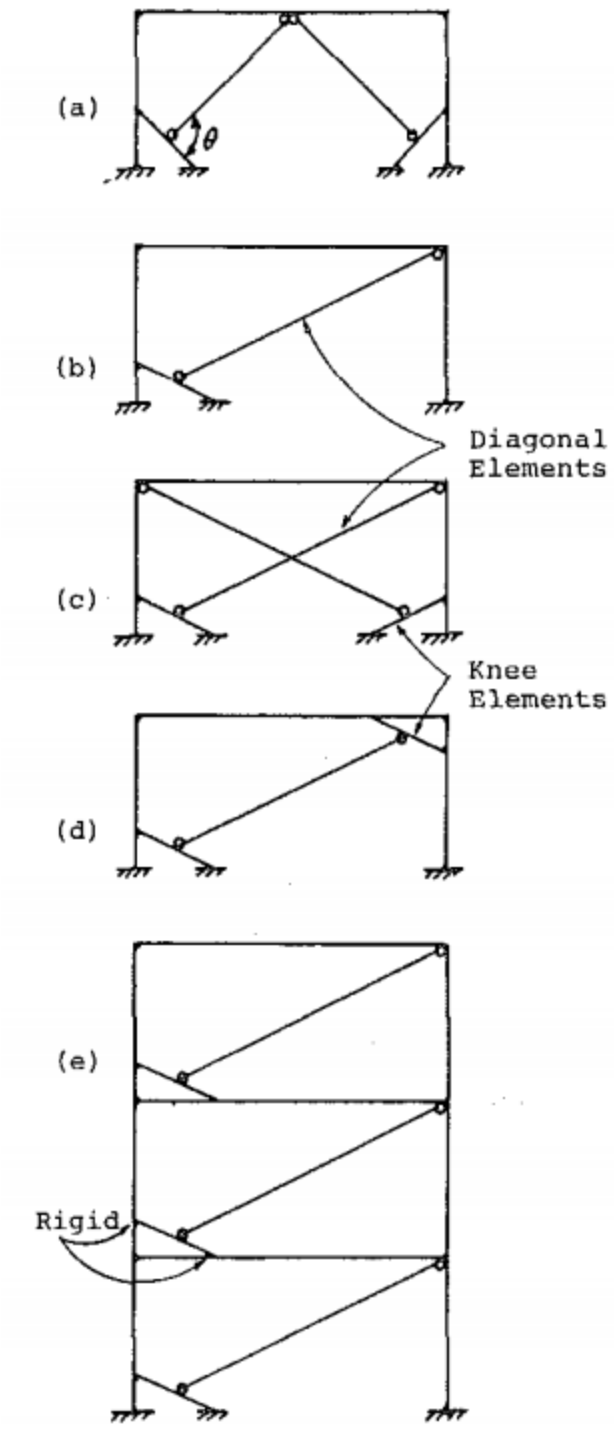

Figure 2-1. Different configurations of frames with disposable knee braces (Adapted from [27]).

The hysteretic response of the connection tested was unpinched and stable, resulting in a displacement ductility of 8.5 and exhibiting acceptable performance for seismic applications.

Notably, the displacement ductility demand was defined as the ratio of maximum displacement applied to displacement at the onset of yielding.

In 1990, Balendra et al. expanded their studies and performed a large-scale test on a single-storey KBF subjected to cyclic loading [29, 30]. A schematic view of their test frame is depicted in Figure 2-3 [29]. A square hollow section was chosen for the knee element. The hysteretic response obtained for the test frame is shown in Figure 2-4 [29]. Their study demonstrated that it is possible to obtain full and unpinched hysteresis loops for KBFs with no deterioration in strength and marginal loss in stiffness. The maximum ductility they achieved in the test was equal to 4.0 before the initiation of cracks in the knee element. It was also suggested that the performance of the KBF system could be improved by implementing better low-cycle fatigue-resistant knee members.

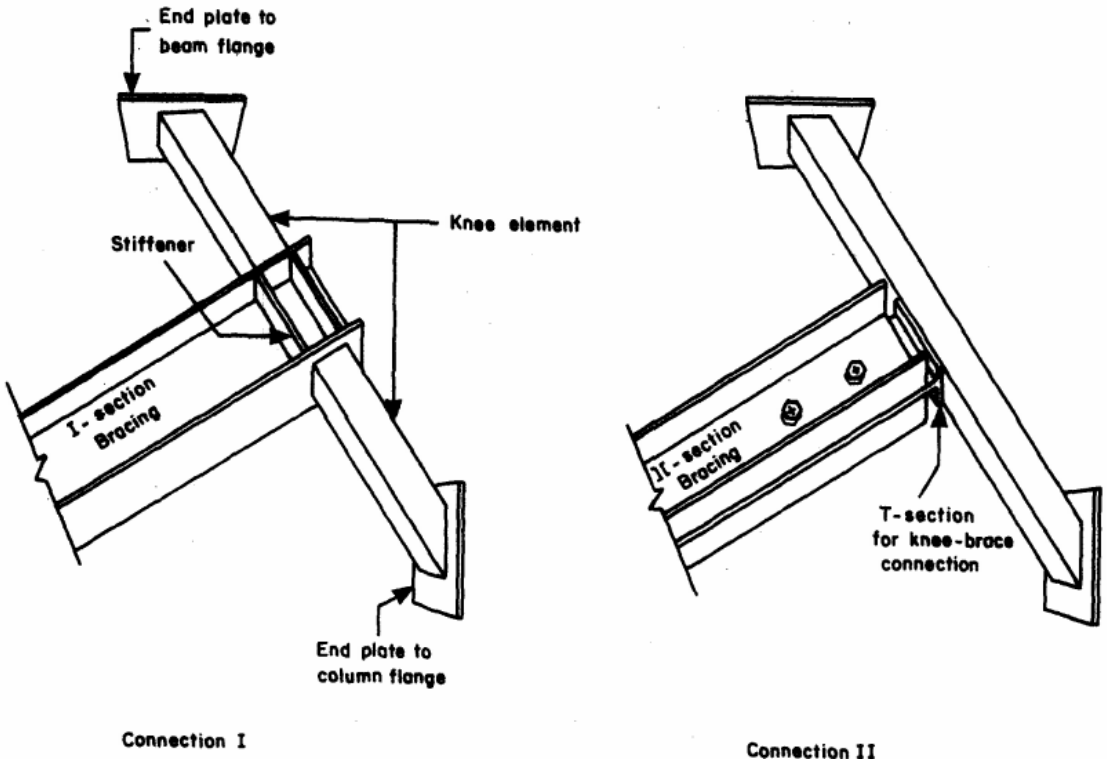

Figure 2-2. Two possible knee brace connections in KBFs (Adapted from [28]).

The application of knee bracing elements with a shear yield mechanism in KBFs was the subject of another study by Balendra et al. in 1992 [31]. They performed a large-scale experiment on a

single-storey KBF subjected to cyclic loads. The knee brace in the previous studies was designed to yield under bending moment, i.e., for flexural yielding. In contrast, a shear yield mechanism was dictated to the knee element in this study. The displacement ductility obtained for the frame under cyclic loads was 6.0, larger than the previous studies and adequate for earthquake-resistant design. It was concluded that an unpinched hysteretic response with no deterioration in strength and stiffness could be achieved, provided that adequate web stiffeners are present to prevent tearing of the knee brace web due to the presence of a diagonal tension field.

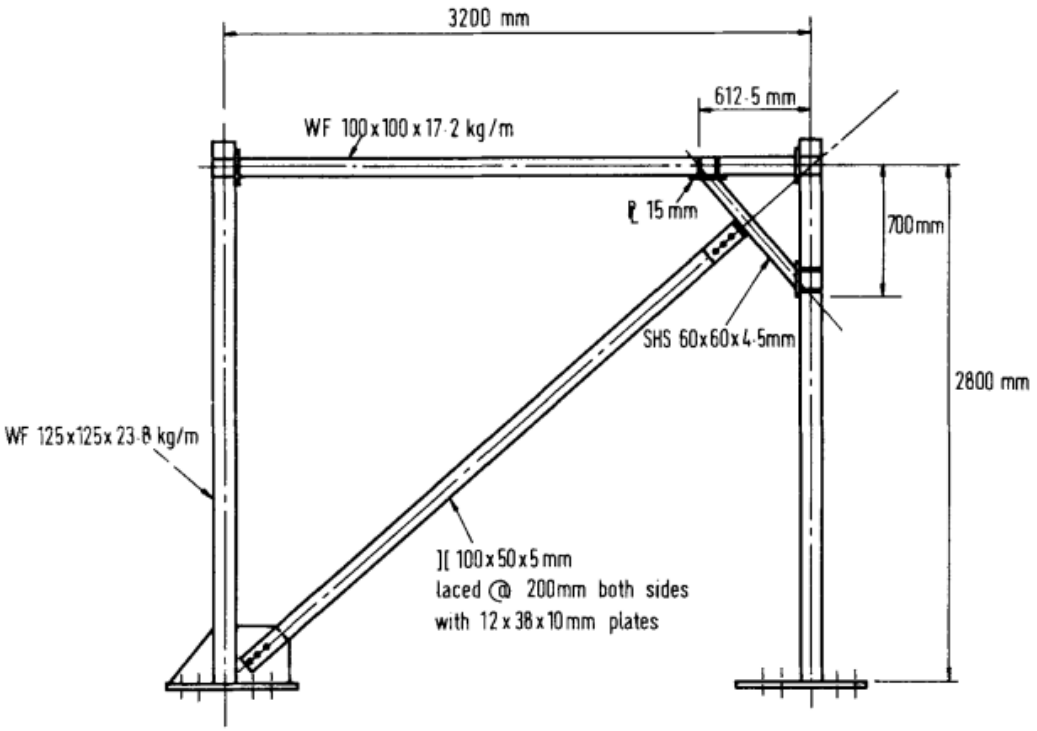

Figure 2-3. Test frame configuration (Adapted from [29]).

Single-bay two-storey KBFs with flexural and shear yield mechanisms in the knee element were designed and tested by Balendra et al. [32, 33] to further investigate the performance of this system. The numerical and experimental results of these studies confirmed the findings of the previous ones on a larger and more detailed scale. In all cases, the damage was confined to the knee elements, indicating that retrofitting the structural frame after an earthquake would be easy and

economical. Moreover, the results revealed that the KBF system could be a viable alternative to EBFs for seismic applications.

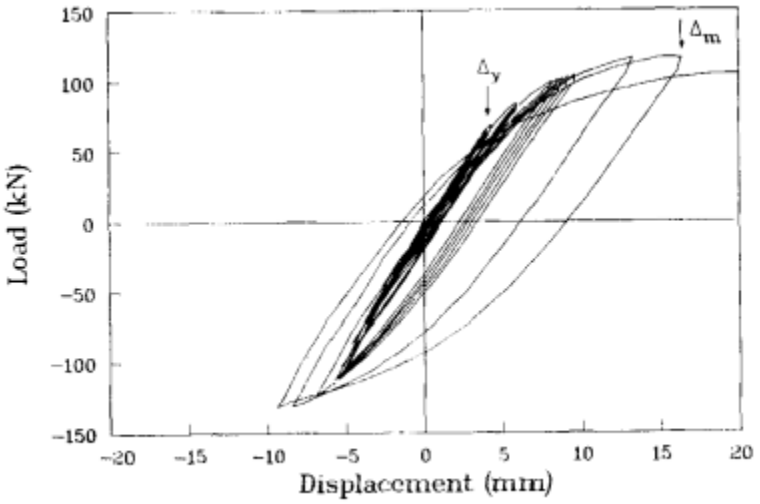

Figure 2-4. Force-displacement hysteresis response of the test frame (Adapted from [29]).

2.2.2. Knee-Braced Moment Frames

As shown in Figure 2-5 [34], structural ductility can be achieved for MRFs subjected to lateral loads when beam-to-column connections are adequately detailed. The applicability of such designs is limited by the excessive drift due to higher structural flexibility and unavoidable stress concentration at the CJP welds. Improved stiffness can be achieved to reduce extreme structural deformations by adding knee brace elements in the corner regions of beams and columns, as illustrated in Figure 2-6 [34]. This system is referred to as the Knee-Braced Moment-Resisting Frame (KBMRF) [34]. Hsu and Li [34] performed a series of full-scale cyclic tests on Special Moment-Resisting Frames (SMRFs) and KBRFs using in-plane and out-of-plane controlled buckling mechanisms in the knee braces. The general configuration of the connections used in their test specimens is depicted in Figure 2-7 [34]. The results showed that the performance of SMRFs could remarkably be enhanced by adding knee braces regardless of the plane of brace

buckling. It was also observed that the allowable drift at which the knee braces reached the buckling stage was higher for KBRFs equipped with in-plane buckling modes.

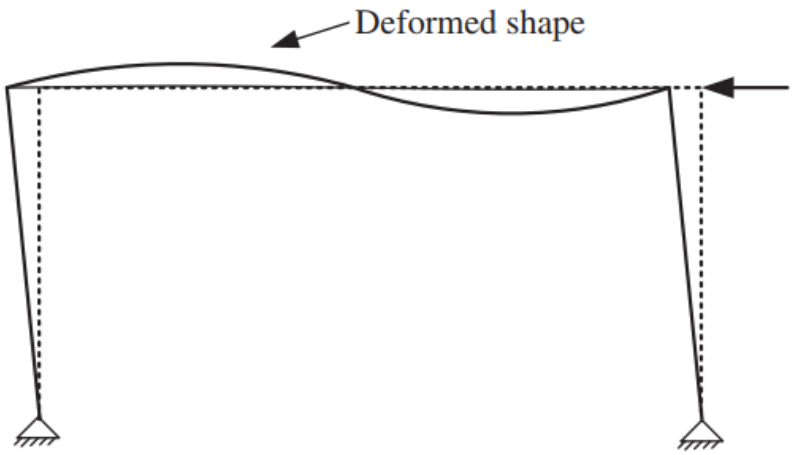

Figure 2-5. MRF subjected to lateral loads (Adapted from [34]).

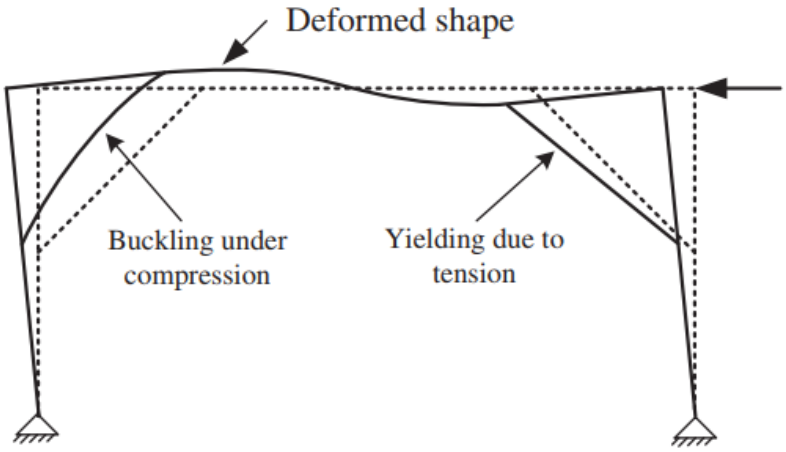

Figure 2-6. KBRF subjected to lateral loads (Adapted from [34]).

Leelataviwat et al. [35] added knee braces to conventional MRFs with and without Reduced Beam Section (RBS) connections and introduced a ductile system referred to as the Knee-Braced Moment Frame (KBMF). This structural system was designed to resist seismic forces through the yielding and buckling of knee elements, followed by the formation of plastic hinges in the beams at the face of beam-to-brace connections. A large-scale experimental program supported by numerical simulations confirmed that the proposed system could reliably resist seismic forces without noticeable degradation or instability. Overall, the system illustrated acceptable

performance under cyclic loads, implicating the system's potential to be used as a viable alternative to conventional MRFs. Details of one of their test specimens, along with its associated hysteretic response under cyclic loads, are shown in Figure 2-8 [35] and Figure 2-9 [35], respectively.

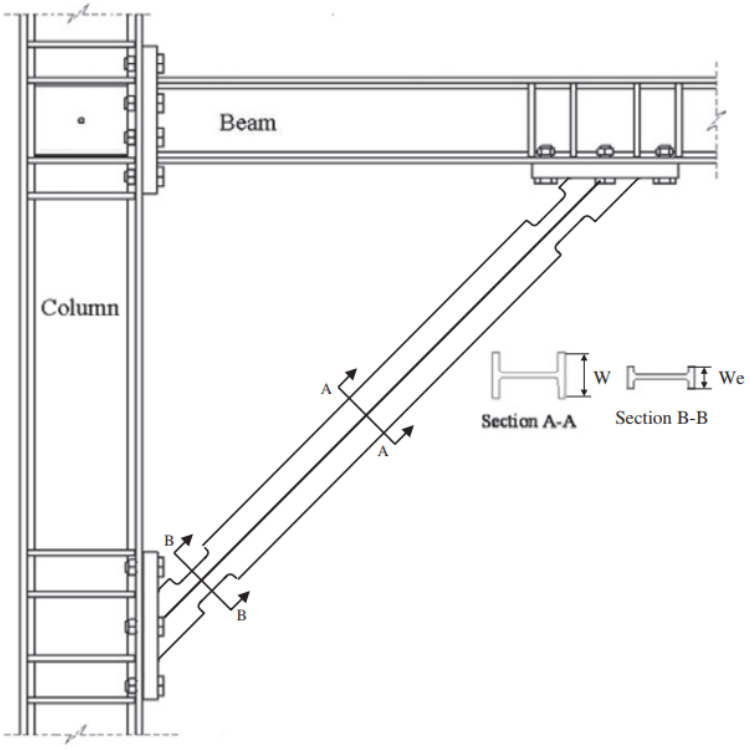

Figure 2-7. The geometry of a knee brace connection with a controlled buckling mechanism (Adapted from [34]).

One of the main disadvantages of this system is the complexity of connections. The rigid beam-to-column connections typically seen in MRFs are not eliminated, yet further complexity is introduced to the system by connecting knee braces to the beams and columns through gusset plates. Also, for the damage to remain localized and confined to the designated locations, the RBS technique should be used, resulting in higher fabrication costs.

2.2.3. Buckling-Restrained Knee-Braced Systems

Steel frames with simply supported beams and buckling-restrained knee brace elements are another innovative LLRS studied by numerous researchers. In these systems, simply supported

beams or open-web trusses carry the gravity loads while buckling restrained braces dissipate the seismic input energy.

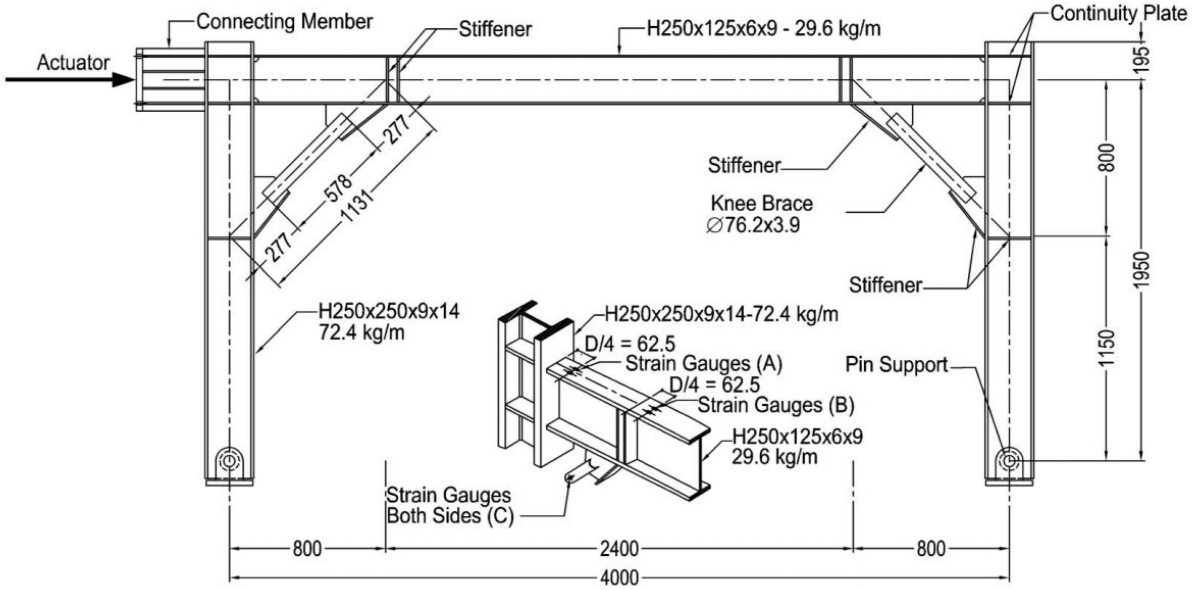

Figure 2-8. Details of specimen KBMF-1 (Adapted from [35]).

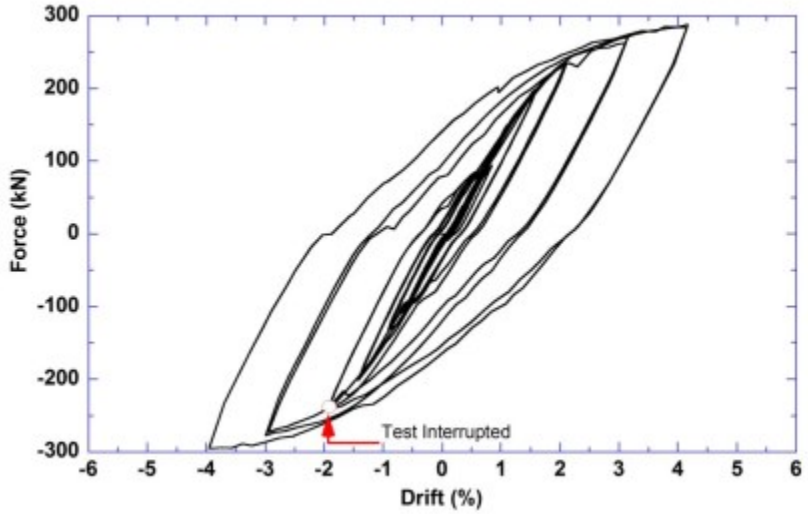

Figure 2-9. Hysteretic loops of specimen KBMF-1 (Adapted from [35]).

Junda et al. [36] evaluated the performance of Buckling-Restrained Knee-Braced Frames (BRKBFs) through cyclic tests and numerical simulations. Shown in Figure 2-10 [36] is the general configuration of their proposed system. In this figure, SPSC stands for Single Plate Shear Connection. This system was claimed to offer relatively simple connections, reparability after an

earthquake, and less architectural obstruction than conventional bracing techniques. The system was designed in a way that all inelastic activities were confined to the BRKBs. In contrast, beams and columns were designed under the maximum probable forces developed by the BRKBs to remain elastic. The outcomes of their study proved that BRKBFs could provide ductile behaviour with a stable hysteretic response. The failure mode of the system would be governed by the failure of BRKBs, provided that the SPSCs, beams, and columns are adequately designed and detailed. One of the essential drawbacks of this system is the extremely large cross-sections obtained for beams and columns under maximum probable forces transferred by the BRKBs that can be remarkably large in mid- and high-rise frames. In some cases, the capacity forces applied to the beams and columns can be so large that none of the standard WF sections available in the market will be able to carry them. Accordingly, the failure mechanism of this system cannot be considered desirable for practical applications.

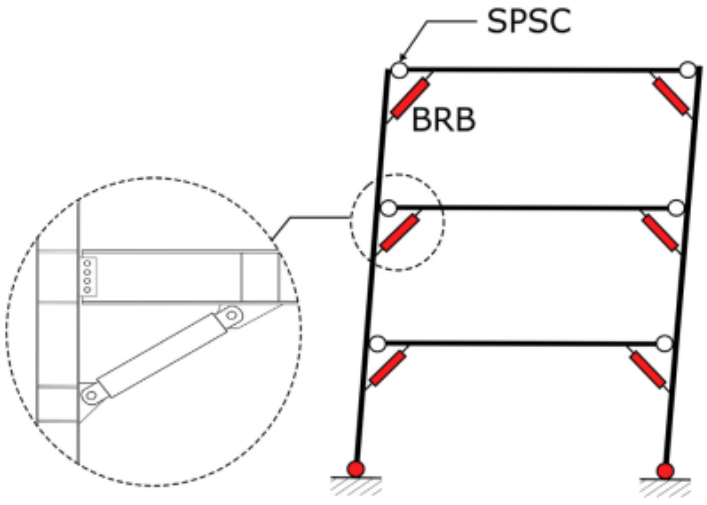

Figure 2-10. Buckling Restrained Knee Braced Frame (Adapted from [36]).

Another innovative system that can overcome the limitations of BRKBFs is the Buckling-Restrained Knee-Braced Truss Moment Frame (BRKB-TMF) [37-40]. Figure 2-11 [37] depicts the general configuration of this system in which open-web trusses carry the gravity loads while

BRKBs dissipate the seismic input energy. Open-web trusses are lighter and offer a more economical and efficient design under gravity plus seismic loads compared to WF beams in BRKBFs. Figure 2-12 [37] and Figure 2-13 [37] show that open-web trusses and columns are designed to remain elastic under the maximum probable forces developed by the BRKBs. Numerical simulations on BRKB-TMFs with different heights, span lengths, brace angles, and modelling approaches have confirmed the robust behaviour of this system under severe seismic loads. BRKB-TMFs consume less material than MRFs, especially in long-span frames, yet offer superior seismic performance by limiting structural damage, repair cost, and probability of collapse. It has also been shown that BRKBs with larger ductility capacities improve the performance of this structural system. Another important finding of these studies was that the peak structural drift and acceleration were not affected considerably by the BRKB angle. Regardless of their satisfactory seismic performance and collapse behaviour, open-web trusses of BRKB-TMFs can sometimes be too deep, resulting in short openings and architectural obstructions.

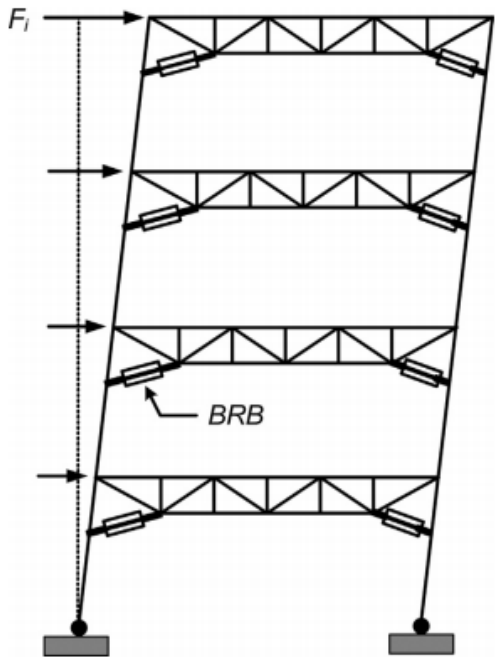

Figure 2-11. Buckling-Restrained Knee-Braced Truss Moment Frame System (Adapted from [37]).

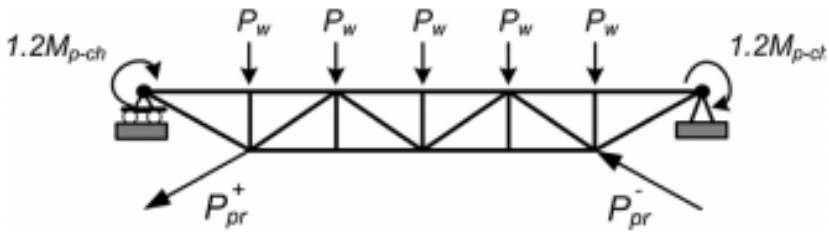

Figure 2-12. Truss design concept (Adapted from [37]).

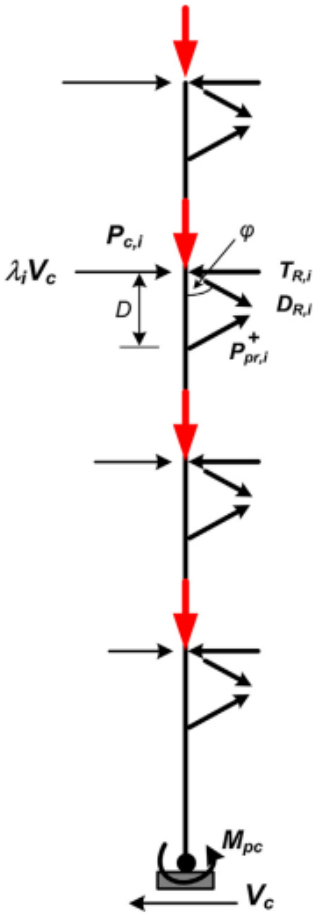

Figure 2-13. Example of an exterior column equilibrium analysis (Adapted from [37]).

2.2.4. Knee Connection Frames

Considering the relatively high cost of BRKBs, their complex fabrication process, and the difficulties one can have in finding them in the market, another LLRS that relies on knee brace elements has been put forward by researchers. Asghari and Saharkhizan [41] replaced the BRKBs in BRKBFs discussed in Section 2.2.3 with conventional knee elements and proposed a system called Knee Connection Frame (KCF). In this system, seismic input energy is dissipated through

the formation of plastic hinges at the face of beam-to-knee connections. At the same time, the flexural behaviour of beams and columns due to the presence of knee braces provides lateral stiffness. Hence, beams are the primary DYMs. At the same time, columns and knee braces must be designed to remain elastic under the maximum probable bending moment developed at the plastic hinges. Figure 2-14 [41] and Figure 2-15 [41] illustrate the components of a KCF connection and the desired yield mechanism dictated to the system, respectively.

The behaviour of the KCF system with flexural yield mechanism is generally identical to MRFs, yet higher levels of lateral stiffness, lower fabrication costs, and simpler connections are offered by KCFs. Since no unified and clear values are available for the seismic design parameters of KCFs, Asghari and Saharkhizan used the seismic design parameters of SMRFs prescribed by ASCE7-SEI10 [42] to design their prototype KCFs. Through numerical simulations in *OpenSees* [43] and the FEMA P695 methodology [13], they concluded that KCFs pass the seismic design parameters of SMFRs. However, a few assumptions can be spotted in their study that are worthy of further investigation. Firstly, the distributed plasticity approach is used to model the beam elements. This assumption fails to capture the strength and stiffness degradation of the system because of the local buckling in beams at the location of plastic hinges. This significant factor plays a crucial role in the seismic response of MRFs or MRF-like LLRSs. Secondly, the knee braces are modelled by truss elements, thereby ruling out the ability to capture any possible global buckling. Third, they set an inter-storey drift ratio of 10% as the local collapse threshold for both MRFs and KCFs in their collapse analyses. This is a bold assumption since previous studies have shown that systems similar to KCFs, such as BRKB-TMFs, tend to reach the incipient state of total collapse at maximum inter-storey drift ratios of 6 to 7% [37]. It is also expected that high shear forces will be developed in the short segment of the columns, which can cause web crippling at

the location of knee-to-column connection due to the application of a significant point load. These can result in local inelasticity at critical locations along the column height. To prevent such an undesired response, stiffeners may be required in detailed design of columns.

Moreover, they used span lengths of 5m in their frames and a braced length ratio of 0.18, resulting in lengths of 0.9 m and 3.2 m for the braced length and intermediate beam span, respectively. Such values are by no means practical since a short beam span would not be able to dissipate energy effectively in flexure. In other words, as the span length becomes shorter, the beam will be more likely to yield in shear, a behaviour that can be seen in the link beams of EBFs. Each of these assumptions can potentially affect the reliability and accuracy of the results regarding the seismic and collapse responses of KCFs. Nonetheless, the results of their study have shown that KCFs possess sufficient built-in stiffness to meet the storey drift criteria prescribed by seismic design provisions. Moreover, it was observed that KCFs tend to collapse at higher ground motion intensities and result in a 7-8% reduction in the material consumed when compared to SMRFs. Finally, it was suggested that KCFs could offer better performance than SMRFs in the case of low- and mid-rise buildings.

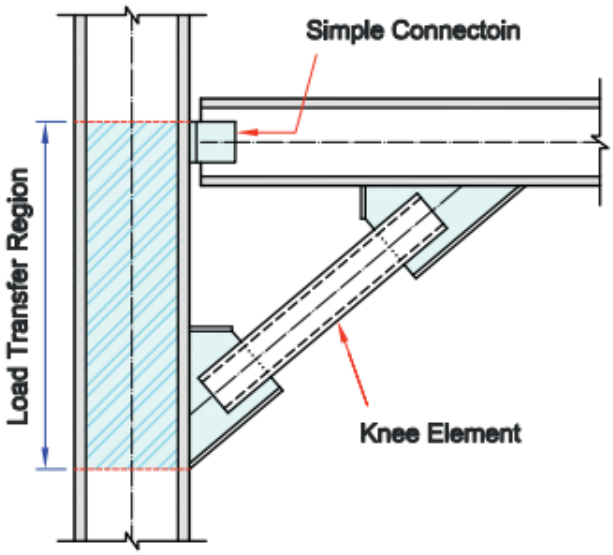

Figure 2-14. Knee element connection in KCFs (Adapted from [41]).

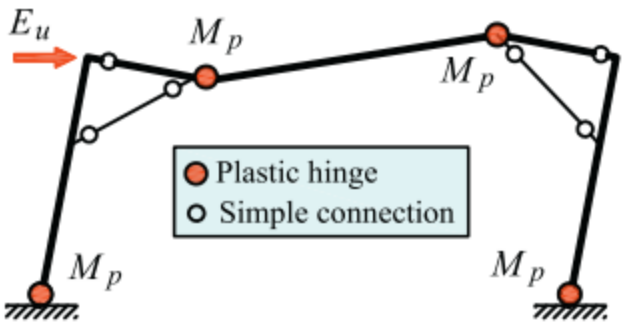

Figure 2-15. Flexural yielding mechanism (Adapted from [41]).

Nekouvaght et al. [44] developed a PBPD method that takes the P-Δ effects directly into account to design KCFs. The same yield mechanism employed in [41] was implemented in their study. In addition, they used the RBS technique at the face of beam-to-knee brace connections to ensure that plastic hinges will not form anywhere else along the beams. Figure 2-16 [44] demonstrates the connections used in their study. HSS sections were utilized for knee braces, while beams and columns were selected from WF sections. In their research, the beam segments were simulated using the concentrated plasticity approach, and force-based nonlinear elements were utilized to model the knee braces. Hence, the nonlinear analyses could capture the strength and stiffness degradation as well as any potential buckling or tensile yielding in the knee braces. Regardless of their design and modelling assumptions, it was observed that the KCFs designed per the PBPD approach could result in promising behaviour under lateral static and seismic loads. Plastic hinges were formed only at the designated locations, i.e., at the face of beam-to-knee brace connections, resulting in well-distributed plasticity along the frames' height. Moreover, KCFs consumed less material than MRFs and provided comparable collapse capacities, thereby confirming the findings of [41].

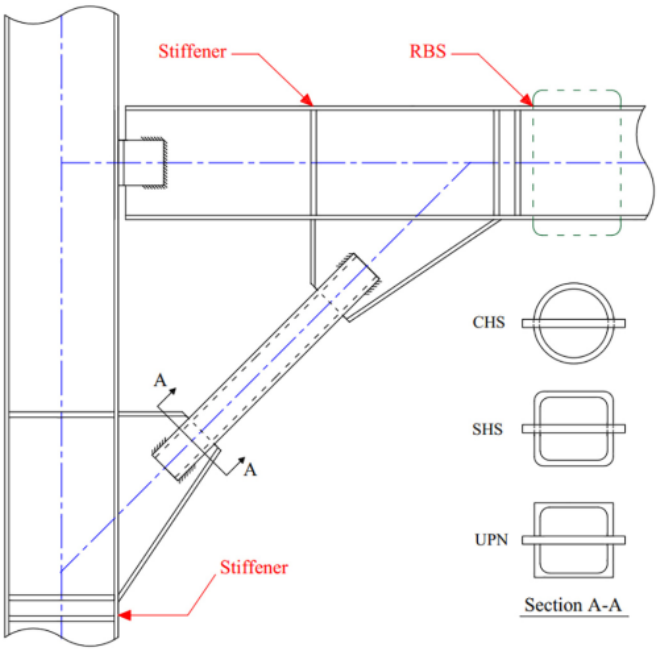

Figure 2-16. Knee element connection details with possible knee element options (Adapted from [44]).

2.3. Seismic Collapse Evaluation

2.3.1. Incremental Dynamic Analysis

Vamvatsikos and Cornell [45] proposed the Incremental Dynamic Analysis (IDA) method to evaluate the collapse response of LLRSs under lateral loads. In this method, an LLRS is subjected to a lateral load, e.g., a ground motion record, with an increasing Intensity Measure (IM) to obtain the corresponding maximum value of the Damage Measure (DM). Elastic spectral acceleration at the fundamental period of the structure and maximum inter-storey drift ratio are considered the most common IM and DM, respectively, in seismic collapse evaluation. In the IDA approach, two collapse thresholds are typically defined, i.e., local and global. The former corresponds to a case in which a maximum predefined limit for the DM is reached at any of the stories (e.g., a maximum inter-storey drift of 5%), while the latter represents a state of numerical instability in the analysis, including non-converging analyses.

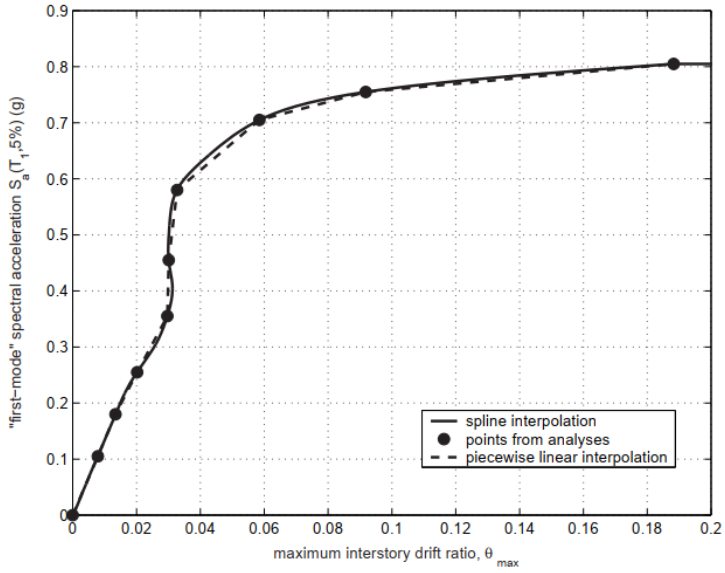

Figure 2-17. Sample IDA curve interpolated using 10 IDA analysis results (Adapted from [46]).

Figure 2-17 [46] shows a sample IDA curve established using 10 points, with each point corresponding to a full nonlinear analysis. In order to obtain a reasonably accurate IDA curve under a given ground motion record, enough nonlinear analyses must be performed to capture all possible complex behaviours that can be observed in collapse analysis, such as softening, hardening, and weaving, as depicted in Figure 2-18 [45]. However, this approach can be computationally expensive, thus decreasing the efficiency of the IDA method. To address this issue, Vamvatsikos and Cornell [45] proposed a Hunt-Trace- Fill (HTF) algorithm. In the conventional IDA, a ground motion record is scaled up based on equally spaced scale factors until collapse is detected. On the other hand, the HTF algorithm can furnish a sufficiently accurate and smooth IDA curve with fewer nonlinear analyses. The HTF algorithm consists of three phases: 1) the Hunting phase, 2) the Tracing phase, and 3) the Filling phase. In the first step, the total number of nonlinear analyses is determined by the user.

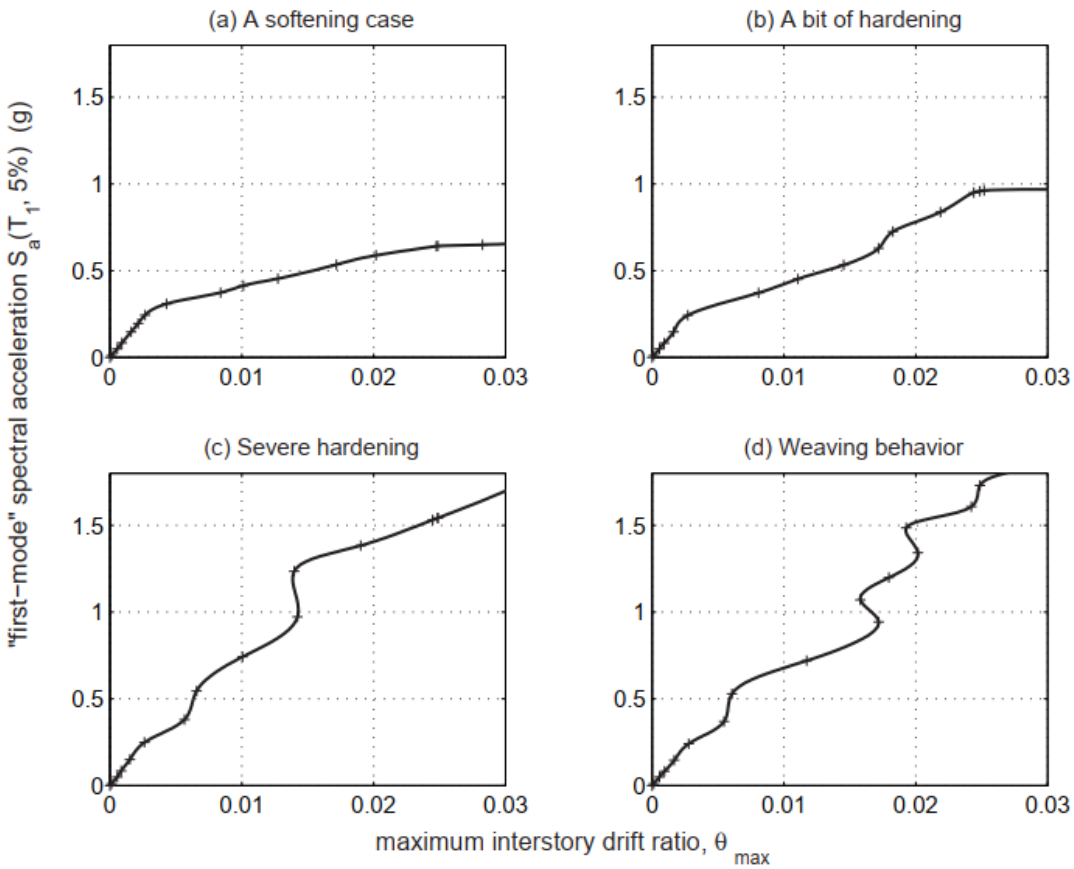

Figure 2-18. IDA curves of a 5-storey steel braced frame subjected to four different records (Adapted from [45]).

Each nonlinear analysis will correspond to a unique point on the final IDA curve. During the Hunting phase, a ground motion record is ramped up in relatively large increments until collapse is achieved. In the Tracing phase, the first collapse point is discarded since the analysis has probably been scaled too far, and tracing in smaller increments is started from the last converging record until a more refined collapse intensity is achieved. In the Filling phase, the algorithm uses the remaining number of analyses determined by the user to fill in the largest gaps in the IDA trace. Once all points have been determined, piecewise linear or spline interpolation functions can be used to plot the final IDA curve.

An example of the application of the IDA method to collapse evaluation of steel knee-braced systems can be found in Yang et al. [40]. They compared the collapse response of long-span

conventional MRFs and BRKB-TMFs under 20 different ground motion records. Sample IDA curves from their study are shown in Figure 2-19 [40].

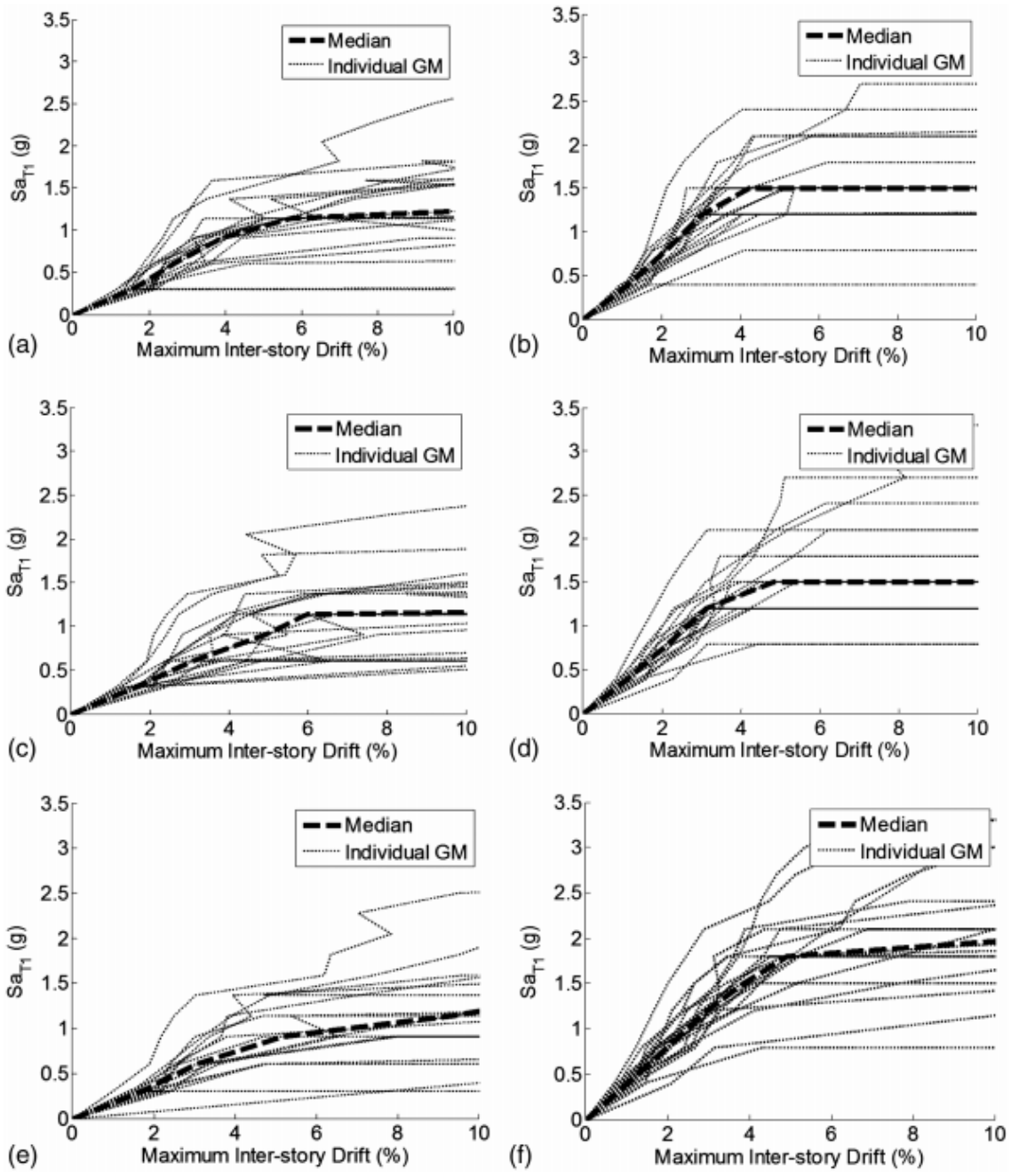

Figure 2-19. IDA response of MRFs and BRKB-TMFs with various span lengths (Adapted from [40]): a, c, e) MRFs with span lengths of 9.1 m, 13.7 m, and 18.3 m, respectively; b, d, f) BRKB-TMFs with span lengths of 9.1 m, 13.7 m, and 18.3 m, respectively.

In this figure, the vertical axis represents the intensity of the ground motion record in terms of the spectral acceleration at the fundamental period of the building while the horizontal axis shows the maximum inter-storey drift as an index to measure the expected damage at a given seismic intensity. It can be observed in the figure that BRKB-TMFs generally collapse at higher ground motion intensities compared to conventional MRFs. However, MRFs tend to experience lateral instability under greater inter-storey drift ratios. The IDA results were used to establish fragility curves for the prototype buildings, and it was also found that BRKB-TMFs result in a lower probability of collapse compared to conventional MRFs at a given seismic intensity. Similar studies can be found in the literature taking advantage of the IDA technique to evaluate the collapse response of other conventional LLRSs such as MRFs, EBFs, CBFs, etc. [15, 17-19, 21, 47-50].

2.3.2. FEMA P695 Methodology for Seismic Performance Evaluation of Structures

FEMA P695 methodology [13] was developed in 2009 and is well-accepted by engineering communities to quantify the seismic performance of building structures. The seismic design parameters of new LLRSs in the framework of U.S. design practice can be evaluated using the guidelines provided in this document. The methodology is consistent with a basic life safety performance objective inherent in U.S. seismic standards and has the potential to be adopted in other design environments, such as Canadian design practice.

For any new system, the methodology starts with selecting several archetype frames part of different performance groups. Performance groups selected to quantify the seismic design parameters should reflect various structural configurations, gravity load levels, and period domains. The archetype frames are first designed using preliminary seismic design parameters, followed by performing a series of nonlinear static and nonlinear dynamic analyses.

The overstrength-related force modification factor, or simply the overstrength factor, is determined using nonlinear static analysis results. Figure 2-20 [13] depicts an idealized nonlinear static curve. FEMA P695 methodology defines the overstrength factor of a given archetype as the ratio of the maximum base shear resistance, V_{max}, to the design base shear, V. The average value of archetype overstrength is calculated for each performance group. The value of the system overstrength factor for use in design shall not be taken as less than the largest average value of calculated archetype overstrength from any performance group.

The response modification factor in the U.S. seismic codes should be evaluated using an ensemble of 44 far-field crustal ground motion records representing the seismic hazard across the U.S. In order to achieve this goal, each archetype is subjected to this ensemble with increasing intensities until collapse is detected. By doing so, 44 IDA plots will be obtained for each archetype frame. Figure 2-21 [13] shows the IDA curves of a four-storey reinforced concrete special moment frame.

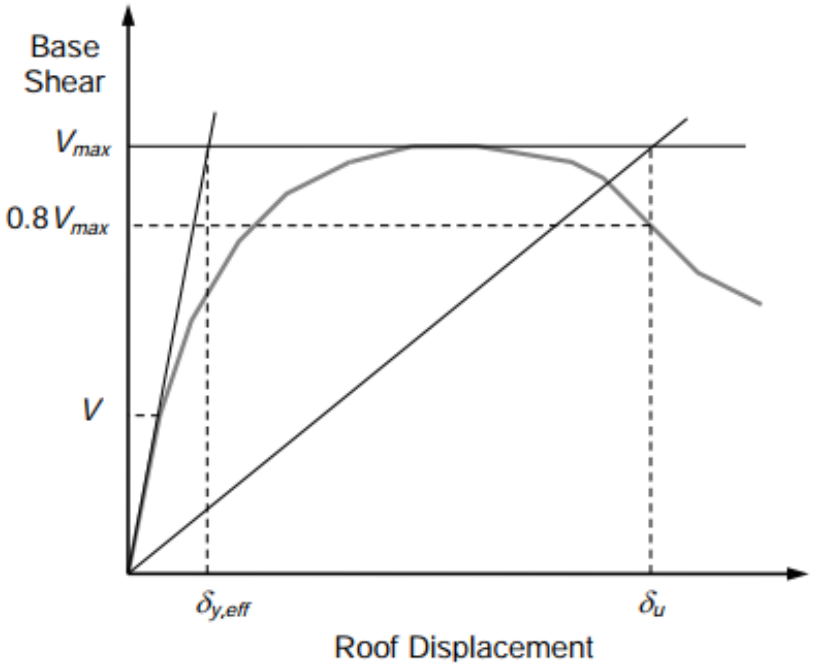

Figure 2-20. Idealized pushover curve (Adapted from [13]).

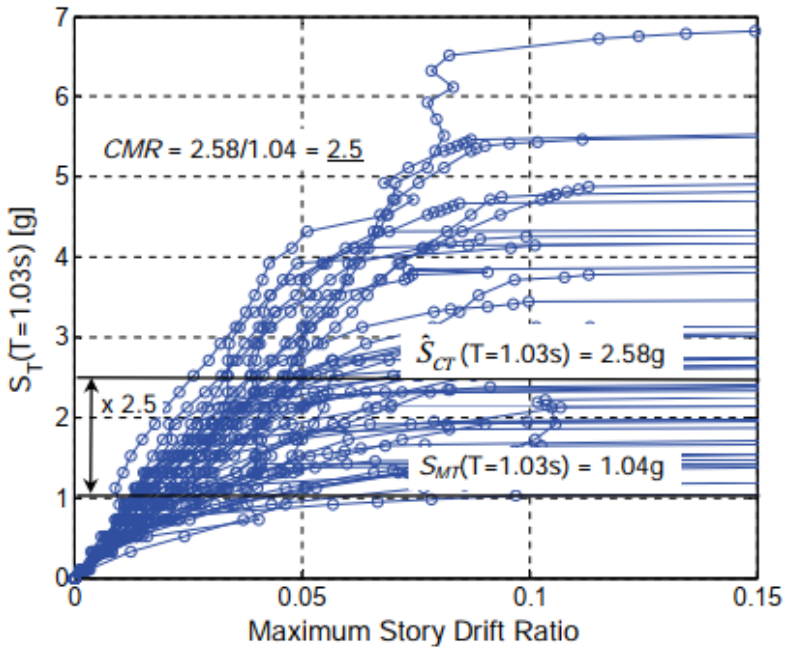

Figure 2-21. IDA curves of a four-storey reinforced concrete special moment frame under the set of 44 far-field records (Adapted from [13]).

It should be noted that the IM and DM measures implemented by the FEMA P695 methodology are the 5% damped elastic spectral acceleration at the fundamental period and maximum inter-storey drift ratio along the frame height, respectively. The collapse capacity ($\hat{S}_{CT}$) of the archetype is considered equal to the median of all collapse intensities under the ensemble of ground motion records. The methodology then defines the Collapse Margin Ratio (CMR) parameter as the ratio of the collapse capacity to the 5% damped elastic spectral acceleration of the Maximum Considered Earthquake (MCE) response spectrum of the site under consideration (S_{MT}). Once the CMR of each archetype has been evaluated, it should be adjusted using the Spectral Shape Factor (SSF) parameter to obtain the Adjusted Collapse Margin Ratio (ACMR). For a system to pass the initially assumed response modification factor, the following criteria must be met:

1) The average of *ACMRs* ($\overline{ACMR}$) of the selected archetype frames should be larger than the maximum value of $ACMR_{10\%}$ within the performance group:

   $\overline{ACMR} \geq ACMR_{10\%}$

2) The conditional collapse probability of 20% for each archetype frame should be satisfied as follows:

$ACMR_i \geq ACMR_{20\%}$

If both conditions are satisfied, the initially assumed response modification factor can be considered adequate for the system. Otherwise, the FEMA P695 methodology recommends that outlier archetypes (i.e., individual index archetypes that perform significantly worse than the average performance of the group) be accommodated by adopting more conservative values of seismic performance factors or be eliminated from the archetype design space by revising the design requirements (e.g., proposing height limits or other restrictions on use). Revision of seismic performance factors or design requirements will necessitate re-designing and re-analyzing index archetypes and re-evaluating the performance of the system.

2.4. Seismic Loss Evaluation

Economic loss due to structural and non-structural damages can be a major consequence of seismic events. A seismic loss study of an LLRS can provide stakeholders and building owners with useful metrics for decision-making such that they can understand whether their specific project goals in terms of economic and lifetime costs will be met. The methodology introduced in the ATC 58 project by the Pacific Earthquake Engineering Research Center (PEER) can measure losses and provide various metrics such as loss of life, economic loss, and downtime.

The PEER loss estimation methodology has been implemented to investigate the earthquake-induced loss of high-performance wood structures [51] and conventional reinforced concrete structures [21]. As another example of PEER loss estimation methodology application, Song et al. [52] evaluated the loss of steel structures subjected to mainshock-aftershock sequences and

demonstrated that aftershocks could considerably affect the economic loss, even when the contribution of aftershocks to the structural response is marginal.

Ramirez and Miranda [47] simplified the PEER methodology by reducing the required data and computational effort. They proposed a series of probabilistic functions to quantify the economic loss due to structural and non-structural damages using various engineering demand parameters such as SDR, PFA, and peak ground acceleration (PGA). This methodology can explicitly account for the main sources of variability related to seismic hazards and structural response and addresses three possible scenarios: (i) collapse does not take place, but the structural and/or non-structural components shall be repaired in the aftermath of an earthquake; (ii) collapse is prevented, but the building may be demolished and rebuilt due to excessive residual deformations; (iii) The building collapses, and it shall be rebuilt.

The methodology developed by Ramirez and Miranda can be applied to assess the earthquake-induced loss of various structural systems. Hwang and Lignos [16] evaluated the seismic loss of steel frame buildings with SMRFs in high seismic regions. Taking into account the effects of gravity framing and the strong-column/weak-beam (SCWB) ratio on the seismic behaviour of SMRFs, they utilized the fragility data provided by FEMA P-58 for structural and non-structural components. Through comprehensive nonlinear analyses on 2-, 4-, 8-, 12- and 20-storey buildings, they showed that in the case of service and/or design earthquakes, damage to non-structural components dominates steel frame building losses. Figure 2-22 [16] shows the expected loss of the frames they studied normalized by the total building replacement cost.

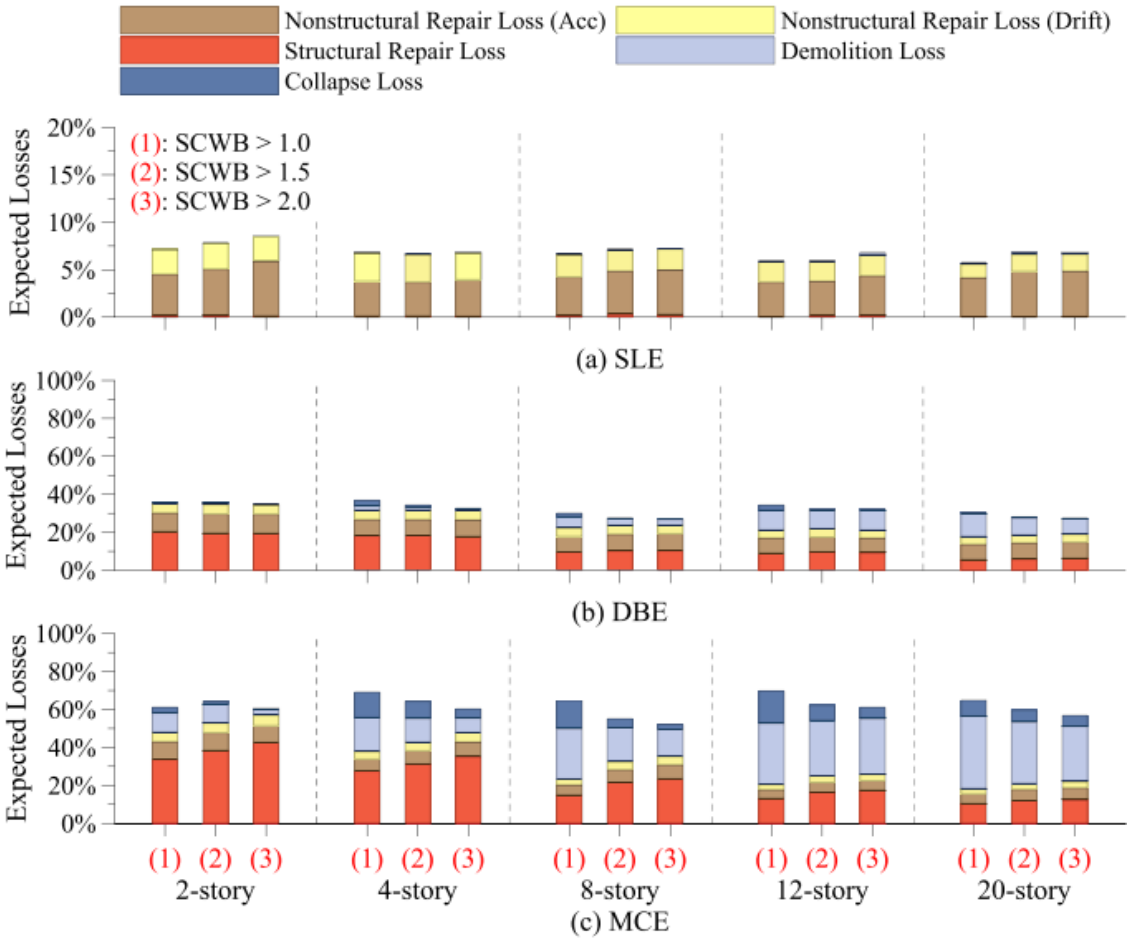

Figure 2-22. The normalized expected loss for steel SMRFs at selected seismic intensities (Adapted from [16]).

In this figure, the contribution of composite gravity beams has been considered, and SLE, DBE, and MCE refer to service level earthquake, design basis earthquake, and maximum considered earthquake, respectively. As the seismic intensity is increased to the MCE level, the expected loss will be governed by structural repairs in low-rise buildings and demolition loss in high-rise buildings. It was also shown that the contribution of gravity framing to the lateral stiffness, strength and collapse capacity of a steel frame building with perimeter SMRFs could reduce the losses due to building demolition and collapse under maximum considered earthquakes by 50%. Considering the gravity framing effects can also lead to a more accurate estimate of the losses due to structural

damage repairs. They also demonstrated that in low- to mid-rise steel frame buildings with SMRFs, the SCWB ratio can play a significant role in earthquake-induced losses under extreme seismic loads. Moreover, it was found that the present value of life-cycle costs for steel frame buildings with SMRFs can vary from about 10% to 20% of their total replacement cost.

In another study by Hwang and Lignos [17], the earthquake-induced losses and collapse risk of steel frame buildings with Special Concentrically Braced Frames (SCBFs) were evaluated. The same loss estimation methodology implemented in [16, 47] was employed, and it was shown that in the case of design earthquakes with a 2% probability of exceedance over 50 years of building life expectancy, losses due to demolition and structural collapse in steel frame buildings with SCBFs located in high seismic regions could be significantly overestimated if the contributions of gravity framing system are neglected in the numerical models. For frequent and moderately frequent seismic events, the building losses are governed by acceleration-sensitive non-structural component repairs and structural repairs because of steel brace flexural buckling.

Elkady et al. [15] developed a methodology that accounts for the effects of residual axial shortening of first-storey steel columns on the earthquake-induced economic loss of steel MRF buildings. They have shown that neglecting the effects of column shortening can lead to an underestimation of the seismic economic loss. Moammer et al. [18] evaluated the collapse risk and earthquake-induced loss of buildings with EBFs. They used the methodology proposed by Ramirez and Miranda and divided the economic loss into three main categories: collapse loss, demolition loss, and structural and non-structural repair loss. By performing comprehensive nonlinear analyses on 4-, 8- and 16-storey EBF buildings, they confirmed that the gravity framing system could lower the collapse loss in all cases. They also showed that when the seismic intensity is below the DBE level, the non-structural loss is dominant. By increasing the seismic intensity,

structural, demolition, and then collapse loss become more significant. It was also found that for mid- and high-rise EBFs, buildings designed using the Equivalent Lateral Force (ELF) procedure perform better than those designed per the RSA method in terms of seismic loss. This behaviour is attributed to the fact that RSA design leads to lighter structural sections.

2.5. Numerical Modeling of Knee-Braced Frames

Steel structural systems equipped with knee braces can resist lateral loads by forming different yield mechanisms. For instance, in BRKBFs, the seismic input energy is dissipated through the yielding of BRKBs in tension and compression, while the rest of the system is typically designed to remain elastic. On the other hand, as discussed earlier, KCFs were found to dissipate lateral seismic loads more efficiently by developing flexural plastic hinges at the face of beam-to-knee connections. Depending on the energy dissipation mechanism, it is crucial to implement appropriate numerical modelling techniques and make use of proper elements in *OpenSees* to accurately capture the inelastic response of steel knee-braced systems and achieve meaningful results. Fibre-based numerical models were extensively used in this research. Accordingly, an overview of some of the key studies addressing the fundamentals and mathematical backgrounds of the numerical techniques built in the *OpenSees* program is presented.

The Force-based beam-column model developed by Spacone et al. [53] for application in the *OpenSees* program was designed for nonlinear analysis of reinforced concrete frames. This model adopts a flexibility-based approach, assuming plane sections remain plane, and utilizes bending moment and axial force to maintain element equilibrium through force interpolation functions. Precise force interpolation functions with a reduced number of elements, robustness and reliability in simulating strength degradation and softening, as well as the capability to accommodate distributed element loads are some of the notable advantages of this model. Consequently, the

force-based formulation offers heightened accuracy, enabling the appropriate prediction of post-buckling axial compressive strength degradation, such as a brace or column buckling, across various levels of inelastic deformation [53-56]. Uriz et al. [57] conducted a validation study on the force-based beam-column element employing fibre discretization of the cross-section, particularly focusing on the single-plane flexural buckling behaviour of braces. Their research demonstrated that this element accurately predicts the brace's hysteretic response, encompassing tension and buckling resistances, as well as post-buckling behaviour. Moreover, the study revealed that local buckling minimally influences the overall hysteretic force-displacement response of steel braces with compact sections. Nevertheless, the utilization of a smooth transition from the elastic to the inelastic region of the material stress-strain response effectively compensates for this minor impact [55]. Agüero et al. [58] investigated the impact of various parameters on the accuracy of numerical models, including the type of elements, e.g., force- and displacement-based elements, the number of elements along the brace length, the number of integration points along the element length, the number of fibres needed to define the brace section, the material model, and the amplitude and number of displacement increments necessary to simulate the cyclic response of bracing members. Numerical predictions were verified against experimental results and the study concluded that elements utilizing force-based formulations yield more precise predictions, albeit requiring more computational time. Additionally, it was determined that the uniaxial Giuffré-Menegotto-Pinto material model [59] is suitable for accurately modelling the cyclic response of steel braces.

Agüero et al. [58] also noted that the brace response is not significantly affected by the number of integration points. In their study, utilizing three integration points per element was recommended. Moreover, they observed that the brace response can be predicted with sufficient accuracy by using

8 elements per brace and 16 fibres for cross-section discretization. They also reported that reducing the number of fibres or elements increases the error in numerical simulations.

While the distributed plasticity approach is more suitable for capturing the inelastic response, buckling, and post-buckling behaviour of braces and columns, the concentrated plasticity technique is capable of simulating strength and stiffness degradations due to localized damage observed in plastic hinges. Lignos and Krawinkler [60] used a database of experimental data on steel components and proposed empirical formulae to model all key parameters that affect the cyclic moment-rotation response at plastic hinge regions in beams. Figure 2-23 [60] shows a calibration example of the deterioration model used by Lignos and Krawinkler [60]. In a recent study by Cravero et al. [61], the calibrated deterioration model proposed by Lignos and Krawinkler [60] was further expanded for application in modelling plastic hinges in columns taking into account the effects of axial load on stability and ductility of the component. The mathematical frameworks developed in these studies can be implemented in the Ibarra-Medina-Krawinkler (IMK) material in *OpenSees* to simulate the response of a flexural plastic hinge using a nonlinear rotational spring element, as illustrated in Figure 2-24 [18]. While the application of the concentrated plasticity approach in modelling nonlinear inelastic response of plastic hinges in knee-braced frames remains limited in the literature [44], extensive research works can be found utilizing this technique in modelling other conventional LLRSs such as MRFs, CBFs, and EBFs [16, 18, 19, 21, 47, 48, 50, 62, 63].

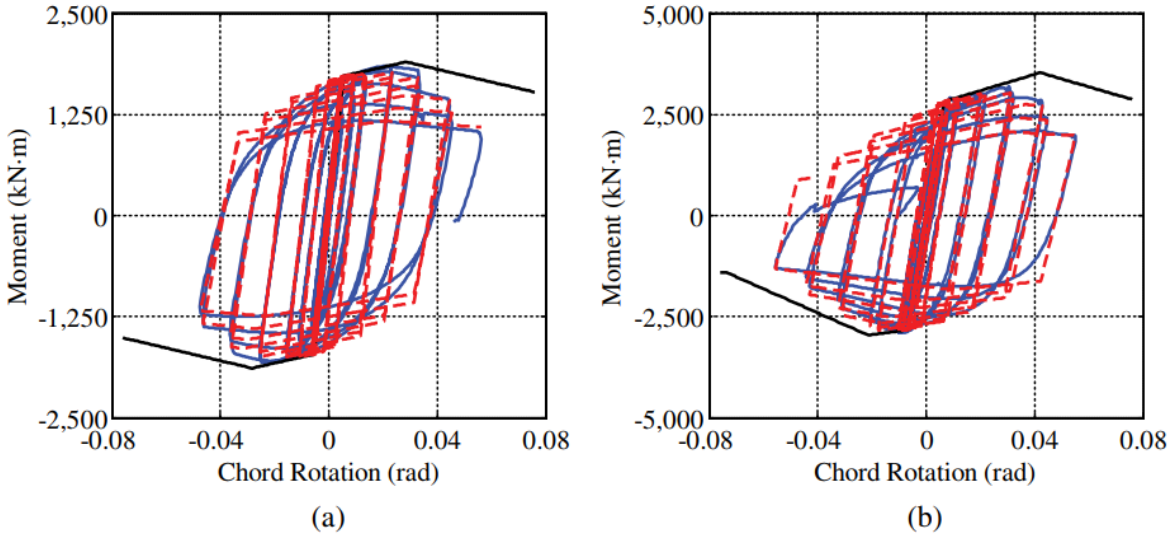

Figure 2-23. Modified Ibarra-Krawinkler deterioration model (Adapted from [60]): (a) beam with Reduced Beam Section; (b) asymmetric hysteretic response with composite action.

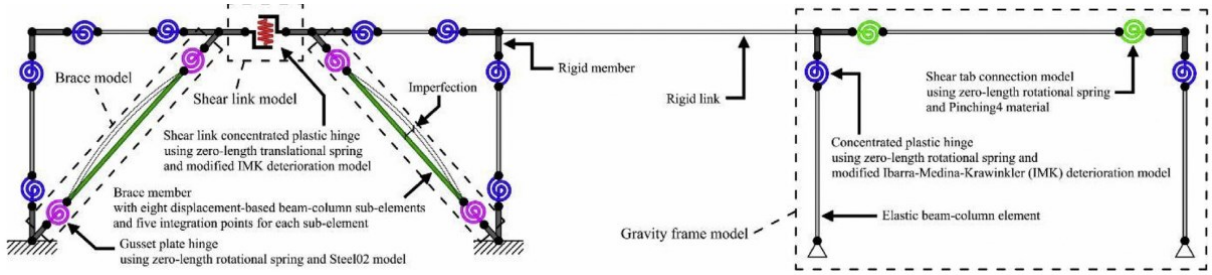

Figure 2-24. Nonlinear model of EBFs in *OpenSees* with concentrated plasticity approach [18].

2.6. Wind Performance Evaluation of Steel Structures

In seismic design of structures, DYMs are accommodated in engineered locations to act as fuses, dissipate the seismic input energy, and push the response of the structure into the nonlinear inelastic range. On the other hand, wind design is typically more straightforward as the structure is aimed to remain elastic under design-level wind intensities and meet rather stringent serviceability criteria under frequent wind loads. Recently, the field of Performance Based Wind Engineering (PBWE), or PBWD, has attracted the attention of researchers as a broad framework to further push the limits of wind engineering in structural design. Traditionally, when designing buildings, engineers often use standard procedures prescribed by design codes, such as equivalent

static forces, to estimate wind forces along the building height. However, PBWE offers a more sophisticated approach and focuses on understanding how buildings react to different wind intensities, considering the unpredictable nature of wind and the unique features of each structure, e.g., aspect ratios, architectural configuration, irregularities, and surrounding environment.

Numerous studies can be found in the literature addressing the design, numerical modelling, and performance assessment of steel LLRSs according to both traditional and PBWE frameworks. Since the last phase of this research sheds light on the design and response evaluation of steel MKFs under wind loads with varying intensities in low-seismic regions of Canada, a brief review of landmark studies on wind engineering of conventional LLRSs is presented here.

A method for evaluating the effectiveness of low-rise light-frame wooden structures within the context of PBWE was presented in 2009 by Van de Lindt and Dao [64]. Using the fragility concept, they calculated the frequency of failures at various performance levels. To optimize the design of structures that undergo wind-induced excitation within the linear response range, Spence and Kareem [65] presented a probabilistic framework for PBWE in 2014. Researchers used fragility analysis to create performance-based design and assessment methods early in the development of PBWE [64, 66-68]. By utilizing ductility, Gani and Le´geron [69] assessed if it would be possible to lower the strength requirement for single-degree-of-freedom systems during strong wind occurrences and suggested a more straightforward technique for estimating nonlinear response. Griffis et al. [70] introduced a PBWE framework that encompasses performance objectives and methodologies for assessing wind hazards. Additionally, this framework incorporates the nonlinear behaviour of steel LLRSs. They showed that their proposed methodology is useful for the performance evaluation of existing buildings and the economically optimal design of new structures subjected to wind loads. Judd and Charney [71] investigated the inelastic response and

risk of collapse in buildings subjected to wind loads by employing single-degree-of-freedom models and the FEMA P695 methodology. They observed that considering a wind load reduction factor would not necessarily improve the response of highly ductile systems. However, a wind load reduction factor of 1.25 was found to be justified for systems with a limited degree of ductility, such as moderately ductile MRFs. In separate studies, the performance of a 10-storey office building under wind loads was studied in terms of risk of life, occupancy, and economic losses [72, 73]. The LLRS used in these studies was a steel MRF consisting of non-ductile pre-Northridge connections as inelasticity and energy dissipation were not expected in design. They used Pinching4 material to simulate non-ductile moment connections, as shown in Figure 2-25 [73]. The prototype building was subjected to short and long wind loads, illustrated in Figure 2-26 [73], and it was revealed that wind loads at the service level did not compromise the habitability of the building. However, windstorms at strength and near-collapse levels caused damage to both cladding and structural components.

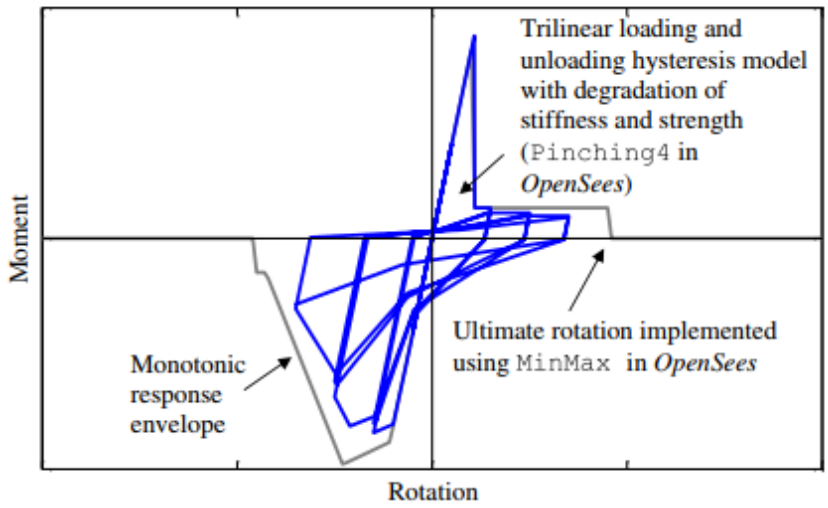

Figure 2-25. Idealized response of pre-Northridge moment connections (Adapted from [73]).

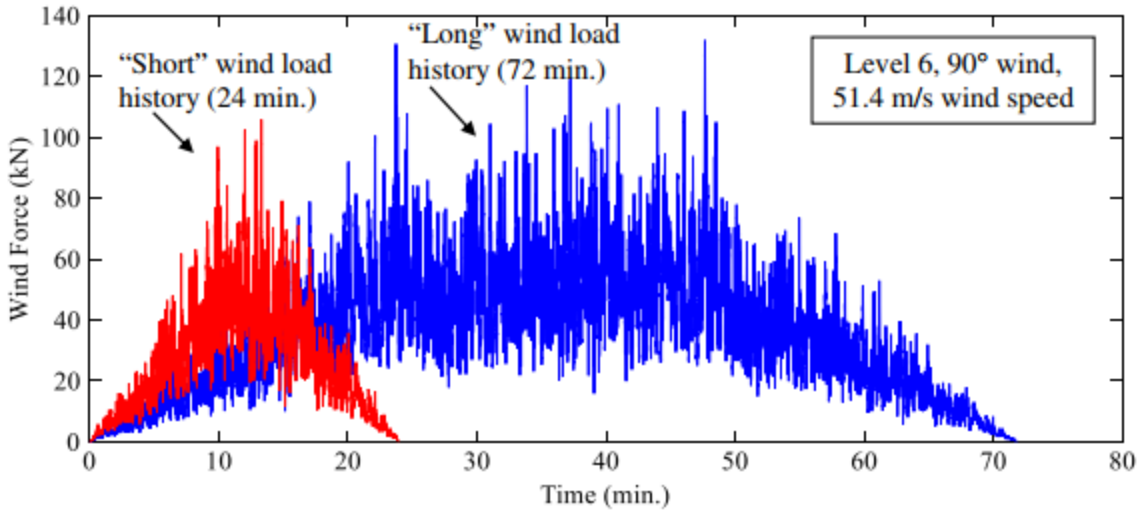

Figure 2-26. Wind load time histories used for the evaluation of the 10-storey steel MRF (Adapted from [73]).

In 2016, Spence et al. [74] introduced a methodology aimed at mitigating structural and non-structural damage and loss in multi-storey wind-excited buildings. They employed the theory of dynamic shakedown to capture the post-yield response of the structural system. The applicability of the methodology was shown by analyzing a 5-storey steel MRF considering the seismic fragility data developed for structural and non-structural components of a building. Mohammadi et al. [75] utilized a three-dimensional nonlinear finite-element model to assess the performance of an existing 47-storey steel Moment-Resisting Frame (MRF) building under multiple experimentally derived wind loads with different angles of approach, estimating performance levels in both structural members and cladding. The findings indicated that while the building exhibited a substantial reserve strength, it did not meet certain serviceability performance criteria across different levels of wind loading. Ghaffary and Moustafa [63] assessed the performance of a 20-storey steel MRF building under various wind hazards until the point of collapse. They determined that existing code-prescriptive design methods often lead to overly conservative structural designs. As an alternative, they proposed adopting a performance-based approach, leveraging controlled nonlinear responses during extreme wind events to achieve safer and more cost-effective designs.

Athanasiou et al. [76] put forward a design methodology capable of addressing multiple hazards and examined the nonlinear behaviour of a 15-storey hospital facility equipped with steel CBFs in Montreal. The study was based on Canadian design practice and the investigation focused on analyzing how the building responded to different levels of wind and seismic forces. They derived experimental wind loading time histories from the TPU database and generated random wind realizations using Monte Carlo simulation to produce load uncertainty for collapse analysis. They found that wind events lead to a higher annual probability of failure compared to earthquakes. The collapse mechanism of the prototype CBF studied in their research is depicted in Figure 2-27 [76]. They also found the current state of practice in wind design, which is based on code-prescriptive static methods, to be overly conservative since the inherent ductility and overstrength and the system are not leveraged in wind design.

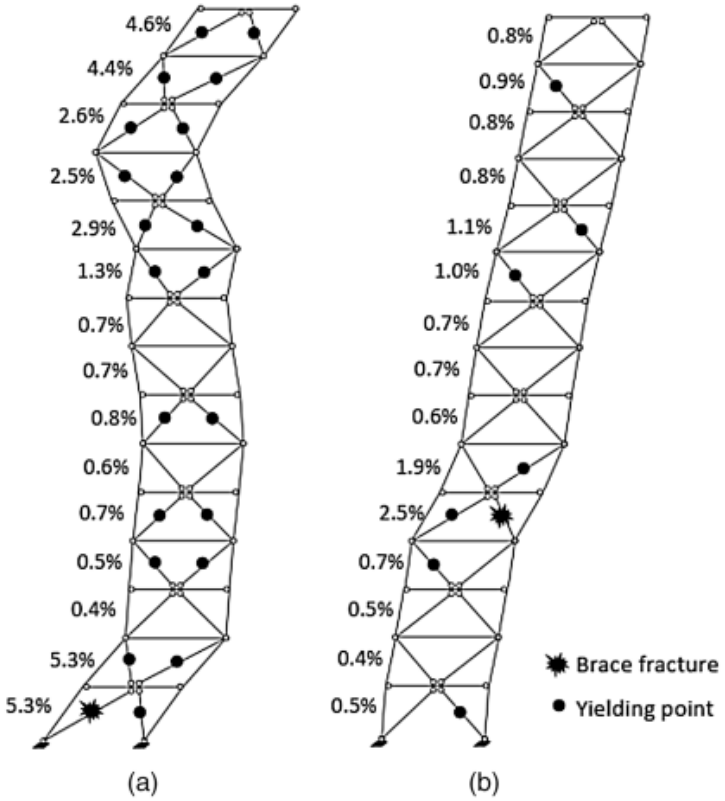

Figure 2-27. Collapse mechanism of the 15-storey hospital under (Adapted from [76]): (a) a sample ground motion record; (b) a sample wind realization.

In a separate investigation, Athanasiou et al. [77] explored the feasibility of implementing a wind-related reduction factor to decrease the design wind load for tall steel buildings in eastern Canada. Through extensive nonlinear analyses, they determined that applying a wind-related reduction factor of 2.0 to the resonant component of the wind load would have negligible effects on the building's response at the design level. However, it would lead to a reduction in collapse capacity within an acceptable range. Further studies delving into the evaluation of building structures' responses to wind loads within a PBWE framework can be referenced in [78-88].

2.7. Summary

Steel-framed structures equipped with knee brace elements have been the subject of many studies in the past. Various knee-braced steel LLRSs have been put forward by researchers to overcome some of the shortcomings of other conventional steel LLRSs such as high flexibility and complicated connections in MRFs and architectural obstructions in braced frames. In most of these studies, the knee brace element either plays the role of the DYM to dissipate seismic input energy or is added to the main LLRS as a complementary component to improve the performance by increasing the lateral stiffness and inherent overstrength. Both approaches can be costly since BRKBs are expensive and complicated to fabricate and adding conventional steel knee braces to a steel LLRS can result in increased steel tonnage and higher construction costs. Accordingly, an alternative LLRS that provides resistance against lateral loads through the application of knee braces but is capable of developing more stable and efficient hysteresis cycles, such as the response of a flexural plastic hinge, should be proposed. There is a knowledge gap within the field of steel knee-braced structural systems regarding the code-compliant design requirements and procedures under lateral seismic and wind loads that can be explored in detail.

CHAPTER 3

DEVELOPMENT, SEISMIC PERFORMANCE, AND COLLAPSE EVALUATION OF STEEL MOMENT-RESISTING KNEE BRACED FRAME

Abstract: This chapter introduces and assesses the seismic and collapse behaviour of a new lateral load-resisting system referred to as steel Moment-Resisting Knee Braced Frame (MKF). A design method following the Performance-Based Plastic Design (PBPD) procedure is proposed to analyze the structure and size the structural members. A prototype frame part of an office building located in Vancouver, British Columbia, Canada is then selected to demonstrate the design method and evaluate the performance of the proposed system. The prototype MKF is also designed using the conventional elastic approach in accordance with the National Building Code (NBC) of Canada. The seismic performance and collapse response of the proposed system are examined using the nonlinear static analysis, nonlinear response history analysis (NLRHA) and incremental dynamic analysis (IDA) performed on the prototype five-storey MKF under potential sources of seismicity in the west coast of Canada including shallow crustal, subduction interface and subduction intraslab events. Fragility curves are finally developed using the results of the IDA to obtain the collapse probability of the system. The results of the analyses are compared to those obtained from a steel Moment-Resisting Frame (MRF) counterpart designed in accordance with the PBPD and elastic approaches. The findings of the study show that the proposed steel MKF can efficiently satisfy the code-specified storey drift limit and manifest the yielding mechanism assumed in the design. The MKF designed according to the PBPD approach offers the lightest structure among all frames studied and yields a collapse probability lower than that of the MKF designed as per the

elastic design method. The proposed system can be used in seismic design of steel multi-storey buildings as an alternative to conventional steel MRFs.

3.1. Introduction

Steel moment-resisting frames (MRFs) have long been considered one of the most desirable lateral load-resisting systems (LLRS) for the construction of multi-storey buildings, particularly in high seismic regions. Steel MRFs offer several advantages over other steel LLRSs among which are minimum architectural obstructions, significant inelastic deformation capacity, and the ability to accommodate long spans. However, there are several constraints associated with the design and construction of conventional MRFs such as low lateral stiffness, prohibitively expensive strengthening requirements for connections and high fabrication and inspection costs related to Complete Joint Penetration (CJP) groove welds, which limit their application in the construction of building structures, often in low-to-moderate seismic regions and sometimes in high seismic regions. Such limitations have inspired the development of novel steel LLRSs based on conventional MRFs. In 1986, Aristizabal-Ochoa [27] first introduced the concept of knee-bracing members in disposable knee-braced frames. In this system, instead of the beam-column intersection, the diagonal bracing member, which is intended to provide additional lateral stiffness, is connected to a short knee element at one of its ends. The system is designed in a way that the seismic-input energy is dissipated through flexural plastic hinging in the disposable knee element while diagonal bracing members remain elastic. Later, significant efforts were put in by Balendra et al. [29] to examine disposable knee-braced frames under seismic loading [28, 30-33, 89].

Leelataviwat et al. [35] added knee braces to conventional MRFs and introduced a ductile system referred to as the knee-braced moment frame. This structural system was designed to resist seismic forces through the yielding and buckling of the knee elements, followed by the formation of plastic

hinges in the beams at the face of beam-to-brace connections. A large-scale experimental program together with numerical simulations confirmed that the proposed system can reliably resist seismic forces without noticeable degradation or instability. The seismic performance of a new LLRS consisting of buckling-restrained knee-braced frames and simple beam-to-column connections, that allow the inelastic seismic demands to be confined to the buckling-restrained knee braces, was studied by Junda et al [36]. The application of buckling-restrained knee braces in knee-braced truss moment frames has been the subject of extensive research studies [38-40]. In this system, open web trusses connected to columns via simple connections are intended to carry gravity loads and seismic-induced lateral forces are resisted by buckling-restrained knee braces through yielding in tension and compression. The results of these studies confirmed that this system can be a viable and efficient alternative to conventional MRFs while offering long spans capable of accommodating large openings typically desired in office and residential buildings.

Hsu and Li [34] performed a series of full-scale cyclic tests on special moment-resisting frames (SMRFs) and knee-braced moment-resisting frames and showed that the performance of moment-resisting frames can remarkably be enhanced by adding knee braces regardless of the plane of brace buckling. The seismic performance of knee connection frames (KCFs) having simple beam-to-column connections was assessed by Asghari and Saharkhizan [41] through a comparative study involving KCFs and SMRFs. This study confirmed that KCFs can be classified as steel MRF and that KCFs feature smaller collapse probabilities compared to SMRFs. Moreover, the validity of the seismic design parameters used to design KCFs, including overstrength, ductility reduction, and deflection amplification factors, was assessed using the procedure recommended by FEMA P695 [13], but no specific response modification factors were recommended.

As the construction industry demands more efficient construction with a reduction in cost and environmental impacts, there is an urge for the development of high-performance and resilient lateral load-resisting systems, e.g., alternatives capable of efficiently overcoming the constraints associated with conventional steel MRFs. This research aims to propose an innovative steel moment-resisting frame that is intended to carry lateral wind or earthquake loads in multi-storey building structures through the application of knee brace elements, develop analysis and design procedures, and verify its seismic performance and collapse response through extensive numerical simulations. The proposed system and research methodology include several novelties while overcoming various shortcomings reported in past studies [41, 44]. First, the proposed system benefits from prefabricated steel segments that can facilitate the fabrication and erection processes in multi-storey steel buildings. Second, a Performance Based Plastic Design (PBPD) approach is proposed to analyze and design the MKF under seismic loading. Third, the seismic design of the MKF is detailed in the framework of the 2015 National Building Code (NBC) of Canada. Finally, the seismic performance and collapse response of the proposed system are examined taking into account the effects of three main sources of seismicity expected in the west coast of Canada including shallow crustal, subduction intraslab and subduction interface earthquakes. In this chapter, the system is first introduced, followed by a discussion on the anticipated plastic mechanism and the development of the seismic design procedure. The seismic performance and collapse response of a five-storey office steel structure designed using the proposed system are then examined and compared to those of a conventional MRF as a reference frame.

3.2. Nonlinear mechanism

The nonlinear mechanism anticipated in the proposed system under lateral seismic loads involves flexural yielding at the ends of intermediate beams away from the connection elements, tensile

yielding and compression buckling of the knee braces, or a combination of these two mechanisms. The failure mechanism involving flexural yielding of intermediate beam segments that act as designated yielding members (DYMs) was considered herein as it typically provides more stable energy dissipation and deformation ductility capacities in comparison to the mechanism involving axial buckling of knee braces [41]. A schematic view of the selected mechanism is illustrated in Figure 3-1. In this figure, the parameter ϕ_p denotes the plastic storey drift ratio. Depicted in Figure 3-2 is the free-body diagram of the beam assembly when flexural plastic hinges have formed and the probable moment resistance M_{prob} is achieved. In Figure 3-2, V_R, V_L, L_b, w, L_{bs}, and θ represent the right hinge shear, left hinge shear, length of the intermediate beam segment, uniformly distributed factored gravity load, length of the beam stub and the angle of the knee braces with respect to the horizontal axis, respectively. Following the capacity design principles, the beam stubs, knee braces and columns shall be designed to remain elastic under the selected yield mechanism, thus allowing the beams to reach and maintain their full plastic capacity. The compression force demand in knee braces neglecting the effects of gravity loads when beams reach their expected bending moment capacity $C_{k,f}$ (Figure 3-2) can be expressed as:

$$\frac{C_{k,f}}{M_p / L} = \frac{R_{sh} R_y}{\sin(\theta)} \left(\frac{1}{\alpha_b} + \frac{2}{1-2\alpha_b} \right) \quad \text{where } M_p = Z_{x,b} F_y \tag{3-1}$$

in which R_{sh}, R_y, L, M_p , Z_x, and F_y are the material strain-hardening factor, the ratio between the probable yield stress and the nominal yield stress of the material, span length, plastic moment capacity of the intermediate beam segment, plastic section modulus of the intermediate beam segment and minimum specified yield strength of steel, respectively. $\alpha_b = L_{bs}/L$ stands for the ratio of the beam-stub length to the beam span.

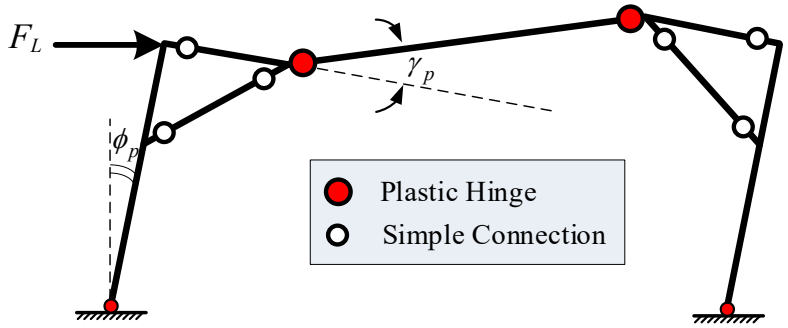

Figure 3-1. MKF desired collapse mechanism (single-storey one-bay frame shown for simplicity).

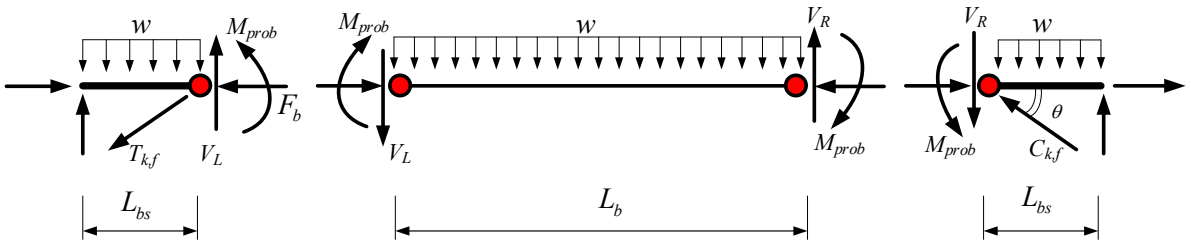

Figure 3-2. Free-body diagram of the beam assembly at flexural plastic hinging.

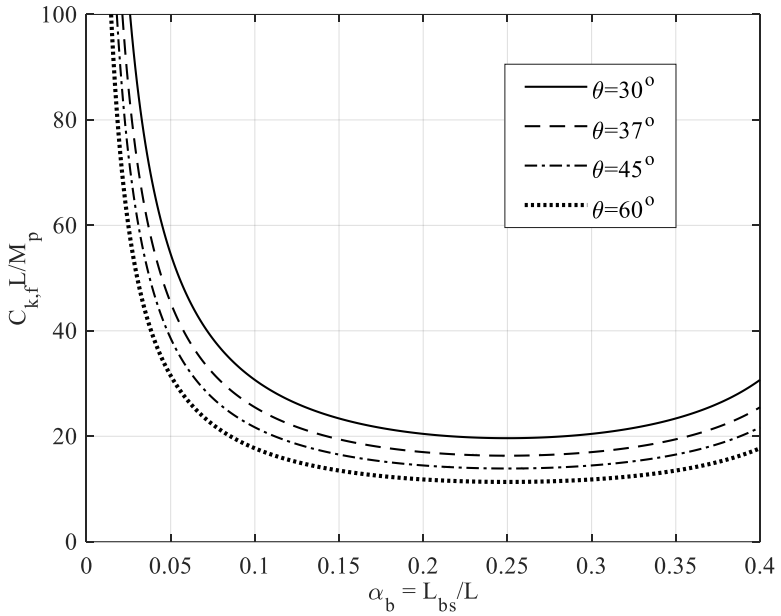

Figure 3-3. Variation of maximum knee brace force against braced length ratio.

Variation of the maximum normalized compression force in the knee brace (left-hand-side of Eq. (3-1)) with respect to α_b is shown in Figure 3-3. As shown, the brace compression force reduces as α_b ranges between 0 and 0.25 and increases beyond $\alpha_b = 0.25$. The brace compression force remains almost constant and close to minimum for α_b ranging between 0.15 and 0.3. To minimize

the brace compression force and, in turn, the size of the braces, $\theta = 45^{\circ}$ and $\alpha_b = 0.2$ were used in this study.

3.3. Analysis of the beam assembly

The beam stub-intermediate beam segment assembly in the proposed MKF creates a continuous beam element that is simply supported at both ends. This assembly is subjected to two concentrated loads generated by the tension- and compression-acting knee braces under gravity plus seismic loads, i.e., T_k and C_k. The gravity loads produce a limited axial force in intermediate beam segments while both gravity and seismic loads induce an axial force in the beam stub. The simple connections, e.g., shear tab or double angle, used to connect beam stubs to columns shall be designed to transfer the axial force developed in the beam stubs in addition to the vertical reaction of the entire beam. The beam stub-intermediate beam assembly isolated from the MKF is given in Figure 3-4a. In this figure, A_{bs} and A_b represent the cross-sectional area of the beam stub and intermediate beam segment, respectively.

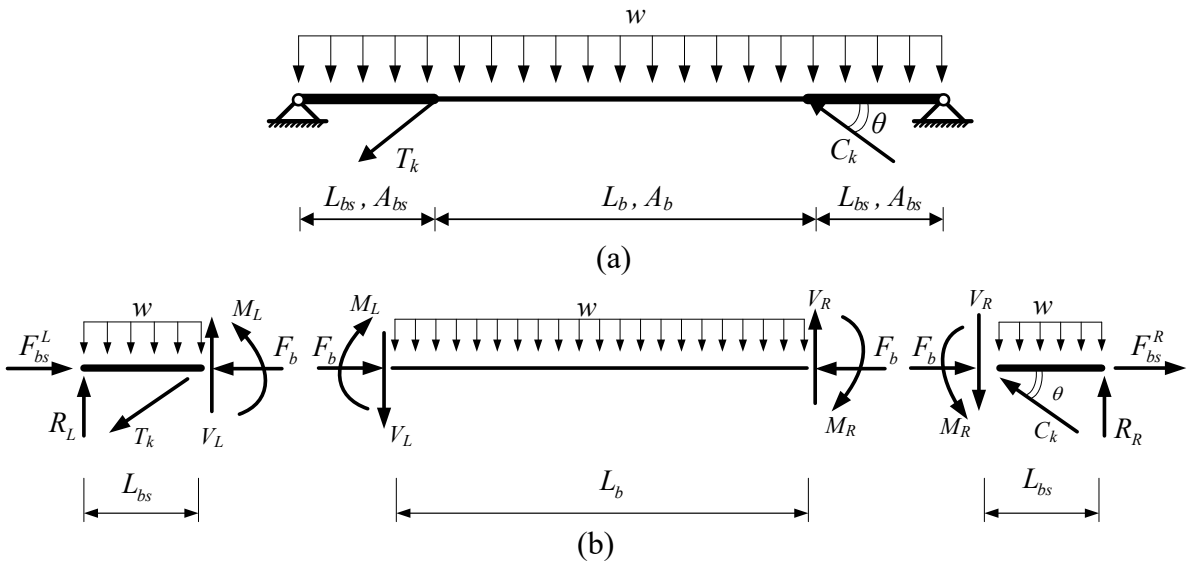

Figure 3-4. a) MKF beam assembly; b) Free-body diagram of beam assembly.

Using equilibrium of horizontal forces and axial deformation compatibility, the axial forces in the left beam stub F_{bs}^L, right beam stub F_{bs}^R, and the intermediate beam segment F_b can be obtained as:

$$F_{bs}^{L} = \frac{\left\{ C_k + T_k \left[1 + \frac{A_{bs}}{A_b} \left(\frac{1}{\alpha_b} - 2 \right) \right] \right\} \cos(\theta)}{2 + \frac{A_{bs}}{A_b} \left(\frac{1}{\alpha_b} - 2 \right)} \tag{3-2}$$

$$F_{bs}^{R} = \frac{\left\{ T_k + C_k \left[1 + \frac{A_{bs}}{A_b} \left(\frac{1}{\alpha_b} - 2 \right) \right] \right\} \cos(\theta)}{2 + \frac{A_{bs}}{A_b} \left(\frac{1}{\alpha_b} - 2 \right)} \tag{3-3}$$

$$F_b = \frac{\left(C_k - T_k \right) \cos(\theta)}{2 + \frac{A_{bs}}{A_b} \left(\frac{1}{\alpha_b} - 2 \right)} \tag{3-4}$$

The forces obtained using Eqs. (3-2)-(3-4) represent the absolute axial force (tension or compression) in the beam stubs and intermediate beam segments. Eq. (3-4) results in zero axial force in the intermediate beam segment under lateral loads only, however, the axial forces developed in the knee braces under gravity loads (both knee braces in compression) lead to gravity-induced axial compression force in the intermediate beam segment.

The free body diagram of the beam assembly showing the forces obtained by Eqs. (3-2)-(3-4) is depicted in Figure 3-4b. In this figure, R_R and R_L refer to the vertical reaction at right and left supports, respectively. As shown, the beam stubs are subjected to combined bending and axial tension or compression force demands. The beam stubs shall therefore be designed as beam-column elements to remain essentially elastic following the capacity design principles. The intermediate beam segment is subjected to bending and compression force demands. However, it can be shown that the effect of axial compression force when compared to that of the bending moment is negligible and the intermediate beam segment can simply be verified as a flexural member. For example, the ratio of the axial force F_b to the axial compression capacity of the intermediate beam segment of the first-storey beam of MKF-P was only 0.02, which can be neglected. Knee braces are designed as

compression members to resist seismic plus gravity load effects. Using moment equilibrium in Figure 3-4b and adding the effect of gravity loads, knee brace forces are obtained as:

$$T_k = \frac{1}{\sin(\theta)}\left(\frac{M_L}{L_{bs}} + \frac{M_L}{L_b} + \frac{M_R}{L_b} - \frac{wL_b}{2} - \frac{wL_{bs}}{2}\right) \tag{3-5}$$

$$C_k = \frac{1}{\sin(\theta)}\left(\frac{M_R}{L_{bs}} + \frac{M_L}{L_b} + \frac{M_R}{L_b} + \frac{wL_b}{2} + \frac{wL_{bs}}{2}\right) \tag{3-6}$$

where M_R and M_L refer to the bending moment at the right and left ends of the intermediate beam segment, respectively. By using the slope-deflection method for the intermediate beam segment, it can be shown that the difference between M_R and M_L can be approximated as:

$$\frac{M_R}{L_{bs}} - \frac{M_L}{L_{bs}} \approx \frac{wL}{6\alpha_b}\left(1-2\alpha_b\right)^2 \tag{3-7}$$

Using Eqs. (3-5)-(3-7) the following equality can then be established:

$$C_k - T_k = \frac{wL}{\sin(\theta)}\left[\left(1-\alpha_b\right) + \frac{\left(1-2\alpha_b\right)^2}{6\alpha_b}\right] \tag{3-8}$$

Substitution of Eq. (3-8) into Eq. (3-4) and performing mathematical manipulations gives rise to:

$$\frac{F_b}{wL} = \frac{\left(1-\alpha_b + \dfrac{1}{2\alpha_b}\right)}{6 + 3\dfrac{A_{bs}}{A_b}\left(\dfrac{1}{\alpha_b} - 2\right)}\cot(\theta) \tag{3-9}$$

in which F_b represents an approximate axial force developed in the intermediate beam segment. Figure 3-5 shows variation of the left-hand-side of Eq. (3-9) against various α_b, brace angle θ and A_{bs}/A_b values. Referring to this figure, the axial force demand in the intermediate beam segment is reduced by increasing the brace angle and A_{bs}/A_b ratio. Increasing the ratio of the braced length, however, results in a higher axial force demand in the intermediate beam segment. For θ and

α_b values chosen in this study, F_b varies between 14% and 22% of the beam gravity load depending on A_{bs}/A_b. It is suggested that the ratio between the cross-sectional area of the beam stub and intermediate beam segment A_{bs}/A_b be selected such that the axial force developed in the intermediate beam segment is minimized.

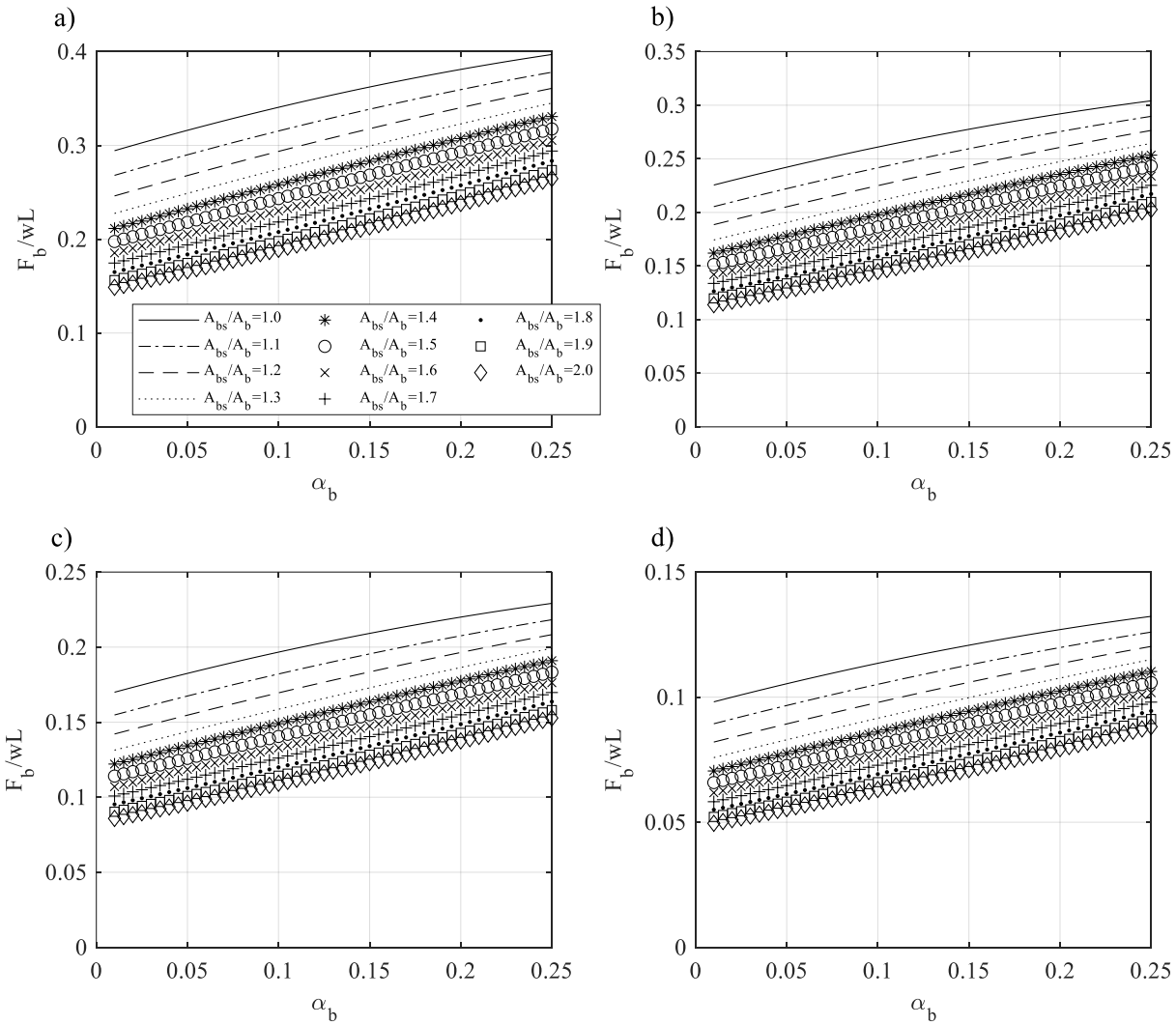

Figure 3-5. Variation of axial force demand in the intermediate beam segment against braced length ratios: a) $\theta = 30$; b) $\theta = 37$; c) $\theta = 45$; d) $\theta = 60$.

3.4. Performance-Based Plastic Design

The Performance-Based Plastic Design (PBPD) approach [6] can be adapted as an efficient technique to analyze MKFs under lateral seismic loads and obtain members' design forces. The design seismic base shear and required member strengths are estimated by equating the work

needed when the structure attains the target roof drift ratio to the energy attracted by an equivalent single-degree-of-freedom (SDOF) system with an elastic perfectly-plastic response [6, 90]. By doing so, the plastic capacity of the structure can be directly accounted for in the analysis using a pre-selected yield mechanism. The target drift ratio was set equal to the inter-storey drift limit specified in 2015 NBC (i.e., 2.5%) at the Maximum Considered Earthquake (MCE) hazard level [5]. The design base shear $V_y^{(base)}$, including P-Δ effects, is then computed as [44]:

$$\frac{V_y^{(base)}}{W} = \frac{-\alpha + \sqrt{\alpha^2 - 4\xi}}{2} \tag{3-10}$$

where W is the total seismic weight of the structure. In this study, the yield drift ratio was assumed to be 1%, which will be verified later using the pushover analysis. The coefficients α and ξ depend on the frame's lateral stiffness, modal properties, and target plastic drift level, and are defined as:

$$\alpha = \left(\sum_{i=1}^{N} C'_{vi} h_i \right) \left(\frac{8\phi_p \pi^2}{T^2 g} \right) \tag{3-11}$$

$$\xi = \left(\frac{4\pi^2 \phi_p^2}{W T^2 g} \sum_{i=1}^{N} Q_i h_i \right) - \gamma S_a^2 \tag{3-12}$$

in which T, h_i, Q_i, γ, S_a, and g are the fundamental period of the structure, elevation of floor i with respect to the base, total gravity load on floor i, energy modification factor [7], spectral response acceleration and gravitational acceleration, respectively. C'_{vi} is the lateral force distribution factor used to obtain the storey force at floor i, F_i (Figure 3-6):

$$F_i = C'_{vi} V_y^{(base)} \tag{3-13}$$

The lateral force distribution pattern proposed by Chao et al. [91] for steel MRFs, which depends on the fundamental period of the structure, was used here. This pattern is defined as:

$$C_{vi}^{'} = \left(\beta_i - \beta_{i+1}\right)\left(W_N\, h_N \Big/ \sum_{j=1}^{N} W_j\, h_j \right)^{0.75T^{-0.2}} \tag{3-14}$$

where W_N is the seismic weight at level N (roof level), h_N is the elevation of the roof with respect to the base, and β_i refers to the ratio of the storey shear at level i to that at the roof. In Eq. (3-14), β_{i+1} should be set equal to 0 when $i = N$. Chao et al. [91] proposed that the plastic demand will be distributed evenly along the height of a Multi-Degrees-of-Freedom (MDOF) structure by using a shear force distribution given as:

$$\beta_i = \frac{V_i}{V_N} = \left(\sum_{j=i}^{N} W_j\, h_j \Big/ W_N\, h_N \right)^{0.75T^{-0.2}} \tag{3-15}$$

Once the seismic base shear and lateral forces are determined, the seismic demands of the intermediate beam segment can be calculated using the energy balance equation:

$$\sum_{i=1}^{N} F_i h_i \phi_p + \sum_{i=1}^{N} \frac{1}{2} Q_i h_i \phi_p^2 = (B-1) M_{pc}^{(\mathrm{int})} \phi_p + 2M_{pc}^{(ext)} + \sum_{i=1}^{N} 2B\gamma_p \left(M_{pb}\right)_i \tag{3-16}$$

where B is the number of seismic load-resisting bays, $M_{pc}^{(int)}$ is the plastic moment capacity of the interior column at its base, $M_{pc}^{(ext)}$ is the plastic moment capacity of the exterior column at its base and $\left(M_{pb}\right)_i$ is the required seismic demand of the intermediate beam segment at each level. Since the knee braces and beam stubs are expected to experience negligible axial deformations, the plastic rotation of the intermediate beam segment γ_p (see Figure 3-1) can be approximated as:

$$\gamma_p = \left(L/L_b\right)\phi_p \tag{3-17}$$

The plastic moments at the base of the interior and exterior columns can be determined based on the rationale that no soft-storey mechanism should occur in the first storey once the target storey drift has been reached [6]. Such a mechanism, which would lead to frame collapse in the presence

of gravity loads and their P-Δ effects [92], can be achieved when two flexural plastic hinges form at two ends of the first-storey column long segments as shown in Figure 3-7a.

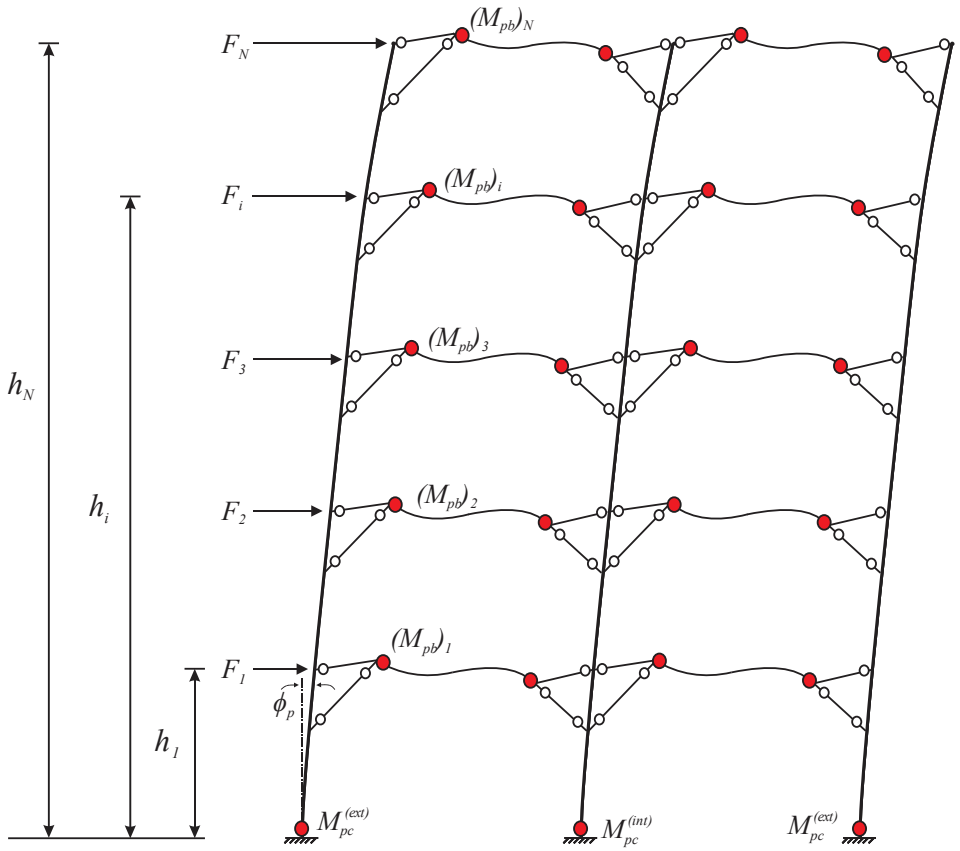

Figure 3-6. MKF nonlinear mechanism assuming uniform storey drift ratio.

The flexural plastic moments of the first-storey columns can therefore be estimated assuming that entire seismic-induced energy is dissipated through the formation of these plastic hinges. According to Figure 3-7a, the flexural plastic moment of the column at its base can be conservatively obtained by equating the total energy dissipated by the plastic hinges to the total input energy by 1.5 times the design shear assuming small deformation [93]:

$$M_{pc}^{(\text{int})} = 2M_{pc}^{(ext)} = \left(\left(1.5V_y^{(base)} + 0.5Q_T\phi_p\right)/2B\right)\left(H_1 - L_v\right) \tag{3-18}$$

Where $Q_T = \sum_{i=1}^{N} Q_i$.

Combining Eqs. (3-16)-(3-18) results in the required second-order flexural demand of the intermediate beam segment at each storey:

$$\left(M_{pb}\right)_i = \beta_i \left(M_{pb}\right)_N = \beta_i \left(\left(\sum_{i=1}^{N} F_i h_i + \sum_{i=1}^{N} \frac{1}{2} Q_i h_i \phi_p - B M_{pc}^{(\text{int})} \right) \Big/ \left(2B \frac{L}{L_b} \sum_{i=1}^{N} \beta_i \right) \right) \tag{3-19}$$

The moment obtained from Eq. (3-19) only accounts for lateral load effects and the moment due to gravity loads should be added to obtain the beam design moment. Upon determining the size of the intermediate beam segments, knee braces, beam stubs and columns should be designed assuming that intermediate beam segments have reached their M_{prob} at both ends.

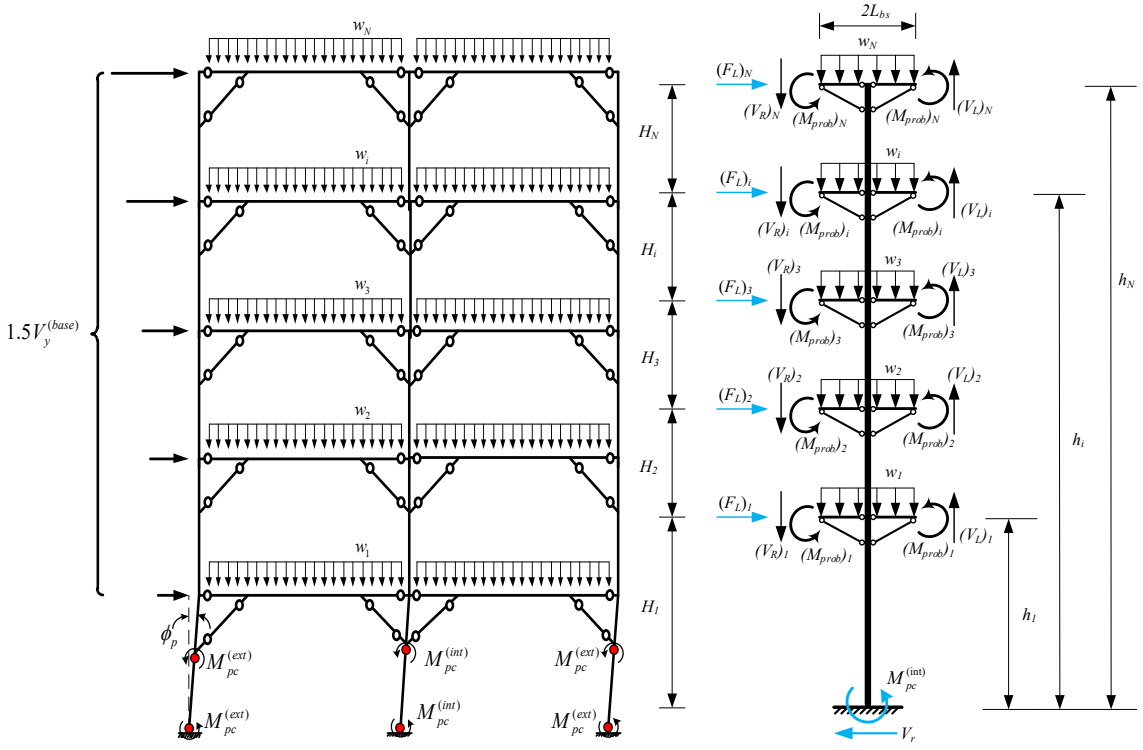

Figure 3-7. a) Development of soft-storey mechanism in the first storey of the MKF; b) Interior column tree at beam plastic hinging.

The column tree concept [7] shown in Figure 3-7b is adopted here to compute the design demands of interior and exterior columns and the balancing forces at each floor level $(F_L)_i$:

$$\left(F_L\right)_i = \lambda_i \left\{ \left(M_{pc}^{(\text{int})} + 2\sum_{i=1}^{N} \left(M_{prob}\right)_i + \sum_{i=1}^{N} \left[\left(V_L\right)_i + \left(V_R\right)_i \right] L_{bs} \right) \Big/ \sum_{i=1}^{N} \lambda_i h_i \right\} \tag{3-20}$$

where $\lambda_i = (\beta_i - \beta_{i+1})/\sum_{i=1}^{N}(\beta_i - \beta_{i+1})$ and $\beta_{N+1} = 0$. The resisting shear force at the base of the column tree V_r can therefore be calculated as:

$$V_r = \sum_{i=1}^{N} (F_L)_i \tag{3-21}$$

Once the balancing force at each floor is obtained, moment and shear distributions along the column tree can be established and used to size the columns.

3.5. Frame design

3.5.1. Selected building

A five-storey office building located on site Class C in Vancouver, British Columbia, Canada was chosen in this study to illustrate the MKF concept and proposed design methodology. The plan view of the building is shown in Figure 3-8. The LLRS of the building consists of the steel MKF or conventional steel MRF (as an alternative design) placed on the perimeter of the building in both principal directions. One of the frames in the long direction of the building was selected and studied. The height of the first storey is 4.3 m while upper stories have a constant height of 4 m. The dead loads consist of 3.4 kPa in the roof and 3.6 kPa in the floors. The design snow and live loads of the roof are 1.64 kPa and 1.0 kPa, respectively. The live and partition loads of the floor levels are 2.4 kPa and 1.0 kPa, respectively. The weight of exterior cladding is assumed as 1.5 kPa. The selected perimeter frame was first designed as a steel MKF and then designed as a conventional steel MRF. Each system was designed using two approaches: 1) elastic design methodology as prescribed by 2015 NBC (MKF-N and MRF-N); and 2) PBPD procedure (MKF-P and MRF-P). The MKF-N and MRF-N were both designed using the seismic design parameters specified for Type D MRF and the nonlinear mechanism described earlier. The MKF-P and MRF-P were analyzed according to the PBPD procedure developed here.

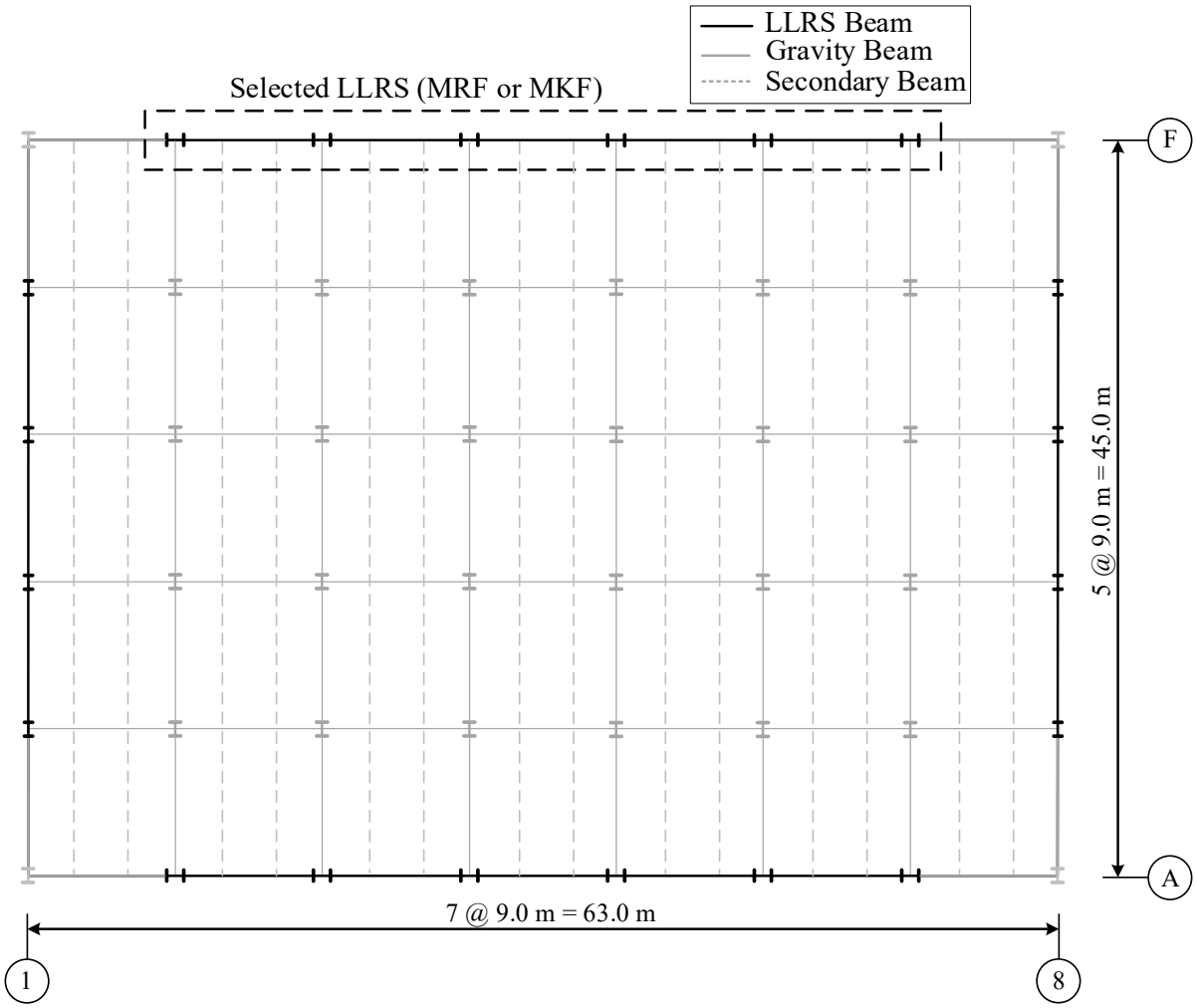

Figure 3-8. Plan view of the selected building.

3.5.2. Seismic design

The structural design was performed in accordance with the 2019 Canadian steel design standard CSA S16-19 [3]. In MKF-N and MRF-N, the effects of P-Delta, notional loads and accidental torsion were factored in when calculating the design base shear. In all frames, beams, beam stubs and columns were selected from wide-flange sections conforming to ASTM A992 steel with minimum specified yield strength $F_y = 345$ MPa and probable yield strength $R_y F_y = 385$ MPa Square Hollow Structural Sections (HSS) made of ASTM 1085 steel with $F_y = 345$ MPa were used to design knee braces. The cross-sections chosen for intermediate beams, beam stubs and first-storey columns comply with the width-to-thickness ratio limits for Class 1 specified in CSA

S16-19; however, Class 1 or Class 2 sections were used for knee elements and upper-storey columns. It is expected that the proposed system will furnish a larger lateral stiffness compared to conventional MRFs through the application of knee elements and contribute to the reduction of construction costs by eliminating complex beam-to-column panel zone joints, which often involve doubler plates, stiffeners, and intricate weld details, by taking advantage of a truss action in the beam-to-column joint. To provide sufficient shear capacity in the short column segments, i.e., segments with the length of L_V in Figure 1-1, deep WF sections, e.g., with an aspect ratio of 2.0, are used, an approach that will also reduce construction costs. Furthermore, the depth of beam stubs d_{bs} is constrained such that $d_b \leq d_{bs} \leq d_b + 20\ mm$, where d_b denotes the depth of intermediate beam segments, to mitigate the eccentricity of axial load transferred from the intermediate beam segment to the beam stub. Design steps for MRFs and MKFs are given in the following sections.

3.5.3. MKF design

The intermediate beam segments, i.e., DYMs, were the first members to be designed. The ratio of beam stub cross-sectional area to intermediate beam segment cross-sectional area was selected between 1.6 and 1.7 to ensure that a reasonably small axial compression force is developed in the intermediate beam segments. The intermediate beam segments were therefore designed as flexural members. Knee braces were designed as compression members to carry in the elastic range the maximum axial force resulting from the probable bending moment developed in the plastic hinges plus the gravity load effects. An effective length factor of 0.75 based on the preliminary design results was used to calculate the net length of knee braces between the working points. In other words, L_k shown in Figure 1-1 was considered $0.75 \times L_{k,g}$.

Beam stubs were designed as beam-columns to carry in the elastic range the probable flexural moment of intermediate beam segments plus the axial force exerted by the knee braces. It was

assumed that a concrete slab fully restrains the top flange's out-of-plane deflections along the entire beam assembly, and sufficient lateral bracing is provided to the bottom flange as per the CSA S16-19 requirements for seismic applications to prevent lateral-torsional buckling (LTB). Therefore, the resisting moment capacity of beam stubs was assumed to be equal to their full plastic capacity. The net length of beam stubs was considered equal to L_{bs} minus half the column depth, and the following limit states were checked:

1- Overall member strength as per Clause 13.8.2(b) of CSA S16-19
2- Combination of bending and tension as per Clause 13.9.2 of CSA S16-19
3- Moment-only capacity as per Clause 13.9.2 of CSA S16-19

Since beam stubs are subjected to transverse distributed gravity loads, the value of ω_1 (defined in Section 3.2 of CSA S16-19) was assumed equal to 1.0, per Clause 13.8.6(b) of CSA S6-19, for all U_{1x} (second-order moment factor) calculations, resulting in U_{1x} values consistently larger than 1.0. Hence, the cross-sectional strength did not govern the design and was not checked.

Appropriate design of column trees is one of the most crucial and challenging parts in designing MKFs. All possible limit states shall be addressed properly to ensure that the column segments perform as expected in the nonlinear mechanism. The columns were designed as beam-column elements to remain elastic under maximum probable forces exerted due to the development of plastic hinges at the ends of intermediate beam segments. The requirements prescribed by Clause 27.2.3.1 of CSA S16-19 were applied to the first-storey columns as plastic hinges were expected to develop at the base of the frame. In order to ensure that the column trees possess sufficient strength and stability, a design subroutine was developed to automate the design procedure of the MKF system as part of this research project by addressing the following limit states for interior and exterior columns in each storey:

1- Overall member strength of the long segment
2- Cross-sectional strength of the long segment
3- Overall member strength of the short segment
4- Cross-sectional strength of the short segment
5- Moment capacity of both short and long segments
6- LTB of the entire column
7- Shear strength of the short segment

When checking the LTB capacity of the columns, the adverse effects of the concentrated horizontal force applied at the location of the knee-to-column connection shall be appropriately addressed. Accordingly, the value of ω_1 was set equal to 1 for all LTB checks per Clause 13.8.6(b) of CSA S6-19. The final selected members for both MKFs are given in Table 3-1.

3.5.4. MRF design

Beams in the conventional steel MRF were the first elements to be designed. They were sized under the combined gravity and seismic loads. The Reduced Beam Section (RBS) moment connection was used to ensure plastic hinges form away from the column face. Additional details on the MRF design can be found in Islam and Imanpour [94]. The selected members for both MRFs are outlined in Table 3-1.

3.5.5. Steel tonnage

Steel tonnage as the quantitative representation of members can shed light on the construction efficiency of the proposed system. The total weight of the primary structural elements of the frames designed, excluding connections and reinforcing plates, was used here as an approximate cost indicator given that steel tonnage is often used by fabricators for cost estimation and bidding. Figure 3-9 shows steel tonnage for four designs including MKF and MRF systems. As shown,

MKF-P and MRF-P offer the lightest and heaviest designs, respectively. The total weight of the knee braces is approximately 13% of the total weight of the MKF in both designs. The comparison of steel tonnage between the frames demonstrates that a more economical design taking into account the influence of material costs only is achieved using an MKF designed as per the PBPD method. It should be acknowledged that the cost of connections (mainly attributed to fabrication) in the MKF system will likely be higher than conventional steel MRFs, which may, in some cases, offset the benefit gained through reducing member sizes. Accordingly, caution should be exercised by the engineer in the assessment of cost saving given the constraints of the project. Details of MKF connections are subject to further study in the future.

Table 3-1. Selected member sizes for prototype frames.

Member		Storey	MRF-P	MRF-N	MKF-P	MKF-N
Beam		5	W530×85	W530×82	W460×52	W410×46.1
		4	W610×125	W610×101	W530×66	W610×82
		3	W610×140	W690×140	W530×74	W610×92
		2	W690×152	W690×170	W610×82	W610×92
		1	W690×152	W690×170	W610×82	W610×92
Exterior	Column	5	W610×174	W610×155	W460×144	W460×113
		4	W610×174	W610×155	W460×144	W460×113
		3	W610×174	W610×155	W460×235	W610×262
		2	W610×217	W610×217	W460×235	W610×262
		1	W610×217	W610×217	W460×235	W610×262
Interior	Column	5	W610×241	W610×195	W610×155	W690×125
		4	W610×241	W610×195	W610×155	W690×125
		3	W610×241	W610×195	W610×195	W690×240
		2	W610×262	W610×217	W610×195	W690×240
		1	W610×262	W610×217	W610×195	W690×240
Beam Stub		5	-	-	W460×82	W410×75
		4	-	-	W530×109	W610×140
		3	-	-	W530×123	W610×153
		2	-	-	W610×140	W610×153
		1	-	-	W610×140	W610×153
Knee Brace		5	-	-	HSS152×152×4.8	HSS114×114×6.4
		4	-	-	HSS127×127×9.5	HSS152×152×12.7
		3	-	-	HSS152×152×9.5	HSS152×152×12.7
		2	-	-	HSS152×152×12.7	HSS152×152×12.7
		1	-	-	HSS152×152×12.7	HSS152×152×12.7

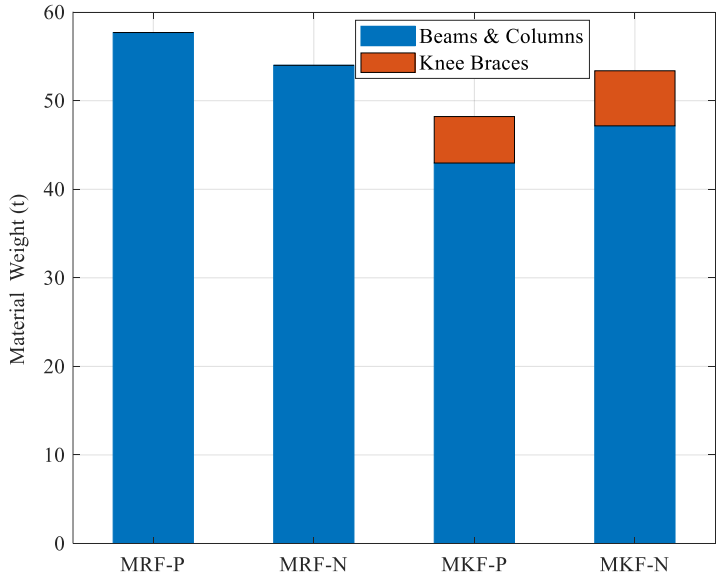

Figure 3-9. Comparison of steel tonnage for LLRS alternatives.

3.6. Numerical model development

The fibre-based numerical model of the MKF and MRF was developed in the *OpenSees* program [43] to examine the seismic and collapse responses of these frames. The knee braces and beam stubs in the MKF as well as columns of both MRF and MKF were modeled using nonlinear force-based beam-column elements. Columns were modelled using 16 elements and 8 elements were used to simulate the knee braces. Five integration points were implemented for each nonlinear beam-column element [95, 96]. Section aggregator technique was used to take account of the shear deformation effects. The uniaxial Giuffré-Menegotto-Pinto material model [97] was assigned to the nonlinear elements to reproduce the Bauschinger effect as well as kinematic and isotropic hardening behaviour of steel, The variables used in the uniaxial Giuffré-Menegotto-Pinto material model include isotropic hardening parameters ($a_1 - a_4$), strain-hardening ratio (b) and parameters that control the transition from elastic to plastic branches (R_0, cR_1, and cR_2). The values of these parameters were calibrated for ASTM A992 steel by Ashrafi and Imanpour [98] and reported as $a_1 = 0.35$, $a_2 = 12.13$, $a_3 = 0.33$, $a_4 = 12.1$, $b = 0.0067$, $R_0 = 23.4$, $cR_1 = 0.89$, and $cR_2 = 0.07$. Modified elastic beam-column elements proposed by Zareian and Medina [99] were used to model beam segments between

end plastic hinges. The Ibarra-Medina-Krawinkler (IMK) spring element [60] was adopted to simulate flexural plastic hinges at the end of the beams of the MRF and the intermediate beam segments of the MKF. The IMK model is capable of reproducing strength and stiffness degradations in steel MRF beams under cyclic loading. The maximum out-of-plane unbraced length ratio of the intermediate beam segment was considered equal to $50r_y$, where r_y represents the weak-axis radius of gyration. The shear span was also considered half the intermediate beam span length. Also, the values of different deterioration parameters were assumed as $LA = 0$, $c_S = 1.0$, $c_K = 1.0$, $c_A = 1.0$, $c_D = 1.0$, $D_P = 1.0$, and $D_N = 1.0$. Elastic beam-column elements with stiffness representing the end connections were used to simulate knee brace-to-beam/column connections. Column web panel zone joints in the MRF were constructed based on the parallelogram model [100]. An initial geometric out-of-straightness representing a parabola with a maximum amplitude of 0.001 times the member's unbraced length was assigned to columns and knee braces to trigger global buckling. A rigid floor diaphragm was not assumed in the analysis to avoid numerical convergence issues. Geometrical nonlinearities were accounted for using the Corotational transformation formulation. A leaning column was modelled to reproduce the P-Δ effects associated with the gravity columns tributary to the selected frame. The bases of seismic force-resisting columns were fixed, while the base of the leaning column was considered pinned. The beams and column ends were braced in the out-of-plane direction representing the floor slab, roof slab, and point bracings provided along the length of the beams. The seismic weight of the structure was simulated using point masses assigned to the top end of columns at each storey. A damping matrix was reproduced using the Rayleigh damping approach with a critical damping ratio of $\xi = 2\%$ in the first and second modes of vibration. Mass-proportional damping was applied to lumped masses and stiffness-proportional damping was assigned to elastic elements as recommended in [99].

3.7. Verification of the numerical model

To verify the accuracy of the numerical modelling technique implemented in this study, the one-storey large-scale knee-braced MRF tested by Leelataviwat et al. [35] was simulated in *OpenSees*. The tested frame is shown in Figure 2-8. Panel zones of the beam-to-column connections were modelled using the methodology proposed by Gupta [101]. A displacement-controlled nonlinear analysis was then performed on the frame under the same cyclic loading protocol used in the experiment, which is shown in Figure 3-10a. Zero-length rotational springs were assigned to the column bases with a small stiffness ($0.1E_cI_c/L_c$) to simulate partial fixity since the base condition of the columns in the experiment may not be considered ideally pinned. Note that E_c, I_c, and L_c represent the elastic modulus of steel material used for columns, the moment of inertia, and the length of columns, respectively. Figure 3-10b compares the hysteretic response obtained from numerical simulation to that of the experiment. The mechanism formed in the numerical simulation consisting of plastic hinges at the face of beam-to-knee connections as well as yielding and buckling of the knee braces agrees well with the experimental observation.

Referring to Figure 3-10b, an acceptable match is obtained between the experimental results and numerical prediction, indicating that the nonlinear modelling technique adopted in this study can well reproduce the expected response of steel knee-braced frames with lateral behaviour and nonlinear mechanism similar to the MKF.

Fibre-based nonlinear beam-column elements used to simulate columns fail to model local buckling, which was deemed not to significantly influence the findings of this study. It should be noted that a nonlinear beam-column element was proposed recently to account for local buckling and axial shortening [102]. This instability is not deemed likely in compact columns used here. Concrete slab in MRF structures is expected to crack at approximately 1.5% storey drift losing its

contribution to the strength and stiffness of the beam. However, since most analyses in this study are intended to study beyond design-level earthquake and wind, the lack of concrete slab in the model is not expected to affect the results noticeably.

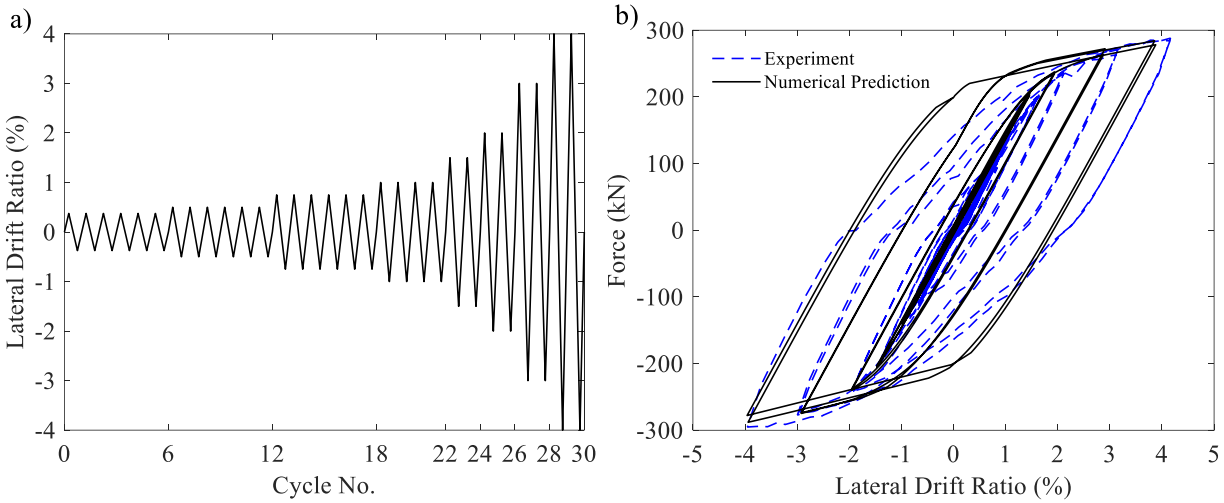

Figure 3-10. System-level verification: a) Loading protocol; b) Lateral force – lateral deformation response of the frame.

A sensitivity analysis was performed to gain insight into the difference among the structural responses obtained using two combinations of dynamic vibration modes of the structure (Modes 1 and 2, and Modes 1 and 3) considered for Rayleigh damping calculation. The axial compression force developed in the leftmost exterior column of the first storey and the roof displacement of MKF-P are compared for two analyses each using one of these combinations to reproduce viscous damping during dynamic analysis. These comparisons are given in Figure 3-11 for roof displacements and in Figure 3-12 for column forces under three crustal, intraslab, and interface ground motion records scaled to design response spectra. It can be observed that both combinations lead to almost the same results.

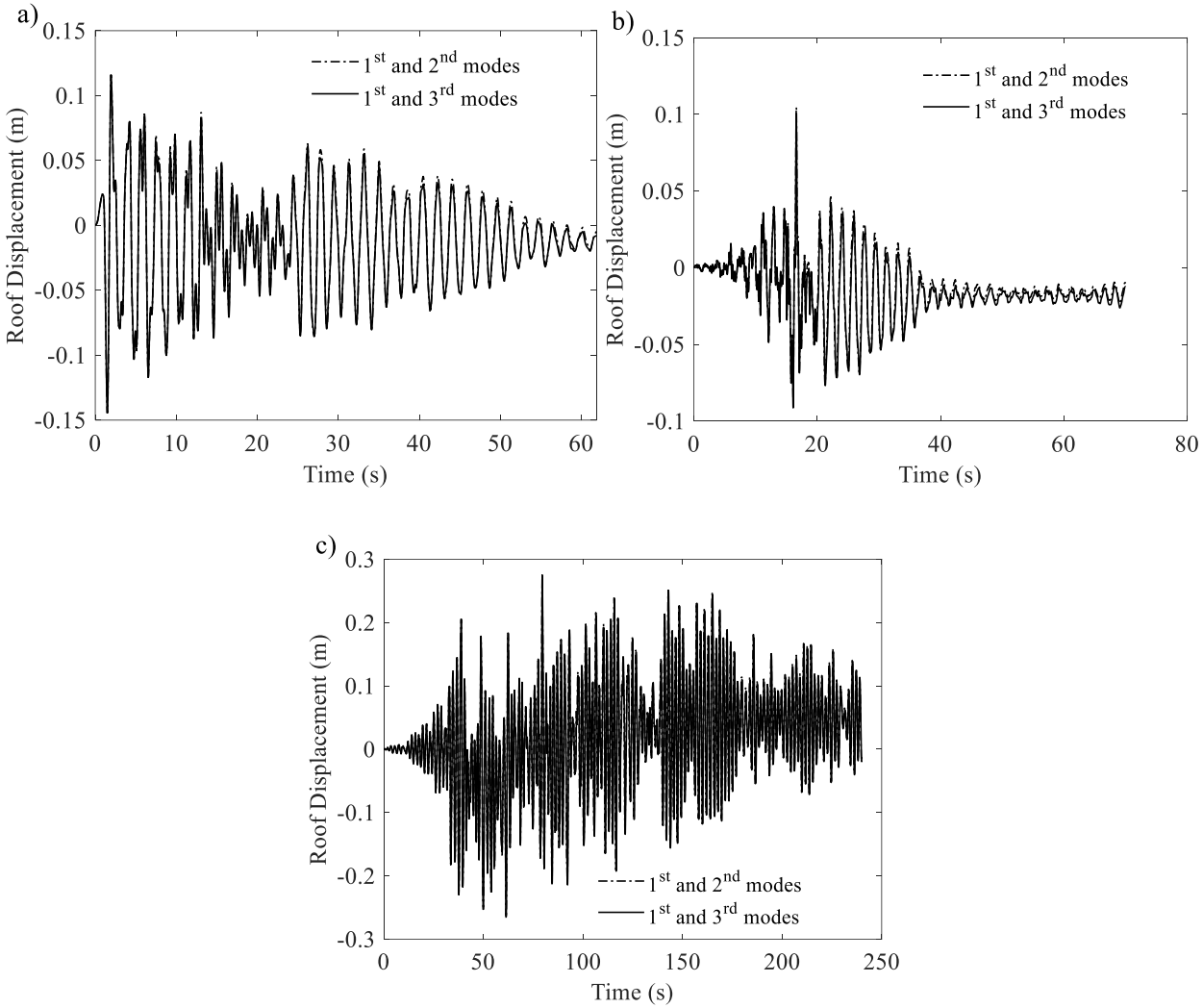

Figure 3-11. Roof displacement of MKF-P using Rayleigh damping based on different modes: a) GM-C01; b) GM-D01; c) GM-I01

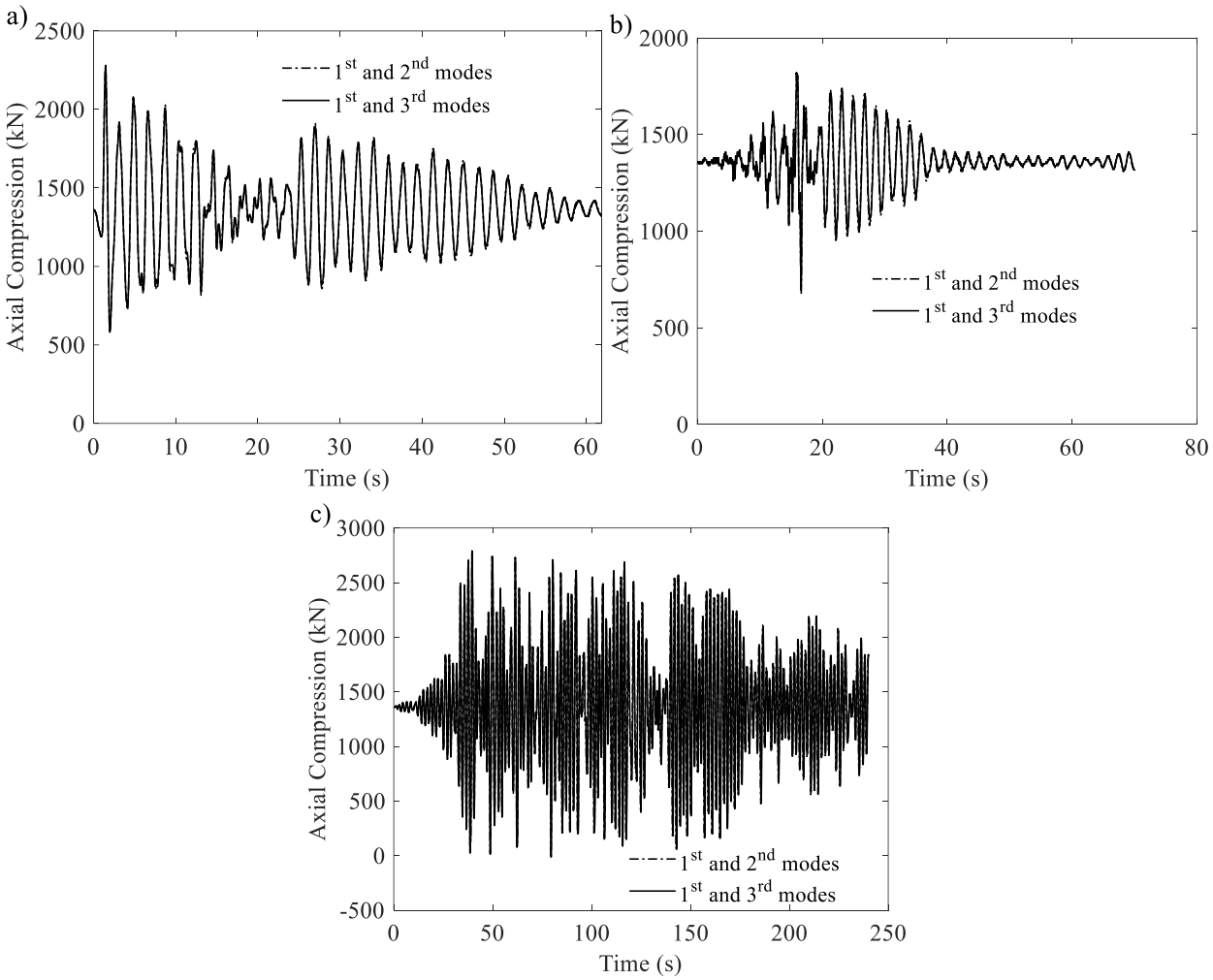

Figure 3-12. Axial compression in the leftmost exterior column of the first storey of MKF-P using Rayleigh damping based on different modes: a) GM-C01; b) GM-D01; c) GM-I01

3.8. Earthquake ground motions

It is crucial to systematically account for all hazard sources anticipated in western Canada as specified in Commentary J of 2015 NBC [12]. The potential sources of seismicity in the region include shallow crustal (or crustal), subduction interface (or interface) and subduction intraslab (or intraslab). Among those, the subduction interface and intraslab earthquakes have the potential to create large demands on building structures, in particular, steel frames [8, 9]. Moreover, a seismic risk assessment in Vancouver has shown that among different sources of seismicity, subduction interface earthquakes have the highest probability of resulting in losses exceeding $100 billion [10].

Subduction earthquakes such as Sumatra, Indonesia with a moment magnitude $M_w = 9.0$ in 2004, Tohoku, Japan with $M_w = 9.1$ in 2011, and Maule, Chile with $M_w = 8.8$ in 2010 [103] occurred as a result of subduction of an oceanic tectonic plate beneath a continental plate, leading to a rupture (a) at the interface of the two plates (interface events) or (b) deep within the subducting plate (intraslab events). The Cascadia subduction zone in the Pacific Northwest region of the U.S. and Canada consists of the Juan de Fuca, Gorda and Explorer plates which are subducting beneath the North American Plate [104]. With the latest one occurring in January 1700, at least seven large subduction earthquakes with $M_w > 9.0$ have taken place in the Cascadia subduction zone in the last 3500 years [105]. The estimated return period of these earthquakes is between 400 and 600 years [103, 105].

Three suites of 11 ground motion records were selected representing all three potential hazard sources, i.e., crustal, subduction interface and subduction intraslab, resulting in a set of 33 records. The earthquake accelerations were extracted from various databases, including PEER NGA-West2 [106], K-Net strong-motion seismograph network [107], and the Center for Engineering Strong Motion Data (CESMD) [108]. The ground motions were first selected based on seismic hazard deaggregation data of the site of interest and then filtered and baseline corrected. The records were eventually scaled to match, on average, the target response spectrum within certain scenario-specific period ranges, as per the recommendations of Commentary J of 2015 NBC. The design level scaling by 2015 NBC represents a 2% probability of exceedance in 50 years to address a major seismic event. Figure 3-13 shows the response spectra for three seismicity sources considered.

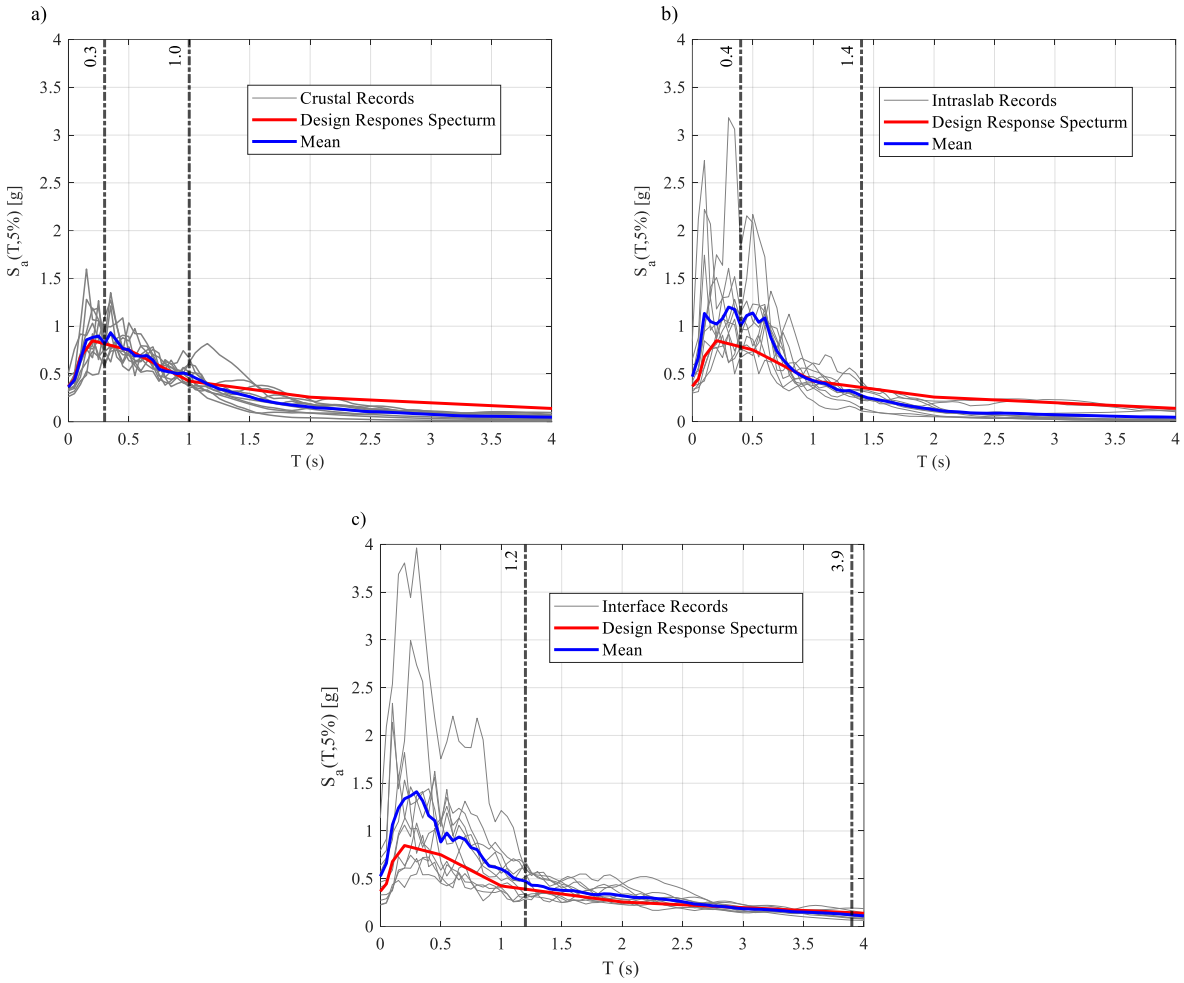

Figure 3-13. Response spectra of selected ground motions: a) Crustal; b) Intraslab; c) Interface.

3.9. Seismic performance assessment

3.9.1. Nonlinear static analysis

Following a static gravity load analysis in which the gravity loads were applied to the frame and the leaning column, a nonlinear static (pushover) analysis was performed under a lateral load pattern corresponding to the first mode of vibration of the structure to assess the seismic response of the MKF as compared to the conventional MRF. The parameters computed using the pushover analysis results include period-based ductility μ_T, overstrength ratio Ω, lateral stiffness, and effective yield displacement of the roof $\delta_{y,eff}$ [13]. The parameters μ_T, Ω, and $\delta_{y,eff}$ are defined as:

$$\mu_T = \frac{\delta_u}{\delta_{y,eff}} \tag{3-22}$$

$$\Omega = \frac{V_{\max}}{V_{design}} \tag{3-23}$$

$$\delta_{y,eff} = C_0 \frac{V_{\max}}{W}\left(\frac{g}{4\pi^2}\right)\left\{\max\left(T_a, T_1\right)\right\}^2 \text{ where } C_0 = \phi_{1,r}\left(\sum_{i=1}^{N} m_i\phi_{1,i} \Big/ \sum_{i=1}^{N} m_i\phi_{1,i}^2\right) \tag{3-24}$$

in which V_{max} and V_{design} are the maximum base shear from the pushover analysis and design base shear, respectively. δ_u is the ultimate roof displacement, defined as the roof displacement associated with the base shear reduced by 20% compared to V_{max}, T_a stands for the upper limit of the empirical code-defined fundamental period, T_1 refers to the fundamental period obtained from an eigenvalue analysis, m_i is the seismic mass at floor level i. $\Phi_{1,i}$ and $\Phi_{1,r}$ denote the ordinate of the fundamental mode at floor i and the roof level, respectively. The modification factor C_0 relates the displacement of an equivalent SDOF system to the roof displacement of the respective MDOF. The lateral stiffness was calculated as the slope of the pushover curve at a base shear equal to 60% of the ultimate strength.

Table 3-2 compares the key response parameters of the prototype frames obtained from pushover and eigenvalue analyses. Referring to this table, the shorter fundamental period of the MKF compared to the MRF counterpart suggests that the lateral stiffness provided by the proposed system is either close to or higher than that offered by the MRF. The lateral force–roof displacement responses (pushover curves) for the four frames analyzed here are presented in Figure 3-14.

Table 3-2. Key response parameters of the prototype frames from eigenvalue and pushover analysis

Response Parameter	MKF-P	MKF-N	MRF-P	MRF-N
Fundamental period (s)	1.75	1.55	1.76	1.75
Ultimate base shear (kN)	4883	6317	4848	4869
Design base shear (kN)	2281	1670	2306	1670
Lateral stiffness (kN/m)	22487	28383	22734	22454
$\delta_{y,eff}$ (mm)	159	164	158	161
δ_u (mm)	542	590	939	924
μ_T	3.41	3.60	5.93	5.75
Overstrength (Ω)	2.14	3.78	2.10	2.92
Roof yield drift (%)	0.88	0.90	0.85	0.95

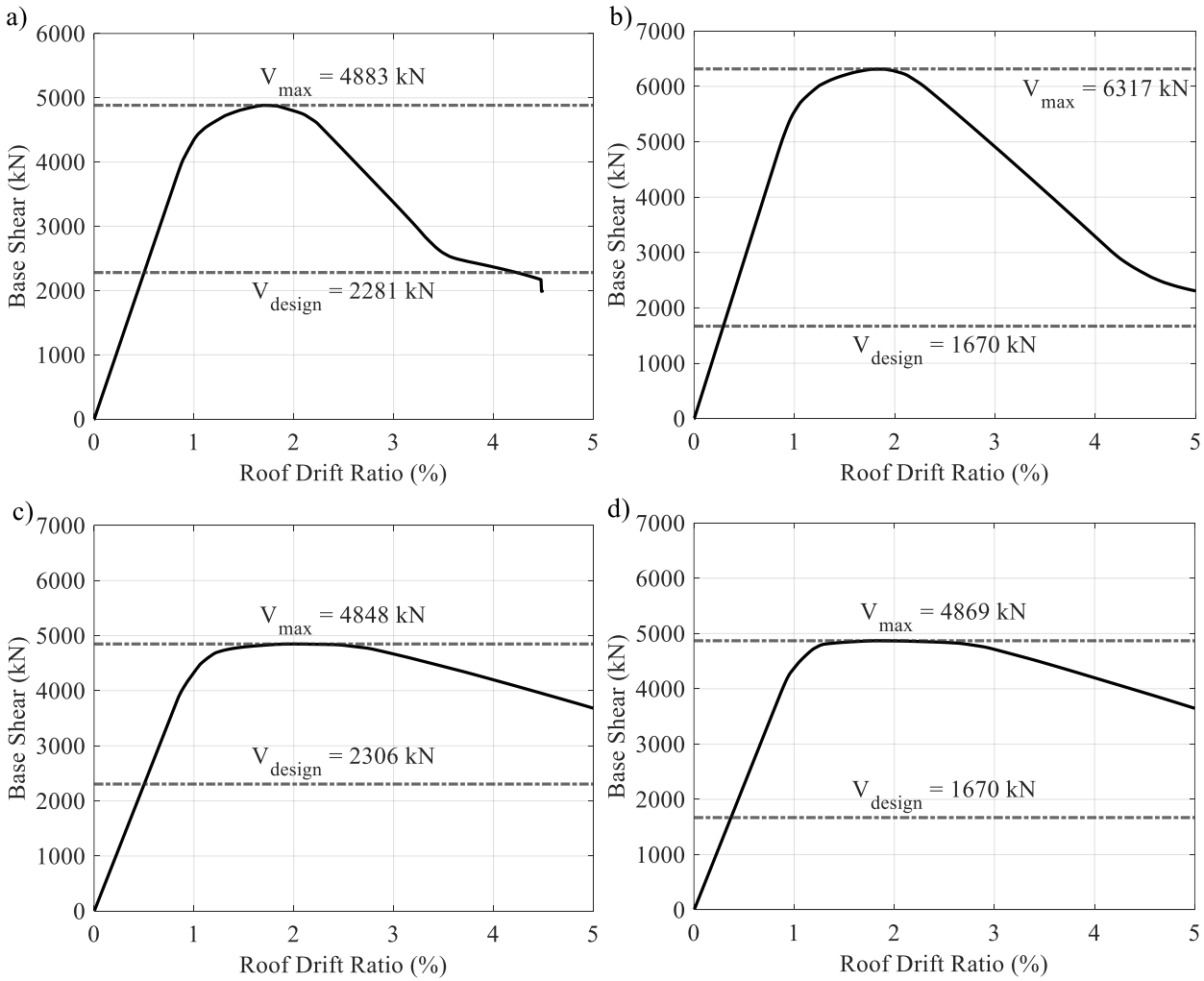

Figure 3-14. Pushover curves: a) MKF-P; b) MKF-N; c) MRF-P; d) MRF-N.

Referring to Table 3-2, the period-based ductility of MRF-P is marginally larger than that of MRF-N, while this parameter for MKF-P is slightly smaller as compared to that of MKF-N. Although MKF-P is lighter than MRF-P by 17%, it provides a larger ultimate strength and nearly the same lateral stiffness. MKF-N and MRF-N have almost the same steel tonnage, yet MKF-N offers around a 25% increase in lateral stiffness and 29% increase in the ultimate strength. The PBPD approach compared to the NBC design offers a smaller overstrength factor both in MRFs and MKFs (see Figure 3-14) while providing sufficient redundancy in the system, indicating that the PBPD method would result in a potentially more efficient design, particularly when the LLRS is designed using a steel MKF.

The MKF system furnishes smaller period-based ductility values in comparison to the conventional MRF system, which is attributed to the shorter intermediate beam segments compared to longer yielding elements in MRFs. Earlier strength degradation observed (2% in MKFs compared to 2.5% in MRFs) is attributed to earlier plastic hinging in the intermediate beam segments of MKFs than the MRF beams as higher curvature is induced in a shorter beam at a given storey drift. Furthermore, the MKF system, may not be considered an LLRS with high ductility capacity as its period-based ductility is on average 40% lower than ductile steel MRFs. This observation deserves more attention in future relevant studies. Finally, the roof yield drift of the frames using the PBPD agrees well with that assumed in the design (0.9% from analysis vs. 1.0% assumed in design).

3.9.2. Nonlinear response history analysis

The inelastic dynamic behaviour of the MKF as compared to the conventional MRFs was examined through Nonlinear Response History Analysis (NLRHA). Following the application of gravity loads to the frame columns and the leaning column, a dynamic analysis was performed

under a ground motion acceleration applied to the base of the frame in the horizontal direction. Figure 3-15 shows the profiles of the peak storey drift ratios for the prototype frames under each seismicity source and the entire suite of ground motions. MKF-P and MKF-N exhibited global dynamic instability under the 1985 Algarrobo-Melipilla earthquake, while MKF-N also experienced dynamic instability under the 2010 Maule-LACH-b earthquake.

Referring to Figure 3-15, on average the drift response of MRFs was similar to MKFs. As median responses show, the maximum storey drift of MKF-P and MRF-P occurred in storey 3, while MKF-N and MRF-N experienced the maximum storey drift in storey 5 and storey 4, respectively. Owing to the fixed base condition of the columns, the minimum drift occurred in the first storey in all frames. For all four frames, the peak drift response was dominated by interface earthquakes in all the stories except the roof levels. Such behaviour is rooted in the long duration and large magnitude of interface events. Intraslab events tend to govern the drift response at the roof level. Overall, subduction earthquakes dominated the displacement demands of prototype frames, further emphasizing the importance of considering subduction events in the seismic evaluation and design of structures located in western Canada. As shown in Figure 3-15a, the peak median storey drift ratios for MKF-P always remained below the target drift of 2.5%, indicating that the proposed system, provided that it is designed in accordance with the PBPD procedure, can result in an acceptable lateral stiffness in the inelastic range comparable to conventional MRFs.

Figure 3-16 and Figure 3-17 show peak bending moments for the exterior and interior columns of MKFs, respectively. No global instability was observed in interior or exterior columns. The moments were normalized by the respective strong-axis plastic moment capacity of the cross-section. In these figures, $M_{c-NLRHA}^{peak}$ refers to the median obtained from the entire ensemble of ground motions.

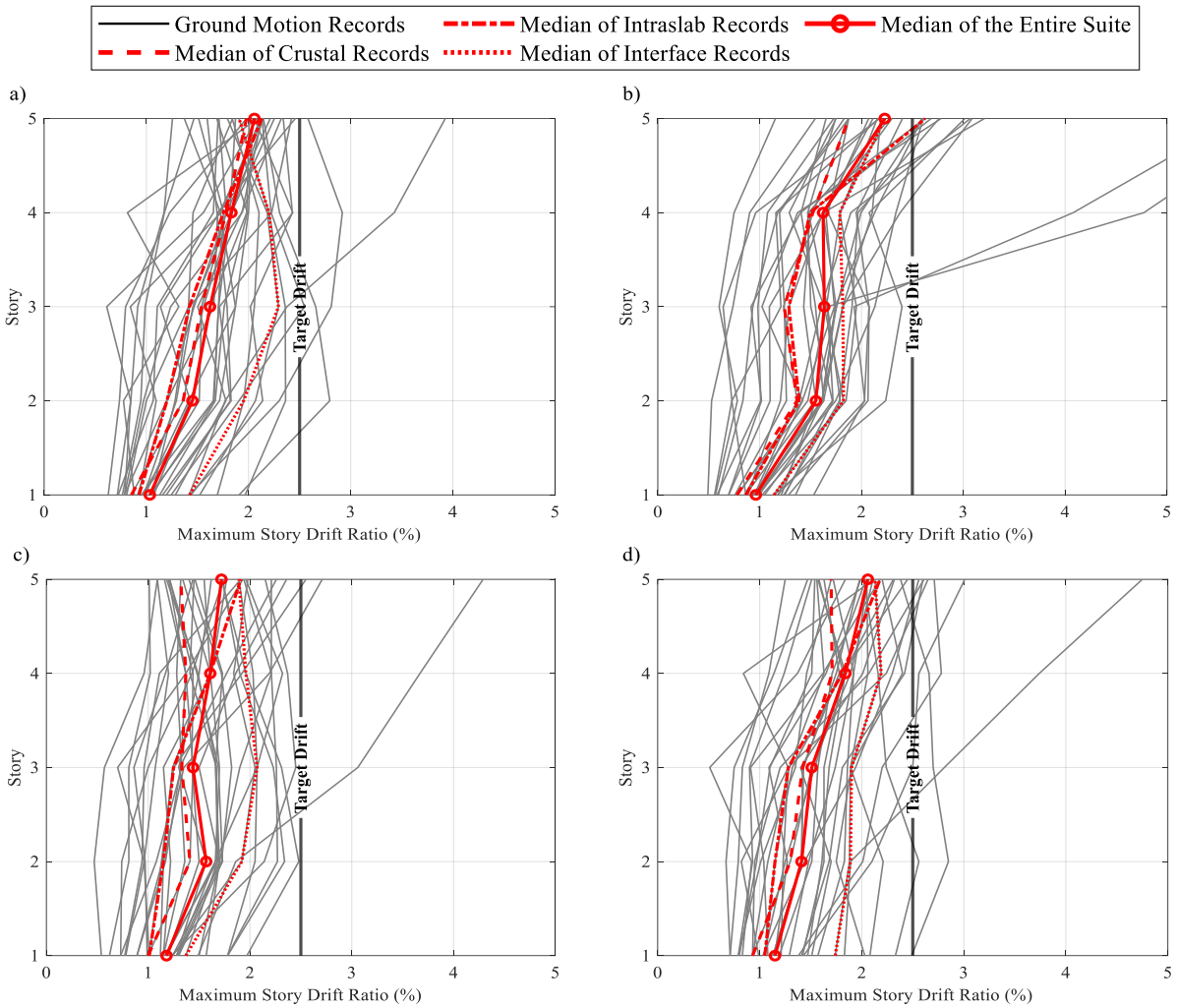

Figure 3-15. Profile of peak inter-storey drift: a) MKF-P; b) MKF-N; c) MRF-P; d) MRF-N.

Referring to Figure 3-16, flexural plastic hinging occurred only at the base of first-storey exterior columns in both MKFs. The normalized moment values always remained below unity in all other critical points of MKF exterior columns, i.e., top of the long segments, bottom of the short segments and top of the short segments. As shown in Figure 3-17, the interior columns of MKF-N experienced flexural plastic hinging at both ends of storey 4 and the bottom of storey 5 in addition to their column bases, indicating that the expected yield mechanism was not properly achieved when the NBC elastic design procedure was applied. Such an undesirable response can be attributed to the distribution of lateral stiffness along the frame height, which was adjusted to meet the stringent code-specified drift limit. Flexural plastic hinging in the MKF-P however only took place at the base of first-storey

interior columns and the normalized moment values remained below 1.0 in all other critical locations (Figure 3-17). The results of NLRHA verified the potential of the PBPD approach developed here in achieving the desired yielding mechanism shown in Figure 3-1.

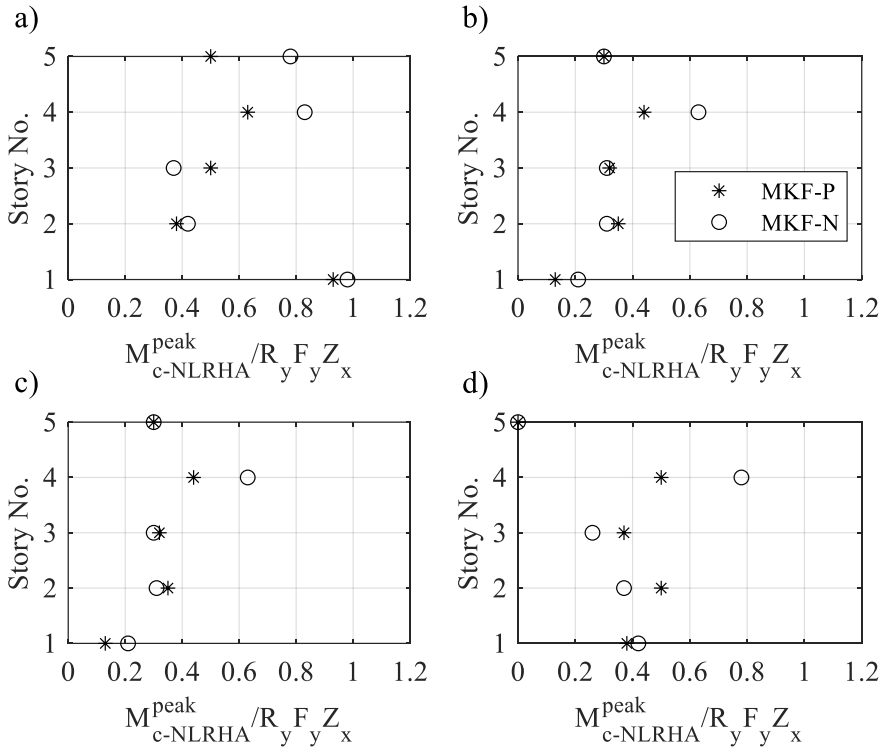

Figure 3-16. Peak moments of MKF exterior columns: a) Long column segment – bottom; b) Long column segment – top; c) Short column segment – bottom; d) Short column segment – top.

3.10. Collapse response

3.10.1. Incremental dynamic analysis

The Incremental Dynamic Analysis (IDA) method [45] was employed to evaluate the collapse behaviour and predict the collapse capacity of the MKF as compared to the conventional MRF. To perform the IDA, each prototype frame was analyzed using the NLRHA method under increasing ground motion intensities until collapse was detected. A total of 1980 NLRHA was carried out to establish the IDA plots. To reduce the computational costs and increase the efficiency of IDA, a Hunt, Trace and Fill (HTF) algorithm was adopted as per the recommendations by Vamvatsikos and Cornell [45]. Various Intensity Measures (IM) have been proposed in the past to study the collapse

response of structures [109, 110]. Elastic spectral acceleration at the fundamental period, i.e., $S_a(T_1)$, is one of the common intensity measures used in literature. However, this method may not properly capture the spectral shape effects of the ground motions, which can remarkably influence nonlinear structural response [109, 110]. The geometric mean of 5% damped spectral accelerations between $0.2T_1$ and $3T_1$, referred to as $S_{a_{avg}}(0.2T_1 - 3T_1, 5\%)$ hereinafter, was employed as the IM in this study since it is deemed to provide a more stable collapse risk estimate [50]. The Damage Measure (DM) used in this study is the maximum storey drift ratio within the entire frame under a given ground motion intensity. Two different collapse thresholds, i.e., local and global, were considered. The local collapse threshold corresponds to the case in which a maximum storey drift ratio of 5% is reached at any of the stories, while the global collapse threshold represents a state of numerical instability in the analysis, including non-converging analyses.

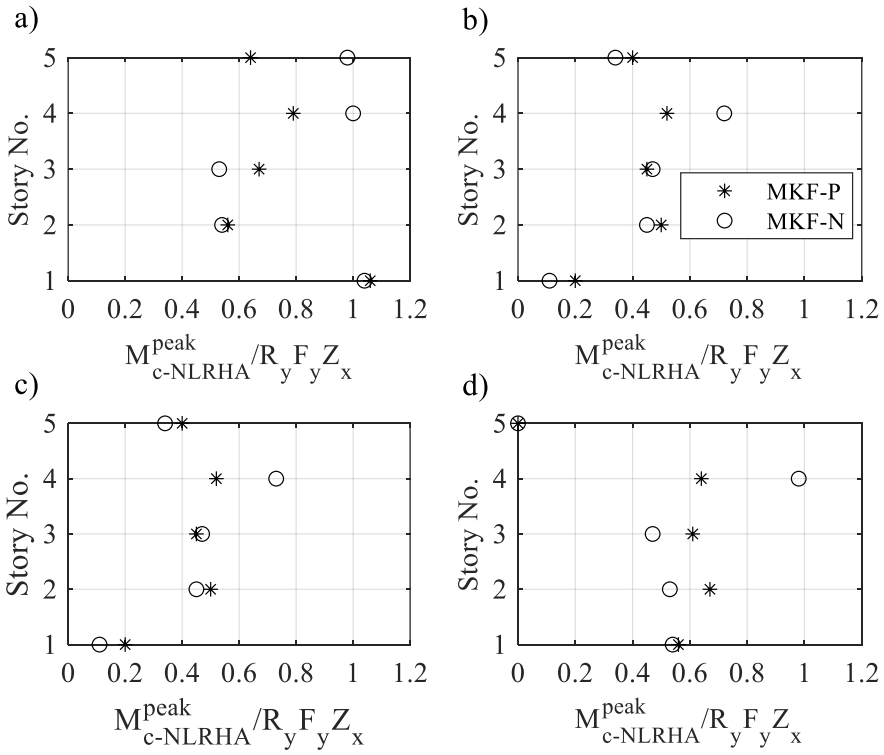

Figure 3-17. Peak moments of MKF interior columns: a) Long column segment – bottom; b) Long column segment – top; c) Short column segment – bottom; d) Short column segment – top.

Figure 3-18 presents the IDA curves for the MKF and the MRF studied here under the selected ground motions. The curves corresponding to the 16^{th}, 50^{th} (median), and 84^{th} percentile values are also plotted for each frame. The proposed MKF-P and MKF-N exhibited median collapse intensities of 0.30g and 0.27g, respectively, at the target DM, i.e., a 5% storey drift ratio. The comparison among the IDA curves of MRFs and MKFs suggests that the proposed MKF system is capable of providing a collapse capacity comparable to that of the conventional MRF. In particular, MKF-P yields a median collapse intensity higher than those obtained for MKF-N and MRF-N. As shown in Figure 3-18a and Figure 3-18c, the 16^{th}, 50^{th}, and 84^{th} percentile curves for MKF-P and MRF-P, respectively, flattened out beyond the target DM. Whereas, MRF-N and MKF-N reached a plateau at a maximum storey drift ratio smaller than 5% based on their 16^{th}, and 50^{th} percentile values. The smallest and largest median collapse intensities correspond to MKF-N with a value of 0.27g and MRF-P with a value of 0.34g, respectively, suggesting that MKF-N exhibits the poorest collapse performance among the prototype frames, which may be attributed to uneven distribution of inelastic deformations along the frame height. Referring to the 16^{th} percentile and median values in Figure 3-18, it is inferred that the NBC frames are more likely to fail before reaching the local dynamic instability threshold while frames designed in accordance with the PBPD procedure benefit from a more uniform distribution of plasticity and tend to collapse at larger inter-storey drifts with higher median collapse intensities, thus offering more robust collapse behaviour.

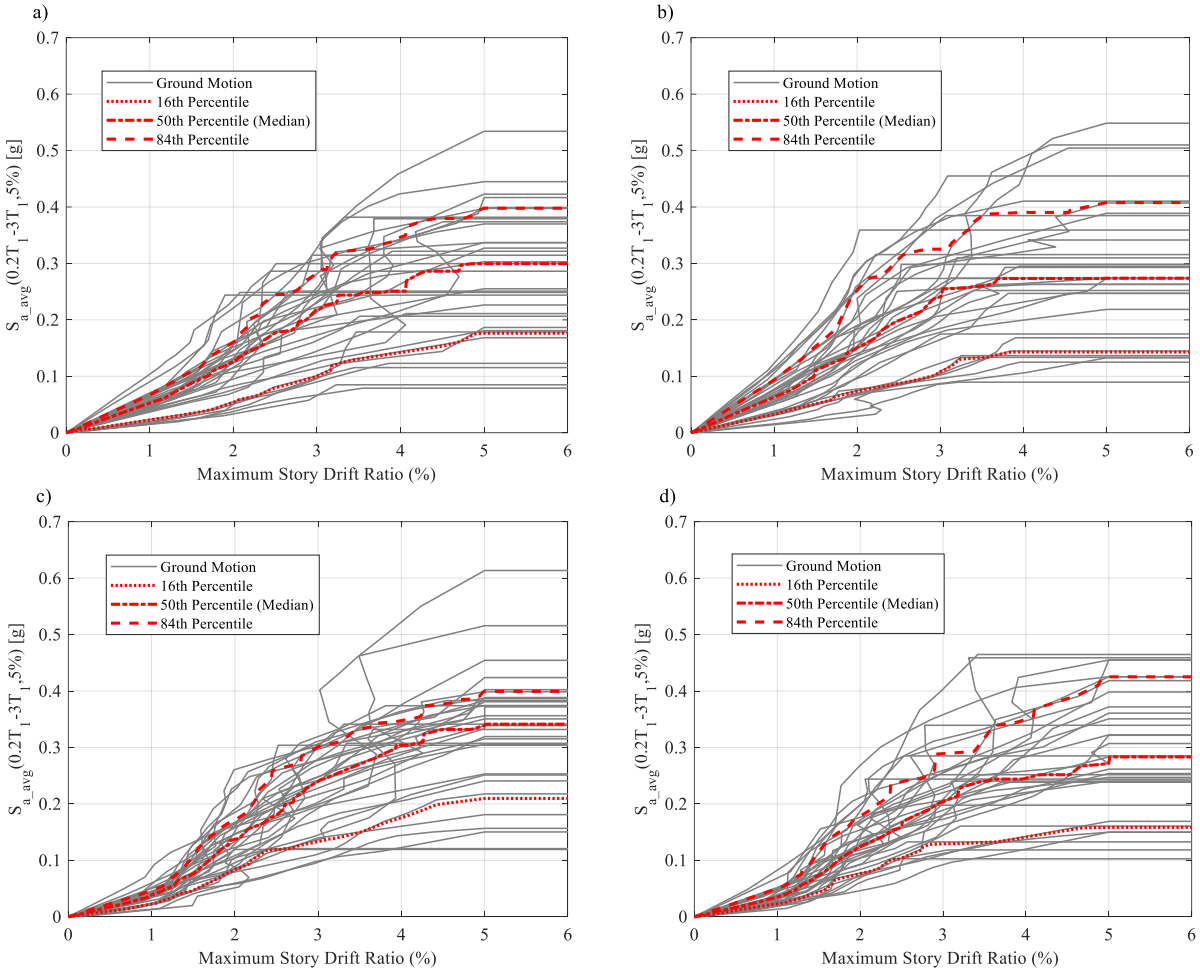

Figure 3-18. IDA curves, the geometric mean of 5% damped spectral accelerations between $0.2T_1$ and $3T_1$ vs. maximum storey drift ratio: a) MKF-P; b) MKF-N; c) MRF-P; d) MRF-N.

3.10.2. Fragility curve

Fragility curves are used in this study to estimate the probability of structural damage under an earthquake as a function of ground motion intensity. The fragility curves were generated using the log-normal cumulative distribution function, which is defined as the cumulative probability of the occurrence of damage equal to or higher than the IM damage level [111]:

$$P\left(Collapse \mid IM\right) = \varphi\left(\left(\ln(IM) - \ln(\rho)\right)/\sigma\right) \tag{3-25}$$

where ρ and σ are the median and lognormal standard deviation of IMs, and φ is the standard normal distribution function.

The fragility curves for the frames studied are shown in Figure 3-19. As shown, MKF-P offers a lower probability of collapse compared to MKF-N under the entire set of ground motions and when crustal and intraslab records are considered alone. This can be attributed to the enhanced seismic response when the PBPD approach is employed. The comparison between the MKF and MRF shows that MRF-P offers the lowest probability of collapse regardless of the event type. When the combined effects of the entire suite of ground motion records are considered, MKF-P furnishes the second lowest probability of collapse among all frames.

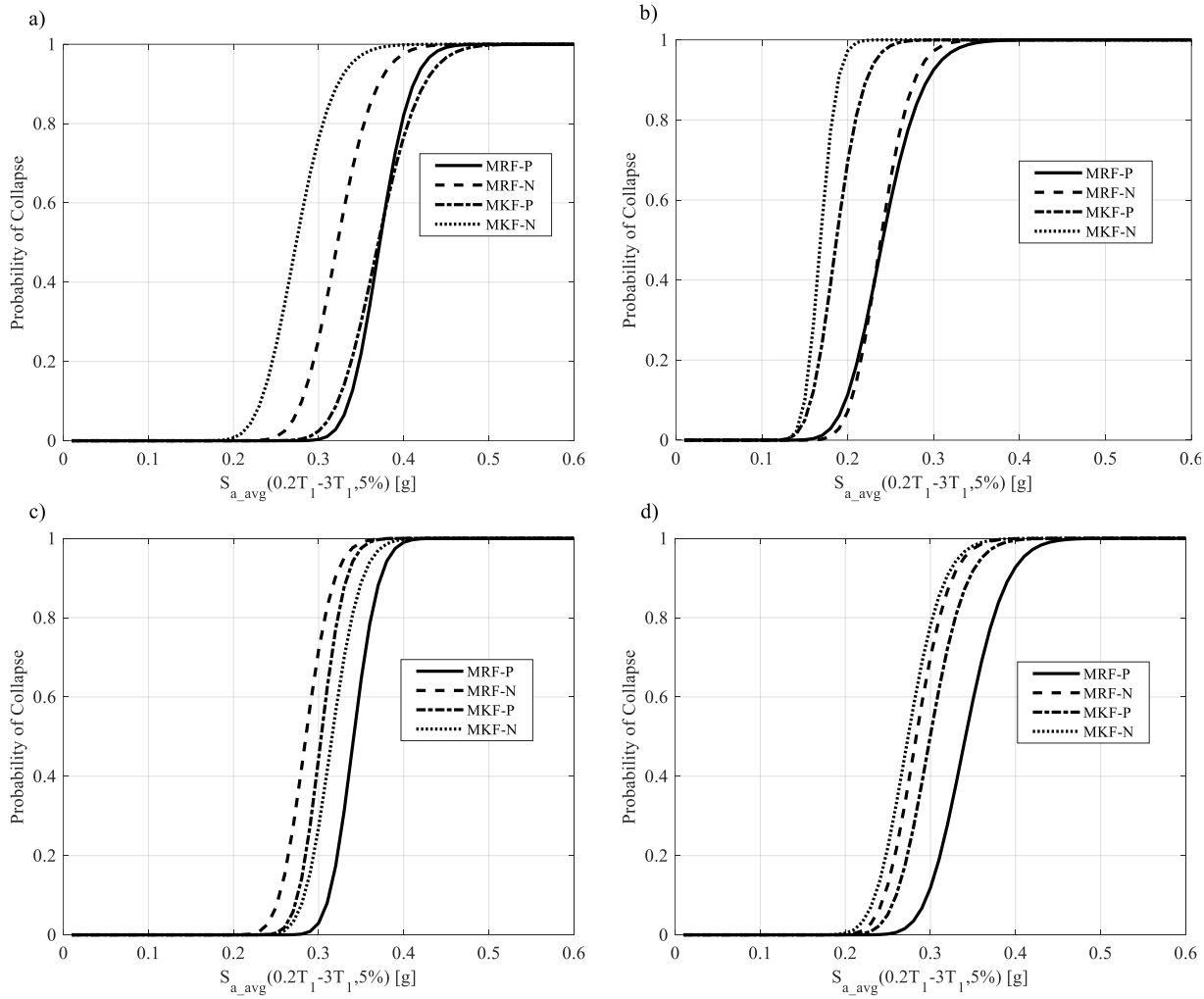

Figure 3-19. Fragility curves for MKF and MRF: a) Crustal records; b) Intraslab records; c) Interface records; d) Entire set of ground motions.

The evaluation of the influence of the seismicity source on fragility curves shows that subduction intraslab events yield the largest probability of collapse, which can be attributed to the frequency content of the intraslab earthquakes dominating damage in all the frames studied here. For instance, the probability of collapse corresponding to $S_{a_{avg}}(0.2T_1 - 3T_1, 5\%)$ is equal to 0.12, 0.50, 0.70 and 0.78 for MRF-P, MKF-P, MRF-N and MKF-N, respectively. All in all, the fragility curves not only confirm the comparable performance of the MKF to the conventional MRF but also prove the effectiveness of the PBPD approach in the design of the MKF system.

3.11. Conclusions

An innovative steel lateral load-resisting system referred to as Moment-resisting Knee-braced Frame (MKF) was introduced followed by a performance-based plastic design methodology proposed to design the frame. Four prototype frames consisting of MKF and MRF designed once using the proposed performance-based plastic design procedure and later in accordance with the conventional elastic method were used to examine the seismic performance and collapse behaviour of the proposed system against the conventional steel MRF. The seismic response and collapse performance evaluations were carried out under ground motions representing potential seismicity sources in western Canada. The key findings of this study are summarized as follows:

- The MKF designed following the PBPD procedure offers a smaller ductility capacity, almost identical lateral stiffness and higher overstrength factor compared to its MRF counterpart.
- The roof yield drift required to design the MKF following the proposed performance-based plastic design procedure is proposed as 1.0% on the basis of the pushover analysis results.

- The proposed MKF features reduced steel tonnage compared to the conventional MRF counterpart and can potentially result in reduced construction costs by also eliminating column panel zone stiffeners and doubler plates.
- The intermediate beam segments of the MKF can be designed as a flexural element ignoring the limited axial compression force induced due to the difference between knee brace forces.
- The five-storey prototype MKF designed as per the proposed PBPD procedure met the stringent drift limit specified by the National Building Code of Canada.
- The results of column moments obtained from dynamic analyses confirmed the proposed yielding mechanism, i.e., flexural plastic hinging in intermediate beam segments, for the MKF designed as per the proposed PBPD method.
- The PBPD procedure proposed to obtain seismic-induced forces in MKF elements manifests an enhanced MKF design by resulting in the anticipated nonlinear mechanism in design.
- The MKF designed in accordance with the proposed PBPD approach showed a collapse behaviour comparable to the Ductile MRF counterpart with respective median collapse IM values of 0.30g and 0.34g for MKF-P and MRF-P, respectively. On average, the MKF designed according to the PBPD approach yielded a collapse probability lower than that of the MKF designed following the elastic design method.
- The MRF and MKF designed using the PBPD method offered the lowest and second lowest probability of collapse, which was dominated by subduction intraslab earthquakes.
- The proposed MKF designed in accordance with the PBPD method can be used in the seismic design of steel multi-storey buildings as a viable alternative to conventional MRFs.

The findings of this study should be used within the range of parameters (e.g., number of stories) considered here. Future studies should further evaluate the performance of the proposed LLRS and propose appropriate seismic design parameters. Moreover, future studies should examine the seismic performance and propose design methods for MKFs with the yielding mechanism that involves tensile yielding and compression buckling of knee braces.

CHAPTER 4

PROPOSED SEISMIC DESIGN PARAMETERS FOR THE MOMENT-RESISTING KNEE-BRACED FRAME SYSTEM

Abstract: This study proposes and verifies the seismic design parameters, including overstrength-related force modification factor, ductility-related force modification factor, deflection amplification factor, and design period, for the steel Moment-resisting Knee-braced Frame (MKF) system. The building selected in this study is an office located in Vancouver, British Columbia, Canada, in which MKFs act as the lateral load-resisting system. 14 prototype frames spanning a wide range of geometrical configurations are designed following the requirements of the 2015 National Building Code (2015 NBC) of Canada. Nonlinear static analyses are carried out on the prototype frames to determine the preliminary ductility and overstrength factors. Six new MKFs (assessment frames) are designed using the proposed overstrength and ductility factors, and their seismic and collapse performances are examined by comprehensive numerical analyses, considering the effects of the potential sources of ground motion expected on the Canadian west coast, namely intraslab, interface and crustal events. This study confirms that the MKF system shall be designed as a moderately ductile lateral load-resisting system using overstrength and ductility factors of 1.60 and 3.0, respectively, with a height not exceeding 40 meters. Furthermore, the results demonstrate that the proposed seismic design parameters can provide a sufficient level of safety required by the 2015 NBC of Canada.

4.1. Introduction

Steel-framed structures shall be designed to dissipate earthquake-induced energy through material nonlinearities. Energy dissipation should be accompanied by sufficient lateral stiffness and strength

to transmit the lateral loads to the foundation without brittle failures or collapse. In order to achieve this goal, various lateral load-resisting systems (LRRSs) have been developed and investigated in the past.

Steel Concentrically Braced Frames (CBFs) provide significant lateral stiffness and strength under seismic loading. However, their inelastic energy dissipation capacity can be negatively affected by the post-buckling behaviour of diagonal braces, particularly if they are used to cover long spans. The buckling of diagonal braces in CBFs can result in an asymmetric cyclic response and low ductility capacity [1]. Moreover, CBF columns are more susceptible to out-of-plane instabilities due to out-of-plane deformations of gusset plates observed during earthquakes. Architectural obstructions and relatively complicated gusset plate details to achieve ductile behaviour may also limit the application of CBFs in seismic regions.

Steel Moment-Resisting Frames (MRFs) are considered one of the most ductile LLRSs for constructing multi-storey buildings, particularly in high seismic regions. Steel MRFs offer several advantages over other steel LLRSs, such as significant ductility capacity, minimum architectural obstructions, and the ability to accommodate long spans. However, there are several constraints associated with the design and construction of conventional MRFs, which can limit their application in the construction of building structures, often in low-to-moderate seismic regions and sometimes in high seismic areas. Some of these constraints include low lateral stiffness that results in large lateral deformations and increased susceptibility to second-order effects [112], prohibitively expensive and complex strengthening requirements for beam-to-column connections, and high fabrication and inspection costs related to Complete Joint Penetration (CJP) groove welds.

In order to address the constraints associated with conventional steel LLRSs, several innovative systems have been developed. The application of knee braces was first proposed by Aristizabal-

Ochoa [27] in disposable steel knee-braced frames. In this system, diagonal bracing members providing the required lateral stiffness were connected to a short knee brace. The system was designed such that seismic energy dissipation could be achieved by forming a flexural plastic hinge in the disposable knee element. At the same time, diagonal bracing members remained essentially elastic. Later, Balendra et al. [28-33, 89] conducted significant research studies to evaluate the behaviour of disposable knee-braced frames under seismic loading. They showed that knee-braced frames have the potential to act as an LLRS in seismic areas, provided that the knee element is designed to resist local and lateral-torsional buckling.

Knee braces were introduced into conventional steel MRFs by Leelataviwat et al. [35] to develop a new ductile LLRS, called the knee-braced moment frame, consisting of braces with round hollow steel sections, wide-flange (WF) columns, and beams. In this system, the beams were continuous between two columns and rigidly connected to the columns. The failure mechanism assumed in the design of this system involved the development of plastic hinges in the beams adjacent to brace-to-beam connections right after buckling and yielding of the knee braces. An experimental program supported by numerical simulations was performed on a single-storey single-bay specimen. Their study demonstrated that the proposed system could efficiently resist seismic forces at the design and maximum considered earthquake levels without significant stiffness or strength degradations, instability, or premature failure. The seismic behaviour of an innovative LLRS composed of simple beam-to-column connections and buckling-restrained knee braces was evaluated by Junda et al. [36]. The buckling-restrained knee braces carried the inelastic seismic demands in this system. The application of buckling-restrained knee braces in buckling-restrained knee-braced truss moment frames was investigated by Wongpakdee et al. [37]. This system carried gravity loads by steel trusses simply connected to columns. At the same time, buckling-restrained knee braces were implemented

to resist the seismic-induced lateral loads through tensile and compressive yielding. Several research studies can be found in the literature addressing the seismic performance evaluation and design of buckling-restrained knee-braced truss moment frames [38-40]. According to these studies, this system can be considered a practicable alternative to conventional MRFs while providing long spans to accommodate large openings of significant interest in residential and office buildings.

Hsu and Li [16] conducted several experiments on conventional Special Moment-Resisting Frames (SMRFs) and SMRFs equipped with knee braces. The results revealed that the seismic performance of SMRFs can noticeably be improved if they are supplemented by knee braces. Asghari and Saharkhizan [41] investigated the behaviour of steel Knee Connection Frames (KCFs) with simple beam-to-column connections. A comparison between KCFs and SMRFs in this study demonstrated that the KCF system could be classified as a steel SMRF in terms of overstrength and ductility capacities. It was also found that KCFs collapse at higher intensities and offer smaller collapse probabilities than SMRFs. Overall, it was suggested that in the case of low- and medium-rise frames, KCFs could provide superior performance compared to steel SMRFs. Moreover, the FEMA P695 methodology [13] was implemented to verify the adequacy of the seismic design parameters used for KCFs; however, no specific design parameters were recommended for the seismic design of this system.

More efficient design and construction practices, as well as lower costs and reduced environmental impacts, are increasingly desired in the construction industry. Therefore, there is an urge to develop high-performance and resilient alternative LLRSs that enable practitioners to overcome the limitations of conventional steel MRFs or CBFs. To achieve this goal, the authors proposed an innovative steel LLRS called the Moment-resisting Knee-braced Frame (MKF) [113]. This system was developed to efficiently resist lateral loads, e.g., earthquake and wind loads, in multi-storey

buildings. The steel MKF system, which consists of column trees, knee braces, beam stubs, and intermediate beam segments, combines the high ductility of conventional steel MRFs and the large stiffness of steel braced frames to resist lateral loads. When comparing the MKF to conventional CBFs, MKF's relatively stocky knee braces provide a stable hysteretic response without significant strength degradation and offer less obstruction, making this system architecturally versatile. The seismic response and collapse behaviour of the MKF system were evaluated in a proof-of-concept study [113]. The results confirmed that the MKF could be a reliable alternative to conventional MRFs. Furthermore, a seismic design procedure was proposed to size this system's beams, braces, and columns. Nonetheless, the MKF system lacks appropriate seismic design parameters, including ductility-related force modification factor, ductility factor hereafter, overstrength-related force modification factor, overstrength factor hereafter, and deflection amplification factor, that match its seismic performance. Such factors can facilitate the implementation of this system in practice. Accordingly, this study aims to propose new seismic design parameters for the steel MKF, followed by a comprehensive verification study using Nonlinear Response History Analysis (NLRHA), Nonlinear Static (Pushover) analysis, and Incremental Dynamic Analysis (IDA) methods and considering the influence of three potential hazard sources expected on the Canadian west coast, i.e., crustal, intraslab, and interface events. The seismic design parameters recommended in this study will aid the implementation of the proposed system in building codes and provide design engineers with reliable inputs to be utilized in the seismic design of steel MKFs.

4.2. Expected nonlinear mechanism

Different nonlinear mechanisms can be imagined for the MKF system under seismic loading, e.g., flexural plastic hinging at the ends of intermediate beam segments or compression buckling and tensile yielding of the knee braces. Alternatively, MKFs can be designed to develop a combination

of these two mechanisms under seismic loading. Suppose the MKF system is designed for the nonlinear mechanism in which the seismic input energy is dissipated through buckling and yielding of the knee braces. In that case, the brace global buckling phenomenon may be observed. Such behaviour results in strength degradation [114-116] and remarkably reduces the energy dissipation capacity of the system. Hence, the flexural yield mechanism was employed in this study so that more stable and efficient deformation ductility and energy dissipation capacities could be achieved [41, 117, 118]. Figure 4-1 presents a simplified representation of the selected mechanism for a three-storey MKF example. As shown, flexural plastic hinges form at the face of intermediate beam segment-to-beam stub connections. However, the knee braces, beam stubs, and columns remain elastic under this nonlinear mechanism to ensure that the intermediate beam segments attain their full plastic flexural capacity.

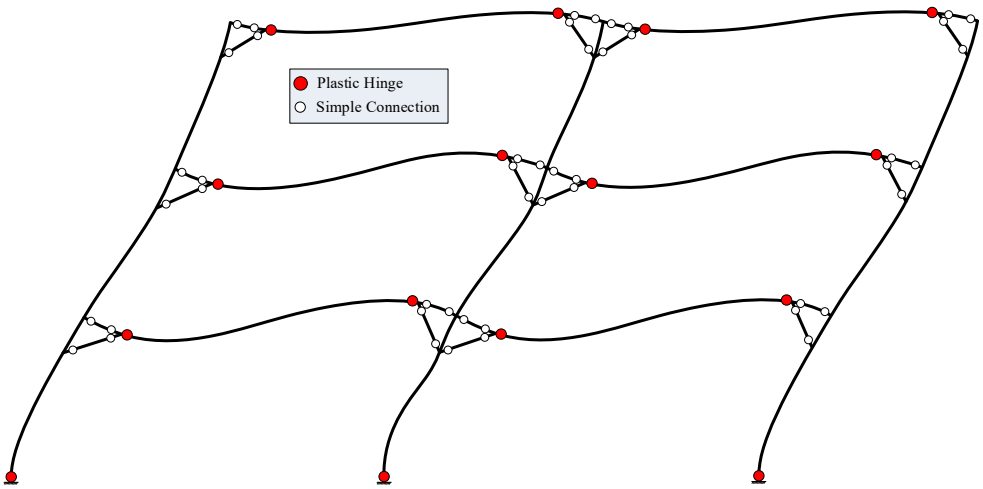

Figure 4-1. MKF nonlinear mechanism under lateral loads (three stories and two bays shown for simplicity).

4.3. Archetype frames

4.3.1. Selected buildings and loading data

To illustrate the seismic analysis and design of the MKF system, an office building located in a high seismic region, i.e., Vancouver, British Columbia (B.C), Canada, was considered. The soil

characteristics of the selected site comply with site Class C according to the site classifications prescribed by the 2015 NBC of Canada [5]. The first storey has a height of 4.3 m, while the upper stories are all 4.0 m high. Three building layouts with varying span lengths were considered, as shown in Figure 4-2.

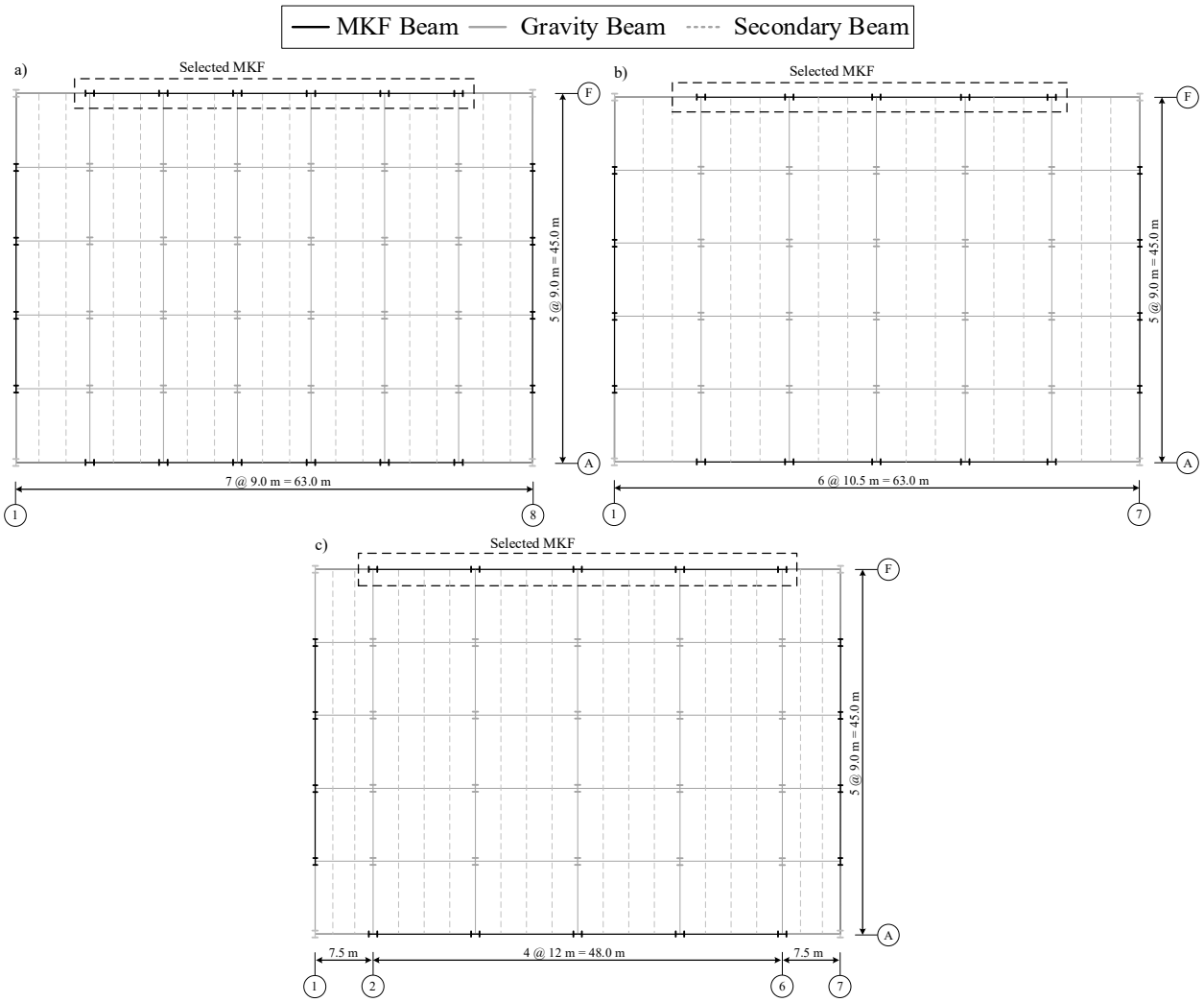

Figure 4-2. Plan view of the selected building: a) 9.0 m long MKF span (Layout 1); b) 10.5 m long MKF span (Layout 2); c) 12.0 m long MKF span (Layout 3).

Steel MKFs placed at the perimeter of the building were used as the LLRS of the building in long (longitudinal) and short (transverse) directions. One of the longitudinal frames was selected for seismic design and performance evaluation. The loading was performed in accordance with the requirements of the 2015 NBC of Canada. The weight of exterior walls was taken equal to 1.5 kPa.

The dead loads applied to the roof and floor levels were 3.4 kPa and 3.6 kPa (excluding the weight of partition walls), respectively. A partition load of 1.0 kPa and a live load of 2.4 kPa were assumed for the floor levels. Moreover, the roof level's design snow and live loads were equal to 1.64 kPa and 1.0 kPa, respectively.

4.3.2. Seismic design

A total of 14 prototype MKFs were selected by varying the number of stories (6, 9, 12, and 15), beam span length, braced length ratio, and knee brace angle. The geometrical features of the selected prototype frames are outlined in Table 4-1. The labelling scheme for each frame consists of the letter "F", which stands for *Frame*, succeeded by the *number of stories*, *span length (in meters)*, *brace angle* (*in degrees*), and *braced length ratio*. For example, F6-12-37-0.20 refers to a six-storey prototype MKF with a span length of 12 m, a brace angle of 37 degrees, and a braced length ratio of 0.20. The lengths $L_{bs}, L_V, L_{k,g}$, and L referenced in Table 4-1 are shown in Figure 1-1. In the absence of specific seismic design parameters for the MKF system, seismic demands were computed using the 2015 NBC seismic design parameters for Ductile MRFs, namely overstrength and ductility factors of $R_o = 1.5$ and $R_d = 5.0$, respectively. The steel members were designed under gravity plus seismic demands obtained from the Equivalent Static Force Procedure as described in the 2015 NBC of Canada. In all designs, the intermediate beam segments were selected sufficiently long such that the shear-moment interaction could be neglected [119]. The second-order P-Δ effects were taken into account in the seismic loading and design phase. Moreover, based on the requirements of 2015 NBC, the accidental torsion was considered by assuming a 10% eccentricity for the seismic loading, resulting in a 4.2% increase in the design base shear.

Table 4-1. Summary of geometric variables of prototype MKFs.

Frame Designation	No. of Stories	α_b	θ (°)	Span Length L (mm)	$L_{bs}(mm)$	$L_V(mm)$	$L_{k,g}(mm)$
F6-9-37-0.25	6	0.25	37	9000	2250	1710	2830
F6-9-42-0.25	6	0.25	42	9000	2250	2000	3010
F6-9-45-0.20	6	0.20	45	9000	1800	1800	2550
F6-10.5-37-0.25	6	0.25	37	10500	2625	2000	3300
F6-12-31-0.25	6	0.25	31	12000	3000	1800	3500
F6-12-37-0.20	6	0.20	37	12000	2400	1810	3010
F9-9-42-0.25	9	0.25	42	9000	2250	2000	3010
F9-9-45-0.20	9	0.20	45	9000	1800	1800	2550
F9-10.5-37-0.25	9	0.25	37	10500	2625	2000	3300
F9-12-31-0.25	9	0.25	31	12000	3000	1800	3500
F9-12-37-0.20	9	0.20	37	12000	2400	1830	3020
F12-9-42-0.25	12	0.25	42	9000	2250	2000	3010
F12-10.5-37-0.25	12	0.25	37	10500	2625	2000	3300
F15-9-42-0.25	15	0.25	42	9000	2250	2000	3010

The structural design of the prototype frames was performed in accordance with the requirements of the 2019 edition of the Canadian steel design standard, CSA S16-19 [3]. ASTM A992 steel WF sections were used for beam stubs, columns, and intermediate beam segments. Specified and probable yield strengths of $F_y = 345$ MPa and $R_y F_y = 385$ MPa, respectively, were considered for this type of steel material. Knee braces were selected from ASTM 1085 square Hollow Structural Sections (HSS) with $F_y = 345$ MPa and $R_y F_y = 460$ MPa. Intermediate beam segments were designed as designated yielding members (DYMs) under factored seismic plus gravity loads to carry the induced flexural and shear demands. After selecting adequate cross-sections for intermediate beam segments, knee braces, beam stubs, and columns were designed to remain elastic under the probable forces imposed by flexural plastic hinging of intermediate beam segments. Beam stubs, intermediate beam segments, and first-storey columns were selected from WF sections conforming to width-to-thickness ratio limits corresponding to Class 1 sections prescribed by CSA S16-19, while Class 1 or Class 2 sections were used for upper-storey columns and knee braces. To obtain the bending moment and axial force demands in the columns under the probable forces imposed by the flexural plastic hinging of intermediate beam segments, exterior and interior columns were individually and separately treated as column trees. Refer to [113] for further details on the design of MKF column trees.

Knee braces were designed as compressive members to carry in tension or compression the axial force induced due to flexural plastic hinging of intermediate beam segments. Figure 4-3 shows the free-body diagram of the beam assembly when the probable moment resistance M_{prob} is developed in its end flexural plastic hinges. In this figure, V_R, V_L, L_b, w, and θ are the right hinge shear, left hinge shear, length of the intermediate beam segment, uniformly distributed factored gravity load, and the angle of the knee brace with respect to the horizontal axis, respectively. Using Figure 4-3,

the compression force demand in the knee brace ($C_{k,f}$), neglecting the effects of gravity loads when the intermediate beam segments reach their probable moment resistance, can be expressed as:

$$\frac{C_{k,f}}{M_p / L} = \frac{R_{sh} R_y}{\sin(\theta)} \left(\frac{1}{\alpha_b} + \frac{2}{1 - 2\alpha_b} \right) \quad \text{where } M_p = Z_x F_y \tag{4-1}$$

in which R_{sh}, R_y, M_p, Z_x, and F_y are the material strain-hardening factor, the ratio between the probable yield stress and the nominal yield stress of the material, the plastic moment capacity of the intermediate beam segment, plastic section modulus of the intermediate beam segment, and minimum specified yield strength of steel, respectively. $\alpha_b = L_{bs}/L$ stands for the ratio of the beam-stub length to the beam span, often referred to as the braced length ratio.

Variation of the maximum normalized compression in knee braces (left-hand-side of Eq. (4-1)) with respect to α_b is presented in Figure 4-4. As shown, the brace compression force reduces α_b varies between 0 and 0.25 and increases beyond $\alpha_b = 0.25$. The geometric properties can significantly affect the axial force demand and size of the knee braces, the axial force demand in the beam stubs and columns, and the design demands of the connections. Accordingly, the influence of the braced length ratio, span length, and brace angle on the performance of the MKF system was explicitly considered in this study by designing prototype frames with different geometrical configurations.

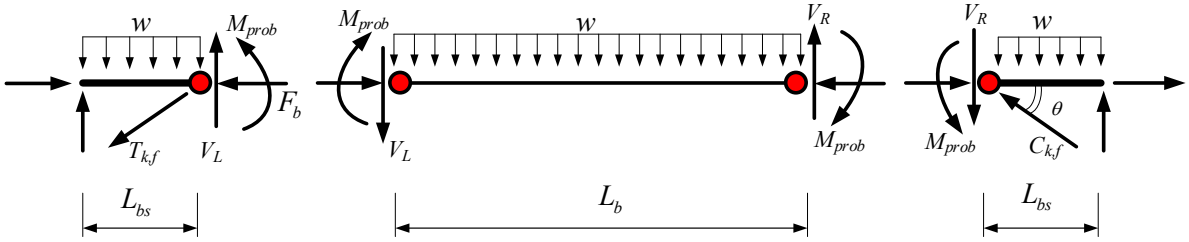

Figure 4-3. The free-body diagram of the beam assembly at flexural plastic hinging.

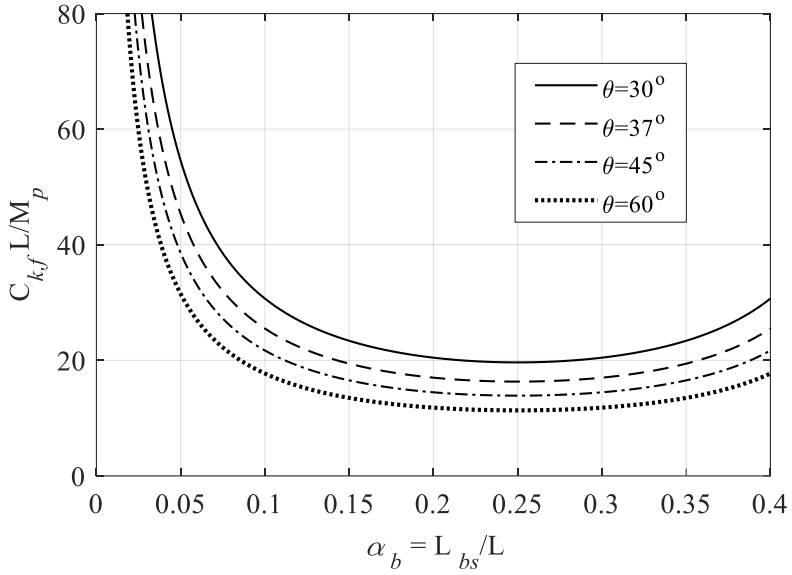

Figure 4-4. Variation of the maximum compression in knee braces with respect to α_b.

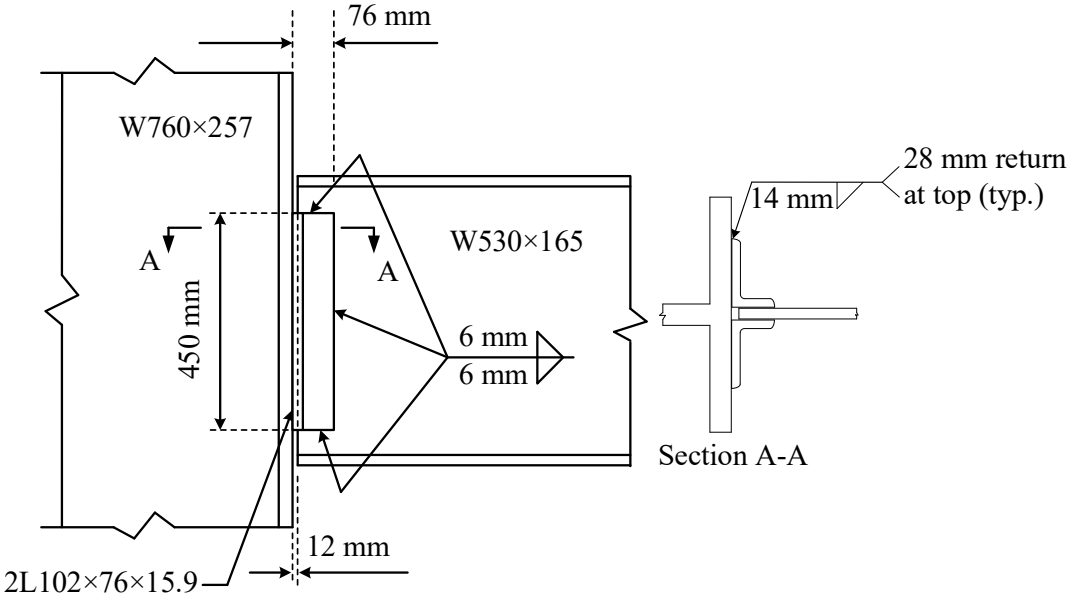

Figure 4-5. Beam stub-to-column connection geometry for the first storey of F6-9-45-0.2.

The beam stub-to-column connections in the MKF system shall be designed to carry the combination of an axial tension force and a shear force. One of the beam stub-to-column connections in the first storey of F6-9-45-0.2 was designed in accordance with CSA S16-19 and AISC 360-16 provisions [120] following the AISC Construction Manual [121] design steps. The connection is composed of all-welded double angles. 2L102×76×15.9 were selected from ASTM

A36 material with nominal yield and ultimate strengths of $F_y = 248$ MPa and $F_u = 400$ MPa. The connection is shown in Figure 4-5.

4.4. Numerical simulation

The *OpenSees* program [43] was implemented to generate two-dimensional (2D) models of the MKF system. These models were used to evaluate the seismic performance of the prototype frames and determine new seismic design parameters for the system. Nonlinear force-based beam-column elements with fibre discretization of the cross-section were used to simulate the knee braces, columns, and beam stubs. Shear deformations were accounted for using the section aggregator technique. All nonlinear frame elements were assigned the uniaxial Giuffré-Menegotto-Pinto Steel02 material model [97] using the material parameters recommended in [98] to capture the steel materials' kinematic and isotropic strain hardening behaviours. The intermediate beam segments were simulated using modified elastic beam-column elements introduced in [99]. The Ibarra-Medina-Krawinkler (IMK) model [60] implemented in a zero-length spring element was used to simulate flexural plastic hinges at the ends of intermediate beam segments. This model can capture the inelastic cyclic response of the beams and accounts for strength and stiffness degradations. Elastic beam-column elements with an approximate stiffness rendering the end connections were implemented to model the knee brace-to-beam/column connections. All degrees of freedom (DOFs) were restrained at the base of MKF columns. In order to trigger any potential global buckling, an initial in-plane geometric imperfection with parabolic distribution was applied to columns and knee braces. The maximum amplitude of the geometric imperfection function was equal to 0.001 times the member's unbraced length. The Corotational transformation technique was applied to capture the geometrical nonlinearities. The second-order P-Δ effects arising from the gravity loads of the gravity load-resisting system were reproduced using a pinned-base leaning column modelled next to

the original MKFs. The rotational DOFs of the leaning column were released at both ends of each storey. Moreover, the rigid diaphragm assumption was neglected in the models to minimize numerical convergence issues and to monitor the axial force demand in the intermediate beam segments. For dynamic analyses, point masses representing the seismic mass of the floor and roof levels were assigned to the top of columns at each storey. Rayleigh's damping approach with a critical damping ratio of $\xi = 2\%$ in the first and second vibration modes was applied to reproduce damping. Mass proportional damping was applied to lumped masses, and all frame elements were assigned stiffness-proportional damping following the recommendation in [99].

4.5. Seismic design parameters

The nonlinear static (pushover) analysis was performed on the prototype MKFs to estimate the overstrength and ductility factors furnished by the MKF system. Gravity loads were first applied to each prototype, followed by the application of monotonically increasing lateral displacements with a distribution pattern representing the fundamental mode shape of the frame. The nonlinear static analyses were used to obtain the overstrength and ductility factors of each prototype frame by establishing base shear versus roof displacement curves, i.e., pushover curves.

4.5.1. Overstrength Factor

The overstrength factor of each prototype frame was calculated using the relationship proposed by FEMA P695 [13]:

$$R_o = V_u / V_{design} \tag{4-2}$$

The peak base shear attained by the pushover results is represented by V_u, while V_{design} denotes the design base shear. Figure 4-6a shows the overstrength factor calculated for the prototype frames. The mean overstrength factor offered by the prototype MKFs, designed using $R_d R_o = 7.50$ was found as $\bar{R}_o = 3.42$. This value is significantly higher than the original overstrength factor of 1.50

assumed in the design. The reason for such a large overstrength factor is the higher redundancy owing to the presence of knee braces and increased member sizes to satisfy the strict code-specified drift limit. The standard deviation (STD) and coefficient of variation of the overstrength factors computed are 0.27 and 0.08, respectively, confirming marginal variation in the results.

4.5.2. Ductility factor

The relationship proposed by Miranda and Bertero [14] was used to calculate the ductility factor furnished by each prototype frame:

$$R_d = \frac{\mu - 1}{\Phi} + 1 \geq 1 \tag{4-3}$$

where μ is the displacement ductility ratio demand. In this study, the displacement ductility ratio demand of the MKF system was set equal to the period-based ductility of the system μ_T defined as [13]:

$$\mu_T = \frac{\delta_u}{\delta_{y,eff}} \text{ where } \delta_{y,eff} = C_0 \frac{V_u}{W}\left(\frac{g}{4\pi^2}\right)\left\{\max\left(T_u, T_1\right)\right\}^2 \text{ and } C_0 = \psi_{1,r}\left(\sum_{i=1}^{N} m_i \psi_{1,i} \Big/ \sum_{i=1}^{N} m_i \psi_{1,i}^2\right) \tag{4-4}$$

In Eq. (4-4), $\delta_{y,eff}$ is the roof's effective yield displacement, δ_u stands for the ultimate roof displacement defined as the displacement associated with a reduction of 20% in the ultimate base shear of the frame on the descending branch of the pushover curve [13], T_u refers to the upper limit of the empirical fundamental period specified by the code, T_1 represents the analytical period in the first mode, and m_i is the seismic mass at floor level *i*. Furthermore, $\psi_{1,i}$ and $\psi_{1,r}$ are the ordinates of the fundamental mode at floor level *I* and the roof level, respectively. The lateral displacement at the roof level of an equivalent single DOF system is related to that of the respective multi-degree-of-freedom (MDOF) system using the C_0 factor. The proposed equation to obtain T_u for the MKF system is presented in Section 4.8.

For stiff soils, which best match the soil condition of the site class considered in this study, the parameter Φ in Eq. (4-3) is given by [14]:

$$\Phi = 1 + \frac{1}{(10-\mu)T_1} - \frac{1}{2T_1}\exp\left[-1.5\left(\ln T_1 - 0.6\right)^2\right] \tag{4-5}$$

Figure 4-6b shows the ductility factors computed for the prototype frames. As shown, the ductility factor tends to decrease by increasing the frame height. Such behaviour can be attributed to taller frames being more susceptible to P-Δ effects [92] and the nonuniform distribution of nonlinear deformations, which leads to damage localization and a reduced ductility capacity. This observation agrees well with the study performed by Krawinkler and Zareian [122]. Referring to Figure 4-6b, the mean ductility factor offered by prototype MKFs is $\bar{R}_d = 3.08$.

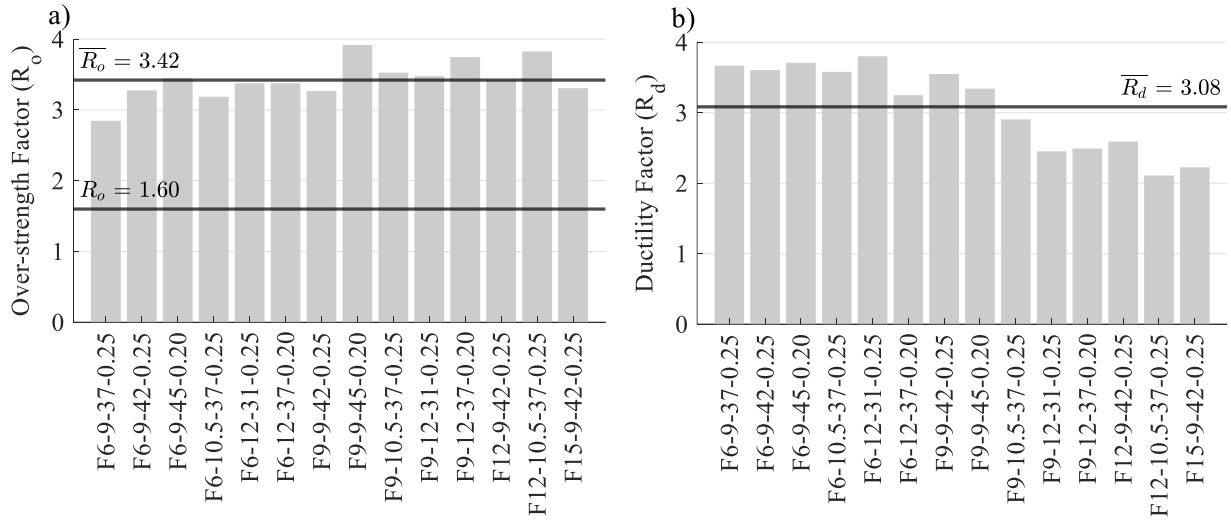

Figure 4-6. a) Overstrength factor of the prototype frames; b) Ductility factor of the prototype frames.

4.5.3. Proposed R_d and R_o factors

Figure 4-7 depicts the product of the ductility factor R_d and the overstrength factor R_o, referred to as the reduction factor in Commentary J of 2015 NBC [12], for the selected prototype frames. The mean value of the reduction factors is 10.48, which is significantly larger than the value initially assumed in the design, i.e., 7.50. This is because the proposed MKF system possesses a considerable

reserve strength, resulting in a large overstrength factor of $\bar{R}_o = 3.42$. When responding to an earthquake representing the design hazard, the primary sources of structural overstrength in steel structures include the ratio of actual yield to minimum specified yield strengths, strain hardening effects, the difference between nominal and factored resistances, and rounding of member sizes [123]. This large overstrength agrees well with the overstrength factor of 3.0 specified by ASCE/SEI 7-16 [124] for the steel truss moment-resisting frame system, a system inherently similar to the MKF. However, a more conservative overstrength factor of $R_o = 1.60$ was adopted here for the MKF system, which is consistent with the overstrength factors prescribed by the 2015 NBC for steel LLRSs in Canada. Setting the overstrength factor of the system equal to $R_o = 1.60$ and rounding the mean ductility factor to $\bar{R}_d = 3.0$, a reduction factor of $R_d R_o = 4.80$ is proposed for the MKF system. This value is compared against the individual $R_d R_o$ values corresponding to the prototype frames in Figure 4-7. All prototype MKFs furnish a unique reduction factor larger than the proposed value of 4.80, confirming the safety implicit in the proposed overstrength and ductility factors. It should be noted that the proposed overstrength-related force modification factor is comparable to that of steel MRFs in the Canadian design practice (1.6 versus 1.5), which is supported by nonlinear analysis results presented here. However future studies should examine a wider range of parameters, including number of stories, failure mechanisms, knee and frame geometry, to verify the proposed R_o.

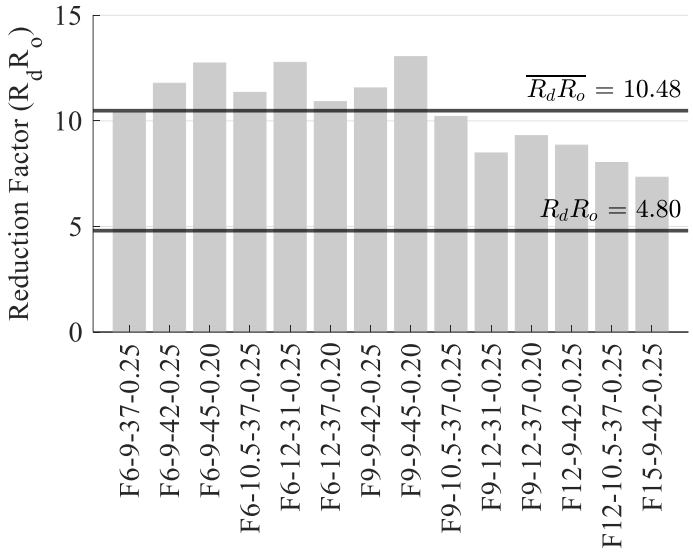

Figure 4-7. Reduction factor (product of R_d and R_o) for prototype frames.

4.6. Verification of the proposed seismic design parameters

4.6.1. Virtual test matrix

To verify the validity of the proposed overstrength and ductility factors, six new frames having 3, 6, 9, 10, 12, and 15 stories, called *Assessment Frames* hereafter, were selected and designed using the proposed reduction factor. These new MKFs were not included in the initial database used to determine R_d and R_o as their purpose was merely to assess the validity of the proposed factors. The same design procedure described in Section 4.3.2 was followed to size the members of these new assessment frames. All assessment MKFs were assumed to have a span length of 9.0 m, a braced length ratio of 0.25, and a brace angle of 42°. The same labelling convention as the initial prototype frames was followed for designating the assessment frames.

4.6.2. Verification methodology

The methodology of FEMA P695 was adopted here to verify the seismic design parameters developed for the steel MKF system. Given that this methodology was developed for application in the U.S., several modifications were made to apply it within the framework of Canadian

standards. The Adjusted Collapse Margin Ratio (*ACMR*) of the assessment frames was computed using the following relationship [13]:

$$ACMR = SSF \times CMR \tag{4-6}$$

where *SSF* denotes the spectral shape factor, which accounts for the spectral content of rare earthquake ground motions and is intended to avoid overestimated nonlinear response. *CMR* stands for Collapse Margin Ratio and is given by [13]:

$$CMR = \hat{S}_{CT} / S_{MT} \tag{4-7}$$

in which $\hat{S}_{CT}$ and S_{MT} represent the median 5%-damped spectral acceleration associated with the collapse level ground motions, i.e., the collapse intensity at which half of the ground motion records result in structural collapse, and 5%-damped design response spectral acceleration at the fundamental period of the system, respectively. $\hat{S}_{CT}$ can be determined for each frame by performing IDAs, which will be discussed later.

The suite of ground motion records recommended by FEMA P695 for seismic performance evaluation has entirely consisted of shallow crustal, crustal events hereafter, leaving out the significant contribution of other potential ground motion sources expected in the Cascadia subduction zone, i.e., subduction intraslab, intraslab events hereafter, and subduction interface, interface events hereafter, to the seismic hazard risk. Considering the location of the building selected in this study, namely Vancouver, it is crucial to factor in the effects of subduction events on the seismic performance evaluation and verification of the proposed seismic design parameters for the MKF system. Hence, the suite of ground motion records recommended by FEMA P695 was replaced by an appropriate ensemble that includes all sources of seismicity expected across southwestern Canada. In addition, various Ground Motion Prediction Equations (GMPEs) – or attenuation functions – developed for each specific source of seismicity were employed to

calculate the *SSF* of the archetype frames. Further details of such adjustments will be discussed in the following sections.

4.6.3. Nonlinear static analysis

First, the assessment frames were studied using the nonlinear static analysis method to evaluate their overstrength factor and period-based ductility. Presented in Figure 4-8 is the base shear against roof drift ratio for the assessment MKFs. Overall, a stable lateral response with appreciable reserve capacity was observed. It can be drawn from Figure 4-8 that the period-based ductility varies between 2.08 and 4.88 and decreases as the frame height increases. This behaviour agrees well with the trend observed in the original set of prototype MKFs.

Table 4-2 summarizes the overstrength factor for each assessment frame, along with the mean and STD values for the entire test matrix. According to Table 4-2, the overstrength factor varies between 1.82 and 2.19, with the mean, STD, and coefficient of variation of 1.95, 0.14, and 0.07, respectively. The overstrength factors computed here are smaller than those obtained for initial prototype frames because the member sizes of the original prototype frames were increased considerably to meet the code-specified drift requirement using a relatively large deflection amplification factor, i.e., $R_d R_o = 7.50$, as required by 2015 NBC. The assessment results confirm that the selected $R_o = 1.60$ can properly represent the reserve strength inherent in the steel MKF.

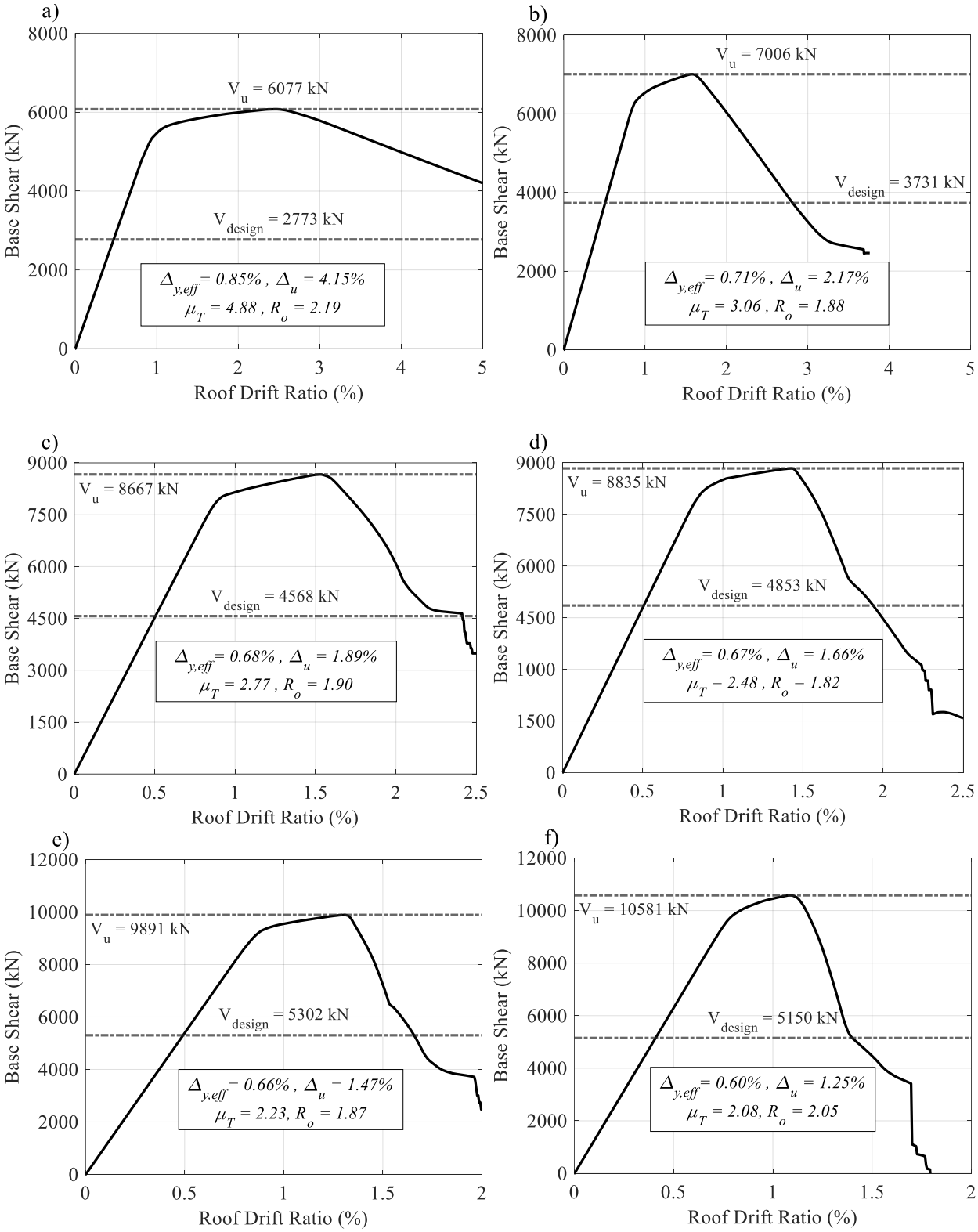

Figure 4-8. Pushover curves and associated overstrength R_o, period-based ductility μ_T, effective yield drift ratio of the roof $\Delta_{y,eff}$ and ultimate roof drift ratio Δ_u: a) AF3-9-42-0.25; b) AF6-9-42-0.25; c) AF9-9-42-0.25; d) AF10-9-42-0.25; e) AF12-9-42-0.25; f) AF15-9-42-0.25.

Table 4-2. Summary of the overstrength factors for the assessment frames.

Frame Designation	R_o
AF3-9-42-0.25	2.19
AF6-9-42-0.25	1.88
AF9-9-42-0.25	1.90
AF10-9-42-0.25	1.82
AF12-9-42-0.25	1.87
AF15-9-42-0.25	2.05
Mean	1.95
Acceptance Criterion	1.60
Pass/Fail	Pass

4.6.4. Ground motion records

The potential seismic hazard sources anticipated in southwestern Canada, i.e., crustal, intraslab, and interface, were accounted for in this study as required by [12]. The subduction events in the selected site would be triggered due to the unique tectonic environment of the Cascadia subduction zone [104]. It is crucial to note that the intraslab and interface earthquakes are expected to impose considerable demands on steel frames with moderate to long fundamental periods, respectively [8, 9]. A seismic risk assessment study conducted on the infrastructures located in the metropolitan area of Vancouver has revealed that the highest probability of structural failure among three different sources of seismicity is furnished by interface events, which would inflict an economic loss exceeding $100 billion [10]. Therefore, three ground motion suites, each including 11 records, were selected in this study to represent all three sources of earthquakes contributing to the seismic hazard in southwestern Canada. The ground motion records were chosen according to the seismic hazard deaggregation data of the site under consideration. Upon filtering all records, they were baseline corrected and scaled to reasonably match the target response spectrum of the chosen site within scenario-specific period ranges, per Commentary J of 2015 NBC. The list of the selected ground motion records, along with their scale factors, is outlined in Appendix A.

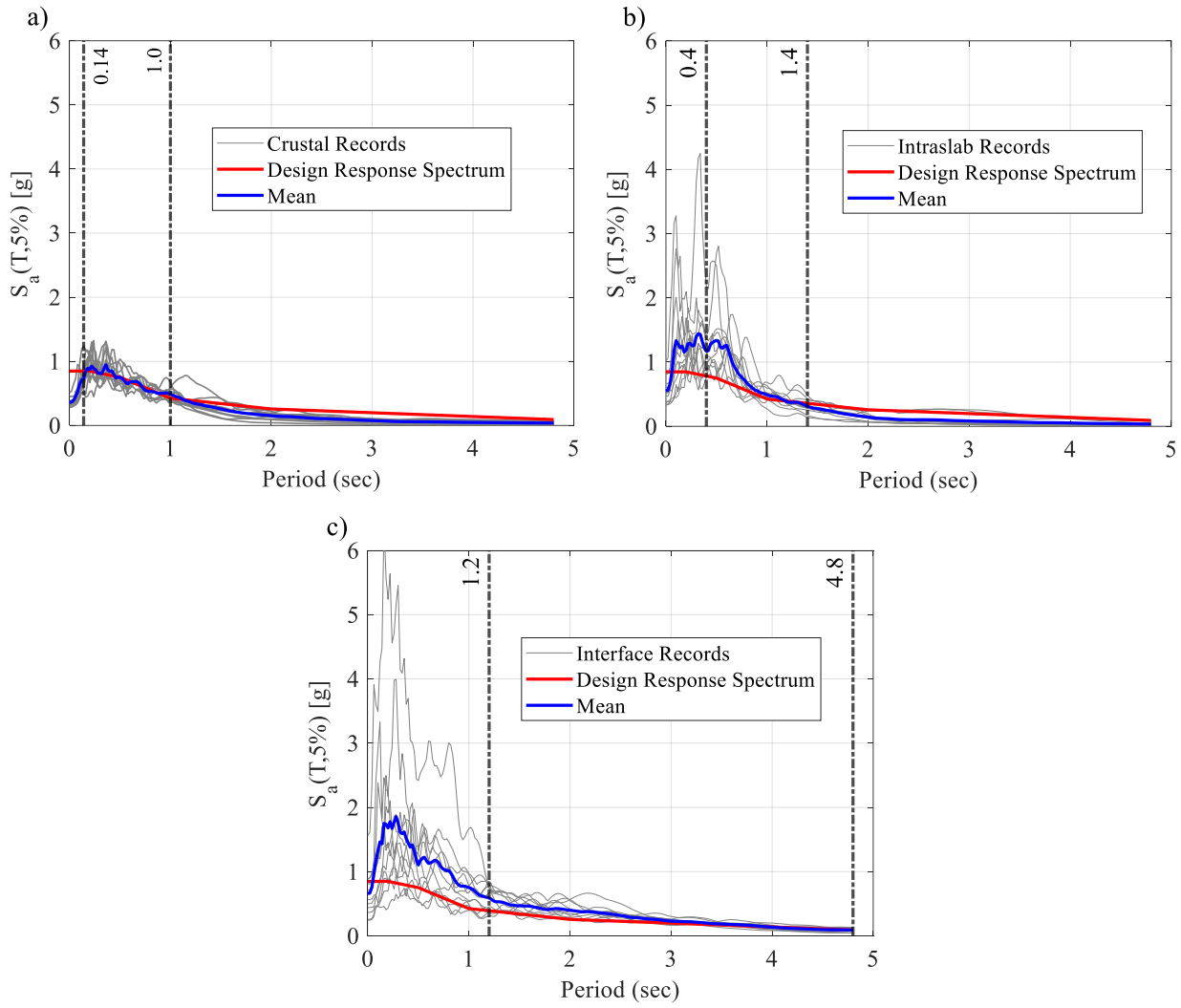

Figure 4-9. Response spectra of the selected records: a) Crustal; b) Intraslab; c) Interface.

Figure 4-9 illustrates the response spectra of the selected records, along with their respective mean and the NBC design spectra, for crustal, intraslab, and interface earthquakes, respectively. In this figure, the vertical axis represents the 5%-damped elastic spectral acceleration of the ground motion records, and vertical dashed lines indicate the boundaries of the scenario-specific period ranges. According to Commentary J of 2015 NBC, in southwestern Canada, buildings with short and moderate fundamental periods are affected mainly by crustal and intraslab events. On the other hand, interface earthquakes often contribute to the long-period hazard and, therefore, tend to impose larger displacement demands on buildings with long fundamental periods [8, 9]. Accordingly, the fact that

the mean response spectra of crustal and intraslab records are below the design response spectrum in long periods in Figure 4-9a and Figure 4-9b is not expected to significantly affect the frames' response.

4.6.5. Spectral shape factor

The spectral shape factor defined in Eq. (4-8) is used to adjust the CMR of each assessment frame as described earlier:

$$SSF = \exp\left[\beta_1\left(\bar{\varepsilon}_o - \bar{\varepsilon}_{records}\left(T_u\right)\right)\right] \tag{4-8}$$

where β_1 is a coefficient that depends on the frame's inelastic capacity and can be estimated as [13]:

$$\beta_1 = 0.14\left(\mu_T - 1\right)^{0.42} \tag{4-9}$$

$\bar{\varepsilon}_o$ in Eq. (4-8) refers to the target epsilon value at the selected site for a period of 1.0 s based on a probability of exceedance of 0.5% in 50 years. For each assessment frame, $\bar{\varepsilon}_{records}$ denotes the average of spectral shapes, or epsilon (ε) values, of the entire ground motion records calculated at T_u. The number of logarithmic standard deviations between the observed spectral value and the median response predicted by an attenuation function is called epsilon [13]. The relationship proposed by FEMA P695 for the epsilon parameter only takes the effects of crustal events into account and is developed for U.S. applications. Therefore, it cannot be implemented here since intraslab and interface events are also considered. In order to obtain a more reliable *SSF* for each assessment frame that can adequately represent the spectral shape effects at the selected site, different GMPE models developed for crustal, intraslab, and interface events were utilized. For crustal and intraslab events, the attenuation functions proposed by Boore and Atkinson [125] and Zhao et al. [126] were used, respectively. The ε value for each interface record was calculated as the weighted average of spectral shapes obtained using three different attenuation functions,

including Atkinson and Macias [127], Ghofrani and Atkinson [128], and Zhao et al. [126]. Based on the comprehensiveness of each model and the uncertainties associated with their application to the ground motion response prediction in the Cascadia subduction zone, these three functions were given respective weights of 0.5, 0.4 and 0.1. The $\bar{\varepsilon}_{records}(T_u)$ value for each assessment frame was eventually calculated by taking the average of three individual $\bar{\varepsilon}$ values, each pertaining to one of the seismicity sources. The Unified Hazard Tool developed by the United States Geological Survey (USGS) [129] was used to obtain the $\bar{\varepsilon}_o$ for the selected site, i.e., $\bar{\varepsilon}_o = 1.52$. The final values of $\bar{\varepsilon}_{records}(T_u)$ along with the β_1 and *SSF* coefficients calculated for the assessment frames are given in Table 4-3.

Table 4-3. Summary of spectral shape factors for assessment frames.

Frame Designation	$\bar{\varepsilon}_{records}(T_u)$	β_1	*SSF*
AF3-9-42-0.25	0.621	0.248	1.249
AF6-9-42-0.25	0.115	0.190	1.306
AF9-9-42-0.25	0.056	0.178	1.298
AF10-9-42-0.25	0.087	0.166	1.268
AF12-9-42-0.25	0.120	0.153	1.239
AF15-9-42-0.25	0.062	0.144	1.234

4.6.6. Collapse margin ratios

The Incremental Dynamic Analysis method [45] was applied to estimate the assessment frames' collapse capacity and CMR value. In order to perform IDAs, the assessment frames were subjected to increasing ground motion intensities using the NLRHA technique until collapse was detected. A total of 2970 NLRHAs (15 per ground motion record resulting in 495 per assessment frame) were performed to develop the IDA curves. The computational efficiency of IDAs was improved by applying a Hunt, Trace, and Fill (HTF) algorithm, as recommended in [45]. According to FEMA P695, 5%-damped elastic spectral acceleration at T_u, i.e., $S_a(T_u, 5\%)$, was used as the seismic Intensity Measure (IM). In addition, the maximum inter-storey drift ratio among all stories under a given ground motion intensity was selected as the seismic Damage Measure (DM). Local and global

collapse thresholds were considered to define the collapse response of the frames. The local collapse threshold was supposed to have been reached when a peak inter-storey drift ratio of 5% was detected within the frame. On the other hand, the global collapse threshold was assumed to represent a state of numerical instability, e.g., non-converging analyses under a scaled record. To ensure conservative collapse capacities were obtained while maintaining the accuracy of numerical analyses, the collapse intensity of each assessment frame was selected as the lesser of local and global collapse thresholds. Also, sufficiently small displacement or energy tolerances were used to perform the dynamic analyses. Figure 4-10 presents the IDA curves for each assessment frame. It can be observed in this figure that the median collapse intensity is reduced as the frame height increases. This agrees well with the results of nonlinear static analysis as taller frames are more impacted by P-Δ effects and are more likely to experience localized damage, thus exhibiting smaller ductility and collapse capacities. In order to assess the validity of the proposed response modification factor, the CMR of each archetype frame was adjusted using the *SSF*s given in Table 4-3, resulting in the respective *ACMR* values. According to the FEMA P695 methodology, the seismic performance of the MKF system designed using the overstrength and ductility factors recommended here is deemed acceptable, provided that the following acceptance criteria are met:

1) The average of *ACMRs* ($\overline{ACMR}$) within the entire test matrix should be larger than the maximum value of $ACMR_{10\%}$:

$$\overline{ACMR} \geq ACMR_{10\%} \tag{4-10}$$

2) The conditional collapse probability of 20% for each assessment frame should be satisfied as follows:

$$ACMR_i \geq ACMR_{20\%} \tag{4-11}$$

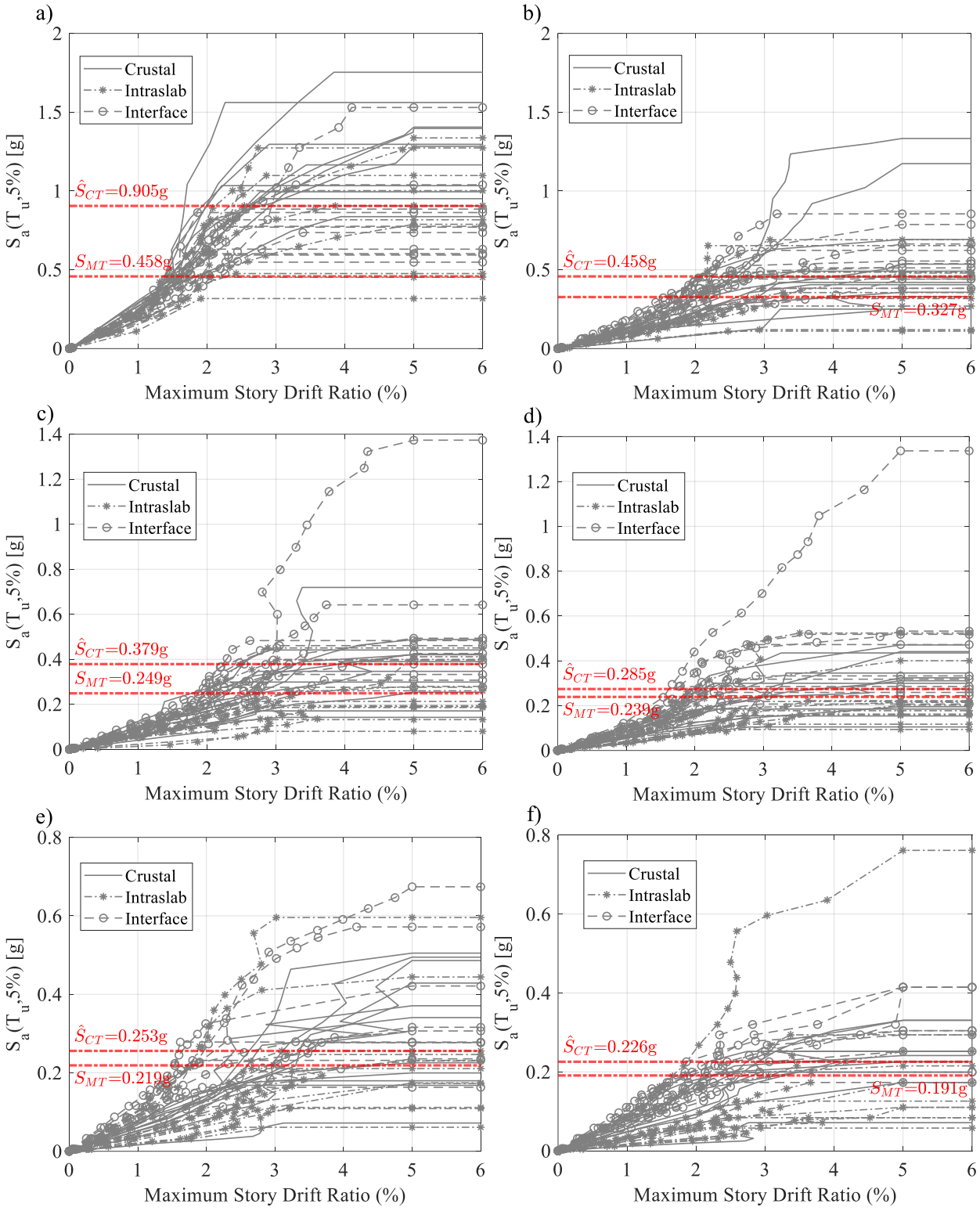

Figure 4-10. IDA curves of the assessment frames: a) AF3-9-42-0.25; b) AF6-9-42-0.25; c) AF9-9-42-0.25; d) AF10-9-42-0.25; e) AF12-9-42-0.25; f) AF15-9-42-0.25.

The total system collapse uncertainty is required to determine the acceptable $ACMR_{10\%}$ and $ACMR_{20\%}$ values. Herein, uncertainty values corresponding to superior design requirements, good analytical modelling, and good test data were combined with the maximum value of record-to-record variability within the performance group, giving rise to a total system collapse uncertainty of 0.50 (Refer to Table 7-2a in [13]). Therefore, the mean *ACMR* value within the performance group and the *ACMR* of each assessment frame should exceed 1.90 and 1.52, respectively, to satisfy Eq. (4-10) and Eq. (4-11) (Refer to Table 7-3 in [13]).

Table 4-4 presents the results of the assessment of the R_dR_o factor proposed for the MKF system when 12- and 15-storey frames were included in the assessment. The 12- and 15-storey frames failed to meet the acceptance criteria outlined in Eq. (4-10) and Eq. (4-11). The 12- and 15-storey assessment frames were then considered outliers. Such cases can be either accommodated by adopting more conservative seismic design parameters or eliminated from the design space by revising the design requirements [13].

Table 4-5 shows the acceptance criteria when the 12- and 15-storey frames were eliminated from the design space. This table shows that the MKF system designed with the proposed reduction factor passed the acceptance criteria. To address the unsatisfactory performance observed for 12- and 15-storey frames in design, a height limit of 40 m is proposed for the MKFs located in high seismic regions of Canada, i.e., Seismic Category 4 (SC4) as per 2015 NBC. An alternative approach is to implement a smaller R_dR_o value for buildings taller than the prescribed limit located in SC4, which necessitates the re-evaluation of the seismic design parameters for the index assessment frames [13, 122]. Further studies are needed to assess the frame performance in other seismic categories and perhaps set more relaxed height limits.

4.6.7. Seismic-induced demands

The seismic-induced demands of the assessment MKFs that passed the performance acceptance criteria, as listed in Table 4-5 were evaluated using NLRHAs. Gravity loads were first applied to the frames, followed by a series of NLRHA performed under 33 ground motion records scaled to the design-level hazard applied in the horizontal direction in the plane of the frames. In order to indirectly account for the increase in seismic demands due to accidental torsion, all ground motion accelerations were amplified by 5%.

The critical response parameters, including the maximum storey drift ratio, peak base shear, and peak roof displacement, were evaluated using the NLRHA results. No member instability or frame collapse was observed in the MKFs analyzed here. However, the NLRHA of AF3-9-42-0.25 and AF6-9-42-0.25 did not complete under records I04 and I11, the NLRHA of AF9-9-42-0.25 did not complete under record I11, and the NLRHA of AF10-9-42-0.25 was stopped under records I06, I07, and I11 due to significant lateral displacements and incompatible member rotations, which created numerical convergence issues. The results of these incomplete ground motion records were then excluded in calculating the median responses.

Figure 4-11 presents the profile of maximum storey drift ratios for the assessment frames of Table 4-5. All four frames exhibited an acceptable lateral response with the median of peak storey drift ratios within the entire suite of ground motion records below the 2015 NBC limit of 2.5%. It can be seen in Figure 4-11 that the 84^{th} percentile curve coincides with the median response of interface records, indicating that large storey drift ratios were generally governed by the interface events.

Table 4-4. Summary of collapse margin ratios and acceptance checks for the assessment frames (12- and 15-storey MKFs included).

Frame Designation	CMR	$ACMR$	$\overline{ACMR}$	Acceptable $ACMR_{20\%}$	Acceptable $ACMR_{10\%}$	$ACMR_i \geq ACMR_{20\%}$	$\overline{ACMR} \geq ACMR_{10\%}$
AF3-9-42-0.25	1.98	2.47	1.78	1.52	1.90	Pass	Fail
AF6-9-42-0.25	1.40	1.83		1.52		Pass	
AF9-9-42-0.25	1.52	1.97		1.52		Pass	
AF10-9-42-0.25	1.19	1.52		1.52		Pass	
AF12-9-42-0.25	1.15	1.42		1.52		Fail	
AF15-9-42-0.25	1.18	1.46		1.52		Fail	

Table 4-5. Summary of collapse margin ratios and acceptance checks for the assessment frames (12- and 15-storey MKFs excluded).

Frame Designation	CMR	$ACMR$	$\overline{ACMR}$	Acceptable $ACMR_{20\%}$	Acceptable $ACMR_{10\%}$	$ACMR_i \geq ACMR_{20\%}$	$\overline{ACMR} \geq ACMR_{10\%}$
AF3-9-42-0.25	1.98	2.47	1.95	1.52	1.90	Pass	Pass
AF6-9-42-0.25	1.40	1.83		1.52		Pass	
AF9-9-42-0.25	1.52	1.97		1.52		Pass	
AF10-9-42-0.25	1.19	1.52		1.52		Pass	

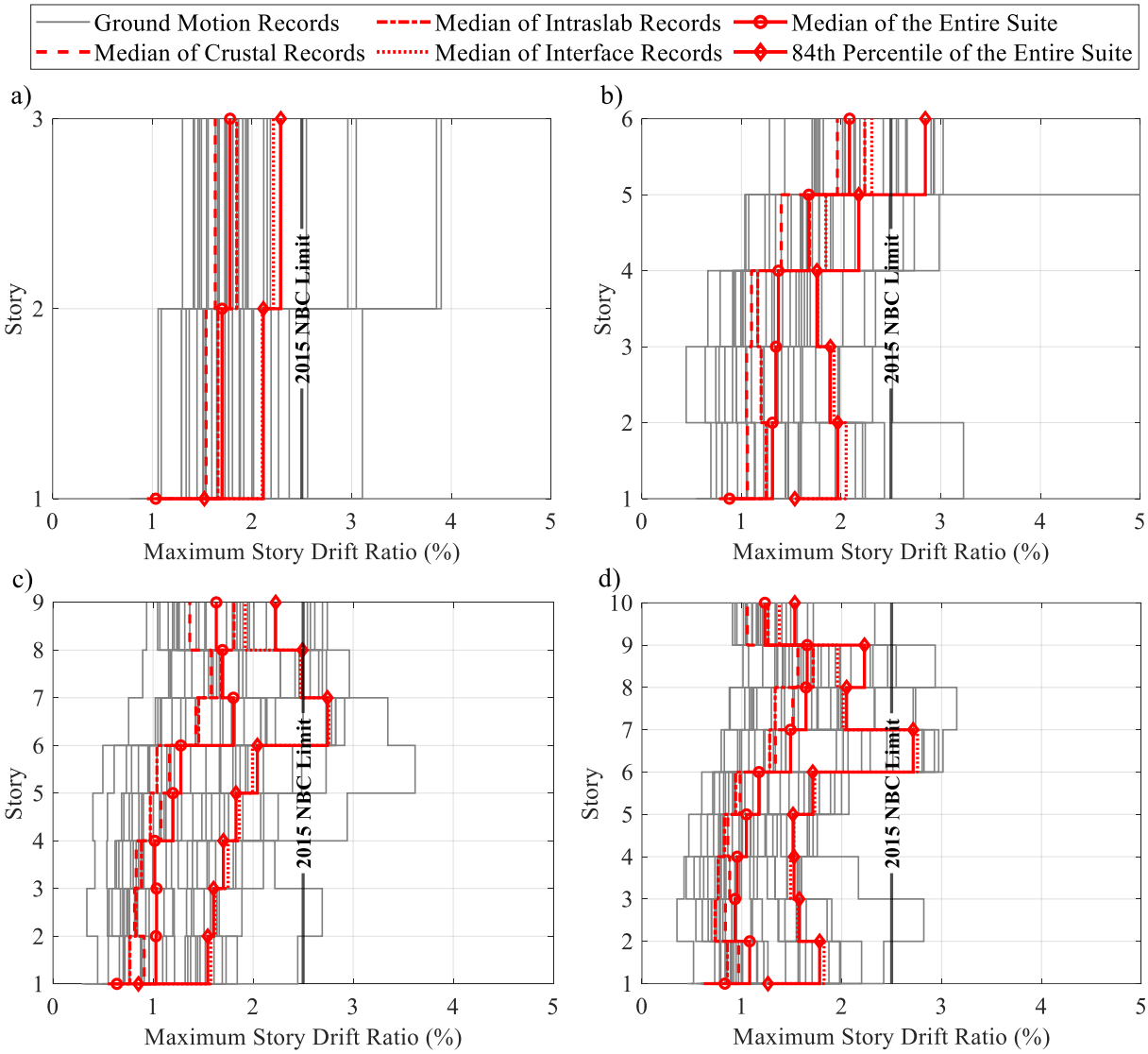

Figure 4-11. Profile of maximum storey drift ratios: a) AF3-9-45-0.25; b) AF6-9-45-0.25; c) AF9-9-45-0.25; d) AF10-9-45-0.25.

This finding highlights the significant impacts of subduction events on the nonlinear response of structures located in southwestern Canada. Table 4-6 shows frame displacement demands and the respective median values for the assessment frames listed in Table 4-5. The ratio of peak roof displacement to the effective yield displacement $\left(\delta_{NLRHA}^{Peak}/\delta_{y,eff}\right)_{Roof}$ was assumed as a measure of dynamic ductility demand. It can be drawn from Table 4-6 that the dynamic ductility demand index increases considerably under interface earthquakes. Moreover, in all cases, the median of peak dynamic ductility demand ratios is smaller than the corresponding period-based ductility

given in Figure 4-8. For example, the median value of $\left(\delta_{NLRHA}^{Peak}/\delta_{y,eff}\right)_{Roof}$ for AF9-9-42-0.25 is 1.29, which is considerably smaller than its period-based ductility $\mu_T = 2.77$ Such a ductility demand is deemed more realistic considering that not all ground motion records scaled to the design-level response spectrum are expected to produce significantly large lateral roof displacements (e.g., 2 – 5% of the building height) imposed in a typical nonlinear static analysis. Furthermore, the dynamic lateral response of the frames is different from that predicted by the static pushover analysis.

To examine the roof displacement demand, the maximum roof displacement from the NLRHA δ_{NLRHA}^{Peak} and $\delta_u = \Delta_u \times h_n$ obtained from the pushover analysis (Figure 4-8) were considered as the roof demand and capacity, respectively. Note that h_n refers to the frame height. The roof drift demand-to-capacity ratio was then defined as $\left(\delta_{NLRHA}^{Peak}/\delta_u\right)_{Roof}$, as shown in Table 4-6. All frames experienced a lower roof drift demand compared to their respective capacity. Furthermore, the median value of $\left(\delta_{NLRHA}^{Peak}/\delta_u\right)_{Roof}$ ratio was sufficiently small and mainly governed by interface records. The inter-storey drift demand was studied using the $\left(\Delta_{NLRHA}^{Peak}/\Delta_{design}\right)_{Stories,max}$ index representing the maximum ratio of the peak inter-storey drift obtained from an NLRHA to the respective design storey drift among all stories. Inter-storey drifts obtained from a linear elastic analysis using the recommended $R_d R_o$ were amplified by the proposed deflection amplification factor (Section 4.7) to calculate the design inter-storey drifts. Referring to Table 4-6, all frames yielded a median $\left(\Delta_{NLRHA}^{Peak}/\Delta_{design}\right)_{Stories,max}$ value smaller than or close to 1.0, reaffirming sufficient built-in lateral stiffness in the MKF system and the reliability of the proposed deflection amplification factor in predicting the expected inelastic deformations.

Table 4-6. Displacement demands of assessment MKFs.

Source of Seismicity	Ground Motion ID	$\left(\delta_{NLRHA}^{Peak}/\delta_{y,eff}\right)_{Roof}$				$\left(\delta_{NLRHA}^{Peak}/\delta_{u}\right)_{Roof}$				$\left(\Delta_{NLRHA}^{Peak}/\Delta_{design}\right)_{Stories,max}$			
		AF3-9-42-0.25	AF6-9-42-0.25	AF9-9-42-0.25	AF10-9-42-0.25	AF3-9-42-0.25	AF6-9-42-0.25	AF9-9-42-0.25	AF10-9-42-0.25	AF3-9-42-0.25	AF6-9-42-0.25	AF9-9-42-0.25	AF10-9-42-0.25
Crustal	C01	1.37	0.88	0.60	0.53	0.28	0.29	0.22	0.21	0.77	0.60	0.63	0.57
	C02	1.47	1.18	1.20	1.69	0.30	0.39	0.43	0.68	0.82	0.74	0.84	0.78
	C03	1.62	1.58	1.42	1.45	0.33	0.51	0.51	0.58	0.85	0.86	0.75	0.93
	C04	1.72	1.99	1.29	1.18	0.35	0.65	0.47	0.48	0.96	1.03	0.65	0.74
	C05	2.17	1.78	1.72	1.08	0.45	0.58	0.62	0.44	1.25	0.89	0.92	0.77
	C06	1.32	1.61	1.08	0.99	0.27	0.53	0.39	0.40	0.74	0.84	0.72	0.64
	C07	1.46	1.84	2.25	1.99	0.30	0.60	0.81	0.80	0.77	1.10	1.22	1.30
	C08	1.66	1.88	1.12	1.26	0.34	0.61	0.40	0.51	0.86	1.01	0.85	0.80
	C09	1.31	0.89	0.31	0.31	0.27	0.29	0.11	0.12	0.81	1.06	0.44	0.48
	C10	1.53	0.65	1.08	0.89	0.31	0.21	0.39	0.36	0.82	0.53	0.84	0.74
	C11	1.49	1.40	1.05	1.04	0.31	0.46	0.38	0.42	0.78	0.82	0.94	0.78
Subduction Intraslab	D01	1.44	0.88	0.76	0.56	0.30	0.29	0.28	0.22	1.47	1.01	1.22	0.67
	D02	1.10	0.91	0.68	0.58	0.23	0.30	0.25	0.23	0.86	1.22	1.28	0.81
	D03	1.62	1.04	0.49	0.60	0.33	0.34	0.18	0.24	0.92	0.87	0.52	0.71
	D04	1.63	1.66	0.78	0.82	0.33	0.54	0.28	0.33	0.99	1.18	0.81	0.94
	D05	1.21	1.44	1.04	0.97	0.25	0.47	0.37	0.39	0.72	0.89	0.77	0.53
	D06	1.81	1.53	1.81	1.77	0.37	0.50	0.65	0.71	0.97	1.26	0.98	0.90
	D07	1.82	1.76	1.22	1.27	0.37	0.57	0.44	0.51	0.98	0.95	0.77	1.16
	D08	1.56	1.70	1.05	1.09	0.32	0.55	0.38	0.44	0.87	1.22	1.05	0.67
	D09	1.84	1.50	1.18	0.94	0.38	0.49	0.43	0.38	1.02	0.87	0.62	0.64
	D10	1.41	1.72	1.66	1.74	0.29	0.56	0.60	0.70	1.05	0.88	1.24	0.89
	D11	1.85	1.34	0.83	1.10	0.38	0.44	0.30	0.44	1.10	0.93	0.89	0.99
	I01	1.43	1.77	1.94	1.86	0.29	0.58	0.70	0.75	0.77	0.85	0.99	1.29

Subduction Interface													
	I02	2.64	2.93	2.26	2.30	0.54	0.96	0.82	0.92	1.51	1.34	1.48	1.47
	I03	2.00	1.88	2.28	2.08	0.41	0.61	0.82	0.84	1.26	1.24	1.39	1.10
	I04	2.57	2.13	1.79	2.14	0.53	0.70	0.65	0.86	1.93	2.21	1.23	1.49
	I05	1.72	1.78	1.88	2.18	0.35	0.58	0.68	0.87	1.05	1.18	1.10	1.13
	I06	1.65	2.02	2.24	2.02	0.34	0.66	0.81	0.81	0.97	1.01	1.29	1.23
	I07	2.32	2.92	2.55	3.44	0.48	0.95	0.92	1.38	2.73	3.84	6.71	5.73
	I08	2.24	2.55	2.13	1.69	0.46	0.83	0.77	0.68	1.34	2.30	1.84	1.18
	I09	3.31	2.66	1.85	1.97	0.68	0.87	0.67	0.79	1.38	1.51	1.34	1.27
	I10	1.67	1.76	1.90	1.66	0.34	0.57	0.68	0.67	1.91	1.29	1.22	1.22
	I11	3.97	3.82	4.88	1.70	0.82	1.25	1.76	0.68	0.90	0.82	1.20	1.39
Median		1.65	1.72	1.29	1.27	0.35	0.56	0.47	0.51	0.97	1.01	0.98	0.90

While the difference between the displacement demands obtained for crustal and intrsalab records is marginal, the average value of all three displacement demands evaluated in Table 4-6 increases appreciably for all frames under the interface earthquakes. This behaviour confirms the significant contribution of subduction interface events to the seismic response of steel MKFs, particularly medium- and high-rise frames, located in the high seismic regions of southwestern Canada.

Figure 4-12 depicts the ratio of peak dynamic base shear V_{NLRHA}^{Peak} to the ultimate base shear obtained from the pushover analysis (Figure 4-8), along with their median values for the assessment frames listed in Table 4-5. This ratio represents the overstrength of the system, considering the frames' dynamic response and the steel material's cyclic hardening behaviour.

All four frames in Figure 4-12 achieved a median V_{NLRHA}^{Peak}/V_u value greater than 1.0, furnishing dynamic overstrength factors 5% to 20% larger than the static ones reported in Table 4-2. This difference mainly roots in the dynamic redistribution of storey shear forces because of higher mode effects. Higher modes tend to amplify storey shear forces compared with those obtained from a monolithically increasing lateral displacement with a pre-determined pattern employed in a pushover analysis [19]. Overall, the peak dynamic base shear results confirm the adequacy of the proposed overstrength factor of 1.60.

To investigate the seismic-induced demands in knee braces, beam stubs, and intermediate beam segments, one of the assessment MKFs, i.e., AF6-9-42-0.25, was selected, and the peak tension and compression forces in knee braces, the peak demand-to-capacity ratio of beam stubs, and the peak axial forces developed in intermediate beam segments were further evaluated for this frame. The peak response was computed by taking the 16th percentile, median, or 84th percentile of maximum responses among all identical members in the same storey over the earthquake ensemble.

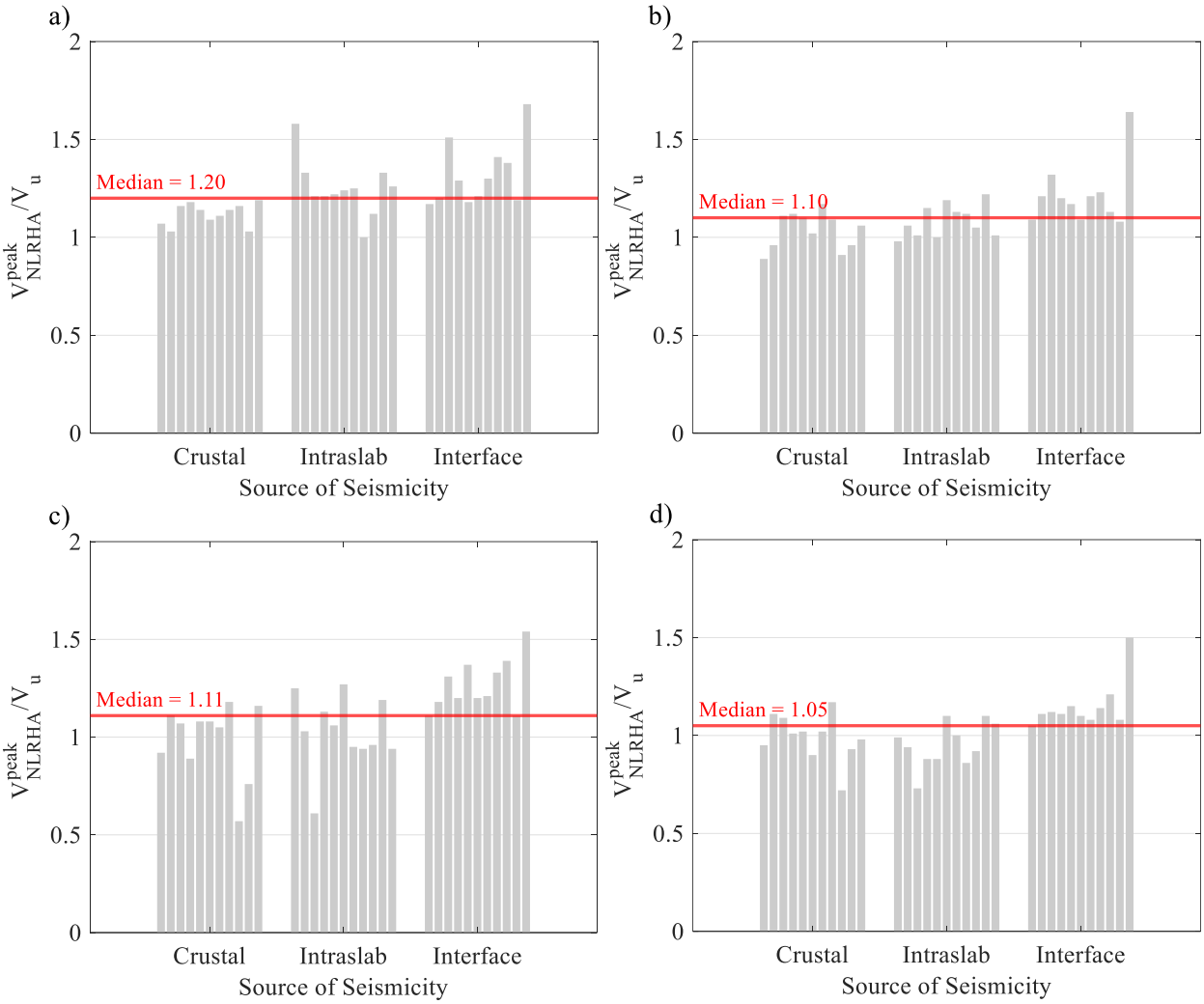

Figure 4-12. Peak dynamic base shear: a) AF3-9-42-0.25; b) AF6-9-42-0.25; c) AF9-9-42-0.25; d) AF10-9-42-0.25.

Figure 4-13a and Figure 4-13b depict the profile of peak axial tension force (T_{NLRHA}) and peak axial compression force (C_{NLRHA}) in knee braces. The peak tension and compression forces of knee braces obtained from NLRHAs were normalized by the expected tensile strength, $R_y F_y A_{br}$, and compressive strength, $1.2C_{n-prob}$, of knee braces, respectively. Here, A_{br} and C_{n-prob} are the cross-sectional area of the member and the nominal compressive strength of the member computed using the probable yield strength $R_y F_y$ as per CSA S16-19, respectively.

According to Figure 4-13a and Figure 4-13b, the median of normalized tension forces varies between 0.39 and 0.50, while the range of the median values for normalized compression forces

is 0.48-0.54, suggesting that the knee braces remained elastic with a sufficient margin of safety when subjected to seismic-induced forces.

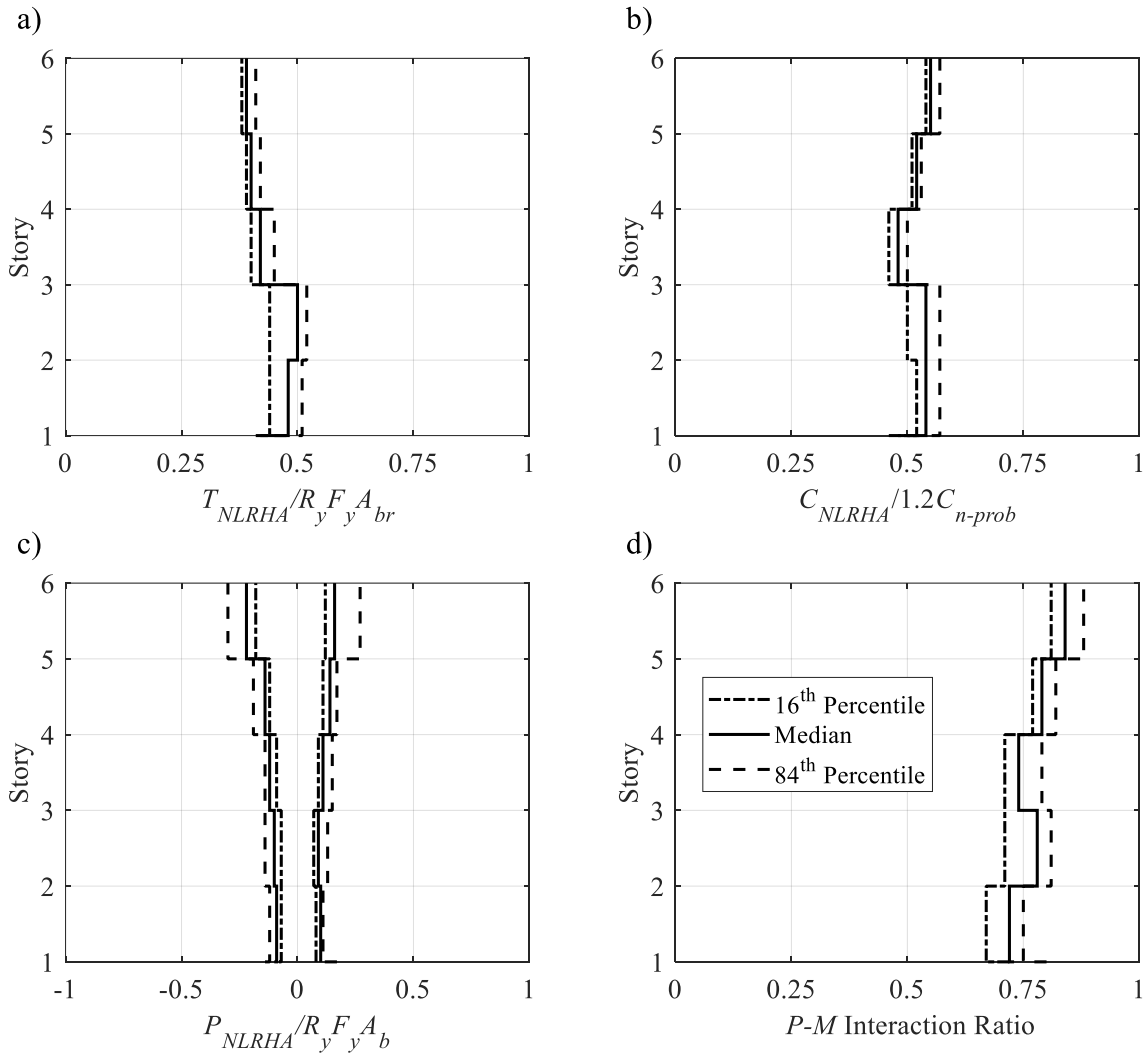

Figure 4-13. Peak dynamic force ratios for frame AF6-9-42-0.25 under design-level earthquakes: a) peak tension in the knee braces; b) peak compression in the knee braces; c) peak axial force in the intermediate beam segments; d) P-M interaction ratio in the beam stubs.

Figure 4-13c illustrates the profile of peak intermediate beam segment axial forces (P_{NLRHA}) normalized by the respective tensile capacity, $R_yF_yA_b$, in which A_b stands for the cross-sectional area of the intermediate beam segment. The negative values of P_{NLRHA} correspond to axial compression, while the positive values of P_{NLRHA} represent axial tension. As shown, limited axial forces are developed in the intermediate beam segments. The median of normalized tension forces

varies between 0.09 and 0.16, while the range of the median values for normalized compression forces is 0.09-0.22. The axial force developed in the intermediate beam segments arises mainly from unequal lateral displacements of columns since the rigid diaphragm assumption was neglected in the numerical models. It is expected that the presence of a concrete slab in practice, which promotes a rigid diaphragm behaviour, significantly reduces the axial force induced in the intermediate beam segments.

The profile of peak axial force–bending moment interaction (*P-M*) ratios in beam stubs is demonstrated in Figure 4-13d. The demands include the peak axial compression/tension and in-plane bending moment. The capacities were computed as the probable axial and strong-axis moment resistances following CSA S16-19 guidelines. As shown in Figure 4-13d, the beam stub *P-M* interaction ratios remain below 1.0 in all stories, confirming the anticipated elastic response under design-level earthquakes and the effectiveness of the seismic design approach.

4.7. Deflection amplification factor

The deflection amplification factor C_d was obtained after dividing $R_d R_o$ by the damping coefficient of the system according to FEMA P695:

$$\boldsymbol{C_d = R_d R_o / B_I} \tag{4-12}$$

where B_I denotes the damping coefficient, a parameter that depends on the effective damping, which can be assumed to be 5% critical for most systems [13]. This value yields a damping coefficient of 1.0, and consequently, $C_d = R_d R_o$, which agrees well with the 2015 NBC approach ($R_d R_o / I_E$) to compute the inelastic deflections of a given LLRS. Note that I_E represents the importance factor and is taken equal to 1.0 for buildings in the normal importance category, e.g., office or residential buildings. When applying the NBC method, lateral deflections of the structure from a linear elastic

analysis under the design base shear should be multiplied by $R_d R_o / I_E$ to obtain inelastic deflections. Therefore, a deflection amplification factor of $4.80/I_E$ is proposed for the MKF system.

4.8. Design period

The design period T_a is obtained using Eq. (4-13) for the calculation of seismic-induced loads and seismic performance evaluation of LLRSs in accordance with 2015 NBC:

$$T_a = min(C_u T_{emp}, T_1) \tag{4-13}$$

where T_{emp} refers to the empirical period, which is $0.085 h_n^{0.75}$ for MRFs. C_u is the upper bound coefficient, which takes the value of 1.5 for MRFs as per 2015 NBC.

The 2015 NBC empirical period equation for moment-resisting frames was adopted here for the MKF system. The analytical periods obtained using the eigenvalue analysis for 20 frames studied here (original prototype frames plus assessment frames) were used to estimate C_u for the MKF system, assuming that the analytical period of each frame is equal to C_u times the empirical period. This assumption may result in a slightly non-conservative C_u coefficient because the period obtained using $C_u T_{emp}$ is typically smaller than that obtained from an eigenvalue analysis, i.e., T_1, to ensure conservative seismic forces are estimated by the code.

The analytical and empirical periods for the MKFs are summarized in Table 4-7. The proposed C_u coefficient for the MKF system was obtained as the mean of the ratios between T_1 and T_{emp} minus one STD to indirectly compensate for non-conservatism implicit in the methodology and achieve a relatively conservative estimate of C_u while accounting for plausible variations in design and numerical modelling. Therefore, a value of 1.70 was proposed for the C_u coefficient of steel MKFs.

Table 4-7. Evaluation of the C_u parameter for the MKF system

No.	Frame Designation	$h_n(m)$	$T_1(s)$	$T_{emp}(s)$	T_1/T_{emp}
1	F6-9-37-0.25	24.30	1.92	0.93	2.06
2	F6-9-42-0.25	24.30	1.75	0.93	1.88
3	F6-9-45-0.20	24.30	1.84	0.93	1.98
4	F6-10.5-37-0.25	24.30	1.86	0.93	2.00
5	F6-12-31-0.25	24.30	1.85	0.93	1.99
6	F6-12-37-0.20	24.30	1.94	0.93	2.09
7	F9-9-42-0.25	36.30	2.36	1.26	1.88
8	F9-9-45-0.20	36.30	2.34	1.26	1.86
9	F9-10.5-37-0.25	36.30	2.36	1.26	1.88
10	F9-12-31-0.25	36.30	2.37	1.26	1.89
11	F9-12-37-0.20	36.30	2.45	1.26	1.95
12	F12-9-42-0.25	48.30	2.74	1.56	1.76
13	F12-10.5-37-0.25	48.30	2.67	1.56	1.71
14	F15-9-42-0.25	60.30	2.98	1.84	1.62
15	AF3-9-42-0.25	12.30	0.97	0.56	1.74
16	AF6-9-42-0.25	24.30	1.65	0.93	1.77
17	AF9-9-42-0.25	36.30	2.18	1.26	1.73
18	AF10-9-42-0.25	40.30	2.39	1.36	1.76
19	AF12-9-42-0.25	48.30	2.68	1.56	1.72
20	AF15-9-42-0.25	60.30	3.12	1.84	1.70
		Mean			1.85
		STD			0.13
		Mean – STD (16th Percentile)			1.72

4.9. Conclusions

This chapter proposed seismic design parameters, including overstrength-related force modification factor, ductility-related force modification factor, deflection amplification factor, and design period, for the steel Moment-resisting Knee-braced Frame (MKF) system within the framework of Canadian practice. An office building located in one of the high seismic regions of Canada (Vancouver, B.C.) was selected, and 14 prototype MKFs were developed as the LLRS of the building by varying the number of stories, span length, brace angle, and braced length ratio. The frames were then designed according to 2015 NBC and CSA S16-19 provisions for Ductile MRFs. The results obtained from the nonlinear static analyses performed on the prototype frames

were used to determine this system's preliminary overstrength- and ductility-related force modification factors. 6 new archetype MKFs (assessment frames) were selected and designed using the proposed overstrength- and ductility-related force modification factors. The Incremental Dynamic Analysis method was used to assess the adequacy of the proposed factors, considering the effects of all potential seismic hazard sources expected In the selected site, i.e., crustal, intraslab, and interface events. The Nonlinear Response History Analysis technique was also implemented to examine the maximum inter-storey drift ratio, peak base shear, and peak roof displacement demands. A deflection amplification factor and an equation to estimate the design fundamental period of the MKF system were finally proposed. The key findings of this study can be summarized as follows:

- An overstrength-related force modification factor of $R_o = 1.60$ and a ductility-related force modification factor of $R_d = 3.0$ were proposed for the MKF, featuring a moderately ductile LLRS ($R_d R_o = 4.80$) in the framework of the Canadian design practice.
- Knee braces and beam stubs remain elastic under design-level earthquakes, as expected in the design.
- The overstrength- and ductility-related force modification factors for the MKF apply to the multi-storey buildings not exceeding 40 m in height in high seismic regions of Canada (Seismic Category 4). A more relaxed $R_d R_o$ factor may be developed for MKFs exceeding this height limit and located in low-to-moderate seismic areas.
- A deflection amplification factor of 4.80 divided by the importance factor of the building was proposed to determine the inelastic lateral deflections of the MKF system under seismic loads.

- The design period T_a of the MKF can be obtained as the lesser of 1.7 times the empirical period specified by 2015 NBC for steel MRFs, and the analytical period computed using an eigenvalue analysis or other established methods of mechanics.
- The MKF system features flexural plastic hinging at the ends of intermediate beam segments under earthquake accelerations, which agrees well with the design assumptions. Subduction interface events in the selected building location governed this response.
- The IDA results of the MKFs designed using the proposed seismic design parameters demonstrated that the adjusted collapse margin ratios for 3-, 6-, 9-, and 10-storey MKFs are 2.47, 1.83, 1.97, and 1.52, respectively, with a mean value of 1.95. The *ACMR* values met the acceptance criteria, i.e., $ACMR_i \geq 1.52$ and $\overline{ACMR} \geq 1.90$ for individual frames and the entire performance group, respectively.
- The results obtained from NLRHA showed that the MKFs designed using the proposed seismic design parameters exhibited an acceptable lateral response. In particular, peak inter-storey drift ratios were, on average, smaller than the code-specified limit, i.e., 2.5%. The median values of peak inter-storey drift ratios within the entire suite of ground motion records were 1.78%, 2.08%, 1.80%, and 1.65% for 3-, 6-, 9- and 10-storey assessment frames, respectively.
- The ratio of the peak roof displacement to the effective yield displacement, which was used as a measure of dynamic ductility demand, ranged between 1.27 and 1.72 and tended to decrease as the frame height increased, except for the 6-storey MKF. This ratio increased appreciably under interface earthquakes, suggesting that interface events can potentially impose huge inelastic deformation demands on steel MKFs.

- The ratio of peak dynamic base shear to the ultimate base shear, which accounts for the influence of the dynamic redistribution of storey shear forces on the structural overstrength, exhibited median values of 1.20, 1.10, 1.11, and 1.05 for 3-, 6-, 9- and 10-storey assessment frames, respectively. These values, all exceeding unity, confirmed the reserve strength inherent in the MKF system.
- The proposed seismic design parameters verified by nonlinear response history analyses demonstrated a promising seismic performance for the MKF system, which can provide a level of safety comparable to that required by 2015 NBC.

The results presented here should be applied within the range of parameters used in this study. Extrapolation of results beyond the geometrical and material ranges considered here should be done with caution.

Failure due to low-cycle fatigue fracture should be simulated in future studies to evaluate the influence of this limit state on seismic and collapse performances of the MKF system [130]. The interaction between axial force and bending moment in the intermediate beam segments should be studied using detailed finite element simulations to examine the redistribution of seismic demands due to axial-flexural yielding in the beams. Furthermore, the details of end plate moment connections between intermediate beam segments and beam stubs should be developed in future research to achieve the system ductility proposed in this study. Additionally, different archetype frame geometries should be evaluated to expand the applicability of the proposed seismic design parameters. Finally, future experimental studies should investigate the cyclic response of the MKF system using subassembly and frame specimens to further verify the proposed seismic design parameters and ductility capacity developed by the system.

CHAPTER 5

EARTHQUAKE-INDUCED LOSS ASSESSMENT OF BUILDINGS WITH STEEL MOMENT-RESISTING KNEE-BRACED FRAMES UNDER SEISMIC HAZARD OF SOUTHWESTERN CANADA

Abstract: Economic loss due to the damage inflicted on structural and non-structural elements of a building following a major seismic event plays a crucial role in the development and selection of a lateral load-resisting system for seismic applications. While a system may demonstrate acceptable seismic performance metrics, including lateral stiffness, strength, ductility capacity, and collapse performance, it may fall short in terms of mitigating earthquake-induced economic losses. This research aims to assess and quantify using a probabilistic storey-based loss estimation procedure the earthquake-induced economic loss performance of multi-storey buildings equipped with a new lateral load-resisting system called the steel Moment-resisting Knee-braced Frame (MKF). Three prototype MKF buildings with varying total heights are selected and designed once in accordance with the conventional perspective method prescribed by the National Building Code of Canada and then based on the performance-based plastic design procedure. Prototype MKFs are then subjected to three suits of ground motion records representing the seismic hazard expected in southwestern Canada. Incremental dynamic analyses are performed to ramp up the intensity of the ground motions and record the engineering demand parameters for the economic loss assessment. The expected economic losses and the expected annual loss values are finally computed and investigated to further our understanding of the structural performance of the MKF. The results suggest that the MKF buildings offer promising seismic loss metrics when used as the lateral load-resisting system of low- to mid-rise buildings in southwestern Canada, particularly when designed as per the National Building Code of Canada. Furthermore, the economic loss of

the MKF system is governed by non-structural repair costs under frequently occurring seismic events, while collapse and demolition dominate building losses in the case of larger seismic intensities associated with lower probabilities of occurrence.

5.1. Introduction

Building structures expected to resist lateral seismic loads are designed using prescribed requirements by building codes and standards, such as the National Building Code (NBC) in Canada [4], and International Building Code (IBC) [131] and ASCE/SEI 7-16 [124] in the United States. The prescriptions by these standards aim to mainly achieve the life safety performance objective. For instance, a building of the normal importance category can be considered safe in the event of an earthquake if non-structural and structural damages do not compromise the structural integrity and collapse is prevented so that occupants can safely evacuate the building. However, a code-compliant design scheme may not necessarily reflect the potentially variable characteristics of earthquakes, e.g., duration, frequency content and amplitude, and the impact of rare earthquakes with greater return periods on a given Lateral Load-Resisting System (LLRS). Furthermore, despite the fact that the extent and consequences, e.g., financial losses, of potential structural and non-structural damages to the building after a moderate or major seismic event are critical when selecting building systems in seismic-prone regions, they are not systematically evaluated or quantified in design based on contemporary building codes. Specifically, lessons learned from the 2010-2011 Christchurch [132, 133] earthquakes underscore the need for detailed evaluation of earthquake-induced losses in building structures and for consideration of such losses in the selection and design of structural systems. Such information can help stakeholders, engineers, architects, owners, contractors and policymakers to make informed decisions to mitigate and reduce seismic risks.

Various methodologies have been proposed to evaluate the economic loss of buildings under earthquake loads. The Pacific Earthquake Engineering Research Center (PEER) loss estimation methodology incorporated in the Applied Technology Council (ATC) 58 project [134] facilitated measuring casualties, economic loss, and downtime of buildings. In fact, this methodology was presented for quantitative assessment of buildings' seismic performance, a goal that is more compatible with the stakeholders' needs. Several studies used the PEER loss estimation methodology for the performance assessment of wood, reinforced concrete, and steel structures [21, 51, 52]. Later, Ramirez and Miranda [47] revisited the PEER loss estimation methodology and made it more efficient in terms of computational expense. Specifically, the functions that directly bridge Engineering Demand Parameters (EDPs), e.g., Storey Drift Ratio (SDR), Peak Floor Acceleration (PFA), and Residual Storey Drift Ratio (RSDR), and economic loss play a critical role in their simplification. In addition, they introduced economic losses due to demolition as one of the possible consequences of seismic events in the PEER loss estimation methodology. Due to its robustness and simplicity, the loss estimation framework developed by Ramirez and Miranda has been applied in numerous studies to evaluate the earthquake-induced economic loss of buildings with different occupancies and LLRSs [15-18, 135-142].

Steel knee-braced frames taking advantage of conventional hot-rolled knee elements or buckling-restrained knee braces (BRKBs) have been the subject of numerous studies [27-41, 44, 89, 143]. Mokhtari et al. [113] developed a new LLRS referred to as the Moment-resisting Knee-braced Frame (MKF) system to overcome some of the limitations of conventional steel braced frames, e.g., architectural obstructions, and with Moment-Resisting Frames (MRFs), such as relatively low lateral stiffness and expensively complex strengthening requirements of beam-to-column connections.

The MKF system is composed of column trees spanning three stories and intermediate beam segments field-bolted to beam stubs. Beam stubs are connected in the shop to column trees through simple connections. Knee brace elements composed of square Hollow Structural Sections (HSSs) are shop-welded to the tip of the beam stubs and to the columns. Intermediate beam segments are connected to their end plates via groove welds. Column trees are bolted together on site to achieve the desired height. MKFs are designed such that seismic energy dissipation takes place through the formation of flexural plastic hinges at the face of beam-to-knee connections rather than axial yielding and buckling of knee elements to achieve a more stable ductile response [41, 117, 118]. Two seismic analysis and design methodologies, i.e., the Equivalent Static Force Procedure prescribed by the 2015 NBC of Canada [5] and the Performance-Based Plastic Design (PBPD) method, were evaluated in [113], and it was confirmed that the MKF system designed using the PBPD method can provide robust seismic performance with a controlled yield mechanism comparable to ductile steel MRFs designed according to 2015 NBC of Canada.

Mokhtari and Imanpour [144] proposed seismic design parameters identical to a moderately ductile system in 2015 NBC for the MKF system. It was confirmed through seismic evaluation and collapse response simulations that the MKF system can offer an attractive alternative to other conventional steel LLRSs in the construction of multi-storey buildings.

As the construction industry aims to develop seismic-resilient structures, understanding and evaluation of the potential economic impacts of earthquakes on buildings and civil infrastructure systems becomes increasingly critical in seismic-prone areas. This is particularly important as it provides further insight into the post-earthquake performance of new LLRSs, such as the recently proposed MKF system.

This study aims to quantify and assess the economic loss performance of steel MKF buildings designed for seismic loads expected in southwestern Canada. Two loss metrics are utilized to conduct building-specific loss assessments, i.e., the expected economic losses conditioned on a seismic intensity and the Expected Annual Loss (EAL). The research first focuses on the seismic design of six prototype buildings with the MKF system and then outlines the seismic loss assessment methodology used. Next, collapse simulation results are presented to compare the collapse behaviour of the selected buildings. Finally, the results of the economic loss assessment under seismic loads are presented, and the parameters affecting the economic loss of the buildings are investigated. The outcomes of this study are expected to help structural design engineers, developers, building owners, contractors, insurers, and policymakers make informed decisions when choosing MKF buildings in seismic regions.

5.2. Selected building and loading

An office building located near the Vancouver City Hall (49.2608° N, 123.1140° W) in British Columbia was chosen for this study. The building is located on site Class C, corresponding to dense soil. The building dimensions in the plan are 45 m × 63 m, as shown in Figure 5-1a. It consists of six 10.5 m bays in the long direction and five 9.0 m bays in the short direction. It's important to note that the dimensions in this figure are not to scale and are provided for conceptual understanding. The building is regular in plan and elevation. The first storey of the building has a height of 4.3 m, while all upper levels are 4 m high. The LLRS of the building consists of steel MKFs placed along the perimeter of the building. Given that the structure is symmetric about both principal axes, one of the MKFs in the long direction was selected for the collapse performance evaluation and, ultimately, for the assessment of seismic-induced economic loss. This frame is shown in Figure 5-1b. The selected MKF is intended to reflect practical geometries, including the

braced length ratio of 0.2, which represents the ratio of the beam stub length to the span length, and a knee brace angle of 39.8 degrees, resulting in gross lengths of 2.1 m and 2.73 m for beam stubs and knee braces, respectively. The impacts of the brace length ratio and knee brace angle on the seismic demands of MKF members and the lateral response of the system can be found in [113, 144]. Dead loads of 3.4 kPa and 3.6 kPa are assumed for the roof and floor levels, respectively. The unit weight of the exterior walls is 1.5 kPa. The unit weight of partition walls and floor live loads are 1.0 kPa and 2.4 kPa, respectively. The snow and roof live loads are 1.64 kPa and 1.0 kPa, respectively.

5.3. Seismic design of prototype MKFs

A total of six prototype buildings, including 3, 6, and 9 stories, were designed using two different methodologies, i.e., the PBPD scheme developed by Mokhtari et al. [113] and the conventional approach prescribed by 2020 NBC, to evaluate the influence of the building height and the design methodology on the earthquake-induced economic loss of the MKF buildings. As reported by Mokhtari et al. [113], a more efficient and economical MKF design can be achieved for the selected building heights. The labelling scheme for the frames designed per the NBC approach consists of the letter "F", Ih stands for *Frame*, succeeded by the number of stories and the letter "N", which refers to the design methodology. For example, F3-N denotes a 3-storey MKF designed as per NBC. The same labelling scheme was used for the MKFs designed using the PBPD method, except that the letter "N" was replaced by "P". For instance, F6-P refers to a 6-storey MKF designed following the PBPD procedure. It is noteworthy that the phrase "prototype frame" is used interchangeably with the phrase "prototype building" in this work.

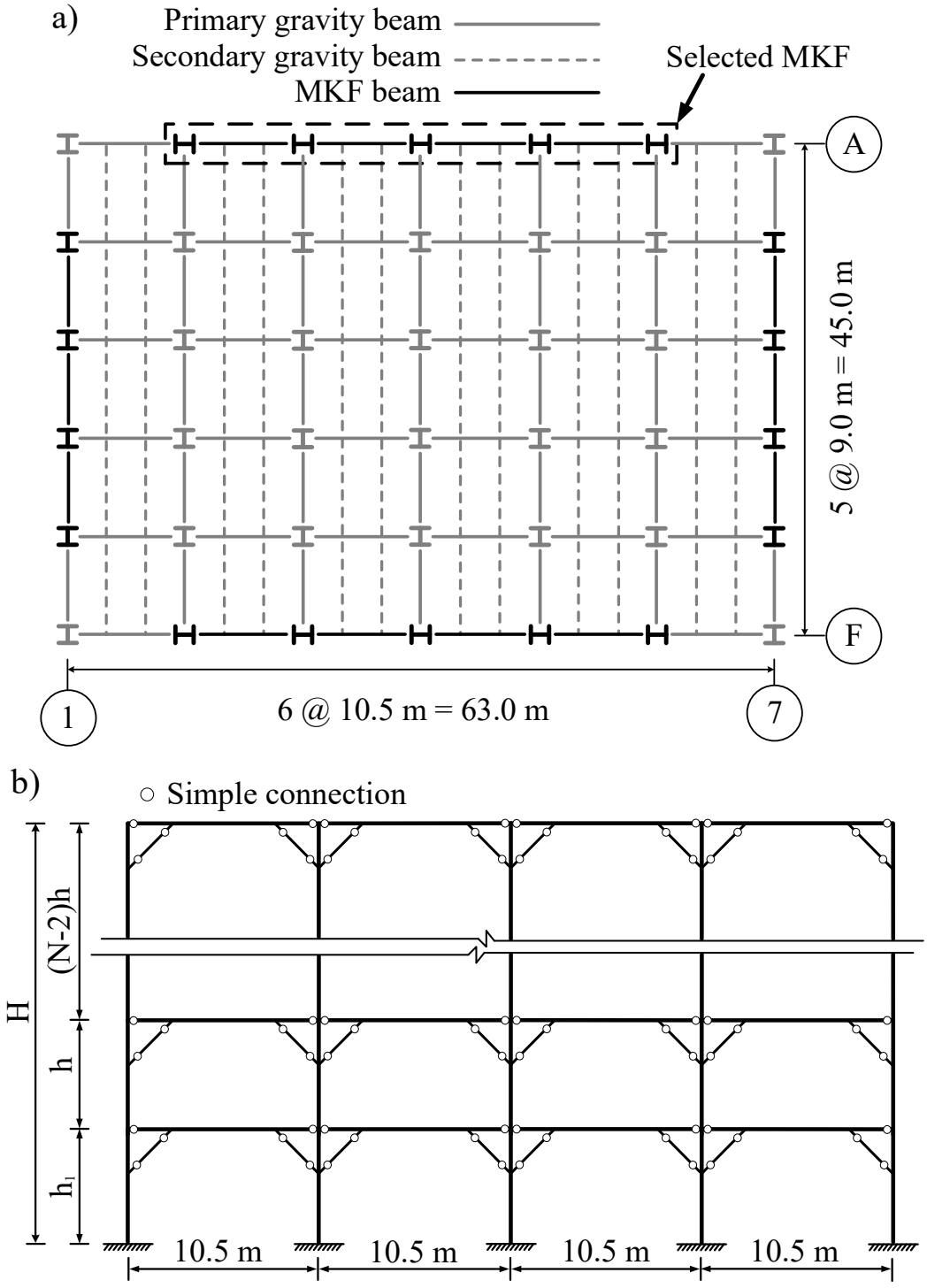

Figure 5-1. a) Plan view of the prototype building; and b) Elevation view of the selected MKFs (Frame total height H = 12.3, 24.3, 36.3 m for N = 3, 6, and 9, respectively).

The seismic design parameters proposed by Mokhtari and Imanpour [144], namely overstrength- and ductility-related force modification factors of $R_o = 1.60$ and $R_d = 3.0$, were used to obtain

the design base shear for the frames per the conventional NBC method. The total seismic weight of the 3-, 6-, and 9-storey prototype buildings were obtained as 37337, 76095, and 114854 kN, respectively. The importance factor was taken as I_E = 1. The design spectral acceleration values, $S_a(T_{design})$, based on the final design period of the frames were 0.55, 0.39, 0.30, 0.47, 0.3, and 0.25 g for F3-N, F6-N, F9-N, F3-P, F6-P, and F9-P, respectively. Following [113], the yield and target drift ratios required for the PBPD approach were set equal to 0.9% and 2.5%, respectively. The P-Δ effects were accounted for in the design. For NBC frames, the effect of notional loads and accidental torsion were also considered.

The structural design of the prototype MKFs and the interior gravity framing system, i.e., gravity beams and columns, was performed according to CSA S16-19 [3]. Steel wide flange sections made of ASTM A992 steel, with a specified yield strength of 345 MPa and a probable yield strength of 385 MPa, were used for the beam stubs, columns, and intermediate beams. Square HSSs conforming to ASTM 1085 steel with a specified yield strength of 345 MPa and a probable yield strength of 460 MPa were used for the knee braces. The intermediate beam segments were designed to undergo flexural yielding under gravity plus design seismic loads. The knee braces, beam stubs, and columns were selected such that they remain essentially elastic under the probable forces induced by flexural plastic hinging at the ends of intermediate beam segments. The cross sections chosen for beam stubs, intermediate beam segments, and first-storey columns meet the width-to-thickness ratio limits corresponding to Class 1 sections specified in CSA S16-19. Class 1 or 2 wide flange and hollow structural sections were used for the upper-storey columns and all knee braces, respectively. In both design approaches, the exterior and interior columns were treated as individual column trees to determine their design demands resulting from the probable forces

caused by flexural plastic hinging of the intermediate beam segments. Further details regarding the seismic design of MKFs can be found in [113, 144].

5.4. Numerical model

A two-dimensional (2D) numerical model of the prototype MKFs was created in the *OpenSees* program [43], following the modelling techniques proposed by Mokhtari and Imanpour [144]. The model was further refined here to include the flexural stiffness and strength of gravity system shear tab connections [15-19]. The numerical model is shown in Figure 5-2.

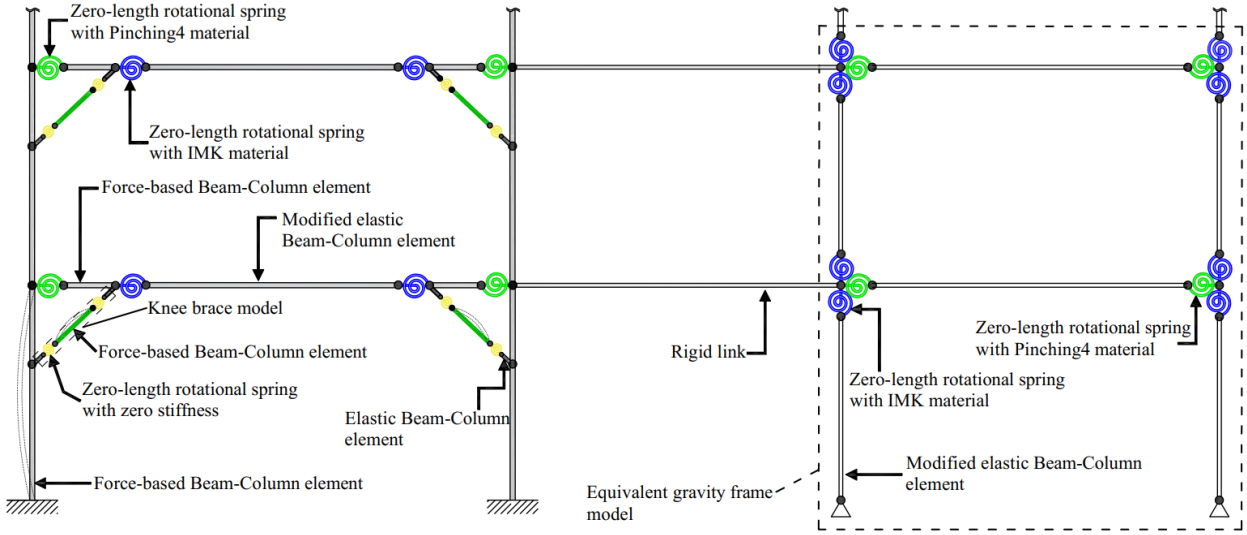

Figure 5-2. MKF numerical model, including the gravity bay (one of the MKF bays and two stories shown for simplicity).

Ideally, a three-dimensional (3D) model of the entire building would be used to examine the collapse response under earthquake loads. However, creating a numerical model of the entire structure may not be feasible due to prohibitively high computational costs or even may not be necessary. For instance, the findings from a full-scale shake table test of a four-storey steel-framed building at the E-Defense shake table in Japan [145] confirmed that a 3D model representation of the prototype buildings would undergo damage that is quite similar, both structurally and non-structurally, to that anticipated from a 2D model, provided that the strong component of the ground motion is applied along the same loading direction.

In this study, the contribution of the bare interior gravity framing system was numerically simulated, neglecting the influence of the composite slab, by attaching a fictitious single-bay frame to the main MKF using axially rigid truss links, as proposed by Gupta and Krawinkler [101]. This frame is referred to as the equivalent gravity frame in Figure 5-2. The gravity loads associated with the simulated gravity framing system were divided equally and applied to the columns of the equivalent gravity frame. At each level, the cross-sectional area, moment of inertia, and flexural strength of half of the interior gravity columns plus the MKF columns in the orthogonal direction to the MKF simulated were summed up, divided by two, and assigned to each column element in the equivalent gravity frame. In a similar manner, the sum of flexural strength and stiffness of half of the interior gravity beams at each level, i.e., 12 gravity beams, was assigned to an elastic beam-column element spanning between gravity columns.

The hysteretic response of steel shear tab gravity connections was simulated using the Pinching4 material model (Figure 5-3). The parameters of this material model were calibrated based on the experimental data of Specimen 1A by Liu and Astaneh-asl [146], which features a shear tab connection to the web of a wide flange column without a concrete slab. The calibrated material model parameters are given in Table 5-1 and Table 5-2. Figure 5-3b compares the numerical prediction against the experimental results for Specimen 1A. Details of the experimental observations attributed to unsymmetrical hysteretic response in Figure 5-3b can be found in [146]. As shown in Fig. 5-3b, the numerical model in *OpenSees* failed to capture the ultimate strength of the specimen past 0.1 radian rotation. However, this will not affect the numerical results of the MKFs studied here since the gravity shear tab connections are not expected to experience such a high rotation even at collapse level.

Gravity loads were applied to the numerical model of the frames, followed by an eigenvalue frequency analysis to determine the fundamental period of vibration considering the reduced stiffness of the system due to the geometrically nonlinear effects. Overall, the PBPD frames were more flexible than the NBC ones since, in general, they are designed for lower seismic demands.

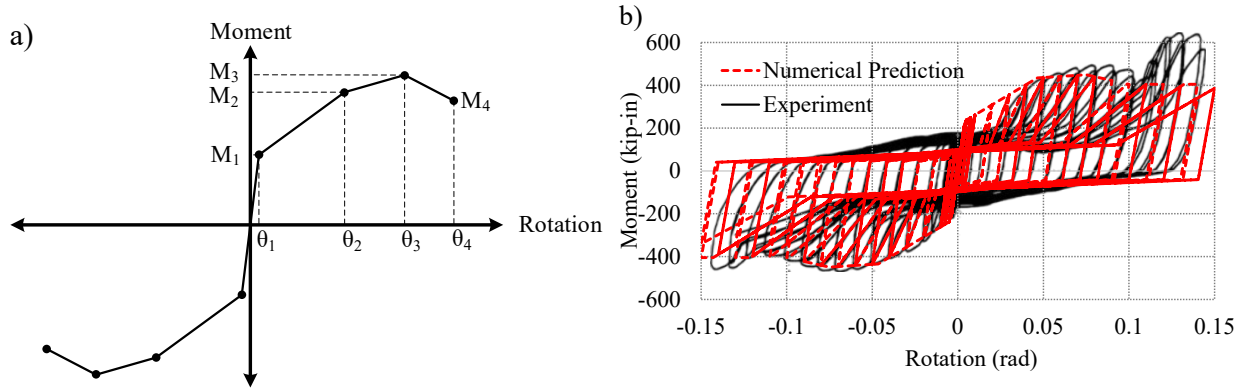

Figure 5-3. a) Backbone curve of the Pinching4 material model; b) Hysteretic response of shear tab connection (Specimen 1A [146]): experiment vs. numerical prediction.

Table 5-1. Monotonic parameters of the Pinching4 material model calibrated against Specimen 1A [20].

$\frac{M_{max}}{M_p^*}$	$\frac{M_1}{M_{max}}$	$\frac{M_2}{M_{max}}$	$\frac{M_3}{M_{max}}$	$\frac{M_4}{M_{max}}$	θ_1 (rad)	θ_2 (rad)	θ_3 (rad)	θ_4 (rad)
0.135	0.521	0.967	1.0	0.901	0.0042	0.0465	0.075	0.1

*M_p is the plastic moment capacity of the gravity beam.

Table 5-2. Cyclic deterioration parameters of the Pinching4 material model calibrated against Specimen 1A [20].

rDisp$^+$	rForce$^+$	uForce$^+$	rDisp$^-$	rForce$^-$	uForce$^-$	gKLim	gDLim	gFLim	gE
0.6	0.3	0.1	0.6	0.3	0.1	0.2	0.1	0	10

Earthquake ground motions were selected and scaled following the recommendations by Commentary J of the 2015 NBC of Canada [12]. Three sets of ground motion records, each containing 11 accelerograms and representing one of the three sources of seismicity expected in southwestern Canada, i.e., shallow crustal, subduction intraslab, and subduction interface [104], were finally selected and scaled to match the 2020 NBC target response spectrum of the site within scenario-specific period ranges. 10 s zero pads were added to the end of each record to estimate

the RSDRs by creating the free vibration response of the prototype frames. The reader is referred to Mokhtari and Imanpour [144] for additional information on ground motion selection and scaling.

5.5. Earthquake-induced economic loss estimation methodology

The probabilistic storey-based loss estimation procedure developed by Ramirez and Miranda [47] was employed to assess the economic loss of the prototype buildings under earthquake loading. According to this method, the total expected economic loss at a given seismic Intensity Measure (IM) is broken down into the summation of losses due to collapse, demolition, structural repair, and non-structural repair, as follows:

$$E[L_T \mid IM] = E[L_C \mid IM] + E[L_D \mid NC, IM] + E[L_R \mid NC \,\&\, ND, IM] \tag{5-1}$$

in which $E[L_C|IM]$ represents the expected economic loss due to collapse conditioned on the seismic intensity IM, $E[L_D|NC, IM]$ denotes the economic loss due to demolition when the building has not collapsed, but it may have to be demolished due to excessively large residual deformations, and $E[L_R|NC \,\&\, ND, IM]$ refers to the expected economic loss due to necessary structural and non-structural repairs when the structure has neither collapsed nor does it have to be demolished.

The collapse economic loss in a specified seismic intensity can be obtained by multiplying the replacement cost of the building and the probability of collapse at the respective intensity, $P(C|IM)$:

$$E[L_C \mid IM] = P(C \mid IM) \times \text{Replacement Cost} \tag{5-2}$$

$E[L_D|NC, IM]$ can be defined as the product of the economic loss due to demolition at a specified intensity, $E[L_D|IM]$, and the probability that collapse does not occur, i.e., $1 - P(C|IM)$:

$$E[L_D \mid NC, IM] = E[L_D \mid IM] \times [1 - P(C \mid IM)] \tag{5-3}$$

The expected economic loss, when demolishing the building is the only choice in the aftermath of an earthquake, can be estimated by multiplying the probability of the event and its associated costs:

$$E[L_D \mid IM] = P(D \mid IM)(\text{Demolition Cost} + \text{Replacement Cost} - \text{Recycled Materials}) \quad (5\text{-}4)$$

This study assumes that the demolition cost is approximately 10% of the total building replacement cost. This 10% can be retrieved by recycling some of the materials recovered from the demolished building [16, 147]. Hence, the cost associated with the expected economic loss due to demolition can be considered the same as the total building replacement cost. $P(D|IM)$ defines the probability of demolition when the building is subjected to a ground motion with the seismic intensity of IM and can be estimated using:

$$P(D \mid IM) = \int_0^{\infty} P(D \mid RSDR)\ f(RSDR \mid IM)\ d\left(RSDR\right) \quad (5\text{-}5)$$

where $P(D|RSDR)$ represents the probability of having to demolish the building conditioned on the maximum RSDR among all stories. Notably, this probability is determined based on engineering judgement and is assumed to have a lognormal distribution with a mean of 0.015 radians and a logarithmic standard deviation of 0.3 [16, 17, 47] (see Figure 5-4). $f(RSDR|IM)$ denotes the lognormal probability density function of distribution of maximum RSDRs for all ground motion records at the seismic intensity IM.

The expected economic loss due to the repair of damaged structural and non-structural components under an earthquake with the seismic intensity of IM is given by:

$$E[L_R \mid NC\ \&\ ND, IM] = \sum_{n=1}^{Nstories} E[L_R \mid IM, n] \times [1 - P(D \mid IM)] \times [1 - P(C \mid IM)] \quad (5\text{-}6)$$

which indicates that the total repair cost of the building, provided that demolition is unnecessary and collapse does not occur, is equal to the summation of the repair costs due to all structural and non-structural damages. In Eq. (5-6), *Nstories* represents the number of stories. $E[L_R|IM, n]$

accounts for the repair costs at storey n and can be computed by summing up the expected economic losses associated with all structural and non-structural components as follows:

$$E[L_R \mid IM, n] = \sum_{i=1}^{nComp} \sum_{j=1}^{nDS} P(DS_{ij} \mid IM) \times \left(\text{Repair Cost}\right)_{ij} \times \left(nUnits\right)_i \tag{5-7}$$

where $P(DS_{ij}|IM)$ indicates the probability of occurrence of damage state j in component I when a ground motion with the seismic intensity of IM excites the building, $(nUnits)_i$ is the number of components experiencing the same EDP at storey n, $nComp$ encompasses all different structural and non-structural elements at storey n, and nDS is the number of damage states considered for each element. $(\text{RepairCost})_{ij}$ is the repair cost associated with damage state j of component i.

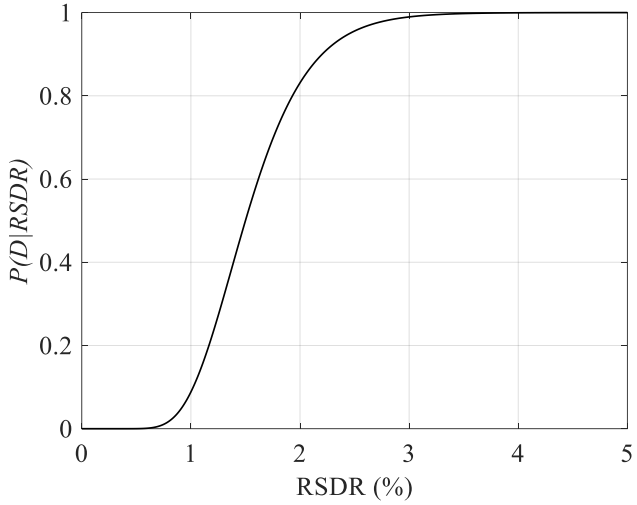

Figure 5-4. Probability of having to demolish a building that has not collapsed as a function of the peak RSDR.

To calculate the probability of occurrence of each damage state in each structural or non-structural component under a specified seismic intensity, the probability of occurrence of each damage state conditioned on a specified EDP, $P(DS_{ij}|EDP_i)$, should be multiplied by the lognormal probability density function of the respective EDP obtained from all ground motion records at the specified seismic intensity, $f(EDP_i|IM)$, and the result should be integrated as follows:

$$P(DS_{ij} \mid IM) = \int_0^{\infty} P(DS_{ij} \mid EDP_i)\ f(EDP_i \mid IM)\ d\left(EDP_i\right) \tag{5-8}$$

Expected annual loss, which represents an estimate of the yearly amount lost due to earthquake-induced damages, is one of the critical metrics used in earthquake-induced economic loss assessment. Once the total expected economic loss as a function of IM has been calculated according to Eq. (5-1), one will be able to combine it with the seismic hazard function of the selected site and evaluate the EAL as:

$$EAL = \int_0^{\infty} E(L_T \mid IM) \left| \frac{d\lambda_{IM}}{d\left(IM\right)} \right| d\left(IM\right) \tag{5-9}$$

where λ_{IM} is the mean annual frequency of exceeding a given IM.

Table 5-3 summarizes key parameters of the structural and non-structural elements considered for the seismic loss evaluation of the prototype buildings in this study, i.e., different damage states, EDP used to assess the state of damage in each component, fragility, and repair cost parameters. Note that the PFA parameter represents peak total floor acceleration since the motion imparted to acceleration-sensitive components is proportional to total floor acceleration [148]. In this table, *W* denotes the weight of the structural element in pounds per linear foot (*plf*).

According to FEMA P-58 [22, 23], there is no information on the repair costs of wide flange steel columns, field-bolted splice connections, and knee brace elements. In addition, previous research has shown that flexural hinging often occurs at the base of the columns under design-level earthquakes, as anticipated in design [113]. Well-designed knee braces and beam stubs in steel MKFs are expected to remain essentially elastic under the Design Earthquake (DE) hazard level with a sufficient reserve capacity [144]. This reserve capacity may be attributed to the overstrength implicit in the design of capacity-protected members. These components were, therefore, neglected in the seismic loss evaluation procedure.

Given the fact that the prototype buildings studied in this chapter are representative of modern steel construction in North America, it was assumed, for simplicity, that the building components suspended from the composite floor system, including mechanical, electrical, and plumbing, as well as stairs and their support, would be securely anchored to the structure. Thus, they can be considered inherently rugged and need not be considered in the loss evaluation procedure. This assumption is consistent with previous studies on building-specific earthquake-induced loss assessment [149]. The suspended ceiling was assumed to be supported both laterally and vertically in accordance with the state of practice in the high seismic regions of North America [22, 23].

Table 5-4 presents an example of estimated quantities of damageable structural and non-structural components for the F3-N prototype building when subjected to ground shaking in the long direction of the building. Notably, the direction of excitation under earthquake loads can affect the number of structural components susceptible to damage. For instance, if the ground motion records were to be applied along the short direction of the building, the quantity of bolted shear tab connections susceptible to damage would change from 168 to 174.

The repair costs reported originally in FEMA P-58 and adopted in Table 5-3 correspond to the U.S. construction practice in 2018, with a particular focus on the state of California. Moreover, the repair costs taken from other sources and shown in Table 5-3 have become obsolete. Accordingly, all repair costs were adjusted to reflect the local practice in Vancouver and then corrected for inflation. The 2022 National Construction Estimator tool [24] suggests a modification factor of 1.0 to convert the average construction costs in California to that expected in the Vancouver metropolitan area. Moreover, the history of the inflation rate in the construction of non-residential buildings in Vancouver was retrieved from the Statistics Canada database [150], and all repair costs were updated according to the data available for the last quarter of 2022.

Table 5-3. Fragility parameters and repair costs of selected damageable structural and non-structural components of steel framed buildings with perimeter MKFs.

Assembly description	Unit	Damage State	EDP	Fragility parameters		Repair cost
				σ_m^*	$\beta_b^\dagger$	χ_m^{**}
Bolted shear tab gravity connection [22, 23]	EA	Yielding	SDR	0.04	0.4	15,773
		Partial tearing		0.08	0.4	16,083
		Complete separation		0.11	0.4	15,773
Steel column base plate $W < 150\ plf$ [22, 23]	EA	Crack initiation	SDR	0.04	0.4	24,192
		Crack propagation		0.07	0.4	32,513
		Complete fracture		0.10	0.4	37,969
Steel column base plate $150\ plf < W < 300\ plf$ [22, 23]	EA	Crack initiation	SDR	0.04	0.4	25,184
		Crack propagation		0.07	0.4	34,993
		Complete fracture		0.10	0.4	42,929
Steel column base plate $W > 300 plf$ [22, 23]	EA	Crack initiation	SDR	0.04	0.4	26,672
		Crack propagation		0.07	0.4	38,713
		Complete fracture		0.10	0.4	49,129
Two-sided post-Northridge moment connection other than RBS with beam depth ≤ W27 [22, 23]	EA	Local buckling	SDR	0.03	0.3	43,400
		Lateral-torsional buckling		0.04	0.3	64,852
		Low cycle fatigue fracture		0.05	0.3	64,852
Two-sided post-Northridge moment connection other than RBS with beam depth ≥ W30 [22, 23]	EA	Local buckling	SDR	0.03	0.3	43,400
		Lateral-torsional buckling		0.04	0.3	72,540
		Low cycle fatigue fracture		0.05	0.3	72,540
Corrugated slab [49]	11 ft^2	Crack initiations	SDR	0.00375	0.13	266
		Crushing near column		0.01	0.22	488
		Shear stud fracture		0.05	0.35	844
Drywall partition [151]	64 ft^2	Visible	SDR	0.0039	0.17	133
		Significant		0.0085	0.23	793
Drywall finish [151]	64 ft^2	Visible	SDR	0.0039	0.17	133
		Significant		0.0085	0.23	382
Exterior glazing [151]	Pane	Crack	SDR	0.04	0.36	663
		Fallout		0.046	0.33	663
Braced automatic sprinklers [151]	12 ft	Fracture	PFA (g)	32	1.4	1,359
Suspended ceiling [22, 23]	2500 ft^2	5% of tiles dislodge	PFA (g)	1.09	0.3	4,495
		30% of tiles dislodge		1.69	0.3	35,185
		Collapse		1.91	0.3	72,385
Hydraulic elevator [22, 23]	EA	Failure	PGA (g)	0.5	0.3	10,168

* Median value of assembly fragility curve.
** Median repair cost in U.S. dollars.
† Logarithmic standard deviation.

After personal communications with several steel fabricators and building contractors in the Vancouver area, the authors concluded that the cost per unit area for the construction of steel

framed buildings would vary significantly because of several uncertainties involved in the construction process, including constantly fluctuating prices of materials and shipping costs caused by potential supply chain disruptions, such as those associated with COVID-19 global pandemic in the time of drafting this dissertation, as well as the varying characteristics of each building, such as the type and quantity of non-structural elements, structural and architectural details, and construction methods. As a result, the replacement cost of office buildings in British Columbia was estimated to be, on average, 2288 US$/m^2 for structures under five stories and 2808 US$/m^2 for structures with five to 10 stories as of the end of 2022, according to the 2023 BTY Market Intelligence Report [152]. A conversion rate of 0.76 was assumed for Canadian to U.S. dollars.

Table 5-4. Example of damageable components in the long direction of F3-N building.

Assembly description	Unit	Quantity
Bolted shear tab gravity connection	EA	168
Steel column base plate $W < 150\,plf$	EA	18
Two-sided post-Northridge moment connection other than RBS with beam depth ≤ W27	EA	48
Corrugated slab	m^2	1134
Drywall partition	5.95 m^2	1431
Drywall finish	5.95 m^2	1431
Exterior glazing	pane (2.79 m^2)	951
Braced automatic sprinklers	3.66 m	687
Suspended ceiling	232.26 m^2	36
Hydraulic elevator	EA	6

5.6. Collapse simulation and evaluation

The Incremental Dynamic Analysis (IDA) technique [45] was used to evaluate and compare the collapse performance of the prototype buildings. Once the gravity loads were applied using static analysis, the model was subjected to the selected ground motion records with increasing intensities until collapse occurred. A Trace-Hunt-Fill (THF) algorithm [45] was implemented to improve the efficiency of the analysis and reduce computational costs. A total of 2970 Nonlinear Response History Analyses (NLRHAs) consisting of 495 analyses per frame (15 analyses per each ground

motion record) were performed. The 5%-damped spectral acceleration at the first-mode period and peak SDR along the frame height were selected as the IM and damage measure (DM), respectively, to generate IDA plots. Two sideways collapse thresholds were considered in this study: local collapse, in which a maximum SDR of 5% is detected along the height of the frame, and global collapse, which represents a state of numerical instability and non-convergence of the NLRHA. Non-simulated collapse modes, such as connection fracture, lateral-torsional, flexural-torsional, and local buckling modes of columns, were neglected due to the uncertainties associated with such complex failure modes and considerable computational costs.

The IDA plots in Figure 5-5 display the collapse capacity of the prototype buildings under individual ground motion records. The 16th, median, and 84th percentile curves are superimposed on the same plots for comparison purposes.

In order to generate the fragility curves, the maximum likelihood optimization procedure [153] was implemented to fit a lognormal cumulative distribution function to the collapse points retrieved from the IDA curves using optimized values of the mean ($\hat{\theta}$) and logarithmic standard deviation ($\hat{\beta}$) that result in the highest probability of having produced the observed data. The fragility curves are shown in Figure 5-6a. Table 5-5 summarizes the critical outputs of the collapse study, including the median collapse intensity $\hat{S}_{CT}(T_1, 5\%)$ normalized with respect to the gravitational acceleration (g), the optimized values of mean and logarithmic dispersion, and the ratio of median collapse intensity to the DE level spectral acceleration at the fundamental period of the prototype buildings typically referred to as the Collapse Margin Ratio (CMR). The DE-level intensity in Canada is calculated using the NBC uniform hazard spectra, which are associated with seismic events having a 2% probability of exceedance in 50 years, corresponding to a return period of 2475 years.

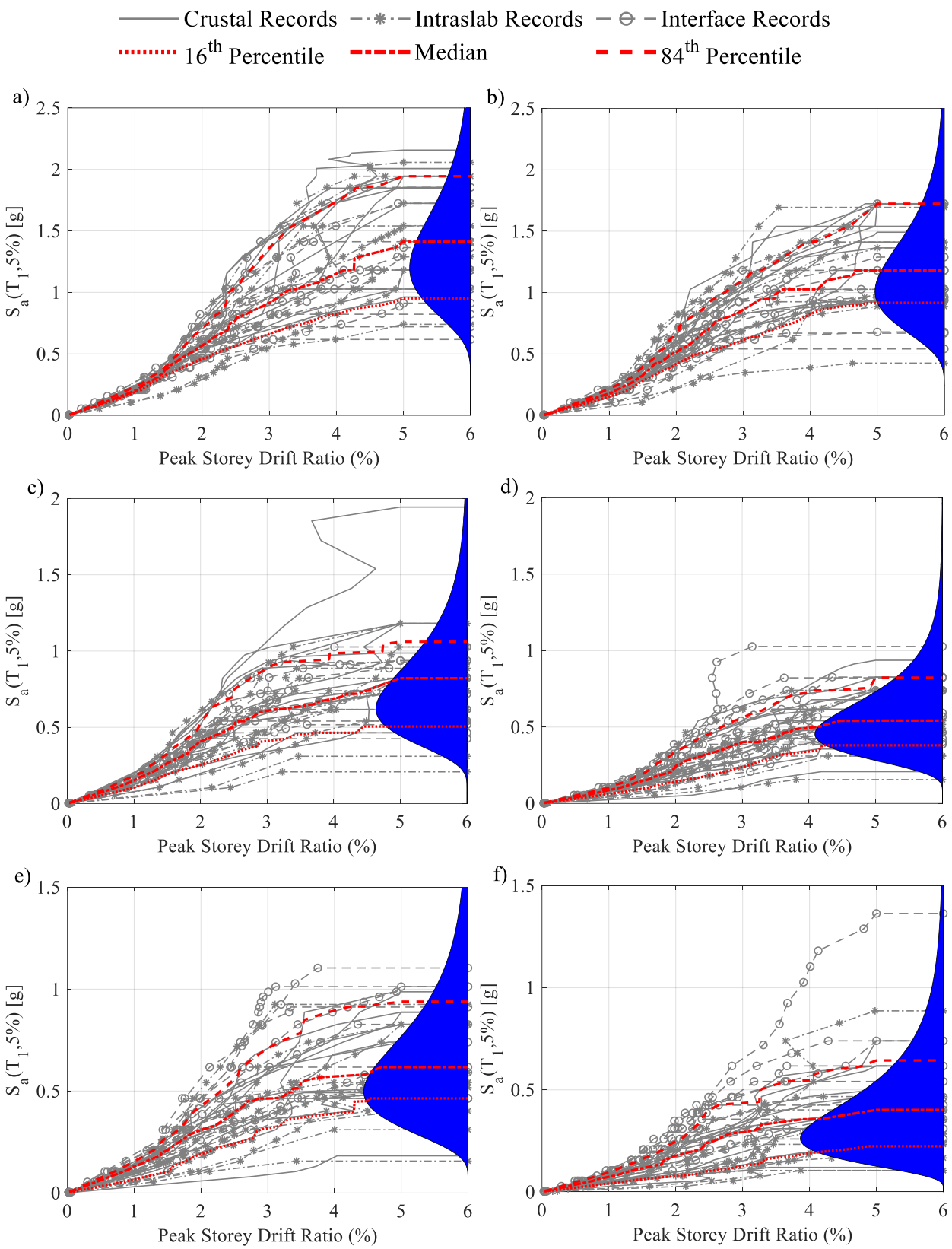

Figure 5-5. IDA curves of the prototype buildings: a) F3-N; b) F3-P; c) F6-N; d) F6-P; e) F9-N; f) F9-P.

Referring to Figure 5-5, Figure 5-6, and Table 5-5, the median collapse intensity decreases considerably while the probability of collapse increases with an increase in the total height of the frame. For instance, the probability of collapse at the DE hazard level is 0.43%, 6.14%, and 6.66% for F3-N, F6-N, and F9-N, respectively. These probabilities increase to 0.66%, 10.50%, and 32.11% for F3-P, F6-P, and F9-P, respectively, primarily due to the fact that the PBPD frames collapse in smaller intensities and generally result in a less favourable collapse performance compared to the NBC frames. $\hat{S}_{CT}(T_1, 5\%)$ values in Table 5-5 show that taller frames have smaller median collapse intensities, suggesting that they are likely more affected by P-Δ effects and nonuniform distribution of nonlinear lateral deformations, which can lead to damage localization, lower system-level deformation ductility capacity, and premature collapse, as confirmed in previous studies [92, 122]. Additionally, frames designed per the NBC approach exhibit higher CMRs than the PBPD frames in the range of 18% to 34%. This is partly because the NBC frames were designed to carry relatively higher lateral seismic demands.

The seismic collapse risk of the prototype buildings can be assessed and compared in terms of the mean annual frequency of collapse (λ_c) by numerically integrating the collapse fragility curve of a given analytical model over the corresponding site-specific hazard curve as [62]:

$$\lambda_c = \int_0^\infty P(C \mid IM) \left| \frac{d\lambda_{IM}}{d(IM)} \right| d(IM) \tag{5-10}$$

According to Commentary I of the 2015 NBC, the implied annual probability of near incipient collapse of the structures designed for seismic loads is 4×10^{-4}. Once the value of λ_c is calculated for a given building, it is compared against this threshold to verify whether the building meets the NBC failure criterion.

Deaggregation of λ_c for a given prototype building can be used to identify the dominant ground motion intensity levels that contribute the most to the total collapse risk. As shown in Figure 5-6b, to obtain a point on the λ_c deaggregation curve, one should plot the product of the probability of collapse at a particular ground motion intensity and the first derivative of the seismic hazard curve as a function of intensity. As indicated mathematically in Eq. (5-10) and illustrated schematically in Figure 5-6b, λ_c is equal to the area under the deaggregation curve. By comparing Figure 5-6a and Figure 5-6b, it can be seen that although high probabilities of collapse may be linked to specific ground motion intensities, their contribution to λ_c may not be significant due to their low probabilities of occurrence compared to the lower intensities on the collapse fragility curve.

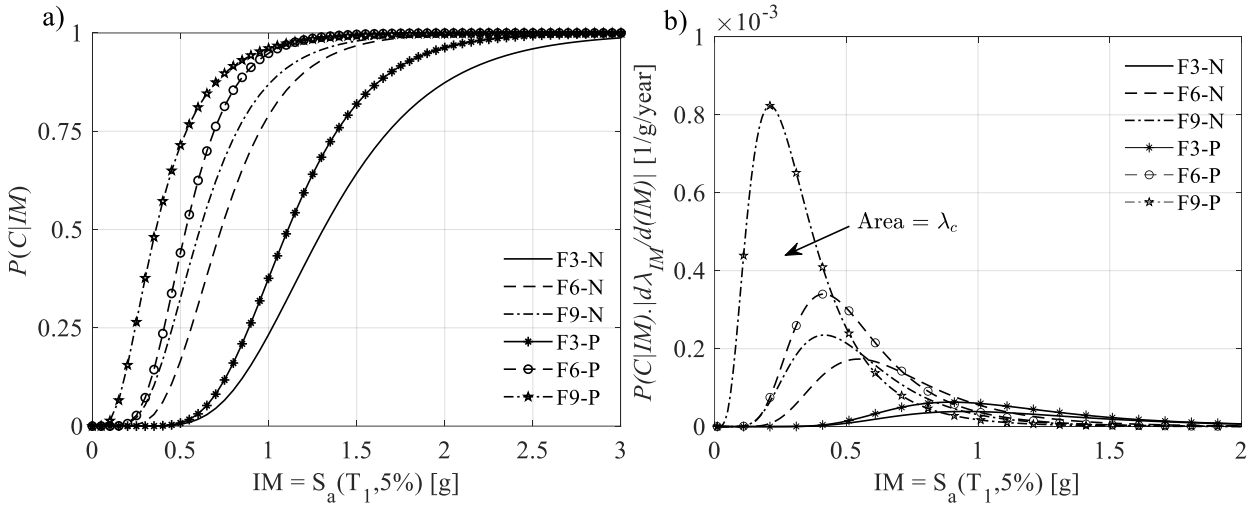

Figure 5-6. a) Collapse fragility curves of the prototype buildings; b) Deaggregation of mean annual frequency of collapse (λ_c).

The values of λ_c evaluated for each prototype building are reported in Table 5-5. As shown, the mean annual risk of collapse increases by increasing the height, with NBC frames having smaller λ_c values than their PBPD counterparts. Moreover, for all buildings, the annual probability of collapse is smaller than the respective NBC limit. The average annual probability of collapse of the buildings is 1.26×10^{-4}, which is approximately 70% smaller than the threshold set by

Commentary I of 2015 NBC. Notably, F9-P exhibits the poorest collapse performance with the largest λ_c value, i.e., 2.88×10^{-4}, which is almost two times the average.

Table 5-5. Collapse parameters of the prototype buildings.

Frame Designation	F3-N	F6-N	F9-N	F3-P	F6-P	F9-P
$\hat{S}_{CT}(T_1, 5\%)$ [g]	1.41	0.82	0.617	1.18	0.54	0.40
$\hat{\theta}$ [g]	1.31	0.73	0.61	1.11	0.53	0.36
$\hat{\beta}$	0.37	0.39	0.44	0.33	0.39	0.58
CMR	2.85	2.06	1.95	2.41	1.65	1.45
$\lambda_c \times 10^4$ [1/year]	0.38	1.03	1.16	0.55	1.58	2.88

Contrary to the PBPD method, where the seismic forces were computed using an imposed plastic mechanism, the NBC seismic design forces were obtained using a linear Response Spectrum Analysis (RSA), which may not accurately reflect the distribution of inelastic demands resulting from seismic excursions. Nonetheless, by referring to Table 5-5, it can be observed that the collapse performance of the MKF buildings designed using the NBC approach with the seismic design parameters proposed by Mokhtari and Imanpour [144] was superior compared to the PBPD frames. This is supported by the fact that NBC buildings result in an average annual probability of collapse of $\lambda_c = 0.86 \times 10^{-4}$ which is almost 50% smaller than that achieved by the PBPD buildings, i.e., $\lambda_c = 1.67 \times 10^{-4}$.

5.7. Earthquake-induced loss performance

The seismic loss vulnerability curves of the prototype buildings are shown in Figure 5-7. In this figure, the vertical axis indicates the economic loss normalized by the total replacement cost of the building, while the horizontal axis represents the variation in seismic intensity. SRL, NSRLAcc, and NSRLDr refer to structural repair loss, non-structural repair loss caused by acceleration-sensitive components, and non-structural repair loss due to drift-sensitive components, respectively. The bar charts of Figure 5-8 give the breakdown of economic loss components for

all prototype buildings at the Service Earthquake (SE) and DE intensities. SE intensity was assumed as a hazard level with a 10% probability of exceedance in 50 years, corresponding to a return period of 475 years.

As shown in Figure 5-7, the magnitude of economic loss due to damages experienced by non-structural acceleration-sensitive components is almost negligible compared to that of drift-sensitive elements in all buildings. This observation can be explained by the fact that the fragility parameters of the acceleration-sensitive components result in small probabilities of failure, given the PFA values obtained from IDAs. Moreover, the quantity of acceleration-sensitive components considered in the study and their total repair costs are minimal compared to those of drift-sensitive components. Referring to Figure 5-7, damages to non-structural drift-sensitive components of the building govern the economic loss below the SE hazard level in all cases and below the DE hazard level in F3-N, F3-P, and F6-N. For F6-P, F9-N, and F9-P, economic loss due to structural collapse prevails over other loss components at the DE level. For example, in the case of F-9N, normalized losses at the DE level intensity due to collapse, demolition, structural damages, non-structural damages to acceleration-sensitive components, and non-structural damages to drift-sensitive components have respective values of 0.091, 0.010, 0.027, 0.007, and 0.062, resulting in a total normalized loss of 0.198.

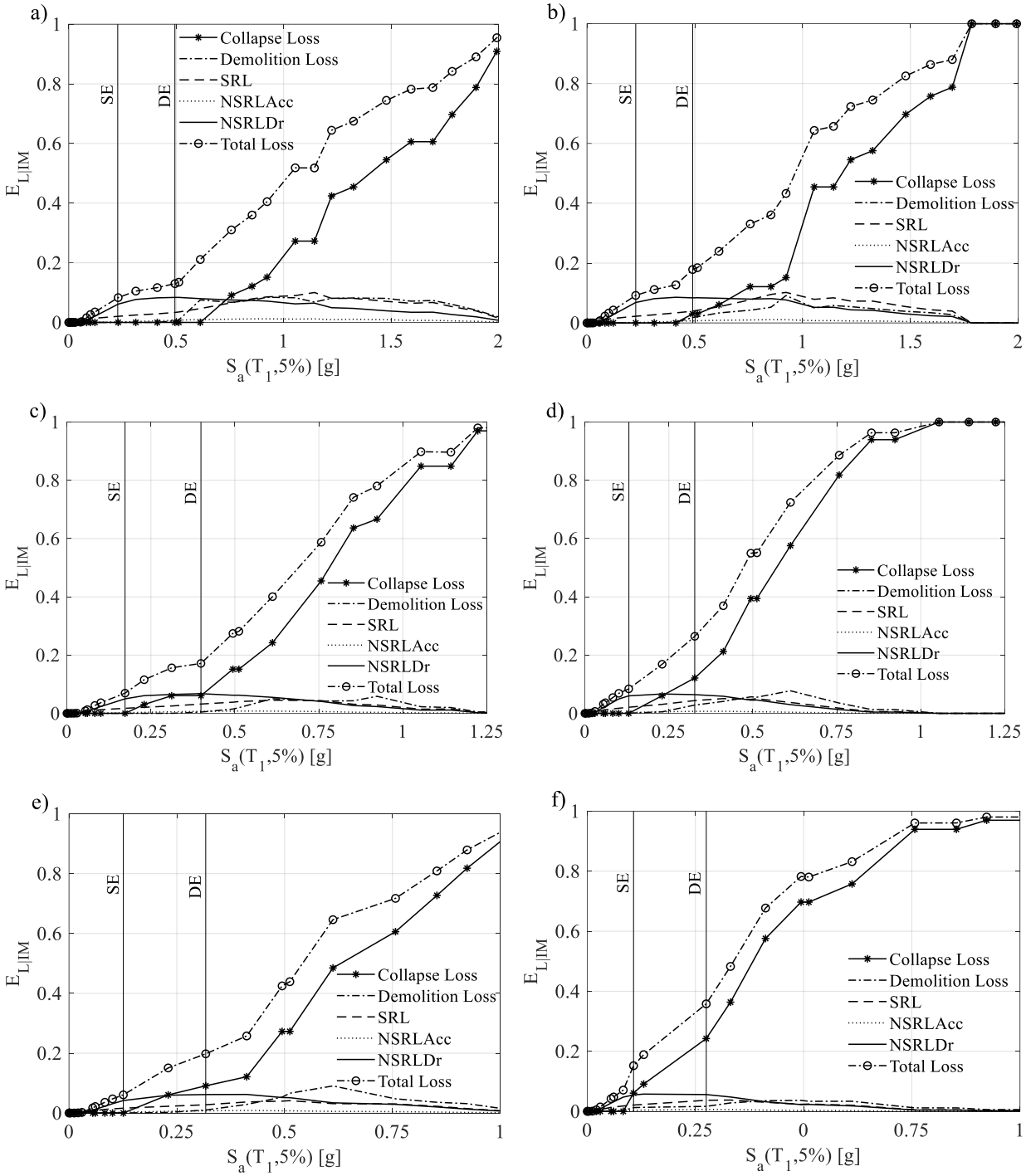

Figure 5-7. Loss vulnerability curves of the prototype buildings: a) F3-N; b) F3-P; c) F6-N; d) F6-P; e) F9-N; f) F9-P.

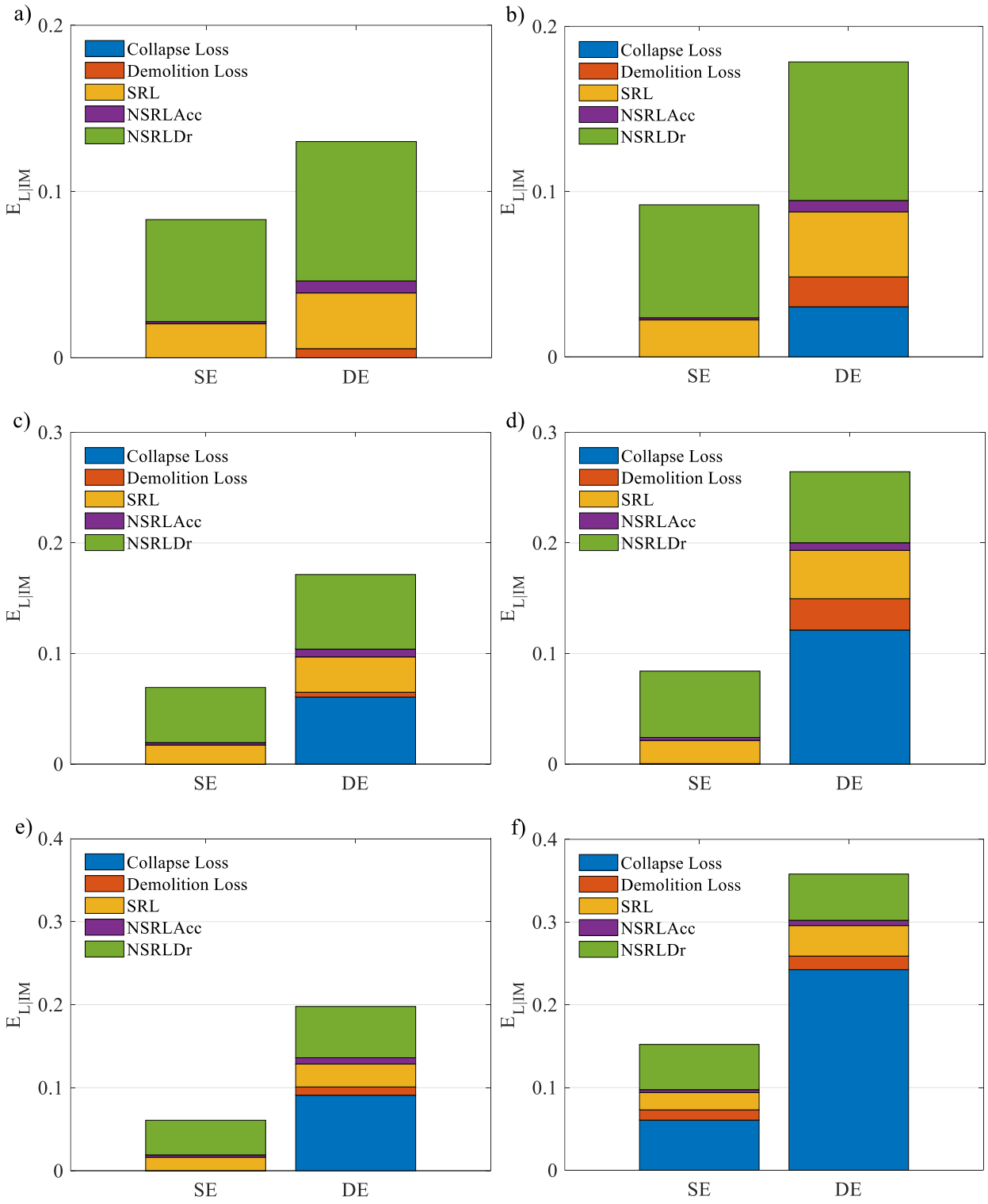

Figure 5-8. Expected economic loss: a) F3-N; b) F3-P; c) F6-N; d) F6-P; e) F9-N; f) F9-P.

In all frames, as the seismic intensity increases above the DE threshold, the repair cost of non-structural drift-sensitive components loses its predominance and structural, demolition, and

collapse losses start to dominate the total economic loss. For instance, when examining the total normalized loss of F3-P at two times the DE level intensity, it is observed that losses due to collapse, demolition, structural damages, non-structural damages to acceleration-sensitive components, and non-structural damages to drift-sensitive components are 0.303, 0.071, 0.090, 0.009, and 0.064, respectively. This observation agrees with the earthquake-induced loss performance of SMRF and Eccentrically Braced Frame (EBF) buildings reported in prior studies [16, 18]. As shown in Figure 5-7, for each design approach, collapse loss starts to dominate the economic loss at smaller seismic intensities as the building height increases. The reason is that for a given seismic intensity, the probability of collapse of a taller building is higher, as discussed earlier.

Referring to Figure 5-8, the total normalized economic loss experienced by the NBC frames is, on average, 0.07 and 0.17 at SE and DE hazard levels, respectively. These average values increase to 0.11 and 0.27 in PBPD frames. This suggests that NBC frames are likely to experience smaller total economic losses for a given number of stories than those designed per PBPD methodology. This can be attributed to their higher seismic demands in design, which favoured higher collapse capacities and lower collapse probabilities. Also, the contribution of collapse loss to the total normalized economic loss is almost zero at SE intensity for all frames except F9-P, which exhibited the poorest behaviour. At the DE intensity level, however, the contribution of collapse loss increases appreciably from an average of 0.05 in NBC frames to an average of 0.13 in PBPD frames. In contrast, the contribution of other components of economic loss remains almost the same. Overall, PBPD frames offer a weaker earthquake-induced economic loss performance than the MKFs designed according to the conventional seismic design method.

Another interesting observation from Figure 5-7 and Figure 5-8 is that demolition loss is smaller than collapse loss for all seismic intensities. For example, the normalized loss of F6-P at the DE level due to collapse and demolition are 0.121 and 0.028, respectively. This stems from the fact that the seismic intensities that do not result in structural collapse according to the criteria set in this study, i.e., a maximum SDR of 5% or non-convergence of the NLRHA, often lead to small peak RSDRs, usually under 1%, that are correlated with small probabilities of having to demolish the building (see Figure 5-4). In other words, the chances for the building to either collapse or be repaired and reoccupied in the aftermath of a seismic event is higher than the likelihood of having to demolish it. Had the local collapse threshold been set to a more relaxed value, such as a maximum SDR of 10%, the prototype buildings would have been allowed to undergo more significant lateral deformations without experiencing collapse. This would have resulted in much larger RSDRs, higher probabilities of demolition, and, therefore, larger demolition and smaller collapse losses. However, this is deemed a liberal assumption contradicting the findings of previous studies, which confirmed that knee-braced structures should be considered to have reached the incipient stage of total collapse at maximum SDRs of 5 to 6% [35, 37, 38].

In order to evaluate the distribution of seismic-induced demands on the prototype buildings under DE hazard level, the key seismic response parameters, including PFA, peak SDR, and RSDR, were obtained from the NLRHAs performed under the scaled ground motion accelerations. The amplitude of the ground motion accelerations was magnified by a factor of 1.05 to account indirectly for the influence of accidental torsion. The storey drift ratio was obtained as a ratio of the difference between the horizontal displacements of two consecutive floors and the storey height. The final storey drift ratios when the structure has come to rest after the free vibration phase

were recorded as the RSDR. Moreover, horizontal absolute floor accelerations were recorded at the top of the left exterior column at each storey (see Figure 5-1b) to obtain PFAs.

Figure 5-9 and Figure 5-10 present the PFA, SDR, and RSDR of the prototype buildings at the DE hazard level. As shown in Figure 5-9, 3-storey and 6-storey frames, designed to NBC and PBPD approaches, exhibit almost similar median PFA values, ranging between 0.75 and 0.80 g for the 3-storey frames and 0.62 to 1 g for the 6-storey frames. However, the difference between the 84th percentile PFAs of NBC frames and that of PBPD frames is more noticeable. For instance, the 84th percentile PFA of F3-P varies between 1.15 and 1.23 g, while this parameter is in the range of 1.24 to 1.48 g for F3-N. The PBPD approach generally leads to lower PFAs than the NBC method. This observation can be linked to the higher lateral stiffness of NBC frames, as confirmed by the pushover results of a previous study [113].

Figure 5-10 indicates that NBC frames, in general, experience lower peak SDRs than PBPD frames. For example, F6-N results in peak median SDRs that are, on average, 8% smaller than those observed in F6-P. Considering the 84th percentile curve as a more conservative measure of the seismic response, all frames reach a peak SDR smaller than or very close to the 2.5% limit prescribed by the 2020 NBC for normal importance category buildings, except for the F6-P, which marginally exceeds this limit with a maximum of 2.7% on the second floor. However, the median peak SDRs are lower than 2.5% in all frames, indicating that both design methodologies result in an acceptable peak SDR under design earthquake hazard level owing to sufficient built-in lateral stiffness of the MKF system as confirmed by previous studies [113, 144]. Figure 5-10 shows a similar pattern for RSDRs, with the PBPD frames having significantly larger RSDRs than the NBC frames. For instance, the PBPD approach results in 84th percentile RSDRs that are, on average, 100% greater than those observed for the frames designed as per NBC. Overall, the distribution of

median RSDRs along the frame height, particularly for 6- and 9-storey frames, is more uniform in NBC design.

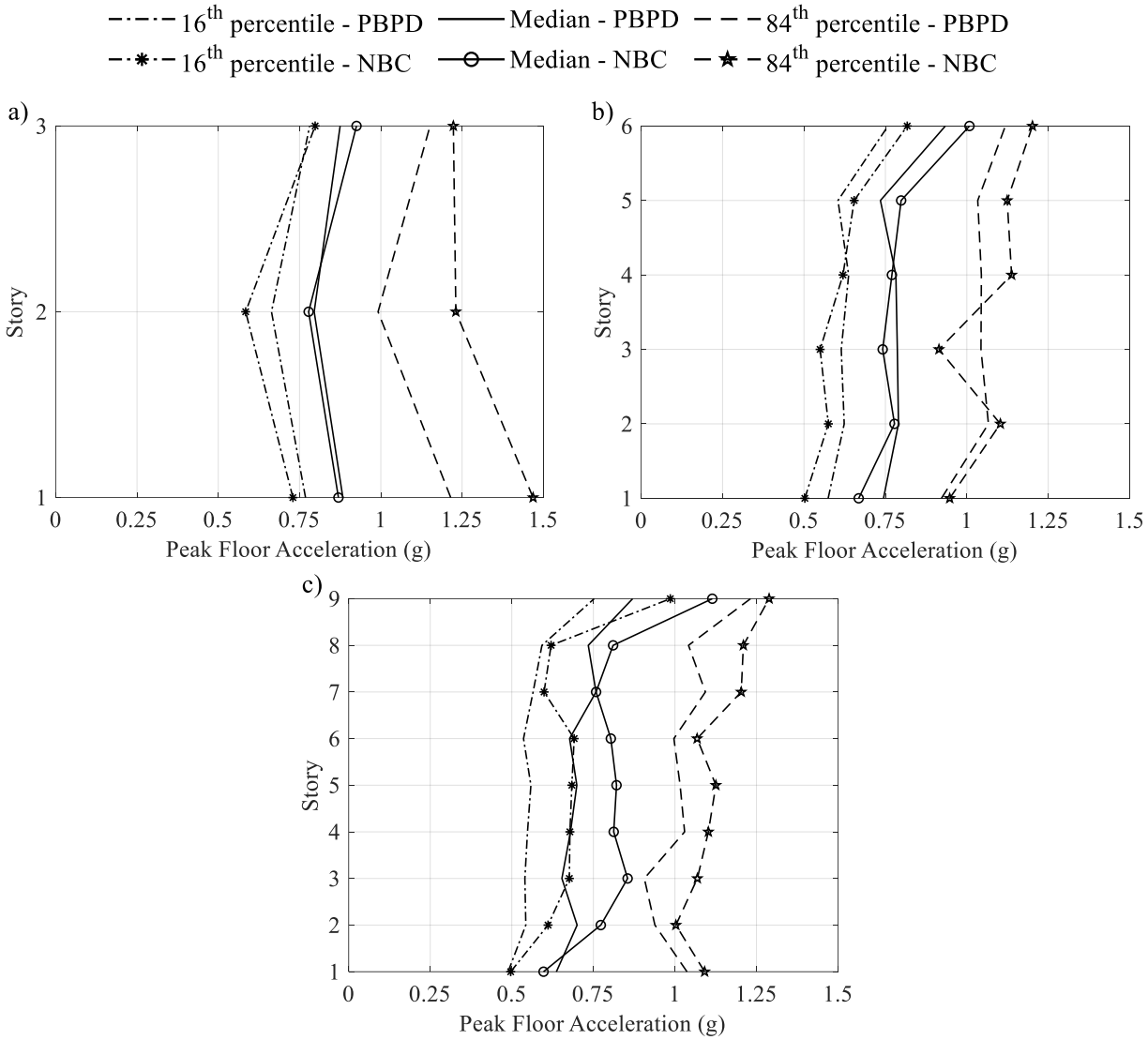

Figure 5-9. Profiles of PFAs under DE hazard level: a) Three-Storey Frames; b) Six-Storey Frames; c) Nine-Storey Frames.

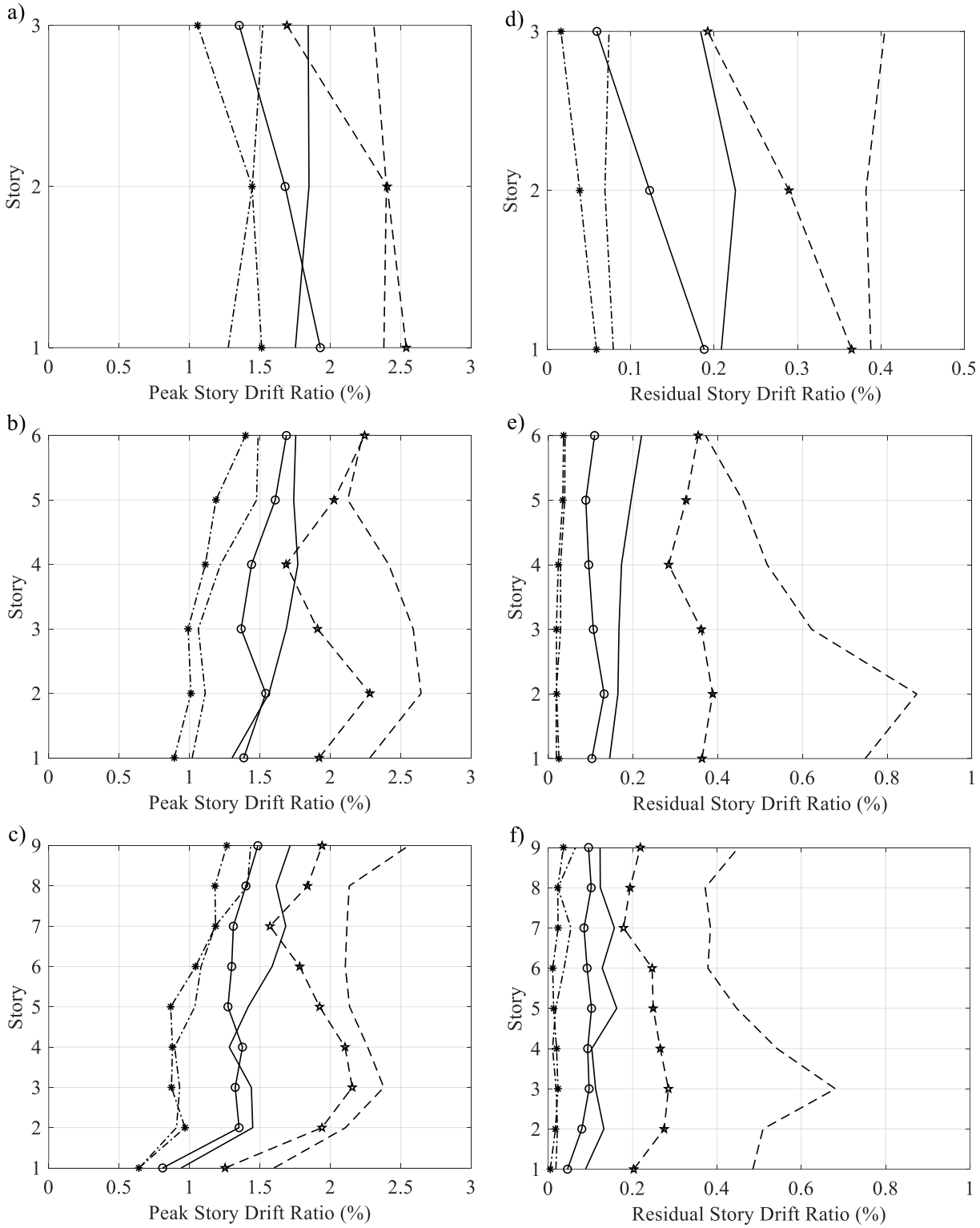

Figure 5-10. Profiles of peak SDRs and RSDRs under DE hazard level: a) SDR of Three-Storey Frames; b) SDR of Six-Storey Frames; c) SDR of Nine-Storey Frames; d) RSDR of Three-Storey Frames; e) RSDR of Six-Storey Frames; f) RSDR of Nine-Storey Frames.

McCormick et al. [154] found that a steel structure can be deemed repairable and safe for the occupants in the aftermath of earthquake events, provided that the maximum RSDR along the height is limited to 0.5% (or 0.005 radians). In all MKFs studied here, the maximum values of median RSDRs along the height are limited to values slightly exceeding 0.2% under design-level earthquakes, indicating that demolition may not be a significant repercussion of design-level earthquakes in buildings with the MKF system. However, if the possibility of having to demolish the building were to be conservatively assessed based on the 84th percentile values of RSDRs, F6-P and F9-P would fail to satisfy this criterion due to experiencing maximum RSDRs of 0.87% and 0.68%, respectively.

5.8. Expected annual loss

The expected annual loss is used in this study as an average measure to further assess the economic loss of MKF buildings due to the earthquake hazard. Figure 5-11a shows the site-specific hazard curves associated with 5%-damped first-mode spectral acceleration at the prototype frames' fundamental period, representing the annual probability of exceeding a specific intensity measure. These curves were obtained using the 2020 NBC Seismic Hazard Tool [25] and the United States Geological Survey (USGS) NSHM Hazard Tool [129]. Since the seismic hazard curves are only available for a limited number of structural periods, the values for other first-mode periods were established using linear interpolation in log-log space.

The EAL is calculated by combining the susceptibility of a building to damage under earthquakes with the probability of occurrence of different hazard levels (see Eq. (5-9)). This approach takes into account both the frequency of ground motions and losses associated with the building. While more frequent earthquakes may result in less overall damage and economic loss, they have a higher

probability of occurrence. Conversely, less frequent but more severe earthquakes representing high intensities are less likely to occur but would likely result in much greater damage and loss.

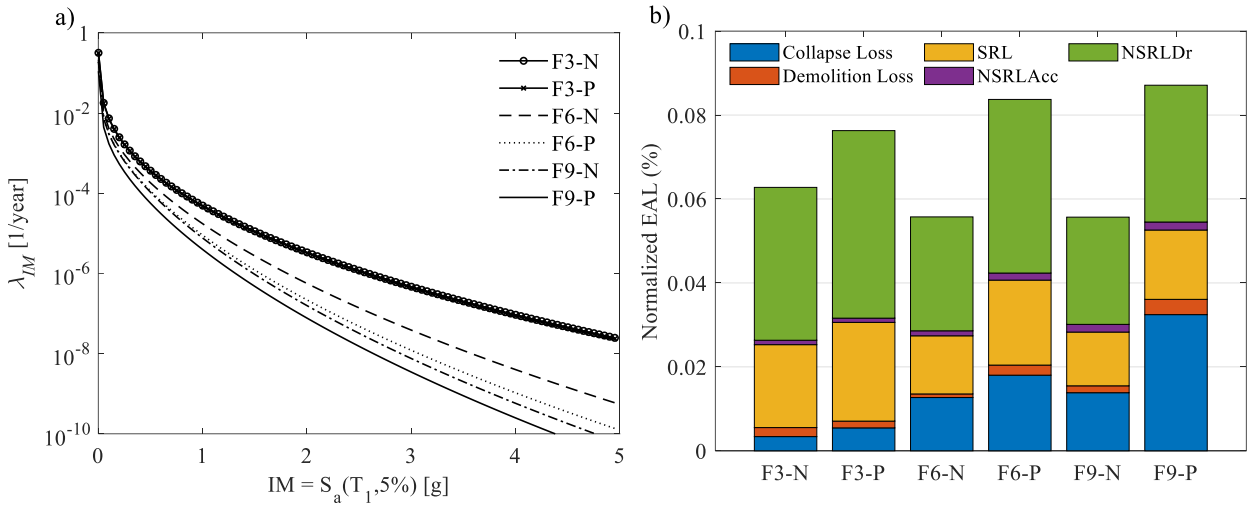

Figure 5-11. a) Site-specific hazard curves of the prototype frames for the selected site; b) Expected Annual Loss of the prototype buildings.

Figure 5-11b shows the estimated EAL of the prototype buildings as a percentage of the total building replacement cost. Although the SMRF and EBF buildings investigated in [16, 18] were designed and evaluated for the seismic hazard of and earthquake sources in California, which are different from those considered in this study, a comparison between the results reveals that the overall EAL is relatively low for all the MKFs studied here. For example, according to Table IV in [16], the total normalized EAL of an 8-storey SMRF with a strong column-weak beam ratio larger than 1.0 is 0.51% based on a numerical model that takes into account both the influence of composite beam effects and the internal gravity framing system contributions. Moreover, the total normalized EAL of an 8-storey EBF building in [18] is approximately 0.6%. Taking a comparable MKF building, F9-P, for comparison, the total normalized EAL was obtained as 0.09%. This difference can be partly attributed to the fact that the slope of the site-specific hazard curves in the site of interest in this study sharply declines to almost zero at seismic intensities around ~1g, which limits the range of effective

Ims within which seismic activities have the most significant impact on the EAL. This reduces the contribution of Ims exceeding ~1g to the total EAL values. This observation agrees well with the λ_c deagreggation results shown in Figure 5-6b. Another possible reason is the fragility parameters used in the loss assessment of acceleration-sensitive components.

As shown in Figure 5-11b, the repair cost of non-structural drift-sensitive elements is the primary contributor to the EAL in all MKF buildings, contributing, on average, 51% and 49% to the total normalized EAL in NBC and PBPD designs, respectively. An exception to this observation is F9-P, where the collapse loss has the highest contribution with an amount of 0.032. On the other hand, losses due to demolition and acceleration are almost negligible in all cases. The contribution of economic loss due to the damage sustained by non-structural acceleration-sensitive components to the total normalized EAL is, on average, 2.3% and 1.8% for NBC and PBPD designs, respectively. Furthermore, demolition composes an average of 2.6% and 3.0% of the total normalized EAL of the buildings designed to NBC and PBPD, respectively. Structural loss is ranked second in contribution (31%) to the total normalized EAL of F3-N and F3-P. Nonetheless, collapse loss comprises the second largest proportion of the EAL for F6-N, F6-P, and F9-N, with respective contributions of 23%, 22%, and 25%. These observations are consistent with the fact that non-structural and structural component repairs govern the economic loss of the 3-storey MKF buildings because of the likelihood of more frequent earthquakes up to the DE hazard level. In contrast, collapse and non-structural repair losses play the most significant role in the total economic loss of 6-storey and 9-storey buildings at more frequent seismic intensities, as shown in Figure 5-7.

A comparison between the design procedures indicates that the contribution of collapse loss to the EAL is greater in the PBPD buildings as opposed to the NBC buildings, on average by 24%. As

the building height increases, the contribution of collapse loss to the EAL increases significantly in the PBPD buildings, but this increase is not as pronounced in the NBC buildings. Moreover, the total EAL of NBC design is smaller than that of PBPD for a given number of stories. For example, the total normalized EAL is 0.06% for F3-N and 0.08% for F3-P. Overall, the frames designed in accordance with the NBC exhibit superior performance in terms of EAL when compared to those designed using the more advanced PBPD procedure. A similar trend was observed in the loss vulnerability curves.

5.9. Conclusion

This study aimed to quantify and assess the earthquake-induced economic loss performance of buildings designed using the recently proposed steel Moment-resisting Knee-braced Frame system. An office building located in Vancouver, BC, a high seismic region in southwestern Canada, was selected. A total of six prototype buildings were designed by varying the total height: 12.3 m for the 3-storey building, 24.3 m for the 6-storey, and 36.3 m for the 9-storey buildings, and the design methodology, encompassing the conventional forced-based procedure prescribed by the NBC of Canada and performance-based plastic design method. A planar fibre-based numerical model of the buildings, including one of the MKFs and an equivalent gravity bay representing the interior gravity system, was developed in the *OpenSees* program to perform incremental dynamic analyses at different seismic intensities. The results of IDAs were used to obtain the EDPs necessary for the economic loss evaluation over a range of intensity measures up to the collapse point. A simplified storey-based loss estimation methodology that directly accounts for the economic losses due to demolition was implemented to evaluate the seismic loss performance of the prototype buildings. The economic loss estimation procedure considered the buildings' key structural and non-structural components expected to be damaged under lateral

seismic loads. EAL, representing the average annual economic loss resulting from seismic-induced damages, was finally computed to gain further insight into the seismic loss performance of the MKF system. The main findings of this study are summarized as follows:

- Among the prototype buildings studied here, an increase in the total height decreases the median collapse intensity and collapse margin ratio (CMR). The average CMR for 3-storey buildings is 2.63, while this value decreases to 1.86 and 1.70 for the 6-storey and 9-storey buildings, respectively. This observation can be attributed to damage localization and premature collapse due to P-Δ effects.
- All frames offer a CMR larger than 1.0, ranging from 45% to 185%, depending on the frame height and design methodology, indicating a sufficient margin of safety against collapse under design-level seismic hazard.
- The annual probability of incipient collapse is 0.38×10^{-4}, 1.03×10^{-4}, 1.16×10^{-4}, 0.55×10^{-4}, 1.58×10^{-4}, and 2.88×10^{-4} for F3-N, F6-N, F9-N, F3-P, F6-P, and F9-P respectively. These values are smaller than the NBC annual probability of collapse limit of 4×10^{-4}.
- The annual probabilities of collapse computed for the MKF buildings designed in accordance with the NBC guidelines reaffirm, within the scope of this work's assumptions and limitations, the adequacy of the ductility- and overstrength-related force modification factors proposed in a past study [144] for the MKF system.
- For all prototype buildings, non-structural repair costs of acceleration-sensitive components are negligible compared to other components of the total economic loss. The economic loss is governed by non-structural repair costs of drift-sensitive components up to the SE level.

- For F3-N, F3-P, and F6-N, the repair cost of non-structural drift-sensitive elements remains the governing economic loss component up to the DE level. For example, the normalized repair cost of non-structural drift-sensitive elements for F3-P at the DE intensity level is 0.084, constituting 47% of the total normalized economic loss, which is equal to 0.178. The collapse loss for taller buildings, F6-P, F9-N, and F9-P, however, overtakes the repair cost of non-structural drift-sensitive elements somewhere between the SE and DE intensities and becomes the primary contributor to the total economic loss at the DE level.
- By increasing the seismic intensity above the DE level, structural, demolition, and collapse losses start to become more pronounced compared to non-structural repair costs. For most of the buildings studied, the economic loss is governed by the collapse loss beyond the DE intensity. For instance, at two times the DE level intensity, losses due to collapse, demolition, structural damages, non-structural damages to acceleration-sensitive components, and non-structural damages to drift-sensitive components of F3-P are 0.303, 0.071, 0.090, 0.009, and 0.064, respectively.
- For a given number of stories and seismic intensity, the PBPD design results in a greater normalized total loss than the NBC design (on average, 0.11 and 0.27 vs. 0.07 and 0.17 at SE and DE hazard levels), which indicates that the NBC design approach likely improves the seismic loss performance of MKF buildings. This finding also holds for the EAL parameter.
- Given the relatively small median RSDRs of the prototype buildings, which range between 0.05 and 0.22%, it is high unlikely that MKF buildings studied here need to be demolished in the aftermath of design-level earthquakes.

- In all frames except F9-P, EAL is governed by the repair costs of non-structural drift-sensitive components. On average, 51% and 49% of total normalized EAL in NBC and PBPD frames, respectively, are due to the repair costs of non-structural drift-sensitive components.
- Overall, the 9-storey MKF building designed based on the PBPD methodology exhibited the poorest collapse and loss performances compared to the 9-storey MKF building designed to the NBC method and all shorter buildings. Future studies should further evaluate and improve the seismic collapse and earthquake-induced loss performances of tall (e.g., > 9 stories) MKF buildings.
- Considering all response metrics evaluated in this study, multi-storey buildings equipped with steel MKFs showed promising seismic collapse and earthquake-induced loss performances for application in high seismic regions.

This study neglected the bi-directional effects of earthquakes and resulting damages in the non-structural and structural components. Future studies should investigate these effects using three-dimensional numerical models of MKF buildings under bi-directional ground motions. Moreover, the seismic-induced economic losses computed for the prototype buildings can be heavily affected by the component fragility data specified in Table 5-3. As more experimental data become available for various structural and non-structural components of a typical steel-framed building, in particular those using the MKF system, more refined component fragility data should be used to improve building-specific loss estimations.

CHAPTER 6

WIND PERFORMANCE EVALUATION OF MID-RISE STEEL MOMENT-RESISTING KNEE-BRACED FRAME STRUCTURES

Abstract: This chapter evaluates the response of steel Moment-resisting Knee-braced Frame (MKF) structures under serviceability, design and beyond design-level wind loads. Specifically, lateral deformations and floor accelerations at the serviceability level, storey shears and member forces at the ultimate level, and collapse response of the structure under severe wind loads are examined. A 12-storey office building located in a low-seismic region in Canada is selected and designed under gravity plus wind loads. Wind pressure time histories obtained from wind tunnel testing of small-scale rigid models are extracted from the Tokyo Polytechnique University database and then scaled in time and intensity to match the characteristics of the selected building. The wind performance evaluation of the MKF system is conducted using the numerical model of the frame under wind pressure time histories. The results show that the steel MKF system offers appreciable reserve strength under wind loads, meets the code-specified serviceability requirements and motion comfort criteria, and is highly unlikely to collapse under severe windstorms expected in eastern Canada.

6.1. Introduction

Wind-induced actions can apply complex pressure profiles on buildings, resulting in lateral and vertical forces that need to be properly estimated and used to size the lateral load-resisting system (LLRS) of the building and other structural and non-structural components subjected to wind loading. Traditionally, wind loads for the design of buildings are determined using either code-prescribed static and dynamic methodologies or by conducting experiments on small-scale models in a wind tunnel. As per the National Building Code (NBC) of Canada [4], the static procedure may

be used when the building is not dynamically sensitive, defined as a building that meets the following three conditions: 1) its fundamental period is less than 1 second, 2) its total height is less than 60 m, and 3) its total height is less than 4 times its minimum effective width. For the design of cladding and secondary structural elements, the NBC prescribes either static or wind tunnel procedures. The specified wind pressure in the NBC for the strength design of the Main Wind Force-Resisting System (MWFRS) corresponds to a return period of 50 years; however, the design wind pressure referred to as Ultimate Limit State (ULS) demand, which is defined as 1.4 times the specified wind pressure, represents a longer return period of approximately 600 years corresponding to 9.5% probability of exceedance in 50 years. While the MWFRS is anticipated to remain elastic under the NBC design wind load when adhering to prescribed design requirements in this standard, evaluating the structural performance of the MWFRS under a more realistic wind pressure history offers insight into the dynamic response of the system under wind loading. Additionally, it helps quantify wind-induced demands in various structural elements to achieve an economical and functional design under wind [86]. This is particularly crucial for new MWFRSs, such as the Moment-resisting Knee-braced Frame (MKF) proposed by the authors for multi-storey buildings. Furthermore, future building codes may require a higher return period for ultimate limit states, emphasising the need for the evaluation of the collapse performance of MWFRSs under wind [85]. More importantly, the emergence of Performance-Based Wind Design (PBWD) methodologies, e.g., the ASCE Prestandard for PBWD, facilitates the development of controlled inelastic response or the utilization of the inherent overstrength and reserve capacities in structural systems. This enables more economical MWFRS designs provided that the integrity of the building envelope, non-structural components, and the structural system is not compromised. In view of this, a systematic investigation of the lateral

response of MKF as a viable MWFRS, including its strength and deformation capacities, local member response and system-level collapse response, is required.

The PBWD methodology has been introduced as an advanced wind analysis and design technique for evaluating the performance of both structural and non-structural elements, which aims to enhance the overall response and behaviour of structures under wind loads by addressing multiple criteria such as occupant comfort and functionality. In the past, various performance levels and corresponding acceptance criteria have been proposed, covering considerations ranging from the serviceability level to potential nonlinear deformations [87, 88, 155].

A relatively large body of knowledge was produced, particularly in the last decade, with a focus on the performance of various MWFRSs [64, 66-68, 78-84]. Van de Lindt and Dao [64] quantified the occurrence of failures due to wind loads in low-rise wooden structures at different performance levels by employing the collapse fragility concept. Spence and Kareem [65] introduced a probabilistic framework that aims at optimizing the design of structures that experience wind-induced excitation. The possibility of reducing wind-induced force demands for general single-degree-of-freedom (SDOF) systems was evaluated by taking advantage of ductility, which resulted in a simplified method to estimate the nonlinear capacity of such systems [69]. A PBWD methodology for quantifying wind hazards and nonlinear behaviour of steel LLRSs plus a framework consisting of respective performance objectives were proposed by Griffis et al. [70]. The goal of their study was to evaluate the nonlinear response of steel structures beyond the design-level wind loads by defining multiple performance objectives. Judd and Charney [156] examined the inelastic response and collapse performance of multiple steel and reinforced concrete LLRSs simulated as SDOF bodies under wind loads using FEMA P695 methodology. The performance of a 10-storey office building with steel MRFs subjected to lateral wind loads was studied in terms

of life safety, occupant comfort, and economic losses [72, 73]. It was found that service-level wind loads may not affect the habitability of the building, while strength- and near-collapse-level windstorms can result in damage to cladding and structural components. Spence et al. [74] proposed a methodology to mitigate structural and non-structural damages and applied the theory of dynamic shakedown to capture the post-yield response of a five-storey steel MRF. Using a three-dimensional nonlinear finite element model, Mohammadi et al. [75] evaluated the performance of an existing 47-storey steel MRF building by estimating performance levels in the structural members and cladding. The results revealed that the building exhibits significant reserve capacities but fails to meet some of the serviceability performance criteria under various levels of wind loading. Ghaffary and Moustafa [63] evaluated the performance of a 20-storey building under different wind hazards up to the collapse point. It was found that current code-prescriptive design methodologies may result in overly conservative structural designs, and a performance-based design approach can be used instead by taking advantage of a controlled nonlinear response under extreme wind events to achieve a more economical design while maintaining an acceptable level of safety and non-structural component performance. Athanasiou et al. [76] studied the nonlinear response of a 15-storey hospital building comprising moderately ductile steel concentrically braced frames in Montreal, Quebec, under wind and seismic loads. It was shown that wind events lead to a higher annual probability of failure compared to earthquakes. The study proposed a multi-hazard assessment methodology to address the challenges faced in the design of buildings subjected to both earthquake and wind events, where both are critical. The same authors investigated the possibility of a wind-related reduction factor to reduce the design wind load of tall steel buildings in eastern Canada and found that a wind-related reduction factor of 2 may not noticeably affect the structural performance at the design-level hazard [77]. They also reported an acceptable drop in

the collapse capacity of the studied buildings when designing using the proposed wind-related reduction factor.

This chapter aims to evaluate the performance of multi-storey MKF buildings, at both component and system levels, under lateral wind loads associated with different hazard levels, serviceability, design and beyond design. Specifically, the frame lateral deformations, wind-induced force demands in the main structural elements, wind-induced deformation demands in non-structural components, and occupant comfort criteria are examined under various wind loading intensities. Moreover, the collapse performance of the MKF under wind loads is examined using incremental dynamic wind analyses (IDWAs). The selected prototype building and loading assumptions are first presented, followed by the key design steps under code-prescribed wind demands. Next, the methodology implemented for extracting and scaling wind pressure time histories is described, and details of the nonlinear model developed for performance evaluation are presented. Finally, the response of the MKF, at both system and component levels, under wind load with varying intensities are discussed.

6.2. Selected building and loading

A 12-storey office building located in Toronto, Ontario (43.85 N, 79.38 W), was selected for the wind performance evaluation of the MKF system. This site was intentionally chosen as it represents Seismic Category 2 according to 2020 NBC ($0.2 \leq I_E S(0.2) = 0.239 < 0.35$ and $I_E S(1.0) = 0.06 < 0.1$, where $S(0.2)$ and $S(1.0)$ are the design spectral acceleration at short period 1.0 s, respectively, and I_E is the seismic importance factor) where lateral wind loads often govern the design of the LLRS of mid- to high-rise buildings. The site class consists of a soil profile with an average shear velocity of 700 m/s. The building dimensions in the plan are 24 m × 48 m, as shown in Figure 6-1. The building is assumed to be regular in plan and elevation. The

first storey of the building has a height of 4.3 m, while all upper levels are 4 m high. Steel MKFs [144] and steel concentrically braced frames (CBF) of the conventional construction category are utilized as the LLRS of the building in the long and short directions, respectively. The selection of the conventional construction system with minimum seismic detailing requirements prescribed in the Canadian steel design standard, CSA S16 [3], is deemed reasonable and practical for a building located in low seismic regions. All four bays in the long direction are equipped with the MKF system, while only the interior bay in the short direction is braced using inverted V-type CBFs. One of the MKFs in the long direction was selected for the wind performance evaluation. A braced length ratio of 0.2 and a knee brace angle of 36 degrees were selected as per the recommendations in [113] resulting in beam stub, intermediate beam, and knee brace centre-to-centre lengths of 2.4, 7.2, and 3.0 m, respectively. The elevation view of the selected MKF is illustrated in Figure 6-2.

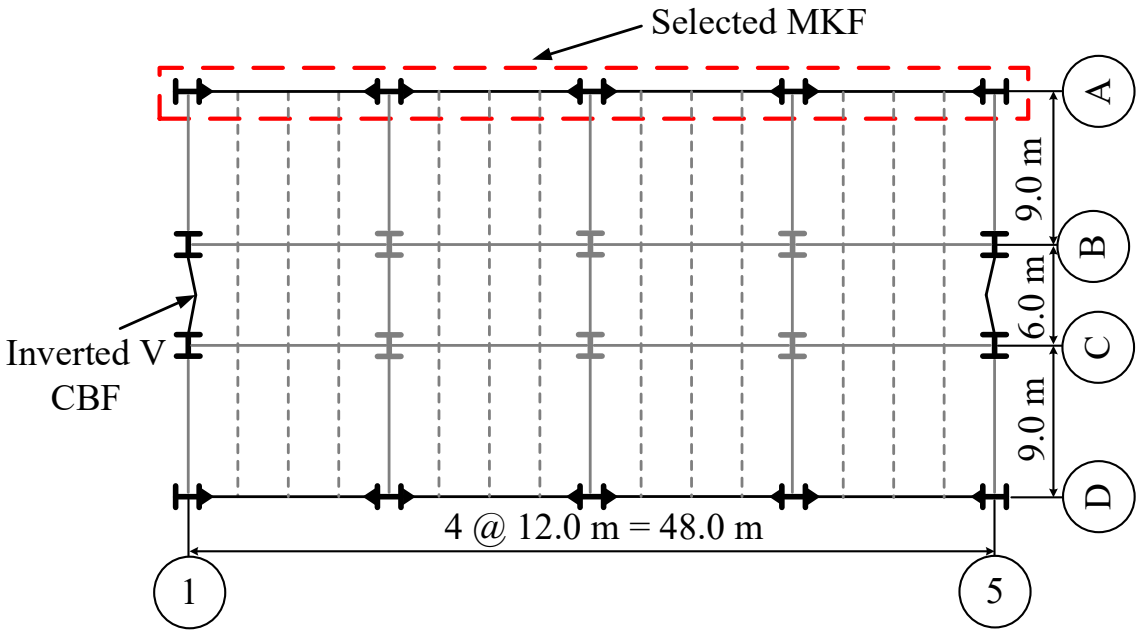

Figure 6-1. Plan view of the prototype building.

The loading was performed as per the 2020 NBC. The roof and floor dead loads are 3.4 kPa and 3.6 kPa (excluding the weight of partition walls), respectively. The unit weight of wall claddings

is 1.5 kPa. Floor live loads and the unit weight of partition walls are 2.4 kPa and 1.0 kPa, respectively. The roof live and snow loads are 1.0 kPa and 1.64 kPa, respectively.

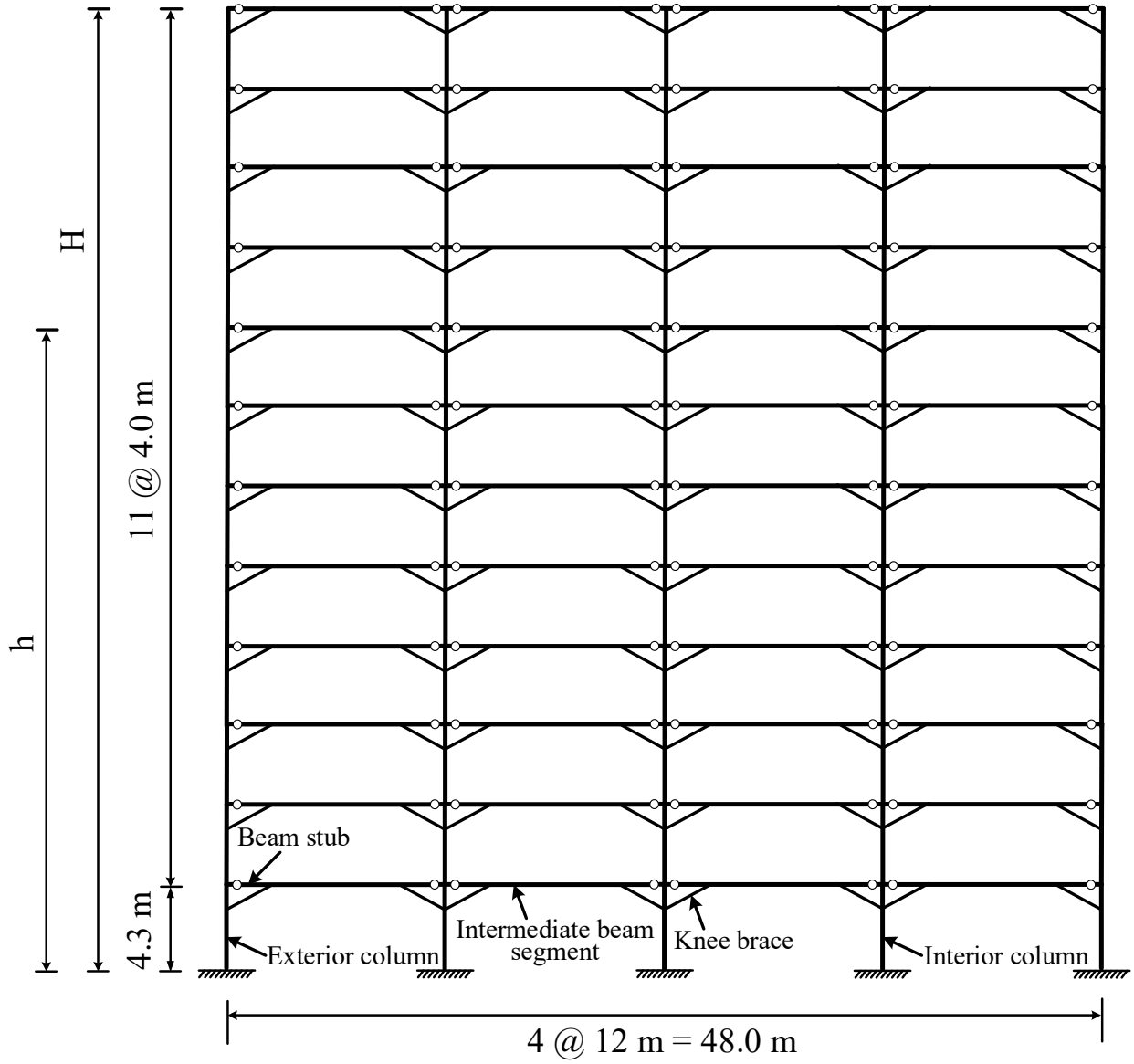

Figure 6-2. Elevation view of the selected MKF.

6.3. Design of the prototype building under wind loading

The fundamental period of the building in the direction of the MKF (Figure 6-1) is 3.22 s, which falls between the 1 and 4 s category of NBC wind design requirements. The building is therefore categorized as dynamically sensitive, and the dynamic procedure shall be used to determine the

design wind pressure. The net design wind load of each floor, also known as drag force, is determined by multiplying the tributary area of the floor in the direction of interest by the net wind pressure p computed as [4]:

$$p = I_W C_t C_g q \left(C_e^{windward} C_p^{windward} - C_e^{leeward} \left(-C_p^{leeward} \right) \right) \quad (6\text{-}1)$$

where I_w is the importance factor for the wind load, q is the 1-in-50 years site-specific velocity pressure, C_t, C_g, C_e, and C_p are the topographic, gust, exposure, and external pressure coefficients, respectively. The topographic factor is equal to 1 in this study since the building is located on a flat surface. For leeward walls, C_e is determined at the mid-height of the building. Additionally, the external pressure coefficient, C_p, is influenced by both the building height, H, and the dimension parallel to the applied wind load, D. When the height-to-width ratio, H/D, exceeds 1.0, like the case study in this research, C_p is set at 0.80 for windward walls and -0.50 for leeward walls. The coefficients C_e and C_g are calculated, for buildings in rough terrain, as:

$$C_e = 0.5 \left(\frac{h}{12.7} \right)^{0.5} \quad 0.5 \leq C_e \leq 2.5 \quad (6\text{-}2)$$

$$C_g = 1 + g_p \frac{\sigma}{\mu} \quad (6\text{-}3)$$

in which h is the reference height, measured from the ground to the level for which the wind load is being computed. The coefficient g_p and σ/μ are the peak factor and a dimensionless parameter, respectively, computed based on Article 4.1.7.8 of 2020 NBC.

For the selected prototype building, wind importance factors of 1.0 and 0.75 were used for the evaluation of the ULS and Serviceability Limit State (SLS) wind loads, respectively. The gust effect factor 3.04 was obtained for the wind load applied on the short side of the building, which is resisted by the two MKFs shown in Figure 6-1. Table 6-1 gives the values of exposure factors

obtained on the windward and leeward surfaces of the prototype building for the wind acting on the short side. The final wind design base shear was computed as 939 kN per the MKF.

Table 6-1. Exposure and pressure coefficients on the windward and leeward surfaces of the prototype building based on 2020 NBC dynamic procedure.

Storey	$C_e^{windward}$	$C_e^{windward}$
12	0.98	0.69
11	0.93	0.69
10	0.89	0.69
9	0.85	0.69
8	0.80	0.69
7	0.75	0.69
6	0.69	0.69
5	0.63	0.69
4	0.57	0.69
3	0.50	0.69
2	0.50	0.69
1	0.50	0.69

To compute the design seismic base shear and seismic forces at the floor and roof levels, the modal response spectrum analysis procedure was used. For conventional construction, the overstrength and ductility-related force modification factors, i.e., R_d and R_o, are 1.5 and 1.3, respectively. The total seismic weight of the building was calculated as 66313 kN, and the seismic importance factor was taken equal to 1.0. The design seismic base shear, including 5% accidental eccentricity, was computed as 390 kN per the MKF. The distribution of lateral seismic (denoted by *E*) and wind storey shears corresponding to the ULS level in the long direction of the building is shown in Figure 6-3 for the prototype MKF. As shown, the lateral wind load governs the design of the MKF selected, except for the last storey, where the difference between the wind and seismic demands is negligible.

A two-dimensional (2D) numerical model of the prototype MKF was created in the SAP2000 program [157] and used to obtain member forces and storey displacements under design and service wind loads, respectively. MKF members were then designed under gravity plus wind-

induced demands in accordance with CSA S16-19. Wide-flange profiles conforming to ASTM A992 with nominal and expected yield strengths of 345 MPa and 385 MPa were used to design intermediate beam segments, beam stubs, and columns. Knee braces were selected from hollow structural sections (HSSs) that conform to ASTM A1085 steel with a yield strength of 345 MPa. Additional details regarding structural design and limit state checks can be found in [113].

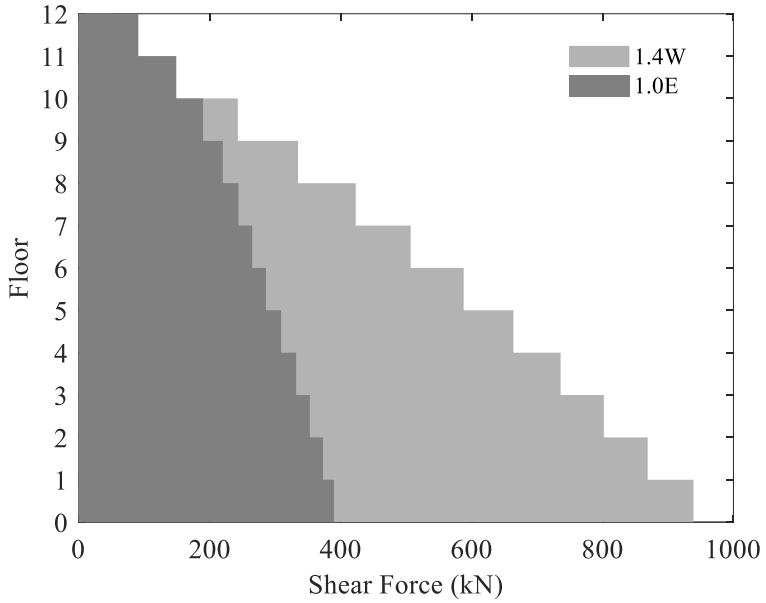

Figure 6-3. Wind loading design forces on the selected MKF (see Figure 6-1).

The wind load corresponding to the serviceability limit state, which represents a velocity pressure with a 10-year return period, was used to verify the lateral deflection of the MKF against the storey drift limit of 0.2% as per the 2020 NBC. The drift limit governed the selection of the final member sizes for most of the structural elements of the selected MKF. Table 6-2 summarizes the final cross-sections selected.

Table 6-2. Member sizes for the selected MKF.

Storey	Beams & Beam Stubs	Knee Braces	Interior Columns	Exterior Columns
10-12	W530×82	HSS127×127×4.8	W610×113	W610×113
7-9	W610×82	HSS127×127×9.5	W610×155	W610×155
4-6	W690×125	HSS152×152×9.5	W690×217	W690×192
1-3	W690×125	HSS152×152×12.7	W690×265	W690×240

6.4. Wind evaluation methodology

The wind performance evaluation in this study encompasses the examination of the response of the steel MKF using WTHA under serviceability, design, and severe wind loads. This section describes the methodology adopted for developing and scaling wind pressure time histories, and the numerical modelling technique implemented for the wind simulation and wind performance evaluation. To evaluate the wind-induced deflections and floor accelerations, dynamic analyses were performed under wind loading time histories scaled to 10-year return periods, which represent the serviceability-level hazard, however, a 600-year return period was selected to examine storey shears, storey drift ratios, residual drift ratios and member forces.

6.4.1. Wind pressure time history

Wind tunnel testing is recognized as the more realistic approach for assessing structures under wind loads, as outlined in the ASCE Prestandard for PBWD. Wind aerodynamic data from wind tunnel tests of sample buildings were obtained from the Tokyo Polytechnique University (TPU) aerodynamic database [26]. These data were used to generate wind pressure time histories required to conduct wind time history analyses (WTHA). The TPU database consists of a collection of dimensionless aerodynamic pressure time history data from wind tunnel testing of small-scale rigid models of low to high-rise buildings with various aspect ratios and exposure conditions. Pressure taps on the surfaces of experimental models were used to record local wind pressure time histories on all surfaces of the building, which were then utilized to derive aerodynamic wind loads for wind response simulations.

A high-rise building model with a geometrical form (Height-Breadth-Depth ratio) similar to the prototype building studied in this chapter was selected from the TPU database. The dimensions of the model tested in the wind tunnel were Height = 0.2 m, Breadth = 0.2 m, and Depth = 0.1 m,

corresponding to an H-B-D ratio of 2-2-1. The dimensions of the reference building in this study, conforming to the wind direction and terminology used in the TPU database, are Height = 48.3 m, Breadth = 48.0 m, and Depth = 24.0 m, associated with an H-B-D ratio of 2-2-1. The pressure distribution pattern observed on different faces of the rigid experimental model would be similar to that expected around the prototype building of this study had the building been placed in an environment with similar surrounding conditions.

The normalized wind pressure coefficient histories, $C_P(t)$, extracted from the TPU database, were first scaled in time by equating the Strouhal number of the prototype building considered in this study to that of the experimental small-scale model following the principles of aerodynamics and past studies [63]:

$$\frac{f_{fs}L_{fs}}{U_{fs}} = \frac{f_{rm}L_{rm}}{U_{rm}} \tag{6-4}$$

where f_{fs}, f_{rm}, L_{fs}, L_{rm}, U_{fs}, and U_{rm} are the sampling frequency, characteristic length, and wind velocity at the roof level of the full-scale building (given with subscript "*fs*") and experimental rigid model (given with subscript "*rm*"), respectively. Using $f_{rm} = 1000$, $L_{rm} = 0.2\,m$ and $U_{rm} = 10.95\,m/s$ for the selected scaled model according to the TPU database, $L_{fs} = 48.3\,m$ as the characteristic length of the prototype building, and U_{fs}, which is determined based on the mean hourly wind speed at 10 m height for any return period of interest based on the relationship provided in Appendix C of 2020 NBC, the sampling frequency of the full-scale building can be determined. This value is then used to estimate the total duration of the scaled wind time history.

Once the wind pressure coefficients are scaled in time, the wind drag force, $F(t)$, at floor *I* on the windward or leeward surfaces of the building is computed as [63]:

$$F^i(t) = \frac{1}{2}\rho U_{ref}^2 C_P^i(t) A_{trib}^i \tag{6-5}$$

in which, ρ is the air density, U_{ref} is the desired wind velocity at the roof level of the prototype building, and A_{trib}^{i} is the tributary area of floor i (or roof) on the windward or leeward surfaces. The pressure tap locations on all surfaces of the small-scale rigid model available on the TPU database are shown in Figure 6-5a. This model was tested for 21 angles of the wind direction ranging from 0 to 100 degrees. In this study, a wind attack angle of 90 degrees was considered as it produces the largest demands on the selected MKF when the wind load is applied on the short side of the building. Figure 6-4 displays the wind attack angles considered with respect to the short and long dimensions of the prototype building. This will be further discussed in Section 6.5.2. Figure 6-5b illustrates the mean wind pressure coefficients on surfaces 1 to 4, from left to right, of the experimental rigid model for a wind attack angle of 90 degrees. Under this loading angle, surfaces 2 and 4 correspond to the windward and leeward surfaces, respectively.

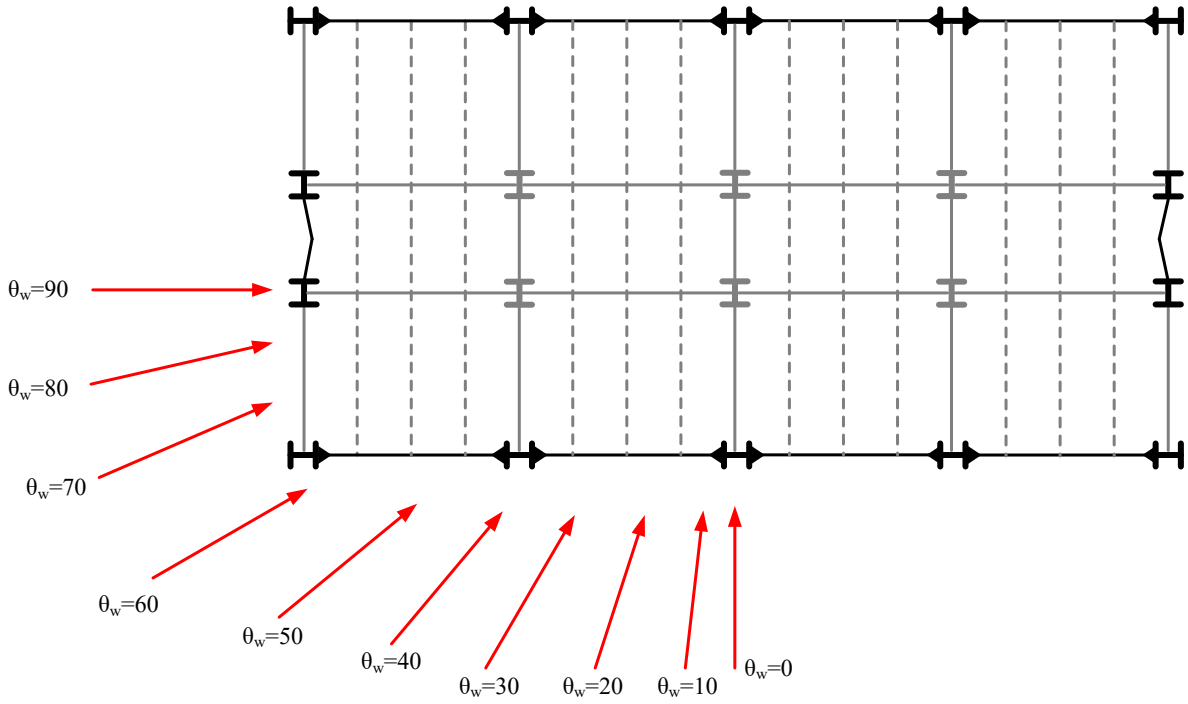

Figure 6-4. Wind attack angles considered in this study.

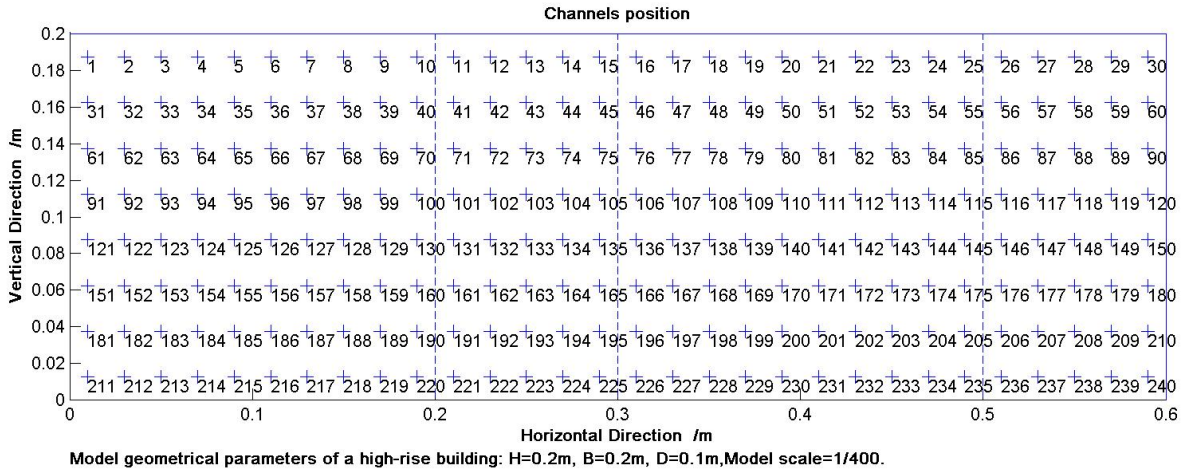

(a)

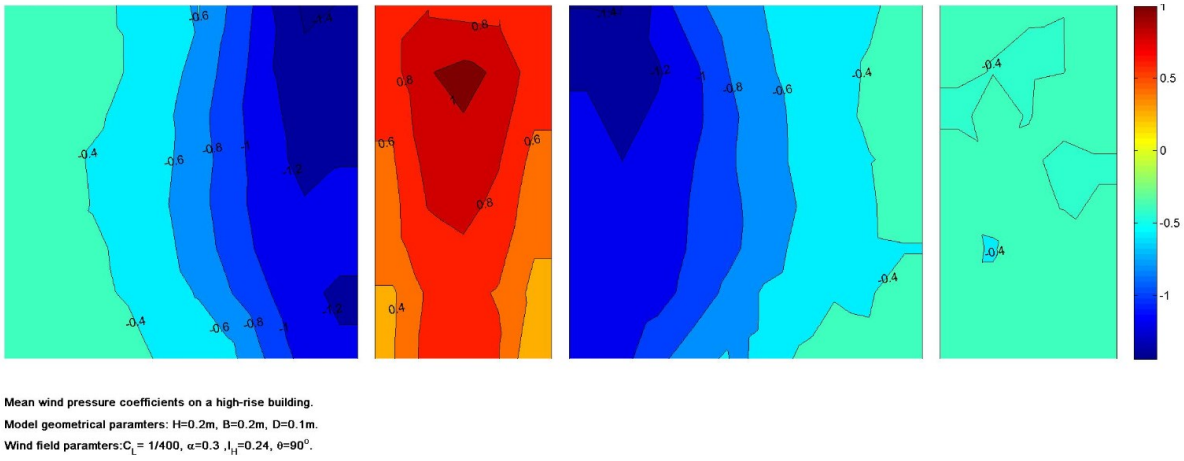

(b)

Figure 6-5. (a) Location of pressure taps on the surfaces of the TPU rigid model with Height = 0.2 m, Breadth = 0.2 m, and Depth = 0.1 m; and (b) Mean wind pressure coefficients on the surfaces of the TPU model under a wind attack angle of 90° [26].

Table 6-3 gives the vertical tributary area and tag numbers of the pressure channels (see Figure 6-5a) used to estimate the windward and leeward drag forces at each floor and the roof. The wind pressure histories acting at each floor, or the roof were calculated by taking the mean of pressure values acting at the pressure taps corresponding to that level. The final wind pressure coefficient histories scaled in time at the design-level hazard are illustrated in Figure 6-6 and Figure 6-7 for the windward and leeward faces, respectively.

Table 6-3. Floor tributary areas and TPU model pressure taps used to estimate wind pressure time histories on the prototype building (see Figure 6-5).

Storey	$A_{trib}(m^2)$	Pressure taps for windward drag forces	Pressure taps for leeward drag forces
12	24	#11-#15	#26-#30
11	48	#11-#15, #41-#45	#26-#30, #56-#60
10	48	#41-#45	#56-#60
9	48	#41-#45, #71-#75	#56-#60, #86-#90
8	48	#71-#75	#86-#90
7	48	#101-#105	#116-#120
6	48	#101-#105, #131-#135	#116-#120, #146-#150
5	48	#131-#135	#146-#150
4	48	#161-#165	#176-#180
3	48	#161-#165, #191-#195	#176-#180, #206-#210
2	48	#191-#195	#206-#210
1	49.8	#221-#225	#236-#240

The wind load was linearly ramped up from zero to the initial value of wind loading histories over a 20 s period to ensure that the response of the frame will not be overestimated due to transient effects [140]. Additionally, the wind load histories were linearly ramped down within 5 minutes to zero from the last point of the pressure history and a 20 s zero pad was added to the end of the wind pressure histories to properly capture the free vibration response.

In this study, the wind-induced torque was neglected because the surrounding environment was assumed to be homogenous and the wind loading direction was considered perpendicular to the building face along the line of symmetry. Moreover, given that little correlation exists between the along- and cross-wind loading directions as discussed in [79], the wind performance evaluation can be performed in two orthogonal uncoupled directions. In this study, only the along-wind response of the selected MKF was evaluated. To examine the collapse performance of the MKF under wind loading, incremental dynamic wind analysis (IDWA), which involves multiple nonlinear dynamic analyses conducted by increasing the intensity of the wind load in each analysis up to the collapse point, was employed here.

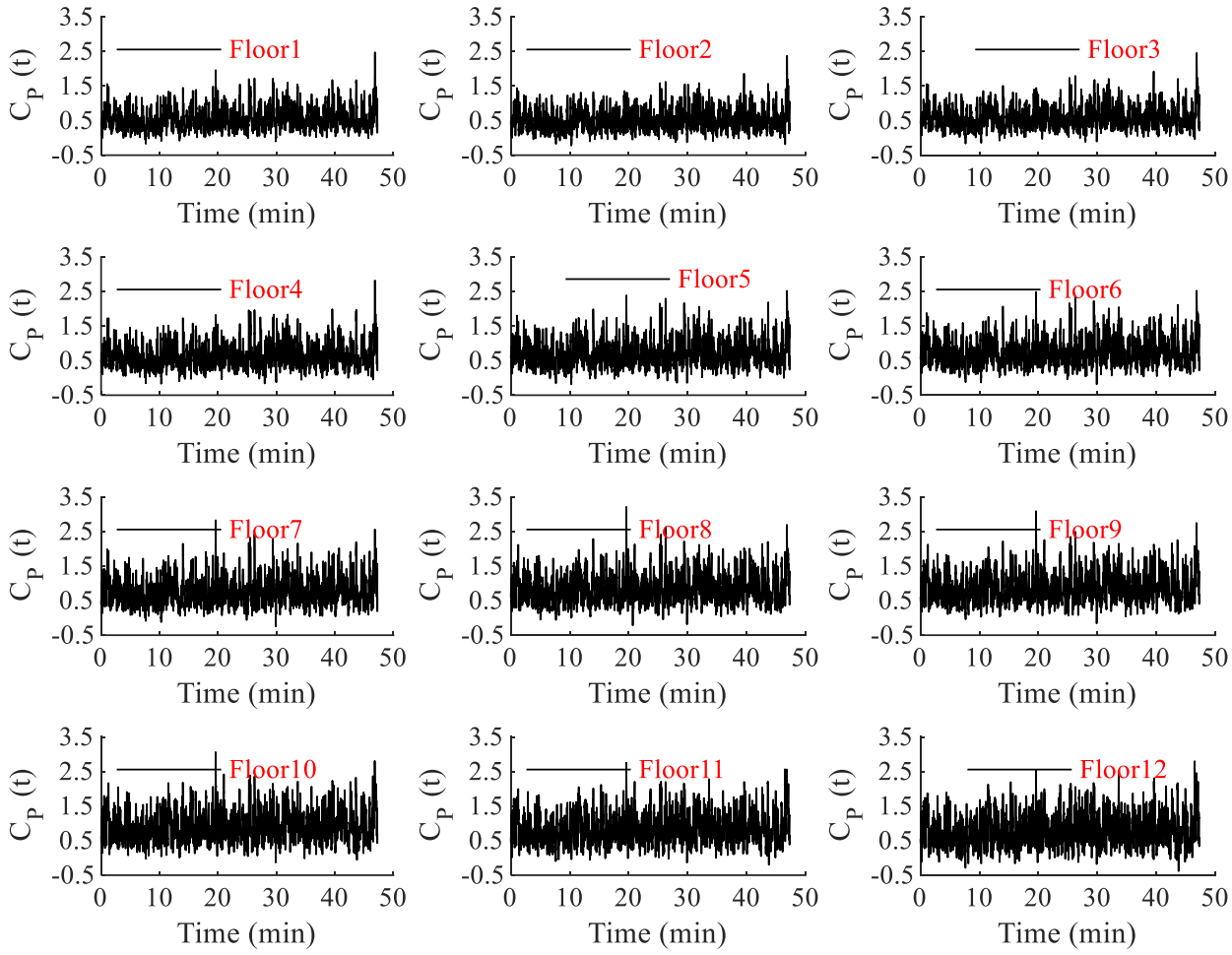

Figure 6-6. Design level wind pressure coefficients for the windward surface of the building under a wind attack angle of 90°.

6.4.2. Wind response simulation

A three-dimensional finite element of the entire building can be developed to ideally apply the wind pressures as a distributed load in the direction of interest across the external walls of the building [76]. However, this approach involves several challenges, including uncertainties in modelling diaphragms and torsional effects, high computational costs, and uncertainties in interpreting potential out-of-plane responses of planar systems. A 2D model of the selected MKF can therefore be used to conduct WTHA and evaluate the global and local force and deformation demands and the collapse response of the MKF when dynamically exposed to design and beyond design-level wind loads. In the 2D model, the lateral wind loads can be approximated as point

loads acting at the roof and floor levels obtained as described in Eq. (6-5). This modelling technique allows for properly assessing the wind performance of the proposed MKF system while achieving a reliable and computationally efficient nonlinear numerical model [76].

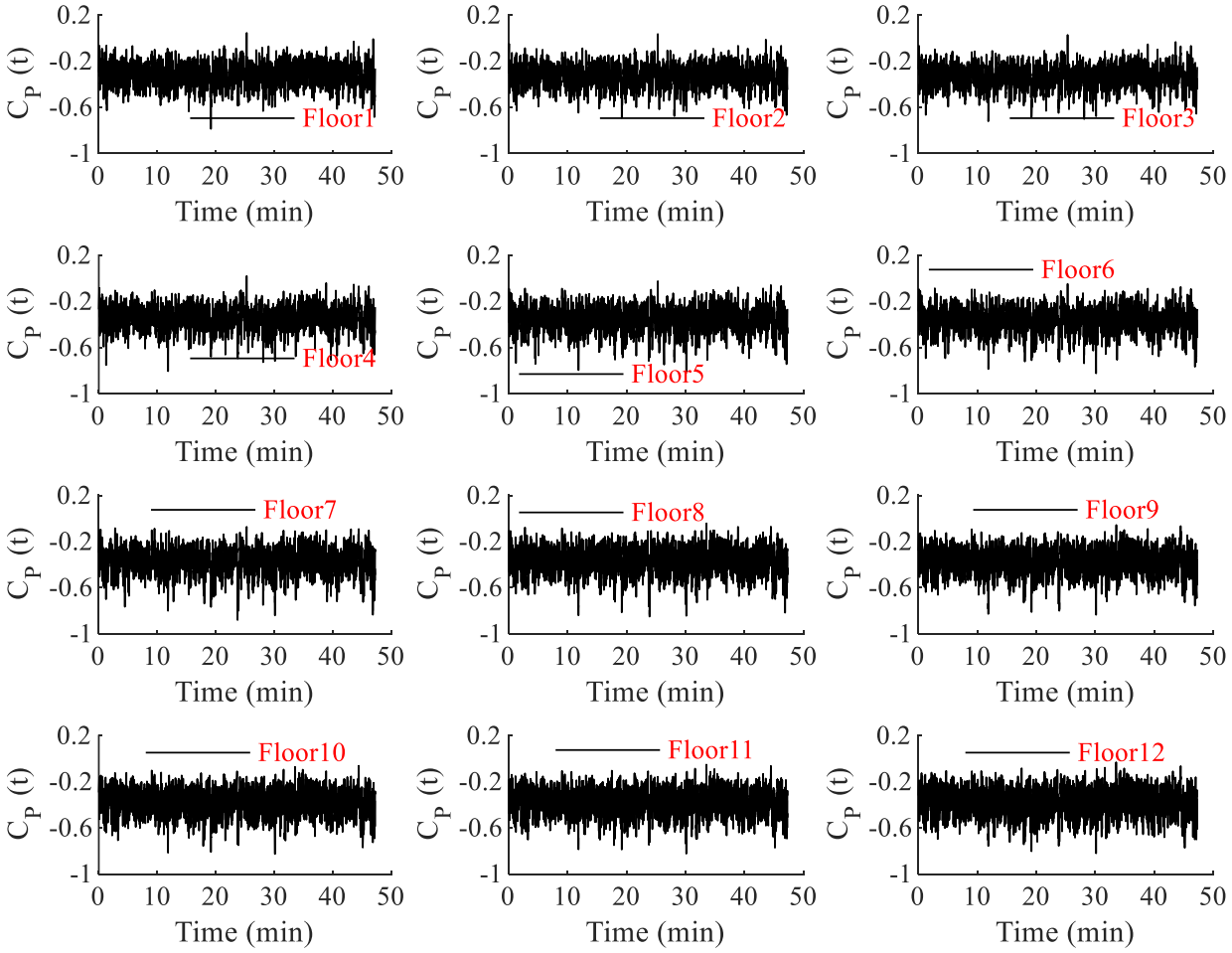

Figure 6-7. Design level wind pressure coefficients for the leeward face of the building under a wind attack angle of 90°.

The structural elements and connections in the LLRSs of the conventional construction category, designed to carry gravity plus seismic-induced forces, such as the MKF in this study, are expected to provide limited energy dissipation capacity through localized yielding and friction that inherently exists in the structure, however, there is no designated element or mechanism that can guarantee such energy dissipation capacity, leading to potential propagation of nonlinear deformations to the locations with high design demands, e.g., ends of intermediate beam segments or column bases.

Under wind loads, MKF members and connections are designed to remain elastic without yielding or instability. However, as described earlier, the prescriptive design methodology does not necessarily guarantee the expected performance of the elements and system under service and design-level demands [75]. This is particularly important for new MWFRSs, e.g., MKF, which are not part of the systems recognized by the NBC, emphasising the need for a more sophisticated numerical model capable of accounting for potential yielding and instability in the MKF structure. Moreover, such a model will facilitate the wind performance evaluation beyond design-level wind loads, which is one of the objectives of this study. To this end, a 2D numerical model of the MKF, capable of reproducing potential nonlinear deformations in the main structural elements carrying the lateral wind load, was developed in the *OpenSees* program [43]. This model is expected to facilitate an inclusive assessment of the MKF under the design wind load where limited nonlinear deformation may develop and allow for a realistic assessment of the wind response beyond the design-level wind. The knee braces, columns, and beam stubs were simulated using nonlinear force-based beam-column elements with fibre discretization of the cross-section and the uniaxial Giuffré-Menegotto-Pinto (Steel02) material model [97]. Modified elastic beam-column elements as described in [99] were used to model the intermediate beam segments. Relatively stiff elastic elements were used to model the rigid-end zones at beam stub-to-column and beam stub-to-knee connections. To trigger potential global instability, initial in-plane geometric out-of-straightness featuring a parabolic distribution and a maximum amplitude of 1/1000 times the member's unbraced length was assigned to column and beam stub elements. A sinusoidal initial imperfection pattern was used for knee braces. Knee brace-to-column and knee brace-to-beam stub connections were modelled as a moment connection representing a direct welded connection between the brace and adjacent members. However, this

assumption would not significantly impact the flexural demands induced in knee braces due to their considerably lower flexural stiffness compared to the beam stubs and columns.

The connections between intermediate beams and beam stubs were simulated as non-seismic (or pre-Northridge) moment connections using a zero-length spring element with the Pinching4 material. The parameters of Pinching4 material model were adjusted to reproduce the hysteretic response of non-ductile steel moment connections given in FEMA P440A [158]. This approach has been implemented in previous similar studies [73]. Figure 6-8 shows the monotonic and cyclic responses of the MKF intermediate beam-to-beam stub connection produced using this methodology with the Pinching4 material parameters given in Table 6-4. In this figure, M_y is the effective yield moment of the intermediate beam segment calculated as $R_{sh}R_yF_yZ_x$, where R_{sh}, R_yF_y, and Z_x are the strain hardening factor taken as 1.1 as per CSA S16, expected yield strength of steel material, and plastic section modulus of the beam section about its strong-axis, respectively, M is the applied moment, and rotation refers to the chord rotation of the connection [73].

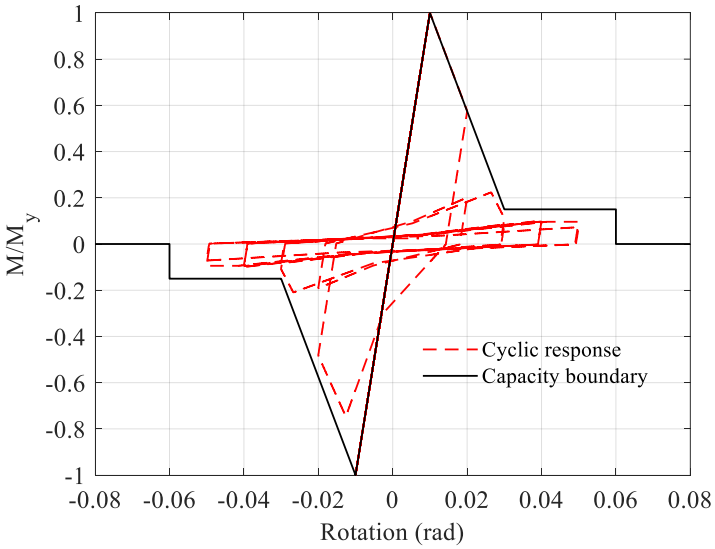

Figure 6-8. Monotonic and cyclic force-displacement responses for a non-ductile intermediate beam-to-beam stub moment connection in the MKF.

The Corotational transformation technique was used to capture geometrical nonlinearity. Second-order P-Δ effects produced by the gravity loads tributary to the prototype MKF were simulated by incorporating a pinned-base leaning column adjacent to the MKF, with rotational degrees of freedom released at both ends of each storey. For modal analysis and simulation of damping, a point mass corresponding to the seismic mass associated with each MKF column was assigned to the top end of the MKF column at each storey. Rayleigh damping approach with mass and stiffness proportional damping coefficient calculated using a critical damping ratio of $\xi = 2\%$ in the first and second structural vibration modes (with the respective periods of $T_1 = 3.22\ s$ and $T_2 = 1.20\ s$) was used to simulate classical damping matrix in WTHA.

The numerical analysis was performed by applying the gravity loads expected to be present in the building during a windstorm (1.25D + 0.5L or 0.5S) to the MKF using a static analysis method followed by either 1) a nonlinear static (pushover) analysis under the load pattern matching the NBC wind load profile by gradually increasing the roof displacement until collapse, or 2) a WTHA by imposing the time histories of the wind load to the roof and floors.

Table 6-4. Pinching4 material model parameters assigned to non-ductile steel moment connections of the MKF based on FEMA P440A [158].

$rDisp^+$	$rForce^+$	$uForce^+$	$rDisp^-$	$rForce^-$	$uForce^-$	gD1	gD2	gD3	gD4	gDLim
0.2	0.4	0.02	0.2	0.4	0.02	0	0.52	0.24	0.24	0.6
gF1	gF2	gF3	gF4	gFLim	gK1	gK2	gK3	gK4	gKLim	gE
0	0.7	0	0.5	0.8	0	0	0	0	0	10

6.5. Wind response evaluation

6.5.1. Global response

The MKF wind pushover curve, normalized wind base shear versus roof drift ratio calculated as the roof lateral displacement divided by the building height, is shown in Figure 6-9. A large overstrength of 5.4 was observed mainly due to the inherent overstrength of the members selected

to satisfy the code-prescribed drift requirement under the service wind load. The overstrength was obtained as the ratio of the maximum base shear using the pushover curve to the design base shear (939 kN) [13, 73]. Strength degradation starts to occur at the roof drift ratio of 1.5% which is 6.7 times the roof drift ratio observed under code-prescribed design wind load.

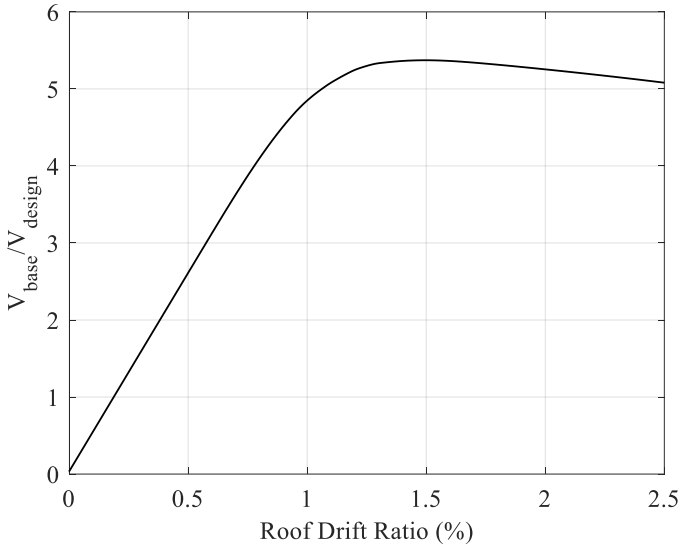

Figure 6-9. Pushover curve and associated overstrength factor under wind.

6.5.2. Deformation response of structural and cladding systems

Figure 6-10a and Figure 6-10b show the profiles of peak storey drift ratios (SDRs) under SLS-level wind time histories and the profiles of storey shears under ULS-level wind time histories, respectively. Wind attack angles (θ_w) varying between 0° and 90° with an increment of 10° were studied. As shown, the wind direction of 90°, which corresponds to the wind pressure applied on the short side of the small-scale rigid model (see Figure 6-5b) in the tunnel test and that of the prototype building (see Figure 6-1), produces the largest relative displacements and wind loads, confirming that this angle is the most critical for the along-wind direction of the prototype MKF studied here. The average maximum base shear obtained under ULS wind loading time histories with different angles is 1064 kN, which is 13% larger than the design base shear (939 kN). This small difference is due to the approximate mapping technique used to relate certain pressure taps

to each story (see Table 6-3). Also, it is expected that the maximum average base shear will converge to the design value when wind load uncertainty is considered by employing multiple wind time histories with different frequency contents. This uncertainty was not studied here and should be investigated in future relevant studies.

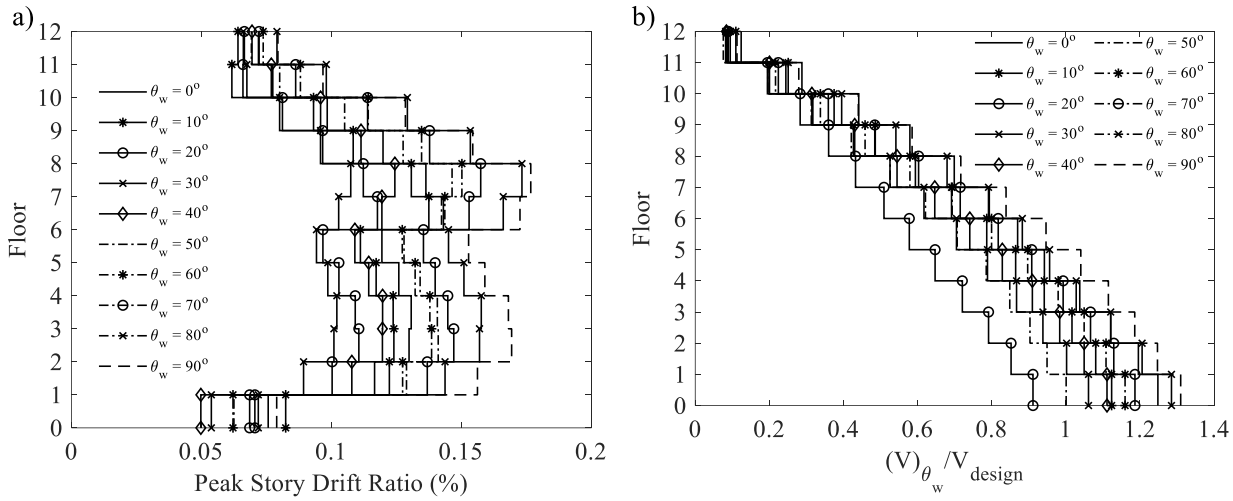

Figure 6-10. a) Profiles of peak storey drift ratios under SLS-level wind hazard; b) Profiles of peak storey shears under ULS-level wind hazard.

The profile of peak storey drift ratios from WTHA is presented in Figure 6-11a. Under frequent wind events (1-in-10 years), the MKF experiences peak SDRs smaller than the limit by 2020 NBC for serviceability and comfort level. The peak SDRs under ULS-level wind hazard satisfy the 1/300 drift limit prescribed by the ASCE Prestandard for Continuous Occupancy Limit State (CO-LS), which matches the NBC-prescribed ULS-level hazard in terms of the return period. The largest SDRs occur in Stories 7 and 8, indicating that the structural (and likely non-structural) damage under beyond design-level wind loads tends to concentrate in these stories. The profile of peak residual storey drift ratios is shown in Figure 6-11b. These values meet with sufficient margin the ASCE Prestandard limit of 1/1000 for CO-LS.

The response of the cladding system under wind loading was evaluated using the Deformation Damage Index (DDI) parameter proposed by Griffis [159]. ASCE Prestandard requires that the peak

DDI throughout the entire cladding system be limited to 0.0025 for the Operational limit state (O-LS), which corresponds to the SLS in this study. Moreover, Mohammadi et al. [75] proposed that the peak DDI shall be limited to 1/140 of the storey height for the Life Safety limit state (LS-LS), which can be approximately translated to a return period of 600 years as per 2020 NBC. Peak DDIs were computed for various cladding panels (labelled from 1 to 49 from left to right and bottom to top of the prototype MKF) based on the results of dynamic analyses under wind load histories scaled to the serviceability- and design-level hazards. These values are plotted in Figure 6-12. As shown, the DDIs at SLS and ULS meet the performance criteria prescribed by ASCE Prestandard and the recommendation by Mohammadi et al. [75], respectively, indicating the satisfactory cladding performance of the steel MKF system.

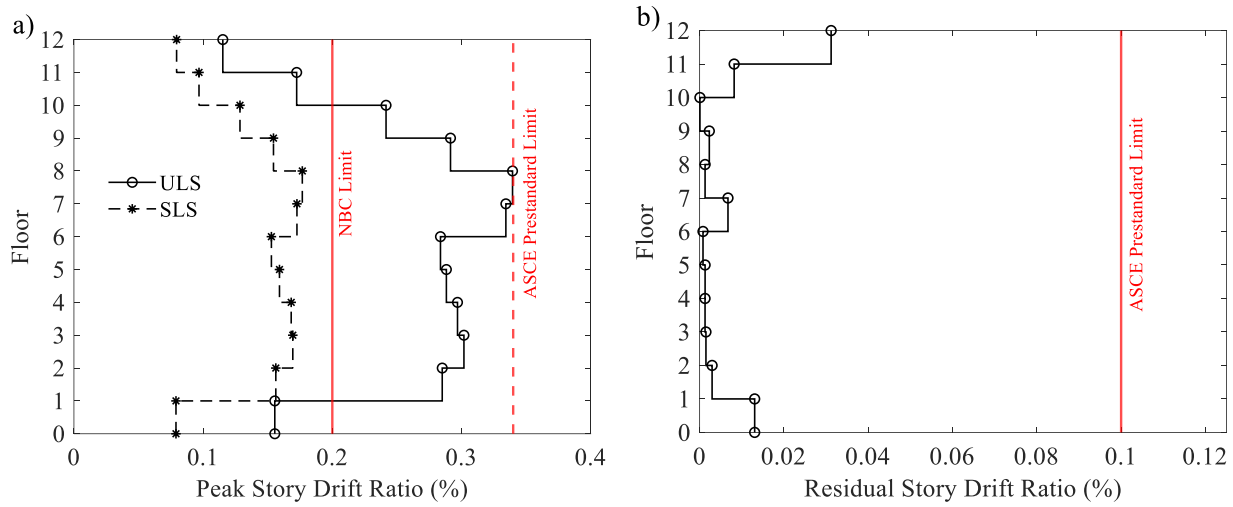

Figure 6-11. a) Profiles of peak storey drift ratios under SLS- and ULS-level wind hazards; b) Profile of peak residual storey drift ratios under ULS-level wind hazard.

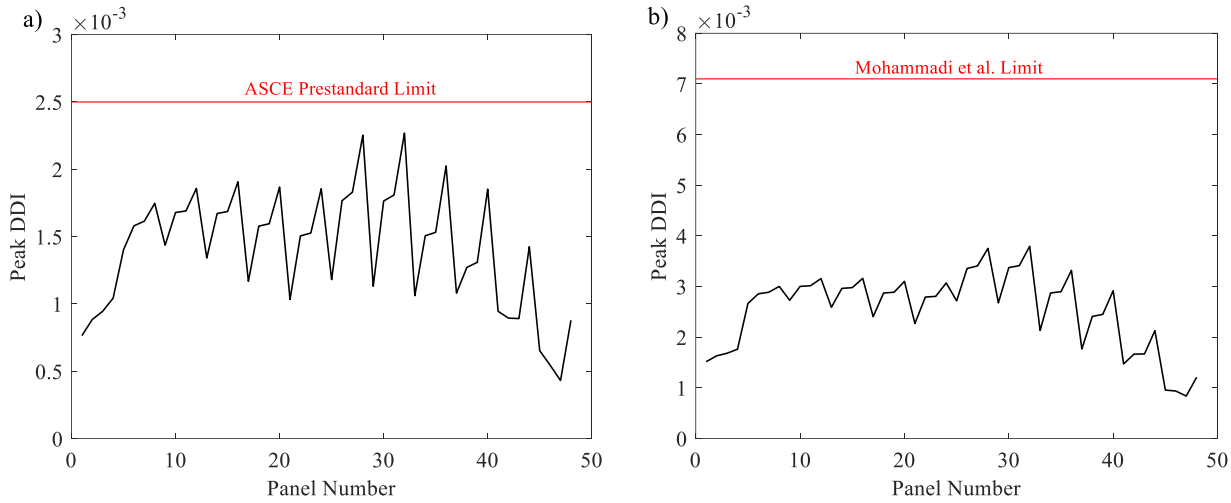

Figure 6-12. Peak DDIs for the selected MKF: a) SLS-level wind hazard; b) ULS-level wind hazard.

6.5.3. Force response of structural components

The peak values of axial force – strong axis bending moment (P-M) interaction ratios are presented in Figure 6-13 for knee braces, columns, intermediate beam segments, and beam stubs under wind loading histories scaled to ULS-level hazard. In this figure, the peak response at each storey and for each component was obtained by taking the maximum of the P-M ratios among all members of the same type within the respective storey. Moreover, member capacities were determined following CSA S16-19. Note that as per 2020 NBC, all members are expected (but not guaranteed) to remain elastic under design-level wind loads. However, ASCE Prestandard allows minor localized yielding in designated elements under CO-LS hazard.

Referring to Figure 6-13a and Figure 6-13b, no yielding is observed in knee braces, intermediate beam segments, beam stubs, and columns under ULS-level hazard, as expected in design. As shown in Figure 6-13b, interior columns experience larger P-M ratios compared to the exterior ones, suggesting higher wind plus gravity-induced demands in interior columns. Overall, it is confirmed that MKF structural members possess an appreciable reserve strength under design-level wind loads, the reason being that their design was controlled by SLS requirements. This

observation also suggests that the structural design of MWFRS, for the prototype building studied here and likely MKF buildings of similar heights, can be enhanced by providing a balance between strength and stiffness criteria under wind loads by taking advantage of PBWD methodology.

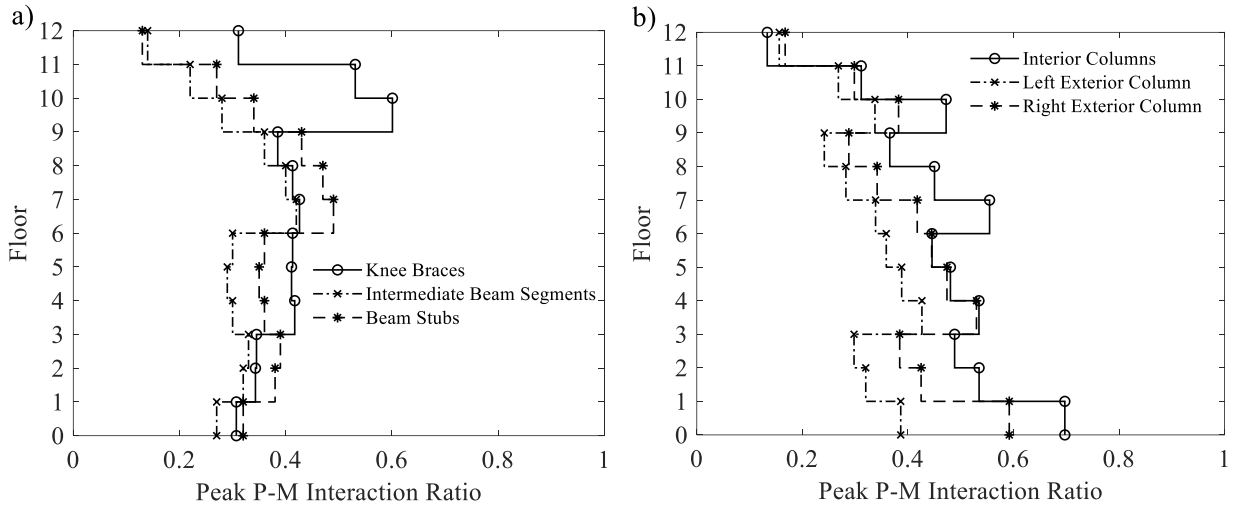

Figure 6-13. Peak P-M ratios of MKF structural elements under ULS-level wind hazard: a) Knee braces, intermediate beam segments, and beam stubs; b) Columns.

6.5.4. Collapse performance

The peak SDR along the height of the building was recorded in each nonlinear dynamic analysis to develop the IDWA curve. Figure 6-14 shows the IDWA curve that relates the hourly mean wind speed at a standard height of 10 m as the intensity measure to peak SDR among all floors as the damage measure. Collapse was identified as a state of lateral instability resulting in non-converging analysis.

Referring to Figure 6-14, the collapse wind speed was obtained as $U_c = 71\ m/s$, whereas the wind speed associated with the ULS-level hazard is $U_{1-in-500yrs} = 30.87\ m/s$, resulting in a Collapse Margin Ratio (CMR) of 2.3. CMR is defined as the ratio of the collapse wind intensity to the wind intensity associated with ULS-level hazard ($U_c/U_{1-in-500yrs}$). The return period corresponding to the collapse wind speed was back calculated as 460 billion years, indicating that it is highly

unlikely that a wind event with such a rare hourly mean wind speed would occur during the building's lifespan.

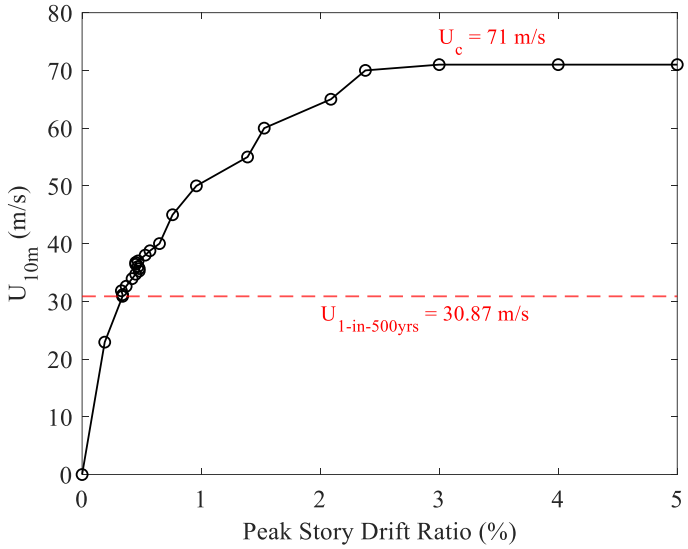

Figure 6-14. IDWA curve of the prototype MKF.

Figure 6-15a presents frame base shear versus roof drift ratio under wind loading time histories scaled to the collapse intensity, which corresponds to $U_c = 71\ m/s$. As shown, the frame exhibits a pushover-like response (see Figure 6-9) experiencing collapse at approximately 2% storey drift, which occurs at t = 13 min of the wind time history shown in Figure 6-15b.

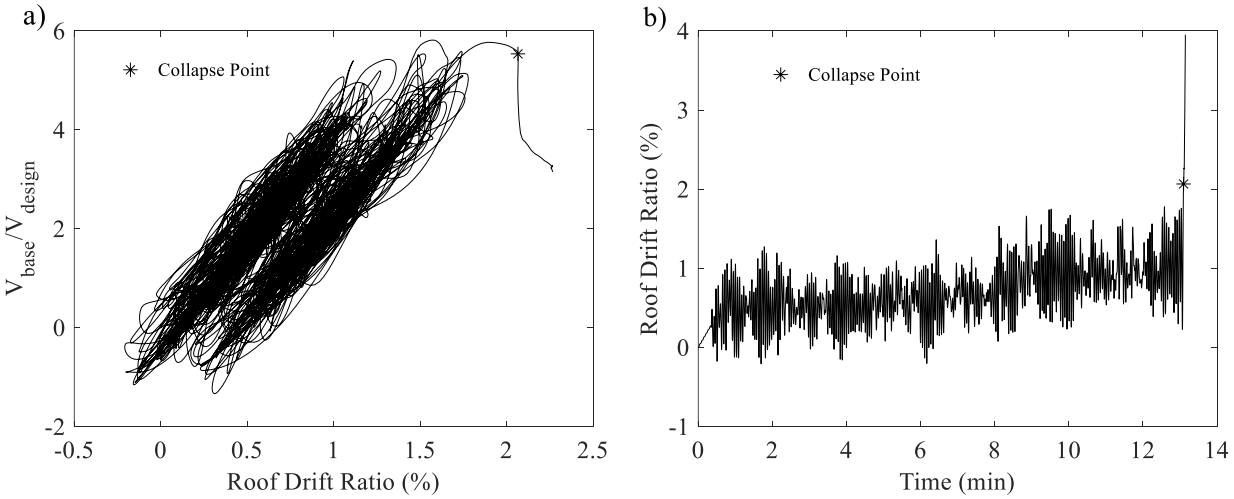

Figure 6-15. Wind response of the prototype building collapse-level wind hazard: a) Base shear versus roof drift ratio; b) Roof drift ratio time history (response well beyond collapse is not shown).

Under collapse-level wind load history, MKF nonlinearity deformation develops in the system through axial yielding in knee braces and flexural plastic hinge formation in some of the beam-to-stub beam connections. Figure 6-16a - Figure 6-16d show normalized axial force–axial deformation responses of knee braces in Storey 6 of the MKF under collapse-level wind load (positive force represents tension). In this figure, P, A_g, δ, δ_y, and F_y are knee brace axial force, gross cross-sectional area, axial deformation, axial deformation at yielding, and the yield strength of steel, respectively. Referring to Figure 15a – Figure 15d, knee braces experience multiple cycles of compressive yielding without instability owing to their low global slenderness ratio ($KL_k/r < 39$ where K is the effective length factor, L_k and r are the length and radius of gyration of the knee braces, respectively). The tensile braces experience modest axial yielding due to the influence of gravity loads, which induces compression in the braces before the application of wind loads, and non-uniform distribution of moments between tensile and compressive knee braces at the knee-to-column connection point. Concentration of yielding in compressive braces caused a significant accumulation of permanent deformations in those elements as the structure leaned on the side (ratcheting response), which was exacerbated by P-Delta effects and eventually led to a soft-storey mechanism in Storey 6 accompanied by plastic hinges forming at the ends of intermediate beams of storey 7; followed by collapse of the frame. Notably, the mechanism formed at storey 6 consisted of axial yielding of the knee braces, whereas flexural plastic hinging of the intermediate beams formed the mechanism in storey 7. This behaviour was expected because no predetermined yielding mechanism was imposed during the design.

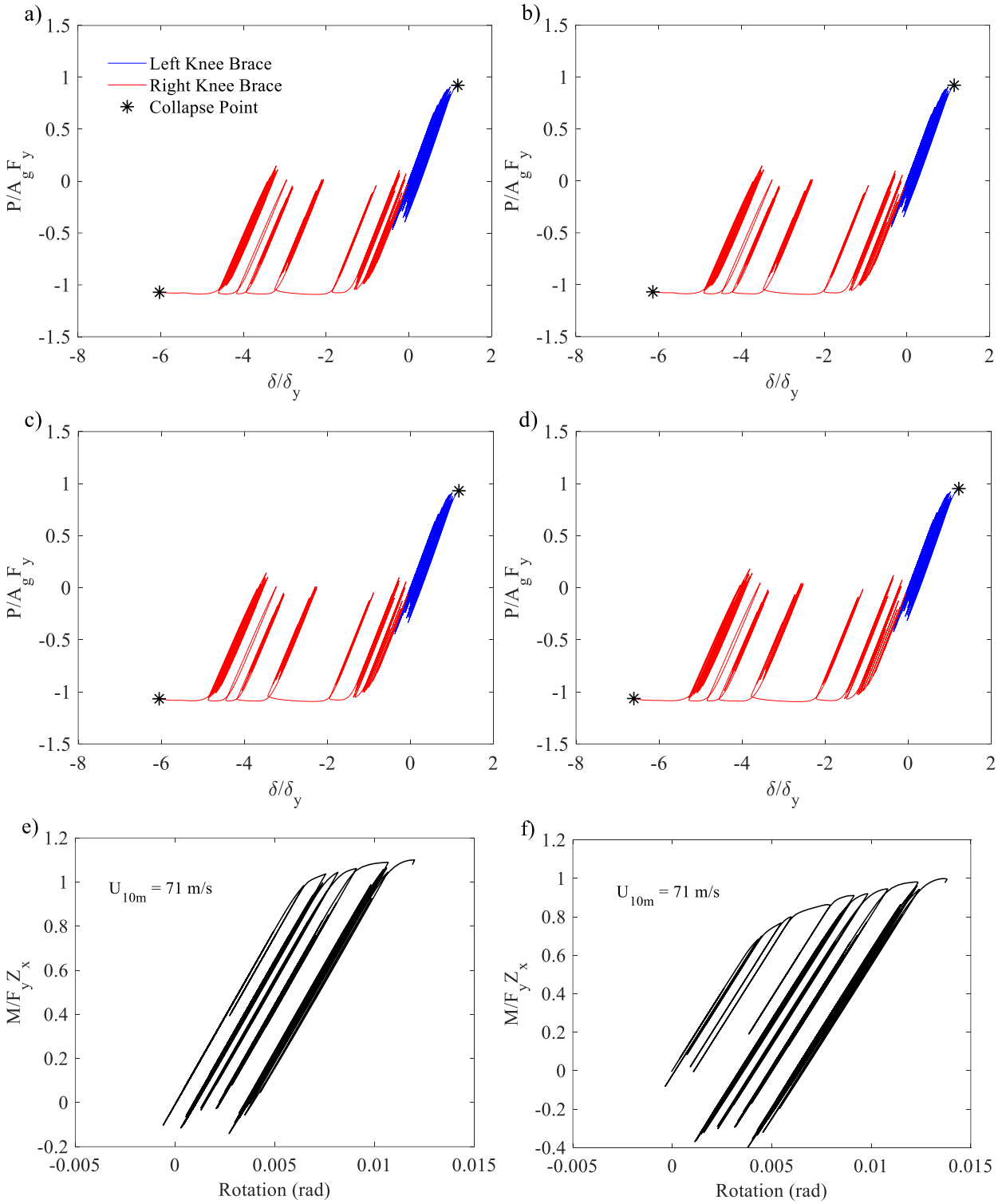

Figure 6-16. Member force responses under the collapse-level wind load: a-d) Axial force – axial deformation response of knee braces at Storey 6 in Bays 1 - 4 (Bay 1 is the left bay in Figure 6-2); e-f) Bending moment – rotation response at the base of the left exterior column and its adjacent interior column.

Figure 6-16e and Figure 6-16f show the bending moment–rotation response at the base of the left exterior column and its adjacent interior column (see Figure 6-2), respectively. It can be observed that plastic hinges form at the base of columns as part of the collapse mechanism anticipated in the MKF [113].

Overall, the wind collapse performance evaluation suggests that the MKF provides a sufficient margin of safety against the design wind load, i.e., a CMR of 2.3, due to reserve capacity and overstrength inherent in the design, which can be leveraged in future studies to achieve a more balanced wind design.

6.5.5. Occupant comfort

Occupant comfort is considered under frequent and less intense wind events when designing wind-sensitive buildings, i.e., buildings in which lateral wind loads govern the design over lateral seismic loads. Qualitative and quantitative criteria were proposed in the past for assessing occupant comfort under wind loads, e.g., those reported in [159-161]. According to Commentary I of 2015 NBC [12], many tall buildings with office occupancy in North America that underwent detailed wind tunnel studies were designed for a Peak Floor Acceleration (PFA) of 2.5% g, where *g* is the gravitational acceleration, under 1-in-10-year wind loads.

The IDWAs were performed under wind loading histories with intensities from zero to collapse. There results were used to obtain peak PFAs along the height of the prototype frame. Figure 6-17 shows the hourly mean wind speed at a standard height of 10 m versus PFA, with a colour-coded legend showing the motion perception ranges recommended by Chang [162].

The maximum PFA was found as 1.4% g under SLS-level wind loading histories, which is smaller than the threshold by the Commentary I of 2015 NBC. Moreover, a maximum PFA of 14 mg (1.4% g) remains within the range of perceptibility according to Chang [162]. An hourly mean wind speed

of 23.45 m/s, which corresponds to a return period of 13 years, marks the beginning of the annoying motion domain.

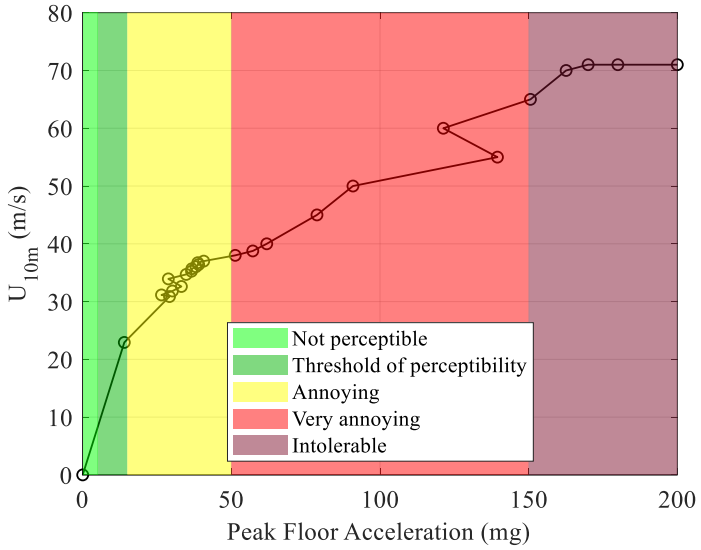

Figure 6-17. MKF motion comfort assessment.

As an alternative approach to evaluating occupant comfort under wind loads, motion comfort assessment was carried out based on ISO practice [163] under the 1-year 10-minute wind speed. For office occupancies, the acceptance criterion based on this criterion is a function of the building's natural frequency f = 0.306 Hz defined as $6.12f^{-0.454}$, which gives a limit of 10.47 mg. The maximum PFA of the prototype frame obtained from the nonlinear dynamic analysis under wind load histories scaled to 1-year 10-minute wind speed was found as 7.8 mg, which meets the ISO limit, reaffirming the satisfactory performance of the MKF building in terms of occupant comfort.

6.6. Discussion on randomly generated wind time histories

Chapter 6 addressed the performance of steel MKFs under experimentally derived wind loads and evaluated key response metrics such as structural and non-structural deformations, accelerations, and wind-induced demands in different structural elements. The wind performance evaluation can be improved in future studies to address the limitations of the current study, namely by generating random wind time histories.

Two critical parameters that should be studied in PBWD of structural systems are the collapse margin ratio and probability of collapse under wind loading time histories with different frequency characteristics. To obtain these two parameters, several wind loading time histories should be implemented in the analysis of the prototype building of interest and IDWA curves should be constructed while accounting for the wind loading uncertainties. However, this is a rather formidable task since not enough data is available on experimental wind loading time histories. Wind pressure coefficients exerted on a structure depend on its aspect ratios, height, natural frequency, architectural features, and surrounding environment. Although wind tunnel testing is acknowledged as a viable method for assessing wind loads, it has drawbacks due to its high cost and lack of adaptability to design modifications.

To produce wind load uncertainty, i.e., generating multiple wind loading time histories that are consistent with the geometrical configuration of the prototype building but are different in terms of frequency content, two methods have been proposed by the researchers. The author examined both methods to generate random wind loading time histories and to perform a more comprehensive wind performance evaluation on the system. However, these attempts were unsuccessful due to the limitations of the methods and the unavailability of data on the procedures. This section briefly discusses the two methods and elaborates on the challenges faced in each approach.

6.6.1. Monte Carlo simulation

This method was employed by Athanasiou et al. [76] to generate 500 random wind realizations for the assessment of wind response in linear and nonlinear ranges. In this approach, the "*pearsrnd"* command in MATLAB was used to generate random wind realizations based on the statistical properties of the TPU-derived wind forces, i.e., mean, standard deviation, skewness, and kurtosis.

In this procedure, the randomly generated wind forces are very noisy. As such, they should be smoothened repeatedly to achieve an acceptable matching between the gust spectra of the TPU-derived and randomly generated pressures. The author investigated this approach and generated a random wind load realization for the roof level of the prototype building. However, this attempt was unsuccessful because the generated wind loading time history was extremely noisy, as mentioned by Athanasiou et al. [76], and no information was available on signal processing, data smoothening, and noise filtering procedures. This time-consuming process requires significant trial and error and a deep understanding of signal processing knowledge, which is outside this project's scope. For more information on this method, the reader can refer to Athanasiou et al. [76].

6.6.2. Stochastic wind load simulation

In a study by Jeong et al. [82], along-wind loading time histories were generated based on the Power Spectral Density (PSD) functions according to a stochastic approach. This method was first proposed by Shinozuka and Deodatis [164]. Jeong et al. [82] based their study on the Korean building code (MOLIT) [165], and employed the Von Kármán PSD function for wind speed, as defined below:

$$\frac{fS_v(f)}{\sigma_v^2} = \frac{4fL_H/V_H}{\left\{1 + 71\left(\frac{fL_H}{V_H}\right)^2\right\}^{5/6}} \tag{6-6}$$

where S_v refers to the PSD of the along-wind speed, f stands for the along-wind vibration frequency, H represents the total height of the building and V_H denotes the design wind speed at the reference height. Moreover, σ_v and L_H define the standard deviation of along-wind speed and turbulence length, respectively, and are estimated as follows:

$$\sigma_v = I_H V_H \tag{6-7}$$

$$L_H = 100\left(\frac{H}{30}\right)^{0.5} \tag{6-8}$$

In recent equations, I_H represents turbulence intensity and is obtained as:

$$I_H = 0.1\left(\frac{H}{Z_g}\right)^{-\beta-0.05} \tag{6-9}$$

In Eq. (6-9), β and Z_g refer to the power law exponent of the mean wind speed profile and height of the atmospheric boundary layer from the ground surface, respectively. The values for these parameters depend on the surrounding environment of the building and are retrieved from the building code.

Once the PSD of wind speed is established, an aerodynamic admittance function should be used to convert it into wind load PSD. MOLIT presents the following aerodynamic admittance function:

$$|\chi(f)|^2 = \frac{0.84}{[1 + 2.1(fH/V_H)][1 + 2.1(fB/V_H)]} \tag{6-10}$$

In which *B* represents the breadth of the building (perpendicular to the along-wind direction).

Using Eqs. (6-6) and (6-10), the following equation can be utilized to express the PSD of the along-wind force at the reference height:

$$S_p(f) = (\rho C_D^* A V_H)^2 S_v(f)|\chi(f)|^2 \tag{6-11}$$

Where $C_D^* = 0.75C_D$ denotes the wind force coefficient for fluctuating wind force and is a function of the external pressure coefficients of the windward and leeward walls determined according to the building code. Also, A is the projection area for a given floor.

Once the PSD of the along-wind force has been obtained, stochastic time histories can be generated as follows:

$$X_P(t) = \sum_{i=1}^{n} \sqrt{2S_p(f_i)\Delta f}\cos\left(2\pi f_i t + \psi_i\right) \tag{6-12}$$

In Eq. (6-12), Δf and ψ are the interval of frequency and randomly generated phase angle ($0 - 2\pi$). Since the vertical distribution of the along-wind force is addressed in the wind force coefficient, the mean and background components of the along-wind time history load are combined according to the following relationship to generate the wind load at different heights from the ground (z):

$$F_D(z,t) = X_P(z,t) + \frac{1}{2}\rho V_H^2 C_D(z) A \tag{6-13}$$

Figure 6-18 is retrieved from Jeong et al. [82] as a sample along-wind loading time history generated for the roof level of a 45-storey building according to the stochastic procedure described here.

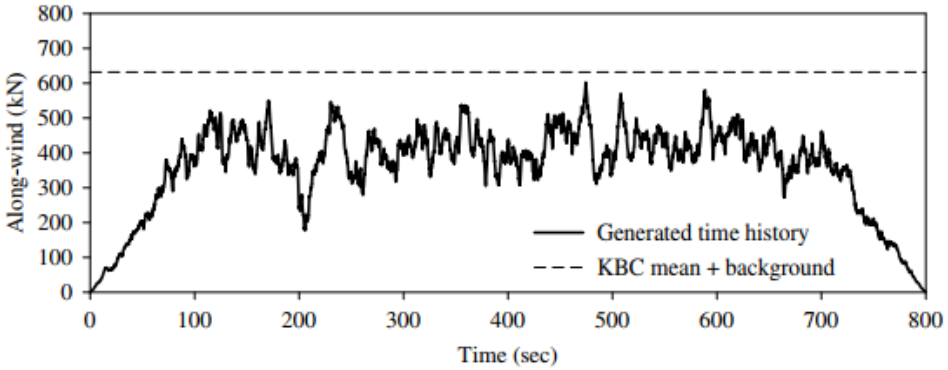

Figure 6-18. Along-wind loading time history for the roof level of a 45-storey building (Adapted from [82])

To verify the methodology described earlier and assess the possibility of generating random wind loading time histories for the prototype building studied in Chapter 6, the author attempted to reproduce the plot shown in Figure 6-18 by using the same wind load conditions and parameters reported by Jeong et al. [82] according to MOLIT. However, in the reference study, the projection area for the top level of the prototype building has not been specified. The height of the last storey and the breadth of the building are 4 and 36 meters, respectively. Figure 6-19 shows the resulting wind loading time history for two different projection areas of 72 m^2 and 144 m^2. According to

Figure 6-19b, a projection area of 144 m^2 is likely to produce a wind loading time history with maximum values close to those observed in Figure 6-18. It can be also seen that the generated wind loading time histories are very noisy and need to be smoothened, filtered, and processed. To do so, signal processing knowledge and guidelines are required within the framework of the research done by Jeong et al. [82], which is outside the scope of this project.

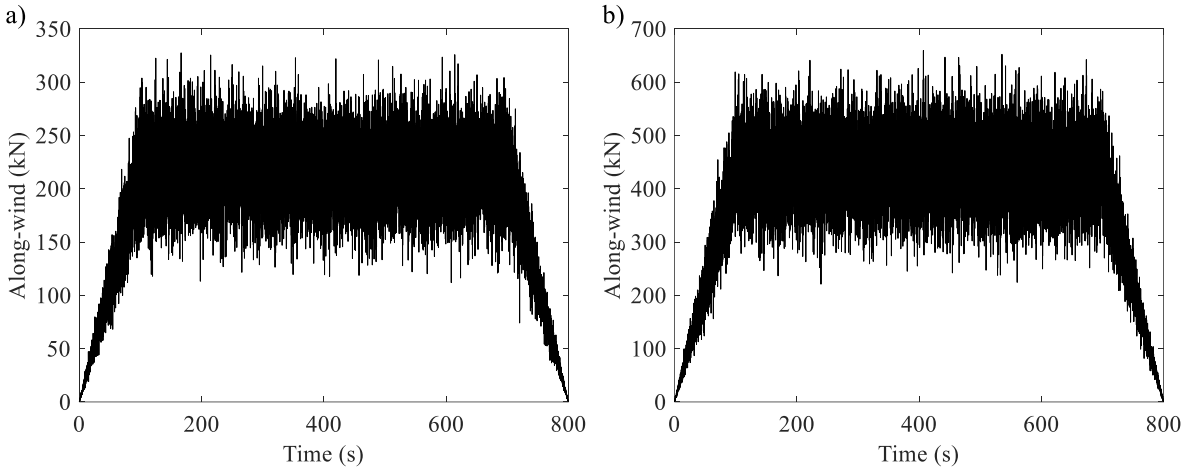

Figure 6-19. Along-wind loading time histories generated according to the stochastic method for the roof level of the prototype building discussed in [82]: a) a wind projection area of 72 m^2; b) wind projection area of 144 m^2

6.7. Conclusions

This chapter assessed the performance of steel Moment-resisting Knee-braced Frames (MKFs) under lateral wind loads varying from frequent up to severe events, beyond design-level wind hazard. A 12-storey prototype building was selected in a low seismic region in eastern Canada. One of the MKFs in the longitudinal direction of the building was then designed under gravity plus wind demands. The wind response of the frame was numerically evaluated under wind loading time histories scaled in time and intensity according to the hourly mean velocity at the roof level of the building to match the anticipated dynamic wind demands. The results were used to study key MKF response parameters, including structural member forces and deformations, non-structural

deformations, peak floor accelerations, and the system collapse performance. The main findings of this study are summarized as follows:

- A wind performance evaluation methodology was developed to numerically examine the response of the steel MKF using wind time history analysis under serviceability-, design- and beyond design-level wind loads.
- Peak storey drift ratios were found as 0.18% and 0.34% under wind loading time histories scaled to SLS and ULS intensities, respectively. These values are both smaller than the limits set by 2020 NBC and ASCE Prestandard, respectively.
- The maximum value of peak residual storey drift ratios was obtained as 0.03% under ULS-level wind time histories, which is smaller than the 0.1% limit set by the ASCE Prestandard.
- The maximum values of the deformation damage index were 0.0022 and 0.0037 under wind loading time histories scaled to SLS- and ULS-level intensities, respectively. These values meet the limits 0.0025 and 0.0071 proposed by the ASCE Prestandard and Mohammadi et al. [75] for SLS and ULS-level hazards, respectively, for the cladding system subjected to wind loading.
- Structural and non-structural deformation results reveal a satisfactory performance and confirm sufficient built-in stiffness of the steel MKF system to limit deformations under lateral wind loads expected during the lifespan of the building.
- The MKF possesses a large overstrength of 5.4 due to structural elements being mainly se; chosen to meet serviceability criteria. The main structural elements of the MKF remain elastic at the ULS-level wind hazard with appreciable reserve capacity.
- The MKF exhibited a collapse capacity of $U_C = 71\ m/s$, which is more than two times its design wind intensity, i.e., $U_{1-in-500yrs} = 30.87\ m/s$. The collapse response evaluation

under wind confirmed that the likelihood of the steel MKF building studied here collapsing during its lifetime under the wind hazard expected in eastern Canada is highly improbable.

- Maximum peak floor acceleration over the height of the prototype building under wind loading time histories scaled to the SLS-level hazard was 14 mg, which meets the limitation recommended by 2015 NBC Commentary I and falls within the perceptibility range according to criteria by Chang [162]. These results indicate that the MKF system can satisfy comfort requirements when used as MWFRS in multi-storey buildings.
- Overall, the steel MKF system showed a satisfactory performance under wind loading as a MWFRS and can be considered a viable alternative to other conventional steel LLRSs.
- The results of this study indicate that the 2020 NBC wind design methodology can be enhanced by taking advantage of the PBWD and potentially leveraging limited inelastic response of the MKF under design- or beyond design-level wind loads, which may lead to more economical structures, while maintaining structural safety and integrity of non-structural components, such as wall cladding and building envelopes.

Future studies should investigate the possibility of introducing wind load uncertainties for wind performance evaluation of the steel MKF. Furthermore, the serviceability performance and probability of collapse of the steel MKF designed for a reduced wind base shear should be investigated to propose a wind load reduction factor in the framework of PBWD methodology.

CHAPTER 7

CONCLUSIONS

7.1. Summary

The objective of this Ph.D. thesis was to develop analysis and design procedures for and evaluate the performance of the proposed steel Moment-resisting Knee-braced Frame (MKF) system under lateral seismic and wind loads within the NBC, CSA S16, and PBPD method. For seismic performance evaluation, prototype MKFs were selected from an office building located in Vancouver (Seismic Category 4). A 12-storey MKF building located in a low seismic region (Seismic Category 2) in Toronto was also studied under extreme wind loading conditions.

A design methodology based on the PBPD approach was developed to analyze and design all structural elements of steel MKFs under an imposed plastic mechanism. Multiple prototype MKFs and highly ductile MRFs were designed considering different design methodologies, i.e., the PBPD approach and the conventional NBC scheme, various frame heights, knee brace angles, and building layouts. Fibre-based numerical models of the prototype frames were created in the *OpenSees* program. The models were used to perform nonlinear static, response history, and incremental dynamic analyses. For seismic evaluations, dynamic analyses were carried out under a set of 33 ground motion records representing three different sources of seismicity expected in southwestern Canada. Various response parameters such as peak SDR, RSDR, PFA, collapse intensity, collapse probability, CMR, in-plane flexural bending demands in columns, axial demands in knee braces and beams, and flexural bending as well as axial demands in beam stubs, were recorded and examined to comprehensively evaluate the performance of the MKF system under different seismic and wind intensities up to the collapse stage. The seismic performance of

the MKF system as well as the material weight were compared against conventional highly ductile MRFs. Overstrength- and ductility-related force modification factors were derived, proposed, and validated for the MKF system. The vulnerability of the MKF system to economic loss due to structural and non-structural damages caused by earthquake events was examined by a probabilistic storey-based loss estimation procedure and loss vulnerability curves as well as EAL bar charts were established. Finally, nonlinear analyses were conducted under experimental wind load histories retrieved from the Tokyo Polytechnic University Aerodynamic Database to assess motion comfort, displacement, and collapse criteria for the MKF system as part of the wind performance evaluation program of a 12-storey office building.

7.2. Scientific Contributions

The main scientific contributions of this Ph.D. research project are as follows:

- Analysis and design methodologies for the steel MKF system in the context of the Canadian steel design standard, National Building Code of Canada, and Performance-Based Plastic Design approach
- Overstrength- and ductility-related force modification factors for seismic design of the MKF system
- Earthquake-induced economic loss recommendations
- Overstrength and dynamic response of structural and non-structural components of the MKF system under serviceability-, design- and beyond design-level wind load time histories

7.3. Conclusions and Recommendations

The main findings of this Ph.D. thesis are summarized below:

The results of the first phase of the study revealed the following:

- The PBPD procedure developed in this phase results in a proper design for low-rise MKFs where sufficient built-in stiffness is achieved to meet the stringent drift limit set by the NBC.
- A verification of the detailed numerical *OpenSees* models indicates that the nonlinear modelling techniques employed in this study can properly predict the expected response of steel knee-braced frames with lateral behaviour and nonlinear mechanism similar to the MKF.
- The MKF system offers reduced steel tonnage compared to the conventional MRFs, having the potential for reduced construction costs by eliminating column panel zone stiffeners and doubler plates.
- NLRHA results confirm that plastic hinges are likely to form at the base of columns as well as the ends of intermediate beam segments when MKFs are designed according to the PBPD procedure.
- The MKF designed per the PBPD method results in a smaller probability of collapse compared to that designed following the NBC approach.
- The proposed MKF designed following the developed PBPD procedure can be used in the seismic design of steel multi-storey buildings as a viable alternative to conventional MRFs.

The study on MKF seismic design parameters confirmed the following:

- Based on a significant number of numerical analyses and collapse evaluations on multiple archetypes with different number of stories and geometrical configurations, overstrength-related and ductility-related force modification factors of $R_o = 1.60$ and $R_d = 3.0$ are proposed for steel MKF buildings not exceeding 40 m in height and located in high seismic regions of Canada (Seismic Category 4).

- The expected inelastic lateral deflections of MKF buildings under seismic loads can be estimated using a deflection amplification factor equal to $\frac{R_d R_o}{I_E} = \frac{4.80}{I_E}$.
- It is suggested that the design period T_a of MKF buildings be considered the lesser of 1.7 times the empirical period prescribed by 2015 NBC for steel MRFs, and the analytical period obtained using an eigenvalue analysis on a detailed numerical model.
- An evaluation of seismic demands developed in force-controlled members, such as knee braces and beam stubs, reveals that they remain elastic under design-level earthquakes, affirming the effectiveness of design assumptions.
- Nonlinear response history analyses used to verify the proposed seismic design parameters demonstrate that the MKF system can provide a level of safety comparable to that specified by 2015 NBC.

The earthquake-induced economic loss assessment phase of the research resulted in the following findings:

- Steel MKFs designed according to the proposed reduction factors and PBPD method are likely to collapse under intensities 45% to 185% larger than their seismic design demands.
- The calculated yearly probabilities of structural failure for MKF buildings designed following the NBC guidelines confirm the effectiveness of the force modification factors associated with ductility and overstrength, given the assumptions and constraints considered in this research.
- In all prototype buildings, the costs associated with repairing acceleration-sensitive components are minimal when compared to the expenses related to other components contributing to the overall economic loss. It is noteworthy that the economic loss primarily stems from the repair costs of drift-sensitive components, particularly up to the SE level.

- As the seismic intensity surpasses the DE level, the economic losses related to structural damage, demolition, and collapse become more significant in comparison to the costs associated with non-structural repairs. In most of the buildings examined, the primary driver of economic loss shifts to collapse loss beyond the DE intensity.
- When considering a specific number of stories and seismic intensity, it becomes evident that the PBPD yields a higher normalized total loss compared to the NBC design. This suggests that the NBC design approach is likely to enhance the seismic loss performance of MKF buildings. This observation remains consistent when considering the EAL parameter as well.
- Considering the relatively low median RSDRs for the prototype buildings, which fall within the range of 0.05% to 0.22%, it is highly unlikely that the MKF buildings examined in this study would require demolition in the aftermath of design-level earthquakes.
- Except for F9-P, the EAL is primarily influenced by the expenses related to repairing non-structural drift-sensitive components in all frames. On average, within the NBC and PBPD frames, approximately 51% and 49% of the total normalized EAL, respectively, can be attributed to the costs associated with the repair of these non-structural drift-sensitive components.
- Taking into account all the response metrics examined in this study, multi-storey buildings incorporating steel MKFs exhibit encouraging seismic collapse and earthquake-induced loss performances, suggesting their suitability for use in high seismic regions.

The wind performance evaluation of the steel MKF system revealed the following key results:

- The steel MKF system meets the key serviceability requirements prescribed by various provisions, including ISO, NBC, and ASCE Prestandard, in terms of structural and cladding deformations as well as horizontal accelerations.
- Structural elements of the steel MKF system remain elastic under design-level wind hazard expected in eastern Canada, as anticipated in design, confirming the robust performance of the system with respect to the structural demand to capacity ratios.
- Steel MKF buildings designed for the wind hazard in eastern Canada are highly unlikely to experience collapse during their lifespan since the return period associated with the collapse wind load intensity is unrealistically large.
- Design of the steel MKF system under wind loads is mainly governed by serviceability requirements. This results in increased member sizes compared to the original design for strength demands because extra lateral stiffness is needed to satisfy the drift and acceleration criteria.
- The steel MKF prototype building possesses a significant reserve overstrength under nonlinear static and dynamic wind loads. This indicates that the code-prescribed requirements for wind design give rise to an unnecessarily conservative outcome, suggesting the potential for revisiting wind analysis and design criteria to improve the structural design efficiency by leveraging the inelastic capacity of the system.
- The response of the steel MKF prototype building under experimental wind loading histories with different intensities reveals the significant potential of this system for replacing other conventional steel LLRSs when the design of the system is solely governed by wind demands.

7.4. Limitations

The author acknowledges the following key assumptions or limitations of this Ph.D. dissertation:

- The prototype frames designed in this study were part of office buildings with different layouts and number of stories located on site Class C in Vancouver and Toronto. These frames were designed in accordance with the 2019 edition of the Canadian steel design standard, CSA S16-19.
- A concentrated plasticity approach was followed to simulate the inelastic response and degradation of flexural plastic hinges at the ends of the intermediate beam segments.
- A distributed plasticity approach was implemented in modelling columns, knee braces, and beam stubs.
- Non-simulated collapse modes, such as connection fracture, lateral-torsional, flexural-torsional, and local buckling modes of columns, were not studied.
- The seismic performance of the system was studied only under seismic conditions in western Canada.
- Only the planar behaviour of the prototype frames was investigated through 2D numerical models and out-of-plane responses were neglected.
- The number of stories for prototype frames studied ranged from 3 to 15 and the total height of the buildings ranged from 12.3 to 60.3 m.
- Uncertainties associated with the frequency content and direction of wind loading time histories were neglected.
- The crosswind response of the prototype building designed for wind performance evaluation was not studied since it would need a detailed 3D numerical model of the

prototype building, which would be extremely computationally expensive due to the complexity of the model.

7.5. Recommendations for Future Work

- Alternative configurations of the MKF system covering different span lengths, brace length ratios, brace angles, and number of stories can be evaluated under seismic and wind loads.
- Using the seismic load reduction factors proposed in this thesis, the collapse response of the MKF system under seismic forces should be evaluated for low- to moderate-seismic regions of Canada to relax the proposed height limit.
- The effects of frame base fixity on the lateral stiffness, collapse capacity, deformation ductility capacity, and overstrength of steel MKFs should be investigated using a continuum-based finite element model accounting for column connection and footing flexibility.
- Appropriate details should be proposed for the moment connections at the ends of intermediate beam segments and verified using continuum-based finite element models as well as experimental testing to achieve the desired ductility at the component level. In particular, the application of a sloped beam-to-stub connection that can potentially facilitate the erection process and cut on the craning and labour costs should be investigated.
- Stability of columns and intermediate beam segments in the out-of-plane direction of the frame should be studied using detailed continuum-based finite element models to propose appropriate lateral bracing requirements and stability design guidelines.
- Failure modes of MKF columns due to significant point loads at the knee-to-column connection zones should be studied in the future and appropriate details consistent with

MKF methodology presented in this dissertation should be proposed to prevent the formation of local inelasticity under severe seismic demands.

- Future studies should investigate the possibility of replacing knee elements in the MKF with a haunch plate or buckling-restrained braces, which offer similar structural benefits but with different characteristics.
- Three-dimensional numerical models of MKF buildings encompassing all elements and connection details can be developed and evaluated under the bi-directional effects of ground motions and wind loads.
- A displacement-based beam-column element capable of simulating interactive local and global lateral-torsional buckling, including member shortening, that can potentially be implemented in *OpenSees* has recently been proposed after the analyses performed in this research were completed [102]. This element can be employed in future studies to refine the proposed numerical model of the MKF, namely the columns and intermediate beam segments, and evaluate the influence of local buckling and member shortening on the seismic and wind performances of the MKF.
- Future studies can investigate more thoroughly the earthquake-induced economic loss performance of steel MKFs by further refining the number and type of structural and non-structural elements evaluated as more data becomes available on fragility curve parameters.
- Future studies should focus on developing methodologies for generating stochastic wind time histories to capture the load uncertainty and evaluate the collapse risk and fragility of MKFs under wind hazards within the framework of Canadian standards.

- The possibility of proposing a wind load reduction factor for the MKF system that can potentially reduce the design wind load without compromising the serviceability criteria can be studied in the future.
- Monotonic and cyclic tests should be performed on large-scale single- and multi-storey steel MKFs to verify the deformation ductility capacity at both system and component levels, failure modes of the structural members, and design recommendations proposed in this thesis.

Bibliography

[1] Costanzo S, D'Aniello M, Landolfo R. Proposal of design rules for ductile X-CBFS in the framework of EUROCODE 8. Earthquake Engineering & Structural Dynamics. 2019;48:124-51.

[2] Engelhardt MD, Popov EP. On Design of Eccentrically Braced Frames. Earthquake Spectra. 1989;5:495-511.

[3] Canadian Standards Association. Design of Steel Structures CSA S16-19. Mississauga, ON, Canada: CSA Group; 2019.

[4] Canadian Commission on Building and Fire Codes. National Building Code of Canada: 2020. National Research Council of Canada; 2022.

[5] Canadian Commission on Building and Fire Codes. National Building Code of Canada: 2015. National Research Council of Canada; 2015.

[6] Leelataviwat S, Goel SC, Stojadinović B. Toward Performance-Based Seismic Design of Structures. Earthquake Spectra. 1999;15:435-61.

[7] Goel SC, Chao SH. Performance-based Plastic Design: Earthquake-resistant Steel Structures: National Council of Structural Engineers Associations, International Code Council; 2008.

[8] Suzuki Y, Lignos DG. Fiber-based hysteretic model for simulating strength and stiffness deterioration of steel hollow structural section columns under cyclic loading. Earthquake Engineering & Structural Dynamics. 2020;49:1702-20.

[9] Suzuki Y, Lignos DG. Experimental Evaluation of Steel Columns under Seismic Hazard-Consistent Collapse Loading Protocols. Journal of Structural Engineering. 2021;147:04021020.

[10] Mahsuli M, Haukaas T. Seismic risk analysis with reliability methods, part II: Analysis. Structural Safety. 2013;42:63-74.

[11] Gocke JW, Civil UoWDo, Engineering A. Response Modification Factor for Inelastic Design of Low-rise Steel Moment Frame Buildings Subjected to Extreme Wind Loads: University of Wyoming; 2020.

[12] Canadian Commission on Building and Fire Codes. Structural Commentaries (User's Guide - NBC 2015: Part 4 of Division B). National Research Council of Canada; 2017.

[13] Applied Technology Council. FEMA P695: Quantification of Building Seismic Performance Factors. Washington, D.C.2009.

[14] Miranda E, Bertero VV. Evaluation of Strength Reduction Factors for Earthquake-Resistant Design. Earthquake Spectra. 1994;10:357-79.

[15] Elkady A, Güell G, Lignos DG. Proposed methodology for building-specific earthquake loss assessment including column residual axial shortening. Earthquake Engineering & Structural Dynamics. 2020;49:339-55.

[16] Hwang S-H, Lignos DG. Earthquake-induced loss assessment of steel frame buildings with special moment frames designed in highly seismic regions. Earthquake Engineering & Structural Dynamics. 2017;46:2141-62.

[17] Hwang S-H, Lignos DG. Effect of Modeling Assumptions on the Earthquake-Induced Losses and Collapse Risk of Steel-Frame Buildings with Special Concentrically Braced Frames. Journal of Structural Engineering. 2017;143:04017116.

[18] Moammer O, Madani HM, Dolatshahi KM, Ghyabi M. Collapse risk and earthquake-induced loss assessment of buildings with eccentrically braced frames. Journal of Constructional Steel Research. 2020;168:105998.

[19] Elkady A, Lignos DG. Effect of gravity framing on the overstrength and collapse capacity of steel frame buildings with perimeter special moment frames. Earthquake Engineering & Structural Dynamics. 2015;44:1289-307.

[20] Liu J, Astaneh-Asl A. Moment–Rotation Parameters for Composite Shear Tab Connections. Journal of Structural Engineering. 2004;130:1371-80.

[21] Ramirez CM, Liel AB, Mitrani-Reiser J, Haselton CB, Spear AD, Steiner J et al. Expected earthquake damage and repair costs in reinforced concrete frame buildings. Earthquake Engineering & Structural Dynamics. 2012;41:1455-75.

[22] Applied Technology Council. FEMA P-58: Seismic Performance Assessment of Buildings, Volume 1 – Methodology Washington, DC.2018.

[23] Applied Technology Council. FEMA P-58: Seismic Performance Assessment of Buildings, Volume 2 – Implementation Guide. Washington, DC.2018.

[24] Pray R. 2022 National Construction Estimator: Craftsman Book Company; 2021.

[25] https://www.seismescanada.rncan.gc.ca/hazard-alea/interpolat/nbc2020-cnb2020-en.php.

[26] http://www.wind.arch.t-kougei.ac.jp.

[27] Aristizabal-Ochoa JD. Disposable Knee Bracing: Improvement in Seismic Design of Steel Frames. Journal of Structural Engineering. 1986;112:1544-52.

[28] Balendra T, Sam MT, Liaw Co, Lee SL. Preliminary studies into the behaviour of knee braced frames subject to seismic loading. Engineering Structures. 1991;13:67-74.

[29] Balendra T, Sam MT, Liaw CY. Diagonal brace with ductile knee anchor for aseismic steel frame. Earthquake Engineering & Structural Dynamics. 1990;19:847-58.

[30] Balendra T, Sam MT, Liaw CY. Design of earthquake-resistant steel frames with knee bracing. Journal of Constructional Steel Research. 1991;18:193-208.

[31] Balendra T, Lim EL, Lee SL. Ductile knee braced frames with shear yielding knee for seismic resistant structures. Engineering Structures. 1994;16:263-9.

[32] Sam MT, Balendra T, Liaw CY. Earthquake-resistant steel frames with energy dissipating knee elements. Engineering Structures. 1995;17:334-43.

[33] Balendra T, Lim EL, Liaw CY. Large-Scale Seismic Testing of Knee-Brace-Frame. Journal of Structural Engineering. 1997;123:11-9.

[34] Hsu HL, Li ZC. Seismic performance of steel frames with controlled buckling mechanisms in knee braces. Journal of Constructional Steel Research. 2015;107:50-60.

[35] Leelataviwat S, Suksan B, Srechai J, Warnitchai P. Seismic Design and Behavior of Ductile Knee-Braced Moment Frames. Journal of Structural Engineering. 2011;137:579-88.

[36] Junda E, Leelataviwat S, Doung P. Cyclic testing and performance evaluation of buckling-restrained knee-braced frames. Journal of Constructional Steel Research. 2018;148:154-64.

[37] Wongpakdee N, Leelataviwat S, Goel SC, Liao WC. Performance-Based Design and Collapse Evaluation of Buckling Restrained Knee Braced Truss Moment Frames. Engineering Structures. 2014;60:23-31.

[38] Yang TY, Li Y, Leelataviwat S. Performance-Based Design and Optimization of Buckling Restrained Knee Braced Truss Moment Frame. Journal of Performance of Constructed Facilities. 2014;28:A4014007.

[39] Yang TY, Li Y. Performance assessment of innovative seismic resilient steel knee braced frame. Frontiers of Structural and Civil Engineering. 2016;10:291-302.

[40] Yang TY, Li Y, Goel SC. Seismic Performance Evaluation of Long-Span Conventional Moment Frames and Buckling-Restrained Knee-Braced Truss Moment Frames. Journal of Structural Engineering. 2016;142:04015081.

[41] Asghari A, Saharkhizan S. Seismic design and performance evaluation of steel frames with knee-element connections. Journal of Constructional Steel Research. 2019;154:161-76.

[42] American Society of Civil E. Minimum design loads and associated criteria for buildings and other structures : ASCE/SEI 7-10 2010.

[43] Mazzoni S, McKenna F, H. Scott M, L. Fenves G. OpenSees Command Language Manual. University of California, Berkeley. 2006.

[44] Nekouvaght Tak A, Mirghaderi SR, Dargahi M. Plastic design of knee-element connection frames (KCFs) using mechanism control. Journal of Constructional Steel Research. 2020;173:106247.

[45] Vamvatsikos D, Cornell CA. Incremental dynamic analysis. Earthquake Engineering & Structural Dynamics. 2002;31:491-514.

[46] Vamvatsikos D, Cornell C. Applied Incremental Dynamic Analysis. Earthquake Spectra - EARTHQ SPECTRA. 2004;20.

[47] Ramirez CM, Miranda E. Significance of residual drifts in building earthquake loss estimation. Earthquake Engineering & Structural Dynamics. 2012;41:1477-93.

[48] Khademi M, Tehranizadeh M, Shirkhani A, Hajirasouliha I. Earthquake-induced loss assessment of steel dual concentrically braced structures subjected to near-field ground motions. Structures. 2023;51:1123-39.

[49] Hwang SH, Elkady A, Al.Bardaweel S, Lignos DG. Earthquake Loss Assessment of Steel Frame Buildings Designed in Highly Seismic Regions. 5th International Conference on Computational Methods in Structural Dynamics and Earthquake Engineering Methods in Structural Dynamics and Earthquake Engineering. Crete Island, Greece2015.

[50] Eads L, Miranda E, Lignos DG. Average spectral acceleration as an intensity measure for collapse risk assessment. Earthquake Engineering & Structural Dynamics. 2015;44:2057-73.

[51] Pei S, van de Lindt JW. Methodology for earthquake-induced loss estimation: An application to woodframe buildings. Structural Safety. 2009;31:31-42.

[52] Song R, Li Y, Van de Lindt JW. Loss estimation of steel buildings to earthquake mainshock–aftershock sequences. Structural Safety. 2016;61:1-11.

[53] Spacone E, Filippou FC, Taucer FF. Fibre Beam-Column Model For Non-Linear Analysis of R/C Frames: Part I. Formulation. Earthquake Engineering & Structural Dynamics. 1996;25:711-25.

[54] Calabrese A, Almeida JP, Pinho R. Numerical Issues in Distributed Inelasticity Modeling of RC Frame Elements for Seismic Analysis. Journal of Earthquake Engineering. 2010;14:38-68.

[55] D'Aniello M, Manna Ambrosino GL, Portioli F, Landolfo R. Modelling aspects of the seismic response of steel concentric braced frames. Steel and Composite Structures. 2013;15.

[56] Wijesundara KK, Nascimbene R, Rassati GA. Modeling of different bracing configurations in multi-storey concentrically braced frames using a fiber-beam based approach. Journal of Constructional Steel Research. 2014;101:426-36.

[57] Uriz P, Filippou FC, Mahin SA. Model for Cyclic Inelastic Buckling of Steel Braces. Journal of Structural Engineering. 2008;134:619-28.

[58] Aguero A, Izvernari C, Tremblay R. Modelling of the Seismic Response of Concentrically Braced Steel Frames using the OpenSees Analysis Environment. Advanced Steel Construction. 2006;2:242-74.

[59] Menegotto ML, Pinto PE. Method of analysis of cyclically loaded RC plane frames including changes in geometry and non-elastic behavior of elements under normal force and bending.

Proceedings of IABSE Symposium on Resistance and Ultimate Deform ability of Structures Acted On by Well Defined Repeated Loads: Scientific Research; 1973. p. 15-22.

[60] G. Lignos D, Krawinkler H. Deterioration Modeling of Steel Components in Support of Collapse Prediction of Steel Moment Frames under Earthquake Loading. Journal of Structural Engineering. 2011;137:1291-302.

[61] Cravero J, Elkady A, Lignos DG. Experimental Evaluation and Numerical Modeling of Wide-Flange Steel Columns Subjected to Constant and Variable Axial Load Coupled with Lateral Drift Demands. Journal of Structural Engineering. 2020;146:04019222.

[62] Eads L, Miranda E, Krawinkler H, Lignos DG. An efficient method for estimating the collapse risk of structures in seismic regions. Earthquake Engineering & Structural Dynamics. 2013;42:25-41.

[63] Ghaffary A, Moustafa MA. Performance-Based Assessment and Structural Response of 20-Story SAC Building under Wind Hazards through Collapse. Journal of Structural Engineering. 2021;147:04020346.

[64] Van de Lindt John W, Dao Thang N. Performance-Based Wind Engineering for Wood-Frame Buildings. Journal of Structural Engineering. 2009;135:169-77.

[65] Spence SMJ, Kareem A. Performance-based design and optimization of uncertain wind-excited dynamic building systems. Engineering Structures. 2014;78:133-44.

[66] Ellingwood BR, Rosowsky DV, Li Y, Kim JH. Fragility assessment of light-frame wood construction subjected to wind and earthquake hazards. Journal of Structural Engineering. 2004;130:1921-30.

[67] Li Y, Ellingwood Bruce R. Framework for Multihazard Risk Assessment and Mitigation for Wood-Frame Residential Construction. Journal of Structural Engineering. 2009;135:159-68.

[68] Ciampoli M, Petrini F, Augusti G. Performance-Based Wind Engineering: Towards a general procedure. Structural Safety. 2011;33:367-78.

[69] Gani F, Légeron F. Relationship between specified ductility and strength demand reduction for single degree-of-freedom systems under extreme wind events. Journal of Wind Engineering and Industrial Aerodynamics. 2012;109:31-45.

[70] Griffis LG, Patel V, Muthukumar S, Baldava S. A Framework for Performance-Based Wind Engineering. Advances in Hurricane Engineering2012. p. 1205-16.

[71] Judd Johnn P, Charney FA. Inelastic Behavior and Collapse Risk for Buildings Subjected to Wind Loads. Structures Congress2015. p. 2483-96.

[72] Judd JP, Charney FA. Wind Performance Assessment of Buildings. Geotechnical and Structural Engineering Congress 20162016. p. 1259-68.

[73] Judd Johnn P. Windstorm Resilience of a 10-Story Steel Frame Office Building. ASCE-ASME Journal of Risk and Uncertainty in Engineering Systems, Part A: Civil Engineering. 2018;4:04018020.

[74] Spence SMJ, Chuang WC, Tabbuso P, Bernardini E, Kareem A, Palizzolo L et al. Performance-Based Engineering of Wind-Excited Structures: A General Methodology. Geotechnical and Structural Engineering Congress 20162016. p. 1269-82.

[75] Mohammadi A, Azizinamini A, Griffis L, Irwin P. Performance Assessment of an Existing 47-Story High-Rise Building under Extreme Wind Loads. Journal of Structural Engineering. 2019;145:04018232.

[76] Athanasiou A, Tirca L, Stathopoulos T. Nonlinear Wind and Earthquake Loads on Tall Steel-Braced Frame Buildings. Journal of Structural Engineering. 2022;148:04022098.

[77] Athanasiou A, Tirca L, Stathopoulos T. Performance-based wind and earthquake design framework for tall steel buildings with ductile detailing. Journal of Wind Engineering and Industrial Aerodynamics. 2023;240:105492.

[78] Aswegan K, Larsen R, Klemencic R, Hooper J, Hasselbauer J. Performance-Based Wind and Seismic Engineering: Benefits of Considering Multiple Hazards. Structures Congress 2017. p. 473-84.

[79] Cui W, Caracoglia L. Examination of experimental variability in HFFB testing of a tall building under multi-directional winds. Journal of Wind Engineering and Industrial Aerodynamics. 2017;171:34-49.

[80] Ghebremariam BT, Judd Johnn P. Windstorm Resilience of a 46-Story Office Building. AEI 2017. p. 735-44.

[81] Nikellis A, Sett K, Whittaker AS. Multihazard Design and Cost-Benefit Analysis of Buildings with Special Moment–Resisting Steel Frames. Journal of Structural Engineering. 2019;145:04019031.

[82] Jeong SY, Alinejad H, Kang TH-K. Performance-Based Wind Design of High-Rise Buildings Using Generated Time-History Wind Loads. Journal of Structural Engineering. 2021;147:04021134.

[83] Alinejad H, Jeong SY, Chang C, Kang TH-K. Upper Limit of Aerodynamic Forces for Inelastic Wind Design. Journal of Structural Engineering. 2022;148:04021271.

[84] Li Y, Song Q, Li C, Huang X, Zhang Y. Reduction of wind loads on rectangular tall buildings with different taper ratios. Journal of Building Engineering. 2022;45:103588.

[85] Elezaby F, El Damatty A. Ductility-based design approach of tall buildings under wind loads. Wind and Structures. 2020;31:143-52.

[86] Larsen R, Klemencic R, Hooper J, Aswegan K. Engineering Objectives for Performance-Based Wind Design. Geotechnical and Structural Engineering Congress 2016. p. 1245-58.

[87] Abdelwahab M, Ghazal T, Nadeem K, Aboshosha H, Elshaer A. Performance-based wind design for tall buildings: Review and comparative study. Journal of Building Engineering. 2023;68:106103.

[88] Bernardini E, Spence SMJ, Kwon D-K, Kareem A. Performance-Based Design of High-Rise Buildings for Occupant Comfort. Journal of Structural Engineering. 2015;141:04014244.

[89] Balendra T, Yu CH, Lee FL. An economical structural system for wind and earthquake loads. Engineering Structures. 2001;23:491-501.

[90] Lee SS, Goel SC, Chao SH. Performance-Based Sesimic Design of Steel Moment Frames Using Target Drift and Yield Mechanism. 2002.

[91] Chao SH, Goel SC, Lee SS. A Seismic Design Lateral Force Distribution Based on Inelastic State of Structures. Earthquake Spectra. 2007;23:547-69.

[92] Tremblay R, Côté B, Léger P. An evaluation of P-Δ amplification factors in multistorey steel moment resisting frames. Canadian Journal of Civil Engineering. 1999;26:535-48.

[93] Goel SC, Liao W-C, Reza Bayat M, Chao S-H. Performance-based plastic design (PBPD) method for earthquake-resistant structures: an overview. The Structural Design of Tall and Special Buildings. 2010;19:115-37.

[94] Islam A, Imanpour A. Stability of wide-flange columns in steel moment-resisting frames: evaluation of the Canadian seismic design requirements. Bulletin of Earthquake Engineering. 2022;20:1591-617.

[95] Lamarche C-P, Tremblay R. Seismically induced cyclic buckling of steel columns including residual-stress and strain-rate effects. Journal of Constructional Steel Research. 2011;67:1401-10.

[96] Sen AD, Roeder CW, Lehman DE, Berman JW. Nonlinear modeling of concentrically braced frames. Journal of Constructional Steel Research. 2019;157:103-20.

[97] Filippou FC, Popov EP, Bertero VV. Effects of bond deterioration on hysteretic behavior of reinforced concrete joints. Berkeley, Calif.; Springfield, Va.: Earthquake Engineering Research Center, University of California ; For sale by the National Technical Information Service, U.S. Dept. of Commerce; 1983.

[98] Ashrafi A, Imanpour A. Seismic response of steel multi-tiered eccentrically braced frames. Journal of Constructional Steel Research. 2021;181:106600.

[99] Zareian F, Medina RA. A practical method for proper modeling of structural damping in inelastic plane structural systems. Computers & Structures. 2010;88:45-53.

[100] Gupta A, Krawinkler H. Seismic Demands for Performance Evaluation of Steel Moment Resisting Frame Structures (SAC Task 5.4.3). Department of Civil Engineering, Stanford University, Stanford, CA, USA: John A Blume Earthquake Engineering Center Technical Report No. 132; 1999.

[101] Gupta A, Krawinkler H. Seismic demands for the performance evaluation of steel moment resisting frame structures;. The John A. Blume Earthquake Engineering Center: Stanford University; 1999.

[102] Maity A, Kanvinde A, Rosa DIH, Sousa AdCe, Lignos DG. A Displacement-Based Fiber Element to Simulate Interactive Lateral Torsional and Local Buckling in Steel Members. Journal of Structural Engineering. 2023;149:04023045.

[103] USGS. United States Geological Survey; 2012a.

[104] Thatcher W. Silent Slip on the Cascadia Subduction Interface. Science. 2001;292:1495-6.

[105] Cascadia Subduction Zone. Pacific Northwest Seismic Network 2012.

[106] Sancheta TD, Darragh RB, Stewart JP, Seyhan E, Silva WJ, Chiou BSJ et al. PEER 2013/03 – PEER NGA-West2 Database.

[107] National Research Institute for Earth Science and Disaster Resilience (2017/04/01-Present). NIED K-NET, KiK-net.

[108] Center for Engineering Strong-Motion Data (CESMD).

[109] Baker JW, Allin Cornell C. Spectral shape, epsilon and record selection. Earthquake Engineering & Structural Dynamics. 2006;35:1077-95.

[110] Haselton CB, Liel AB, Deierlein GG, Dean BS, Chou JH. Seismic Collapse Safety of Reinforced Concrete Buildings. I: Assessment of Ductile Moment Frames. Journal of Structural Engineering. 2011;137:481-91.

[111] Zareian F, Krawinkler H. Simplified performance-based earthquake engineering, John A Blume Earthquake Engineering Center Technical Report No. 169. Department of Civil Engineering, Stanford University, Stanford, CA, USA2009.

[112] Tartaglia R, D'Aniello M, Landolfo R. Seismic performance of Eurocode-compliant ductile steel MRFs. Earthquake Engineering & Structural Dynamics. 2022;51:2527-52.

[113] Mokhtari M, Islam A, Imanpour A. Development, seismic performance and collapse evaluation of steel moment-resisting knee braced frame. Journal of Constructional Steel Research. 2022;197:107262.

[114] Sabelli R. Research on improving the design and analysis of earthquake-resistant steel-braced frames. NEHRP fellowship report no. PF2000-9. Oakland. CA: Earthquake Engineering Research Institute; 2001.

[115] Uriz P, Mahin SA. Toward earthquake-resistant design of concentrically braced steel-frame structures. PEER Rep. 2008/08. Univ. of California, Berkeley, CA: Pacific Earthquake Engineering Research Center; 2008.

[116] Tremblay R, Archambault M-H, Filiatrault A. Seismic Response of Concentrically Braced Steel Frames Made with Rectangular Hollow Bracing Members. Journal of Structural Engineering. 2003;129:1626-36.

[117] Nakashima M, Roeder CW, Maruoka Y. Steel Moment Frames for Earthquakes in United States and Japan. Journal of Structural Engineering. 2000;126:861-8.

[118] Zhang X, Ricles JM. Experimental Evaluation of Reduced Beam Section Connections to Deep Columns. Journal of Structural Engineering. 2006;132:346-57.

[119] Montuori R, Nastri E, Piluso V. Rigid-plastic analysis and moment–shear interaction for hierarchy criteria of inverted Y EB-Frames. Journal of Constructional Steel Research. 2014;95:71-80.

[120] American Institute of Steel Construction. ANSI/AISC 360-16 Specification for Structural Steel Buildings. AISC; 2016.

[121] American Institute of Steel Construction. Steel Construction Manual. 15 ed: American Institute of Steel Construction; 2017.

[122] Krawinkler H, Zareian F. Prediction of collapse—how realistic and practical is it, and what can we learn from it? The Structural Design of Tall and Special Buildings. 2007;16:633-53.

[123] Mitchell D, Tremblay R, Karacabeyli E, Paultre P, Saatcioglu M, Anderson DL. Seismic force modification factors for the proposed 2005 edition of the National Building Code of Canada. Canadian Journal of Civil Engineering. 2003;30:308-27.

[124] American Society of Civil Engineers. Minimum design loads and associated criteria for buildings and other structures : ASCE/SEI 7-162017.

[125] Boore DM, Atkinson GM. Ground-Motion Prediction Equations for the Average Horizontal Component of PGA, PGV, and 5%-Damped PSA at Spectral Periods between 0.01 s and 10.0 s. Earthquake Spectra. 2008;24:99-138.

[126] Zhao JX, Zhang J, Asano A, Ohno Y, Oouchi T, Takahashi T et al. Attenuation Relations of Strong Ground Motion in Japan Using Site Classification Based on Predominant Period. Bulletin of the Seismological Society of America. 2006;96:898-913.

[127] Atkinson GM, Macias M. Predicted Ground Motions for Great Interface Earthquakes in the Cascadia Subduction Zone. Bulletin of the Seismological Society of America. 2009;99:1552-78.

[128] Ghofrani H, Atkinson GM. Ground-motion prediction equations for interface earthquakes of M7 to M9 based on empirical data from Japan. Bulletin of Earthquake Engineering. 2014;12:549-71.

[129] NSHM Hazard Tool. United States Geological Survey; 2023.

[130] Bosco M, Tirca L. Numerical simulation of steel I-shaped beams using a fiber-based damage accumulation model. Journal of Constructional Steel Research. 2017;133:241-55.

[131] International Code Council, Building Officials, International Code Administrators, International Conference of Building Officials, International Southern Building Code Congress. *International Building Code: IBC 2000*. International Code Council; 2000.

[132] Bruneau M, MacRae G. Reconstructing Christchurch: A Seismic Shift in Building Structural Systems. 2017.

[133] Uang C-M, Bruneau M. State-of-the-Art Review on Seismic Design of Steel Structures. Journal of Structural Engineering. 2018;144:03118002.

[134] Hamburger RO. The ATC-58 Project: Development of Next-Generation Performance-Based Earthquake Engineering Design Criteria for Buildings. Structures Congress2006. p. 1-8.

[135] Kitayama S, Morales Moncayo EA, Athanasiou A. Inspection and repair considerations for downtime assessment of seismically isolated buildings. Soil Dynamics and Earthquake Engineering. 2023;164:107618.

[136] Yazdanpanah O, Dolatshahi KM, Moammer O. Rapid seismic fragility curves assessment of eccentrically braced frames through an output-only nonmodel-based procedure and machine learning techniques. Engineering Structures. 2023;278:115290.

[137] Shahnazaryan D, O'Reilly GJ, Monteiro R. On the seismic loss estimation of integrated performance-based designed buildings. Earthquake Engineering & Structural Dynamics. 2022;51:1794-818.

[138] Peres R, Couto R, Sousa I, Castro JM, Bento R. Modelling and evaluation of brittle shear effects on the seismic performance and loss assessment of RC buildings. Engineering Structures. 2023;275:115230.

[139] Hwang S-H, Mangalathu S, Shin J, Jeon J-S. Estimation of economic seismic loss of steel moment-frame buildings using a machine learning algorithm. Engineering Structures. 2022;254:113877.

[140] Athanasiou A, Dakour M, Pejmanfar S, Tirca L, Stathopoulos T. Multihazard Performance-Based Assessment Framework for Multistory Steel Buildings. Journal of Structural Engineering. 2022;148:04022054.

[141] Kitayama S, Cilsalar H. Seismic loss assessment of seismically isolated buildings designed by the procedures of ASCE/SEI 7-16. Bulletin of Earthquake Engineering. 2022;20:1143-68.

[142] Skoulidou D, Romão X. Are seismic losses affected by the angle of seismic incidence? Bulletin of Earthquake Engineering. 2021;19:6271-302.

[143] Moradnezhad F, Zeinoddini M, Fanaie N, Moghaddam H, Khanmohammadi M, Zandi AP et al. A novel ductile CHS knee bracing system for rehabilitation of earthquake-damaged buildings: The case of Sarpol-e-Zahab (Iran) earthquake. Journal of Building Engineering. 2023;65:105748.

[144] Mokhtari M, Imanpour A. Proposed seismic design parameters for the moment-resisting knee-braced frame system. Engineering Structures. 2023;276:115318.

[145] Lignos DG, Hikino T, Matsuoka Y, Nakashima M. Collapse Assessment of Steel Moment Frames Based on E-Defense Full-Scale Shake Table Collapse Tests. Journal of Structural Engineering. 2013;139:120-32.

[146] Liu J. Experimental and Analytical Studies of the Cyclic Behavior of Simple Connections in Steel Frame Buildings: University of Berkely; 2000.

[147] Baradaran Shoraka M, Yang TY, Elwood KJ. Seismic loss estimation of non-ductile reinforced concrete buildings. Earthquake Engineering & Structural Dynamics. 2013;42:297-310.

[148] Chopra AK. Dynamics of Structures: Theory and Applications to Earthquake Engineering: Pearson; 2017.

[149] Mitrani-Reiser J, Beck JL. Incorporating Losses due to Repair Costs, Downtime and Fatalities in Performance-based Earthquake Engineering. 2007.

[150] Statistics Canada. https://www.statcan.gc.ca/en/subjects-start/construction

[151] Goulet CA, Haselton CB, Mitrani-Reiser J, Beck JL, Deierlein GG, Porter KA et al. Evaluation of the seismic performance of a code-conforming reinforced-concrete frame building—

from seismic hazard to collapse safety and economic losses. Earthquake Engineering & Structural Dynamics. 2007;36:1973-97.

[152] BTY Group. Canadian Market Intelligence Report. https://www.bty.com/; 2022.

[153] Baker JW. Efficient Analytical Fragility Function Fitting Using Dynamic Structural Analysis. Earthquake Spectra. 2015;31:579-99.

[154] McCormick J, Hiroshi A, Ikenaga M, Nakashima M. Permissible residual deformation levels for building structures considering both safety and human elements. The 14th World Conference on Earthquake Engineering. Beijing, China Seismological Press of China; 2008.

[155] Prestandard for Performance-Based Wind Design,: American Society of Civil Engineers; 2019.

[156] Judd JP, Charney FA. Inelastic Behavior and Collapse Risk for Buildings Subjected to Wind Loads. Structures Congress 20152015. p. 2483-96.

[157] CSI. SAP2000 Integrated Software for Structural Analysis and Design. Berkeley, California: Computers and Structures Inc.

[158] Applied Technology Council. FEMA P440A: Effects of Strength and Stiffness Degradation on Seismic Response. Washington, D.C.2009.

[159] Griffis LG. Serviceability Limit States Under Wind Load. Engineering Journal. 1993;30:1-16.

[160] Lamb S, Kwok KCS, Walton D. A longitudinal field study of the effects of wind-induced building motion on occupant wellbeing and work performance. Journal of Wind Engineering and Industrial Aerodynamics. 2014;133:39-51.

[161] Lamb S, Kwok KCS. The fundamental human response to wind-induced building motion. Journal of Wind Engineering and Industrial Aerodynamics. 2017;165:79-85.

[162] Chang F-K. Human Response to Motions in Tall Buildings. Journal of the Structural Division. 1973;99:1259-72.

[163] ISO 10137: Basis for Design Structures : Serviceability of Buildings and Walkways Against Vibrations: British Standard; 2007.

[164] Shinozuka M, Deodatis G. Simulation of Stochastic Processes by Spectral Representation. Applied Mechanics Reviews. 1991;44:191.

[165] MOLIT (Ministry of Land I, and Transport);. Korean building code. KBC 2016. Sejong, South Korea: Sejong, South Korea: MOLIT (Korea); 2016.

Appendix A

This appendix presents key design calculations for the 5-storey MKF-P presented in Chapter 3. Design bending moment demands in the intermediate beam segments were calculated under gravity plus seismic loads according to the PBPD procedure developed in Chapter 3. The final design moments denoted by M_f are summarized in Table A-1 and design steps for intermediate beam segments are outlined in Table A-1.

Table A-1. Flexural demands in the intermediate beam segments of MKF-P.

Storey	M_f $(kN-m)$	$w(\frac{kN}{m})$	$L_b\ (m)$	$L_c\ (m)$	$L_{k,g}\ (m)$
5	284	17.55	5.4	1.8	$L_{k,g}=\frac{1.8}{\cos(45)}=2.54$
4	439	32.1	5.4	1.8	2.54
3	523	32.1	5.4	1.8	2.54
2	579	32.1	5.4	1.8	2.54
1	611	32.1	5.4	1.8	2.54

Step 1) Design of intermediate beam segments assuming sufficient lateral bracing to prevent LTB:

Table A-2. Summary of design calculations for the intermediate beam segments of MKF-P

Storey	Cross-Section	$\frac{b_f}{2t_f}$	$\frac{h}{t_w}$	Flange Class	Web Class	Strength Check	Utilization Ratio $(\frac{M_f}{M_r})$
5	W460×52	7.06	53.5	1	1	$M_r=0.9Z_xF_y=0.9\times1090\times10^3\times345\times10^{-6}=338\ kN-m$	0.84
4	W530×66	7.22	53.6	1	1	$M_r=0.9\times1560\times10^3\times345\times10^{-6}=484\ kN-m$	0.91
3	W530×74	6.10	49.4	1	1	$M_r=0.9\times1800\times10^3\times345\times10^{-6}=559\ kN-m$	0.94
2	W610×82	6.94	54.6	1	1	$M_r=0.9\times2200\times10^3\times345\times10^{-6}=683\ kN-m$	0.85
1	W610×82	6.94	54.6	1	1	$M_r=0.9\times2200\times10^3\times345\times10^{-6}=683\ kN-m$	0.89

Step 2) Design of beam stubs:

The beam stubs are subject to a combination of axial tension and flexural moment or a combination of axial compression and flexural moment. Based on Figure 3-2, the axial tension and compression in the knee braces can be obtained as follows:

$$V_R = \frac{2M_{pr,b}}{L_b} + \frac{wL_b}{2} \quad \text{(A-1)}$$

$$V_L = V_R - wL_b \quad \text{(A-2)}$$

$$C_k = \frac{1}{\sin(\theta)}\left(\frac{M_{pr,b}}{L_c} + V_R + \frac{wL_c}{2}\right) \quad \text{(A-3)}$$

$$T_k = \frac{1}{\sin(\theta)}\left(\frac{M_{pr,b}}{L_c} + V_L - \frac{wL_c}{2}\right) \quad \text{(A-4)}$$

The axial forces in the first storey knee braces of MKF-P are given below:

$M_{pr,b} = R_{sh}R_yF_yZ_x = 1.3 \times 385 \times 2200 \times 10^{-3} = 1101\ kN-m$

$V_R = 2 \times \frac{1101}{5.4} + 32.1 \times \frac{5.4}{2} = 495\ kN$

$V_L = 495 - 32.1 \times 5.4 = 322\ kN$

$C_k = \frac{1}{\sin(45)}\left(\frac{1101}{1.8} + 495 + 32.1 \times \frac{1.8}{2}\right) = 1606\ kN$

$T_k = \frac{1}{\sin(45)}\left[\frac{1101}{1.8} + 322 - 32.1 \times \frac{1.8}{2}\right] = 1280\ kN$

The axial forces in the first-storey beam stubs assuming adequate lateral bracing provided to the bottom flange and full lateral bracing to the top flange and ignoring the counteracting effect of the intermediate beam segment's axial force are:

$C_f = T_k \cos(45) = 905\ kN$

$T_f = C_k \cos(45) = 1135\ kN$

$M_f = 1101\ kN - m$

Try W610×140 for the first-storey beam stubs:

$$\frac{b_f}{2_{tf}} = 5.2 < \frac{140}{\sqrt{F_y}} = 7.6 \rightarrow Flange\ is\ Class\ 1$$

$$\frac{h}{t_w} = 42 < \frac{1100\left(1 - \frac{0.39C_f}{AF_y}\right)}{\sqrt{F_y}} = \frac{1100\left(1 - \frac{0.39 \times 905}{17900 \times 345 \times 0.001}\right)}{\sqrt{345}} = 56 \rightarrow Web\ is\ Class\ 1$$

$$\omega_{1x} = 1.0\ (distributed\ load) \rightarrow C_{ex} = \frac{\pi^2 EI_x}{L_c^2} = \pi^2 \times \frac{200000 \times 1120 \times 10^3}{1800^2} = 682343\ kN \rightarrow U_{1x} = \frac{1}{1 - \frac{C_f}{C_{ex}}} = \frac{1}{1 - \frac{905}{682343}}$$

$$= 1.001$$

$$\lambda_x = \frac{K_x L_c}{\pi r_x}\sqrt{\frac{F_y}{E}} = 1 \times \frac{1800}{\pi \times 251}\sqrt{\frac{345}{200000}} = 0.0955$$

$$C_{rx} = \frac{0.9AF_y}{(1 + \lambda_x^{2n})^{\frac{1}{n}}} = \frac{0.9 \times 17900 \times 345 \times 10^{-3}}{(1 + 0.0955^{2\times 1.34})^{\frac{1}{1.34}}} = 5552\ kN$$

$$M_{rx} = 0.9 Z_x F_y = 0.9 \times 4160 \times 345 \times 10^{-3} = 1292\ kN - m$$

$$Overall\ Member\ Strength: \frac{C_f}{C_{rx}} + \frac{0.85 U_{1x} M_{fx}}{M_{rx}} = \frac{905}{5552} + \frac{0.85 \times 1.001 \times 1101}{1292} = 0.89 < 1.0$$

$$Tension\ and\ Bending: \frac{T_f}{T_r} + \frac{0.85 M_{fx}}{M_{rx}} = \frac{1135}{0.9 \times 17900 \times 345 \times 10^{-3}} + \frac{0.85 \times 1101}{1292} = 0.93 < 1.0$$

$$Moment\ Only: \frac{M_{fx}}{M_{rx}} = \frac{1101}{1292} = 0.85 < 1.0$$

The selected section for the beam stub meets all the requirements for wide flange beam-columns.

Step 3) Design of knee braces:

The first-storey knee braces are designed as follows:

Try HSS152×152×12.7 for the knee brace element of the first storey:

$$\frac{b_o}{t} = 10 < \frac{525}{\sqrt{F_y}} = 28.3 \rightarrow Section\ is\ Class\ 2$$

$$L_k = 0.75 \times \left(2540 - \frac{0.5 d_{bs}}{\sin(45)} - \frac{0.5 d_c}{\cos(45)}\right) = 0.75 \times \left(2540 - \frac{0.5 \times 617}{\sin(45)} - \frac{0.5 \times 500}{\cos(45)}\right) = 1260\ mm \rightarrow \lambda = \frac{K L_k}{\pi r} \sqrt{\frac{F_y}{E}}$$

$$= 1 \times \frac{1400}{\pi \times 56.6} \sqrt{\frac{345}{200000}} = 0.33$$

$$C_r = \frac{0.9AF_y}{(1+\lambda^{2n})^{\frac{1}{n}}} = \frac{0.9 \times 6683 \times 345 \times 10^{-3}}{(1+0.33^{2\times 1.34})^{\frac{1}{1.34}}} = 2018 \rightarrow \frac{C_f}{C_r} = \frac{1606}{1999} = 0.8 < 1.0$$

The selected section is adequate to carry the maximum expected axial compression.

Step 4) Design of column trees:

Upon applying the maximum probable moments and shear forces expected at the ends of intermediate beam segments, the distribution of moments, axial, and shear demands are presented for the rightmost exterior column tree of MKF-P in Figure A-1.

Try W460×235 section for the exterior column tree extending from stories 1 to 3. Assuming plastic hinges form at the base of the first-storey column, the following requirements shall be met according to Clause 27.3 of CSA S16-19:

$$\frac{L_{cr}}{r_y} = \frac{4300}{69.6} = 62 < \frac{25000}{Fy} = 72$$

$$\frac{b_f}{2_{tf}} = 3.92 < \frac{140}{\sqrt{F_y}} = 7.6 \rightarrow Flange\ is\ Class\ 1$$

$$C_f = 2954\ kN < 0.5AF_y = 0.5 \times 29900 \times 345 \times 0.001 = 5157\ kN\ (The\ building\ is\ located\ \ in\ SC4\ according\ to\ 2015\ NBC)$$

$$C_f = 2954\ kN > 0.15AF_y = 1547kN \rightarrow \frac{h}{t_w} = 19.8 < \frac{700}{\sqrt{F_y}} = \frac{700}{\sqrt{345}} = 38 \rightarrow Web\ is\ Class\ 1$$

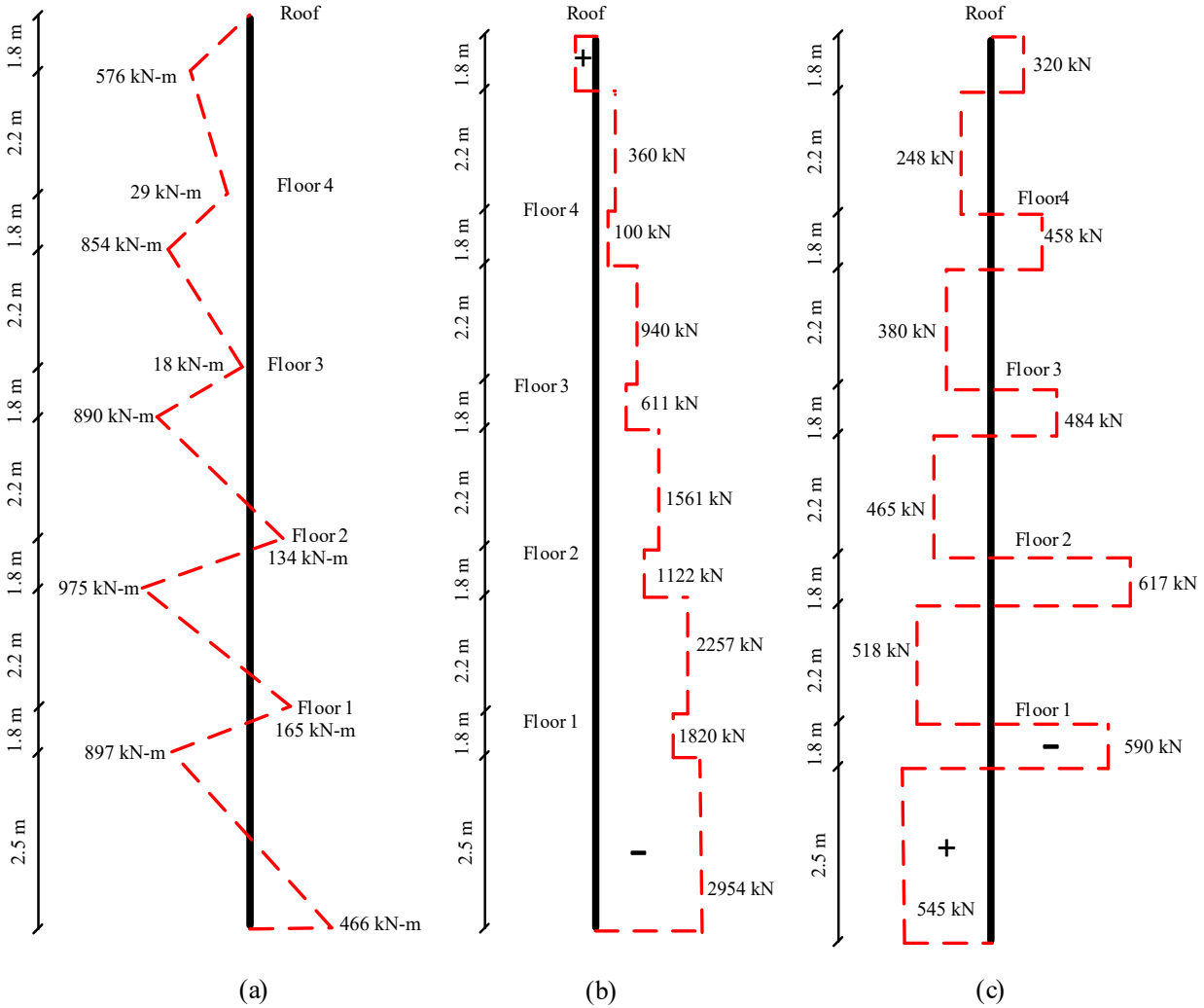

Figure A-1. Distribution of design flexural, axial, and shear demands under gravity plus lateral loads along the rightmost exterior column tree of MKF-P

Check the long segment of the column:

$C_f = 2954\ kN, M_{fx} = 897\ kN - m$

$\kappa = \frac{466}{897} = 0.52 \rightarrow \omega_{1x} = \max(0.4, 0.6 - 0.4\kappa) = 0.4$

$C_{ex} = \frac{\pi^2 E I_x}{L^2} = 0.001 \times \frac{\pi^2 \times 200000 \times 1270 \times 10^6}{2500^2} = 401100\ kN \rightarrow U_{1x} = \frac{0.4}{1 - \frac{2954}{401100}} = 0.403$

$\lambda_x = \frac{KL}{\pi r_x}\sqrt{\frac{F_y}{E}} = \frac{1 \times 2500}{\pi \times 206} \times \sqrt{\frac{345}{200000}} = 0.16 \rightarrow C_{rx} = \frac{0.9 \times 29900 \times 345 \times 0.001}{(1 + 0.16^{2 \times 1.34})^{1/1.34}} = 9234\ kN$

$M_{rx} = 0.9 F_y Z_x = 0.9 \times 345 \times 5830 \times 10^{-3} = 1810\ kN - m$

$Cross\ Sectional\ Strength: \frac{C_f}{C_{r0}} + \frac{0.85 \times \max(U_{1x}, 1.0) \times M_{fx}}{M_{rx}} = \frac{2954}{9284} + \frac{0.85 \times 1.0 \times 897}{1810} = 0.74 < 1.0$

$Overall\ Member\ Strength: \frac{C_f}{C_{rx}} + \frac{0.85 \times U_{1x} \times M_{fx}}{M_{rx}} = \frac{2954}{9234} + \frac{0.85 \times 0.403 \times 897}{1810} = 0.49 < 1.0$

Check the short segment of the column:

$C_f = 1820\ kN, M_{fx} = 897\ kN - m$

$\kappa = \frac{165}{897} = 0.18 \rightarrow \omega_{1x} = \max(0.4, 0.6 - 0.4\kappa) = 0.53$

$C_{ex} = \frac{\pi^2 E I_x}{L^2} = 0.001 \times \frac{\pi^2 \times 200000 \times 1270 \times 10^6}{1800^2} = 773726\ kN \rightarrow U_{1x} = \frac{0.53}{1 - \frac{1820}{773726}} = 0.53$

$$\lambda_x = \frac{KL}{\pi r_x}\sqrt{\frac{F_y}{E}} = \frac{1 \times 1800}{\pi \times 206} \times \sqrt{\frac{345}{200000}} = 0.12 \rightarrow C_{rx} = \frac{0.9 \times 29900 \times 345 \times 0.001}{(1 + 0.12^{2 \times 1.34})^{1/1.34}} = 9260\ kN$$

$$Cross\ Sectional\ Strength\text{:}\ \frac{C_f}{C_{r0}} + \frac{0.85 \times \max(U_{1x}, 1.0) \times M_{fx}}{M_{rx}} = \frac{1810}{9284} + \frac{0.85 \times 1.0 \times 897}{1810} = 0.62 < 1.0$$

$$Overall\ Member\ Strength\text{:}\ \frac{C_f}{C_{rx}} + \frac{0.85 \times U_{1x} \times M_{fx}}{M_{rx}} = \frac{1810}{9260} + \frac{0.85 \times 0.53 \times 897}{1810} = 0.42 < 1.0$$

Check lateral-torsional buckling of the entire column segment:

$C_f = 2954\ kN, M_{fx} = 897\ kN - m$

$$C_{ex} = \frac{\pi^2 E I_x}{L^2} = 0.001 \times \frac{\pi^2 \times 200000 \times 1270 \times 10^6}{4300^2} = 135580\ kN$$

$$\omega_{1x} = 1.0\ (column\ subjected\ to\ a\ point\ load\ at\ knee - to - column\ connection) \rightarrow U_{1x} = \frac{1}{1 - \frac{2954}{135580}} = 1.022$$

Using the moment distribution diagram at the first storey, the moment demands for LTB calculations are as follows:

$M_a = 122\ kN - m, M_b = 707\ kN - m, M_c = 469\ kN - m, M_{max} = 897\ kN - m$

$$\omega_2 = \min\left(2.5, \frac{4M_{max}}{\sqrt{M_{max}^2 + 4M_a^2 + 7M_b^2 + 4M_c^2}}\right) = \min(2.5, 1.57) = 1.57$$

$$M_u = \frac{\omega_2 \pi}{L}\sqrt{EI_y GJ + \left(\frac{\pi E}{L}\right)^2 I_y C_w}$$

$$= 10^{-6} \times 1.57$$

$$\times \frac{\pi}{4300}\sqrt{200000 \times 144 \times 10^6 \times 77000 \times 10500 \times 10^3 + \left(\pi \times \frac{200000}{4300}\right)^2 \times 144 \times 10^6 \times 7790 \times 10^9}$$

$$= 7783\ kN - m \rightarrow\ M_u > 0.67M_p \rightarrow M_r = \min\left(0.9M_p, 1.15 \times 0.9 \times M_p \times \left[1 - \frac{0.28M_p}{M_u}\right]\right) = 1810\ kN - m$$

$$\lambda_y = \frac{KL}{\pi r_y}\sqrt{\frac{F_y}{E}} = \frac{1 \times 4300}{\pi \times 69.6} \times \sqrt{\frac{345}{200000}} = 0.82 \rightarrow C_{rx} = \frac{0.9 \times 29900 \times 345 \times 0.001}{(1 + 0.82^{2 \times 1.34})^{1/1.34}} = 6580\ kN$$

$$LTB\text{:}\ \frac{C_f}{C_{ry}} + \frac{0.85 \times U_{1x} \times M_{fx}}{M_r} = \frac{2954}{6580} + \frac{0.85 \times 1.022 \times 897}{1810} = 0.88 < 1.0$$

Moment only check:

$$\frac{M_{fx}}{M_{rx}} = \frac{897}{1810} = 0.5 < 1.0$$

Shear check:

$$V_f = 590\ kN$$

$$\frac{h}{t_w} = 19.8 < \frac{1014}{\sqrt{F_y}} = 55 \rightarrow F_s = 0.66F_y = 228\ MPa \rightarrow V_r = 0.9dt_wF_s = 0.9 \times 500 \times 20.6 \times 228 \times 0.001 = 2113\ kN \rightarrow \frac{V_f}{V_r}$$

$$= 0.28 < 1.0$$

The selected cross section meets all the stability and strength requirements. Since the selected cross section is meant to extend from stories 1 to 3, the same calculations presented here shall be performed to verify the strength and stability of the column in stories 2 and 3.

Appendix B

This appendix provides the details of the selected ground motions used throughout different phases of this study.

Table B-1. Selected Ground Motion Records

Source	ID	Event	Magnitude* (M_w)	Depth† (km)	Year	Recording Station‡	Scale Factor (Phase I)	Scale Factor (Phase II)	Scale Factor (Phase III)
Crustal	C01	San Fernando	6.6	9.0	1971	Castaic - Old Ridge Route	1.33	1.33	1.65
	C02	San Fernando	6.6	9.0	1971	Pasadena - CIT Athenaeum	2.67	2.67	3.20
	C03	Loma Prieta	6.9	17.2	1989	Coyote Lake Dam - Southwest Abutment	2.08	2.08	2.50
	C04	Loma Prieta	6.9	17.2	1989	Gilroy Array #6	3.04	2.85	3.60
	C05	Hector Mine	7.1	13.7	1999	Hector	1.78	1.70	2.10
	C06	Landers	7.3	1.1	1992	Desert Hot Springs	2.26	2.20	2.70
	C07	Northridge-01	6.7	18.2	1994	LA - Brentwood VA Hospital	1.86	1.86	2.20
	C08	Northridge-01	6.7	18.2	1994	Sunland - Mt Gleason Ave	2.53	2.53	3.10
	C09	Superstition Hills-02	6.5	10.9	1987	Superstition Mtn Camera	0.61	0.61	0.70
	C10	Morgan Hill	6.2	8.2	1984	Anderson Dam (Downstream)	0.91	0.98	1.15
	C11	Kern County	7.4	6.0	1952	Taft Lincoln School	2.05	2.05	2.50
Subduction Intraslab	D01	Geiyo, Japan	6.8	50.0	2001	HRS020	2.21	2.65	2.53
	D02	Geiyo, Japan	6.8	50.0	2001	HRSH07	1.85	2.30	2.53
	D03	Geiyo, Japan	6.8	50.0	2001	EHM015	1.05	1.17	1.54
	D04	Miyagi, Japan	7.1	42.0	2011	IWT026	1.39	1.55	1.87
	D05	Miyagi, Japan	7.1	42.0	2011	MYG016	2.10	2.42	2.75
	D06	Miyagi, Japan	7.1	42.0	2011	IWTH24	2.34	2.88	2.86
	D07	Nisqually, WA	6.8	51.8	2001	Seattle, WA Ship Canal Bridge	4.09	4.57	4.95
	D08	Nisqually, WA	6.8	51.8	2001	Olympia, WSDOT Test Lab	1.79	2.30	2.20
	D09	Nisqually, WA	6.8	51.8	2001	Seattle Crowne Plaza Hotel	2.83	3.16	3.63
	D10	Olympia, WA	6.8	70.0	1949	Olympia Hwy Test Lab	2.16	2.42	2.75

	D11	Puget Sound, WA	6.7	59.0	1965	Seattle Federal Building	4.57	4.77	5.5
Subduction Interface	I01	Tohoku, Japan	9.1	29.0	2011	AKT017	4.14	4.37	5.30
	I02	Southern Peru	8.4	33.0	2001	POCONCHILE	1.08	1.37	1.82
	I03	Tokachi-Oki, Japan	8.2	27.0	2003	TKCH04	3.58	3.99	4.51
	I04	Tokachi-Oki, Japan	8.2	27.0	2003	HKD084	1.22	1.48	1.65
	I05	Tokachi-Oki, Japan	8.2	27.0	2003	HKD087	3.03	3.76	4.18
	I06	Tohoku, Japan	9.1	29.0	2011	AKT017	4.34	5.76	6.11
	I07	Pisco, Peru	8.0	39.0	2007	UNICA	1.11	1.48	1.60
	I08	Maule, Chile	8.8	22.9	2010	Santiago Centro	2.28	2.85	3.30
	I09	Maule, Chile	8.8	22.9	2010	LACH (Component b)	1.49	1.81	1.43
	I10	Tohoku, Japan	9.1	29.0	2011	AOM008	4.00	4.57	5.40
	I11	Algarrobo, Chile	8.0	33.0	1985	Melipilla	2.15	2.96	3.19

* PEER Ground Motion NGA-West2 Database for Crustal events, USGS Database for Intraslab and Interface events

† Based on USGS Database

‡ Station name or code